UNIVERSITÉ DE STRASBOURG

ÉCOLE DOCTORALE DE PHYSIQUE ET CHIMIE-PHYSIQUE

Institut de Physique et Chimie des Matériaux de Strasbourg

THÈSE présentée par :

Olga GLADII

soutenu le 16 décembre 2016

pour obtenir le grade de : **Docteur de l'Université de Strasbourg**
Discipline/ Spécialité : Physique/ Physique de la Matière Condensée

Spin wave propagation and its modification by an electrical current in Py/Al_2O_3, Py/Pt and Fe/MgO films

DIRECTEUR DE THÈSE :

M. Matthieu BAILLEUL	Chargé de recherche CNRS, IPCMS

RAPPORTEURS :

M. Christian BACK	Professeur, Universität Regensburg
M. Laurent VILA	Chercheur CEA, Spintec

EXAMINATEURS :

M. Abdelmadjid ANANE (membre invité)	Maître de conférences, Unité mixte de physique CNRS, Thales
M. Robert STAMPS	Professeur, University of Glasgow

Acknowledgement

These three years of my PhD at IPCMS have been an amazing time during which I have learned a lot of things and have met the interesting people. I have worked in a small friendly team well-organized by my advisor Matthieu Bailleul. It is thanks to him and to people who directly worked on our project I could get these high quality results. Therefore I would like to express my acknowledgements to all of them.

First of all, I want to thank my advisor Matthieu Bailleul for his continuous support from the first days of my stay at IPCMS. He helped me to deepen my general knowledge in magnetism and to discover a particular world of spin waves. He patiently guided me through all period of my PhD, starting from the advices on samples preparation and the use of experimental setup, and ending by a huge help in writing this thesis. He is a person always open to the questions and discussions. I also thank him for supporting my attendance at various conferences giving me the opportunity to expand my scientific outlook and to meet a lot of amazing people. Apart from his research assistance, I'm grateful to Matthieu for his understanding, emotional support and encouragement whenever I needed.

Beside my advisor, I would like to express my gratitude to Yves Henry, a person full of energy and enthusiasm. As Matthieu, he always founds the time for discussions and teaching. Special thanks to him for providing me the basic knowledge in numerical modeling and for correcting me in my English and French.

I'm grateful to the members of jury, Christian Back, Laurent Vila, Robert Stamps and Abdelmadjid Anane for reviewing and commenting on this manuscript.

I want also to thank the excellent staff of clean room, Sabine Siegwald, Romain Bernard and Hicham Majjad, with whom I have spent a large amount of time working on samples fabrication. Thanks to them for their valuable guidance and for providing me the experience working with nanofabrication tools. Special thanks to Sabine and Romain for their support not only in professional way, but also in my personal life.

My sincere gratitude also goes to David Halley and Manuel Acosta for their help in thin films growth and to Alain Carvalho for giving me the necessary knowledge for working with electron microscopy.

Also I acknowledge our collaborators from Thales group led by Abdelmadjid Anane and the group from Institut d'Electronique Fondamentale led by Joo-Von Kim for their valuable contributions and fruitful discussions on our mutual project.

I also thank the secretary of our department Veronique Wernher for her help in administrative assistance and for her quotidian amiability.

I appreciate the good time spent together with the students and postdocs: Guillaume Froehlicher, Damien Louis, Julien Bran, Etienne Lorchat, Oksana Toma, Oleksandr Kovalenko, Stanislav Makarchuk, Dominik Metten, Tindara Verduci, Olivia Zill, Florian Godel, Silvia Zanettini, Nicolas Bachellier, Michael Chong, Kerstin Bucker.

Last but not least, I would like to thank my family who support me throughout all my life and always believe in me. I want to express my gratitude to my dear husband for his love and care, moral support in everyday life and precious help in my academic endeavors, which enabled me to complete this thesis.

Olga GLADII
Strasbourg 2016

Contents

Introduction

State of the art and objectives

Although the concept of spin wave as collective excitation of electron's spin was introduced by Bloch 80 years ago [13], the study of magnetic dynamics has recently attracted a renewed interest from both the fundamental and applied points of view. The research field which deals with magnetic phenomena related with spin waves is called magnonics. The aim of magnonics is to generate, detect and manipulate the spin waves to carry and store the information. The functionality of magnonics devices depends on a large extent on the damping factor of the ferromagnetic material used (which defines the distance over which the information is carried). That's why the search of ***materials*** with a small damping factor is essential. A possibility to propagate spin waves over long distances in materials with a moderate damping, is to amplify them. Among the different proposed methods of ***spin wave amplification***, such as parametric amplification [63, 14], magneto-electric amplification [66, 19], the amplification by spin Hall effect induced spin transfer torque (SHE-STT) [27, 39] is particularly promising. The principle of spin wave amplification by SHE-STT is to compensate part of the intrinsic Gilbert damping of the material by means of a transfer of spin momentum from the conduction electrons to the magnetization. An attractive aspect in using spin waves for practical application is their ***wave nature***. It was shown, that the spin waves, as sound or light waves, can reflect [41], interfere [103], be subjected to a Doppler effect [135], etc, and that these wave effects can be used for data processing [68]. Moreover, in certain circumstances, spin waves also shows a very specific property of non-reciprocal propagation, which means that two counter-propagating spin waves can possess different amplitude and/or phase [65, 116, 40]. It was proposed to use this non-reciprocal character for spin-wave logic devices, where the logic operations are based on difference between the amplitude and/or phase, which can be tuned by a field or dc-current [60, 113]. Let us now develop a little bit more each of these points, which are of particular importance for an efficient manipulation of spin waves.

Materials

Up to now, research in magnonics has concentrated on a few materials containing iron, such as Permalloy (Py), CoFeB, Yttrium Iron Garnet (YIG), or Heusler alloys. Among all these materials, the ferrimagnetic insulator YIG has the lowest known damping factor in the range of 10^{-4} [140, 80]. A drawback of YIG is its low saturation magnetization (about 0.18 T), which translates into a relatively small group velocity and weak signals in both inductive and magneto-optical measurements. Moreover, it is still difficult to grown high quality thin YIG films. Among the ferromagnetic metals, the most widely used is permalloy (Py=$Ni_{80}Fe_{20}$), which is magnetically very homogenous and has a moderate damping of about 0.008 and a saturation magnetization of 1 T. This plus this easy deposition by standard magnetron sputtering makes Py suitable to build many different magnonic devices [21]. Recently, Heusler alloys have been used [145, 115]: due to their half-metallic character, they have a small damping of the order of 0.003 and a high degree of spin polarization about of 0.8-0.9. As for YIG, the deposition process is quite complicated. Another promising material for magnonics devices is pure iron. Despite its promising properties, namely a low damping factor, a high saturation magnetization and a well-defined magneto-crystalline anisotropy, there is no study of spin wave propagation in this material. To fill this gap, we decided to study the propagation of spin waves, as well as a spin-polarized electrical transport in single crystal iron films grown on MgO.

Spin wave amplification

In the context of spin wave amplification, the electrical control of the spin wave relaxation rate is of particular interest. Suitable systems allowing to do so are bilayer structures composing of a ferromagnetic material (FM) and a heavy metal (HM) possessing a strong spin-orbit coupling. In such systems, the spin current generated by the spin Hall effect in the heavy metal can penetrate through the FM/NM interface and modify the relaxation rate in the ferromagnet via spin transfer torque. The effect of SHE-STT on magnetization relaxation was reported in numerous publications [6, 109, 97, 93, 99, 54, 144], both theoretical and experimental. One of the most commonly used experimental technique to put it in evidence is the ferromagnetic resonance (FMR) spectroscopy, where the modification of the damping factor caused by the spin transfer torque is analyzed by measuring the modification of the width of the FMR spectra [6, 89]. Numerous studies were also carried out by the technique of spin-torque ferromagnetic resonance (ST-FMR), where an AC torque leads to the spin precession, that results in DC voltage generation due to the anisotropic magnetoresistance [79, 97].

The limitation of these techniques is that they can be used to study the excitation/modification of only the uniform mode with $k = 0$ and does not provide access to the non-uniform excitations. The techniques allowing to do so are micro-focus Brillouin light scattering (μ-BLS) and propagating spin wave spectroscopy (PSWS). The advantages of μ-BLS is the possibility of mapping spin wave propagation by simply changing the position of the laser spot. In this way, Demidov et al. [27] could show a modification of spin wave propagation due to SHE-STT. However, the quantitative analysis of the effect was not reported. In PSWS, following the spin wave propagation along the magnetic strip requires several devices with different distances between emitting and receiving antenna, which requires a lot of time and resource. However, the great advantage of PSWS is that it is a very accurate technique, which provides a lot of information in the same spectrum. We will show that by analyzing PSWS measurements in Py/Pt bilayers one can quantify the modifications of the non-uniform spin dynamics induced by both the spin pumping and the spin Hall effect.

Propagation properties of spin waves

Spin waves are highly dispersive and their dispersion characteristics $[\omega(k)]$ depend strongly on the strength and direction of applied magnetic field. One of the most interesting spin wave configuration for both fundamental and applied points of view is the so-called magnetostatic surface spin wave (MSSW), which is generated when the magnetic field is applied in the film plane perpendicularly to the wave vector. The most peculiar property of this wave is its non-reciprocal propagation, which reveals in the different amplitude, modal profile and frequency for the two counter-propagating spin waves. While the amplitude non-reciprocity arising from the coupling between the excitation field and the dynamical magnetization is well understood, the origin of the frequency non-reciprocity is not so clear. It was shown, that a frequency non-reciprocity appears as soon as the top/bottom symmetry of the ferromagnetic film is broken. The reason of the broken symmetry can be the presence of a metallic ground plane in vicinity to one of the film surfaces [65], an inhomogeneity of saturation magnetization of the film [71], a difference of magnetic surface anisotropies at the two film surfaces [56], or an electrical current flowing in the film (Oersted field effect) [51]. While such frequency non-reciprocity has been predicted theoretically and observed experimentally in some very specific cases, a dedicated investigation of this phenomenon is still needed.

Recently, a renewed interest in the frequency non-reciprocity was observed due to the fact that it can be used as an efficient method for the extraction of the magnitude of the interfacial Dzyaloshinskii-Moria interaction (iDMI) in ultra-thin films [31, 10, 125, 98]. Indeed, when included into the Landau-Lifshitz equation of motion for MSSW, iDMI translates directly into a frequency non-reciprocity (see section 1.7). However, this effect always combines with the effects arising from the magnetic asymmetry of the film, because both contributions to the spin wave frequency obey the same symmetry (odd in wave vector $\mathbf{k}$ and applied field $\mathbf{H}_0$). Therefore, it is of primary interest to determine precisely the magnitude of the frequency non-reciprocity induced by asymmetries of the magnetic properties across the film thickness, so as to be able to disentangle it from the iDMI non-reciprocity [125]. For this purpose, we report here a detailed investigation of spin-wave frequency non-reciprocities in Al_2O_3/Py/Al_2O_3 layers (used as a reference with very low iDMI) and Py/Pt bilayers.

Manuscript organization

The manuscript contains six chapters.

In the first chapter, the general theoretical background on the magnetization dynamics in ferromagnetic materials is presented. It includes a brief description of uniform magnetization precession and of spin wave dynamics in the magnetostatic regime, as well as a more detailed description of spin wave excitations in the dipole-exchange regime.

In the second chapter, we discuss the generation of spin current in metals by different processes, which include spin-dependent electron transport in ferromagnetic metals and spin Hall effect in non-magnetic metals. The effect of spin current on the magnetization dynamics via the spin transfer torque is then considered, together with its reciprocal effect, namely spin pumping.

In the third chapter, we describe the experimental technique used and the fabrication process of the studied devices.

In the fourth chapter, we discuss the experimental results on the frequency non-reciprocity measured for Py/Al_2O_3 and Py/Pt films using PSWS. The main result of this chapter is to show that the frequency non-reciprocity arises from combined contributions of both iDMI and a magnetic asymmetry across the film thickness.

In the fifth chapter, we study the spin wave propagation in Py/Pt devices and its modification by different spin transfer torques using PSWS. First, the influence of the spin pumping and SHE-STT on the spin wave is analyzed. The later effect leads to the modification of the magnetization relaxation rate, which is extracted from the current-induced change of the amplitude of the inductance signal.

In the sixth chapter, we investigate the spin wave propagation and its modification by an electrical current in Fe/MgO films. We deduce the main propagation parameters of spin waves and extract the value of the degree of spin polarization of the electrical current by means of current-induced Doppler shift measurements.

Chapter 1

Magnetization dynamics

1.1 Landau-Lifshitz equation of motion

The response of a magnetic moment to an external magnetic field can be treated by an analogy with the response of a spinning top with an angular momentum $\mathfrak{J}$ to some external force $\mathbf{F}$ [46]. The equation of motion of such a spinning top can be written as

$$\frac{\partial \mathfrak{J}}{\partial t} = \gamma \mathfrak{J} \times \mathbf{F}. \tag{1.1.1}$$

If we consider now an atom with an electron moving around, the orbital motion of the latter will create a magnetic moment $\mathfrak{M}$, which is related to the angular moment by the gyromagnetic ratio γ as

$$\mathfrak{M} = -\gamma \mathfrak{J}. \tag{1.1.2}$$

The ferromagnetic system can be considered as a sum of individual atomic magnetic moments where the magnetization density $\mathbf{M}$ in the volume V is

$$\mathbf{M} = \frac{\sum_V \mathfrak{M}}{V}. \tag{1.1.3}$$

Therefore, considering an external force in the form of magnetic field $\mu_0 \mathbf{H}_{\text{eff}}$ the equation of motion for the magnetization is written as

$$\frac{\partial \mathbf{M}}{\partial t} = -\gamma \mu_0 \mathbf{M} \times \mathbf{H}_{\text{eff}}. \tag{1.1.4}$$

where μ_0 is the permeability of a vacuum. Eq.(1.1.4) is the well-known Landau-Lifshitz equation [76], which describes a precessional motion of the

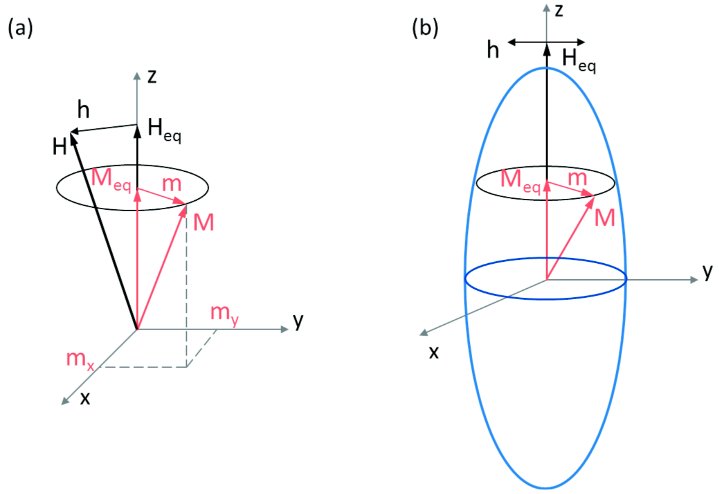

Figure 1.1: (a) Magnetization precession around an effective magnetic field. Static components of $\mathbf{M}$ and $\mathbf{H}$ is along z-axis, dynamical components precess in xy plane. (b) Uniform oscillation of magnetization in an ellipsoid

magnetization. Here, $\mathbf{H}_{\text{eff}}$ is the effective magnetic field

$$\mathbf{H}_{\text{eff}} = \mathbf{H}_0 + \mathbf{H}_{\text{d}} + \mathbf{H}_{\text{ex}} + \mathbf{H}_{\text{k}}, \tag{1.1.5}$$

which represents the sum of all fields acting on the magnetization: the applied magnetic field $\mathbf{H}_0$, the dipolar field $\mathbf{H}_{\text{d}}$, the exchange field $\mathbf{H}_{\text{ex}}$ containing both symmetric (Heisenberg) and antisymmetric (Dzyaloshinskii-Moriya) exchange interactions, and an anisotropy field $\mathbf{H}_{\text{k}}$ including magnetocrystalline and surface magnetic anisotropies. An important feature of this equation is the conservation of the magnitude of the magnetization vector

$$\frac{\partial \mathbf{M}^2}{\partial t} = 0, \tag{1.1.6}$$

that means that the magnetization vector moves on the surface of a sphere.

1.2 Susceptibility tensor

Let us now solve the Landau-Lifshitz (LL) equation for the ferromagnetic system under the effect of a magnetic field, which consists of a static part $\mathbf{H}_{\text{eq}} \parallel z$ and a small-amplitude time-dependent part $\mathbf{h}(t)$ oriented in the xy

plane. The equilibrium magnetization $\mathbf{M}_{\rm eq}$ is aligned along the static field and the small dynamic component $\mathbf{m}(t)$ rotates around the equilibrium position [see Fig. 1.1(a)]. The total magnetic field and the total magnetization in Eq. (1.1.4) can be thus written as

$$\begin{aligned} \mathbf{H}_{\rm eff} &= \mathbf{H}_{\rm eq} + \mathbf{h}(t) && (1.2.1) \\ \mathbf{M} &= \mathbf{M}_{\rm eq} + \mathbf{m}(t), && (1.2.2) \end{aligned}$$

with

$$h << H_{\rm eq}, \qquad m << M_{\rm eq} \tag{1.2.3}$$

The substitution of Eqs. (1.2.1)-(1.2.2) into the equation of motion (1.1.4) gives

$$\frac{\partial \mathbf{m}}{\partial t} = -\gamma\mu_0[\mathbf{M}_{\rm eq} \times \mathbf{H}_{\rm eq} + \mathbf{M}_{\rm eq} \times \mathbf{h} + \mathbf{m} \times \mathbf{H}_{\rm eq} + \mathbf{m} \times \mathbf{h}], \tag{1.2.4}$$

where the first term vanishes since the equilibrium magnetization is parallel to the static field, and the last term can be neglected too due to the fact that both $\mathbf{h}$ and $\mathbf{m}$ are small compared to the magnitude of the static components and their product is of second order in small quantities. As a result one obtains the linearized LL equation

$$\frac{\partial \mathbf{m}}{\partial t} = -\gamma\mu_0[\mathbf{M}_{\rm eq} \times \mathbf{h} + \mathbf{m} \times \mathbf{H}_{\rm eq}]. \tag{1.2.5}$$

We solve Eq. (1.2.5) assuming that the time dependent variation of $\mathbf{h}$ and $\mathbf{m}$ is harmonic, $\mathbf{h}(t) = \mathbf{h}e^{i\omega t}$ and $\mathbf{m}(t) = \mathbf{m}e^{i\omega t}$:

$$\begin{aligned} i\omega\mathbf{m} &= -\gamma\mu_0[M_{\rm eq}\mathbf{z} \times \mathbf{h} + \mathbf{m} \times H_{\rm eq}\mathbf{z}] \\ &= -\mathbf{z} \times [\omega_M\mathbf{h} - \omega_H\mathbf{m}], && (1.2.6) \end{aligned}$$

where $\omega_M = \gamma\mu_0 M_{\rm s}$ and $\omega_H = \gamma\mu_0 H_{\rm eq}$. The projection onto the axes of a coordinate system defined in Fig. 1.1 gives:

$$\begin{aligned} i\omega m_x &= \omega_M h_y - \omega_H m_y \\ i\omega m_y &= -\omega_M h_x + \omega_H m_x && (1.2.7) \\ i\omega m_z &= 0, \end{aligned}$$

where the solution for the components of magnetic field are:

$$\begin{pmatrix} h_x \\ h_y \end{pmatrix} = \frac{1}{\omega_M}\begin{pmatrix} \omega_H & -i\omega \\ i\omega & \omega_H \end{pmatrix}\begin{pmatrix} m_x \\ m_y \end{pmatrix}. \tag{1.2.8}$$

Equation (1.2.8) can be written in the form $\mathbf{m} = \overline{\chi}_p \mathbf{h}$, where $\overline{\chi}_p$ is the Polder susceptibility tensor defined as

$$\overline{\chi}_p = \begin{bmatrix} \chi & i\kappa \\ -i\kappa & \chi \end{bmatrix} \tag{1.2.9}$$

with $\chi = \frac{\omega_H \omega_M}{\omega_H^2 - \omega^2}$ and $\kappa = \frac{\omega \omega_M}{\omega_H^2 - \omega^2}$.

The Polder tensor is a non-diagonal nonsymmetric tensor that indicates the gyrotropic property of the medium. Indeed, the transverse components of the magnetic field (h_x and h_y) couples not only with the dynamical magnetization parallel to them (m_x and m_y, respectively), but also with the corresponding perpendicular components m_y and m_x with a phase shift of $\pi/2$ according to the factor i in Eq. (1.2.9). This is actually the demonstration of the precessional motion of a magnetization vector as a response to the microwave field excitation.

One should also nitece the resonance character of the components of the Polder tensor, whose components diverge when the frequency ω approaches the pole

$$\omega \equiv \omega_H = \gamma \mu_0 H_{\text{eq}}. \tag{1.2.10}$$

This corresponds to the uniform resonance condition of a bulk isotropic ferromagnet. In a finite sample and/or in the case of a non uniform mode the resonance condition differs from that defined by Eq. (1.2.10) since the dynamic effective field also contains the demagnetizing field defined by the sample geometry, the magnetocrystalline anisotropy field, and the exchange field. These aspects will be discussed in the following sections.

1.3 Ferromagnetic resonance for different sample geometries

In 1947 Kittel has shown that the resonance frequency depends strongly on the sample shape and, that this effect can be described using the demagnetizing factors [67]. Let us consider the resonance condition for an uniform oscillation of magnetization in an ellipsoid, whose principle axes are parallel to the x, y, z axes, as shown in Fig. 1.1(b). A static external field $\mathbf{H}_0$ is applied along z, and a small amplitude external oscillating field $\mathbf{h}_1$ is applied in the x, y plane. The effective field in the system is thus defined as:

$$\mathbf{H}_{\text{eff}} = \mathbf{H}_0 + \mathbf{H}_{\text{dem}}, \tag{1.3.1}$$

where $\mathbf{H}_{\text{dem}}$ is the demagnetizing field given by the demagnetizing tensor $\overline{N}$ as

$$\mathbf{H}_{\text{dem}} = -\overline{N}\mathbf{M} = -\begin{bmatrix} N_x & 0 & 0 \\ 0 & N_y & 0 \\ 0 & 0 & N_z \end{bmatrix} \begin{pmatrix} m_x \\ m_y \\ M_{\text{s}} \end{pmatrix}, \tag{1.3.2}$$

with N_x, N_y, N_z being the demagnetizing factors.

The static and dynamical components of the effective field can be thus written as

$$\begin{aligned} h_x &= h_{1x} - N_x m_x \\ h_y &= h_{1y} - N_y m_y \\ H_{\text{eq},z} &= H_0 - N_z M_{\text{s}} \end{aligned} \tag{1.3.3}$$

By solving the linearized LL equation (1.2.5) for $\mathbf{h}_1$ we obtain the Kittel susceptibility tensor

$$\mathbf{h}_1 = \overline{\chi}_K^{-1}\mathbf{m} = \begin{pmatrix} h_{1x} \\ h_{1y} \end{pmatrix} = \frac{1}{\omega_M}\begin{pmatrix} \omega_x & -i\omega \\ i\omega & \omega_y \end{pmatrix}\begin{pmatrix} m_x \\ m_y \end{pmatrix}. \tag{1.3.4}$$

where $\omega_x = \omega_H + N_x\omega_M$, $\omega_y = \omega_H + N_y\omega_M$ and $\omega_0 = \gamma\mu_0(H_0 - N_z M_{\text{s}})$.

The tensor's components diverge ($\det(\overline{\chi}_K^{-1}) = 0$) when the frequency ω approaches the pole

$$\omega = \sqrt{\omega_x\omega_y}. \tag{1.3.5}$$

For the ω_x and ω_y defined above the resonance frequency can be written in the form of the Kittel formula

$$\omega_{\text{res}} = \gamma\mu_0[(H_0 + (N_x - N_z)M_s)(H_0 + (N_y - N_z)M_s)]^{1/2}. \tag{1.3.6}$$

Demagnetizing factors differ for different sample geometries and so do the resonance frequency, as it is shown in Fig. 1.2. Indeed, considering a spherical sample where the demagnetizing factors are $N_x = N_y = N_z = 1/3$ the expression for the resonance frequency takes its simplest form $\omega_{\text{res}} = \gamma\mu_0 H_0$, while for a magnetic film magnetized in-plane for which $N_x = N_z = 0$ and $N_y = 1$, the resonance frequency is given by the expression $\omega_{\text{res}} = \gamma\mu_0[H_0(H_0 + M_s)]^{1/2}$.

1.3.1 Influence of an uniaxial magnetic anisotropy on the resonance frequency

The magnetic anisotropy energy is an important factor, which affects the resonance condition by modifying the total effective field. In an uniaxial crystal the first order term of the anisotropy energy density is written as

$$U_{\mathrm{an}} = -K_u \cos^2\theta = -K_u(\frac{M_i}{M_s})^2, \tag{1.3.7}$$

where K_u is the anisotropy constant, θ is the angle between the magnetization and the main axis, and M_i is the component of $\mathbf{M}$ along this axis. The effective field associated to this energy writes:

$$\mathbf{H}_{\mathrm{an}} = -\frac{1}{\mu_0}\frac{\partial U_{\mathrm{an}}}{\partial \mathbf{M}}, \tag{1.3.8}$$

which for the uniaxial crystal can be written as

$$\mathbf{H}_{\mathrm{an}} = \frac{2K_u M_i}{\mu_0 \mathbf{M}_s^2}\mathbf{e}_i, \tag{1.3.9}$$

Let us consider the general ellipsoid case when the uniaxial anisotropy axis $\mathbf{e}_i$ is along y and $\mathbf{H}_0$ is along z. Expressing the anisotropy field in a form similar to that of the demagnetizing field $\mathbf{H}_{\mathrm{an}} = -\overline{N}_{\mathrm{an}}\mathbf{M}$ one can write the *effective* field as a sum of a shape and an uniaxial anisotropy contributions:

$$\mathbf{H}'_{\mathrm{dem}} = -(\overline{N} + \overline{N}_{\mathrm{an}})\mathbf{M} = -\begin{bmatrix} N_x & 0 & 0 \\ 0 & N_y + \frac{2K_u}{\mu_0 \mathbf{M}_s^2} & 0 \\ 0 & 0 & N_z \end{bmatrix} \begin{pmatrix} m_x \\ m_y \\ M_{\mathrm{s}} \end{pmatrix} \tag{1.3.10}$$

We can now rewrite the resonance condition accounting for the uniaxial anisotropy by replacing the demagnetizing factor N_y in Eq. (1.3.6) by a new factor $N_y + \frac{2K_u}{\mu_0 \mathbf{M}_s^2}$.

For the case of the film magnetized in-plane, where $N_x = N_z = 0$ and $N_y = 1$, the resonance frequency can therefore be written as

$$\omega_{\mathrm{res}} = \gamma\mu_0[H_0(H_0 + M_s - 2K_u/\mu_0\mathbf{M}_s)]^{1/2} = \gamma\mu_0[H_0(H_0 + M_{\mathrm{eff}})]^{1/2}, \tag{1.3.11}$$

where $M_{\mathrm{eff}} = M_s - 2K_u/\mu_0\mathbf{M}_s$ is the effective magnetization.

In thin magnetic films the magnetic anisotropy can be induced by the symmetry breaking at the surface of the film [8, 15]. In this case, the anisotropy constant can be phenomenologically divided into two parts, where the first part is related to the volume contribution and the second one represents the surface contribution: $K_u = K_v + \sum K_s/t$ ($\sum K_s$ indicates the contribution of the two interfaces). The uniaxial surface anisotropy constant K_s leads to a thickness dependence of K_u and consequently to a thickness dependence of the effective magnetization:

$$M_{\mathrm{eff}} = M_s - 2\sum K_s/(\mu_0\mathbf{M}_s t). \tag{1.3.12}$$

The presence of an uniaxial anisotropy leads to the modification of the dispersion relation as it is shown in Fig. 1.2.

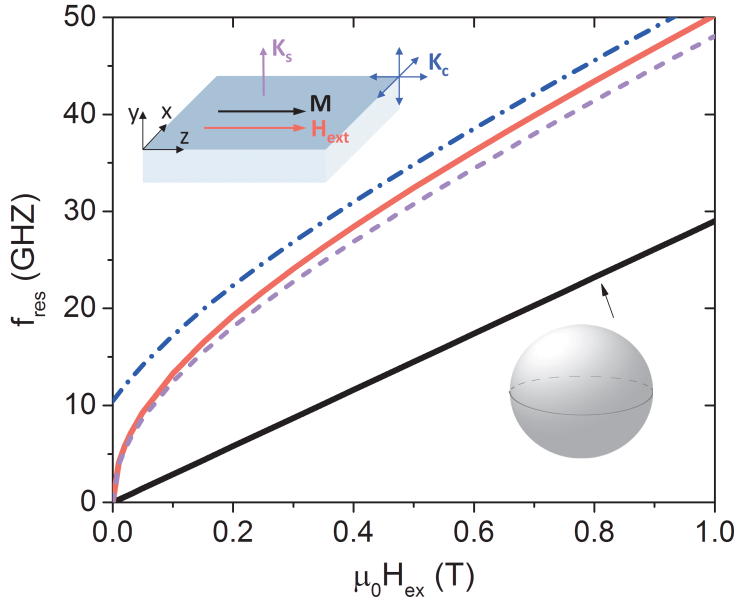

Figure 1.2: Dispersion relations calculated for an in-plane magnetized film (red line) and for a sphere (black line) with parameters $\mu_0 M_\mathrm{s} = 2$ T and $\gamma/(2\pi) = 29$ GHz/T. The dashed and dash-dotted lines correspond to the dispersion relations for the thin film modified by an out-of-plane uniaxial anisotropy with $K_u = 100$ kJ/m^3 and a cubic anisotropy with $K_c = 50$ kJ/m^3, respectively

1.3.2 Influence of a cubic magnetic anisotropy on the resonance frequency

In the case of a cubic crystal, the magnetocrystalline anisotropy energy in lowest order is written as

$$U_{\mathrm{c}} = K_c(\alpha_1^2\alpha_2^2 + \alpha_2^2\alpha_3^2 + \alpha_3^2\alpha_1^2), \tag{1.3.13}$$

and the anisotropy field is given by

$$H_{\mathrm{c}} = -\frac{2K_c}{\mu_0 \mathbf{M}_s^4}\begin{pmatrix} M_1(M_2^2 + M_3^2) \\ M_2(M_3^2 + M_1^2) \\ M_3(M_1^2 + M_2^2) \end{pmatrix}. \tag{1.3.14}$$

Considering $\mathbf{M}$ as a sum of a static component $\mathbf{M}_0$ and a small time-dependent component $\mathbf{m}(t)$ we can express the anisotropy field in a form similar to that of the demagnetizing field as [124]:

$$H_{\mathrm{c}} = -\frac{2K_c}{\mu_0 \mathbf{M}_s^4}\begin{pmatrix} M_{01}(M_{02}^2 + M_{03}^2) \\ M_{02}(M_{03}^2 + M_{01}^2) \\ M_{03}(M_{01}^2 + M_{02}^2) \end{pmatrix} + \overline{N}_{\mathrm{c}}\mathbf{m}, \tag{1.3.15}$$

where the off-diagonal elements of the anisotropy tensor $\overline{N}_{\mathrm{c}}$ are

$$N_{\mathrm{c}}^{ij} = -\frac{4K_c}{\mu_0 \mathbf{M}_s^4} M_{0i}M_{0j} (i \neq j) \tag{1.3.16}$$

and the diagonals elements are

$$N_{\mathrm{c}}^{ii} = -\frac{2K_c}{\mu_0 \mathbf{M}_s^4}[M_s^2 - M_{0i}^2]. \tag{1.3.17}$$

Let us assume that the directions of $\mathbf{M}$ is along $\langle 001 \rangle$ axis, for which $K_c > 0$ (easy axis). Therefore, the effective field is now expressed as

$$\mathbf{H}_{\mathrm{dem}}^{'} = -(\overline{N} + \overline{N}_{\mathrm{c}})\mathbf{m} = -\begin{bmatrix} N_x + \frac{2K_c}{\mu_0 \mathbf{M}_s^2} & 0 & 0 \\ 0 & N_y + \frac{2K_c}{\mu_0 \mathbf{M}_s^2} & 0 \\ 0 & 0 & N_z \end{bmatrix}\begin{pmatrix} m_x \\ m_y \\ M_s \end{pmatrix} \tag{1.3.18}$$

and thus the dispersion relation for the film magnetized in plane takes the following form:

$$\omega_{\mathrm{res}} = \gamma\mu_0[H_{\mathrm{eff}}(H_{\mathrm{eff}} + M_{\mathrm{s}})]^{1/2}, \tag{1.3.19}$$

where $H_{\mathrm{eff}} = H_0 + \frac{2K_c}{\mu_0 \mathbf{M}_s^2}$. The dispersion relation accounting for cubic anisotropy is shown in Fig. 1.2 as a dashed line.

1.4 Spin waves

Up to now, we discussed the uniform mode of precession of the magnetization. We will now focus on the non-uniform modes of precession, in which the spins are oscillating at the same frequency but with different phases, which are called spin waves. We will first analyze the magnetostatic waves, for which the dipolar interaction between spins dominates the exchange interaction since the wavelength λ is much higher than the exchange length Λ ($\lambda >> \Lambda$). Then, we describe the theory of dipole-exchange spin waves, where the exchange interaction is important. The general term 'spin wave' will be used for both dipole and exchange dominated excitations.

1.5 Magnetostatic waves

In the magnetostatic regime the propagating uniform plane waves are described by the magnetostatic equations

$$\nabla \times \mathbf{h} = 0 \tag{1.5.1}$$

$$\nabla \times \mathbf{b} = 0, \tag{1.5.2}$$

where $\mathbf{b} = (1 + \overline{\chi})\mathbf{h}$ is the magnetic flux density. Expressing magnetic field $\mathbf{h}$ in term of a scalar potential ψ as $\mathbf{h} = -\nabla\psi$ and using the definition of $\mathbf{b}$, one obtains from Eq. (1.5.1)-(1.5.2) the generalized Walker's equation [137]:

$$\nabla[(1 + \overline{\chi}_p) \cdot \nabla\psi] = 0, \tag{1.5.3}$$

that is the basic equation for the magnetostatic modes in homogeneous media. For a uniform plane wave, the scalar potential has the form $\psi = \psi_0 e^{i(\omega t - \mathbf{kr})}$. The solution of the Walker's equation will depend on the propagation direction $\mathbf{k}$ and the direction of the magnetization vector $\mathbf{M}$. Let us briefly consider three main spin wave configurations and the corresponding dispersion relations for a wave propagating in a thin film with a thickness t.

A magnetostatic wave, which propagates in the film plane ($\mathbf{k} \perp \mathbf{n}$) with the magnetization perpendicular to the plane ($\mathbf{M} \parallel \mathbf{n}$), is called **Magnetostatic Forward Volume Wave** (MSFVW). The dispersion relation for the MSFWV mode, which writes as [124]

$$\omega^2 = \omega_H[\omega_H + \omega_M(1 - \frac{1 - e^{-2kt}}{kt})], \tag{1.5.4}$$

depends on the magnitude of the wave vector and does not depend on its direction. Following (1.5.4), the resonance frequency increases with k increasing (Fig. 1.3) indicating a forward wave character (positive group velocity,

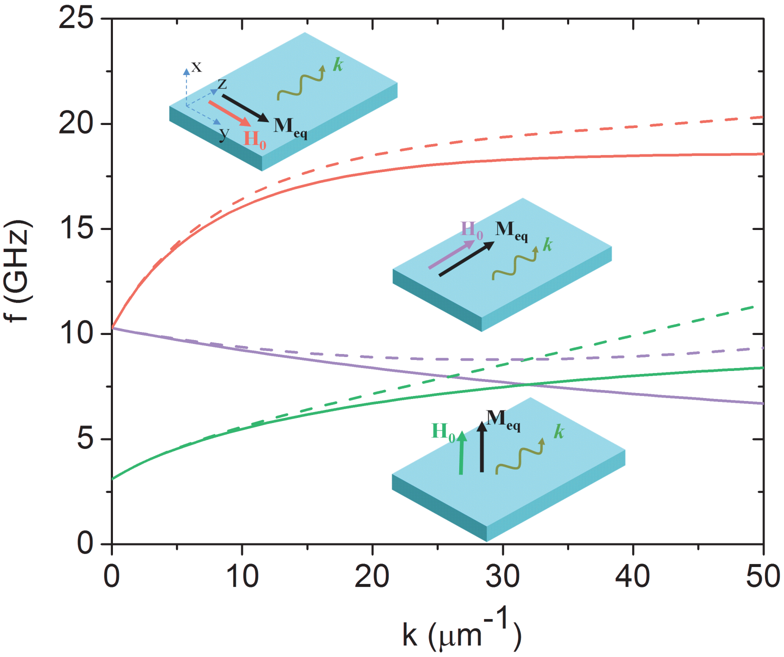

Figure 1.3: Dispersion relations plotted for the MSFVW, MSBVW and MSSW geometries in the magnetostatic regime (solid lines) and in the dipole-exchange regime (dashed lines). Parameters used for calculations: film thickness $t = 50$ nm, magnetic field $\mu_0 H_0 = 100$ mT, saturation magnetization $\mu_0 M_s = 1$ T and exchange constant $A = 11$ pJ/m.

from where the name comes). The wave amplitude is distributed sinusoidally through the volume of the film.

The wave is called **Magnetostatic Backward Volume Wave** (MSBVW), when it propagates in a tangentially magnetized film, $\mathbf{M} \perp \mathbf{n}$, parallel to the magnetization vector direction $\mathbf{k} \parallel \mathbf{M}$. The dispersion relation for a given mode takes the form

$$\omega^2 = \omega_H[\omega_H + \omega_M(\frac{1 - e^{-kt}}{kt})]. \tag{1.5.5}$$

Contrary to MSFVW, the resonance frequency decreases when the wave vector increases (magenta line in Fig. 1.3), which corresponds to a negative group velocity, which points in the direction opposite to the phase velocity (**k**) indicating a backward wave character. As for MSFWV configuration, the wave amplitude has a sinusoidal character through the film volume.

The wave is called **Magnetostatic Surface Wave** (MSSW) or Damon-Eshbach wave when it propagates in a tangentially magnetized film, $\mathbf{M} \perp \mathbf{n}$, but perpendicularly to the magnetization vector direction $\mathbf{k} \perp \mathbf{M}$. The dispersion relation is given by the expression

$$\omega^2 = \omega_H(\omega_H + \omega_M) + \frac{\omega_M^2}{4}(1 - e^{-2kt}), \tag{1.5.6}$$

that shows the frequency increases with k, which corresponds to a positive group velocity (red line in Fig. 1.3). Contrary to both MSFWV and MSBWV, the mode amplitude is maximum near one of the film surface and decays accros the film thickness [23]. Accounting for an uniaxial out-of-plane anisotropy the dispersion relation for MSSW takes the form

$$\omega^2 = \omega_H(\omega_H + \omega_{\text{eff}}) + \frac{\omega_{\text{eff}}\omega_M}{4}(1 - e^{-2kt}), \tag{1.5.7}$$

where $\omega_{\text{eff}} = \gamma\mu_0 M_{\text{eff}}$.

1.6 Dipole-exchange spin waves

We will now discuss the dispersion characteristics of spin waves, when both dipole and exchange interactions are important. The theory of dipole-exchange spin wave was developed by Kalinikos and Slavin [64] and we will refer to their calculation method to obtain a general formula of dispersion relation for an arbitrary direction of magnetic field. More detailed calculations will be done for the particular case of the magnetostatic surface spin wave geometry, which is the main object of study within the framework of this thesis.

Consider a spin wave propagating along the ζ direction in a ferromagnetic film of a thickness t whose film normal is along the ξ direction [Fig. 1.4(a)]. We introduce another coordinate system xyz, where the y axis is parallel to the saturation magnetization. The transition from one coordinate system to another is performed by rotations through the angles θ and φ, where θ is the angle between the equilibrium magnetization and the normal of the film, and φ is the angle between the in-plane projection of the magnetization and the wave vector.

We describe the magnetization dynamics in the film using the Landau-Lifshitz equation for a plane spin wave of the form $\mathbf{m} = \mathbf{m}(\xi)e^{i(\omega t - k_\zeta \zeta)}$

$$i\omega\mathbf{m} = \gamma\mu_0 H_{\text{eq}}\mathbf{u}_y \times \mathbf{m} - \gamma\mu_0 M_{\text{s}}\mathbf{u}_y \times \mathbf{h}_{\text{eff}}, \tag{1.6.1}$$

where the dynamic component of the effective magnetic field consists of both exchange and dipolar fields $\mathbf{h}_{\text{eff}} = \mathbf{h}_{\text{ex}} + \mathbf{h}_{\text{d}}$. We can now use the method of effective demagnetizing factor described in previous sections and rewrite the effective magnetic field in the form

$$\mathbf{h}_{\text{eff}} = -\overline{N}\mathbf{m} = -(\overline{N}_{\text{d}} + \overline{N}_{\text{ex}})\mathbf{m}. \tag{1.6.2}$$

The dynamic component of the dipolar field $\mathbf{h}_{\text{d}}$ can be obtained by integrating the magnetostatic Green's function $\overline{G}_k(\xi,\xi^{'})$ inside the film

$$\mathbf{h}_{\text{d}} = -\int_0^t \overline{N}_{\text{d}}\mathbf{m}(\xi)d\xi^{'} = \int_0^t \overline{G}_k(\xi,\xi^{'})\mathbf{m}(\xi)d\xi^{'}, \tag{1.6.3}$$

where $\overline{G}_k(\xi,\xi^{'})$ is a tensorial function of the form

$$\overline{G}_k(\xi,\xi^{'}) = \begin{pmatrix} -\delta(\xi-\xi^{'}) + G_p(k) & 0 & iG_q(k) \\ 0 & 0 & 0 \\ iG_q(k) & 0 & -G_p(k) \end{pmatrix}. \tag{1.6.4}$$

Here, $G_p(k) = \frac{|k|}{2}\exp(-|k||\xi-\xi^{'}|)$, $G_q(k) = \text{sign}(\xi-\xi^{'})G_p(k)$ and $\delta(\xi-\xi^{'})$ is the Dirac delta function [48].

In the same way we can determine the exchange field. From the definition of the exchange energy

$$E_{\text{ex}} = A\int_V (\frac{\nabla\mathbf{M}}{M_s})^2 dV \tag{1.6.5}$$

one finds the exchange field

$$\mathbf{h}_{\text{ex}} = -\frac{\partial E_{\text{ex}}}{\mu_0\partial\mathbf{M}} = \Lambda^2\nabla^2\mathbf{m}(\xi,t) \tag{1.6.6}$$

where $\Lambda^2 = 2A/(\mu_0 M_s^2)$ is the exchange constant. The operator $\overline{N}_{\text{ex}}$ is therefore given by the expression

$$\overline{N}_{\text{ex}} = \delta(\xi-\xi^{'})(-\Lambda^2\frac{\partial^2}{\partial\xi^2} + \alpha k_\zeta^2). \tag{1.6.7}$$

By substituting Eq.(1.6.2) in the equation of motion (1.6.1), we obtain

$$i\omega\mathbf{m} = \omega_H\mathbf{u}_y \times \mathbf{m} + \omega_M\mathbf{u}_y \times \overline{N}\mathbf{m} = \mathbf{u}_y \times \overline{C}\mathbf{m}, \tag{1.6.8}$$

where $\mathbf{u}_y\times$ can be written as a matrix $\begin{pmatrix} 0 & 1 \\ -1 & 0 \end{pmatrix}$ and operator $\overline{C}$ is

$$\overline{C} = \int_0^t\int_0^t \begin{pmatrix} \omega_H + \omega_M N_{xx} & \omega_M N_{xz} \\ \omega_M N_{zx} & \omega_H + \omega_M N_{zz} \end{pmatrix} \mathbf{m}(\xi)\mathbf{m}(\xi^{'})d\xi d\xi^{'}. \tag{1.6.9}$$

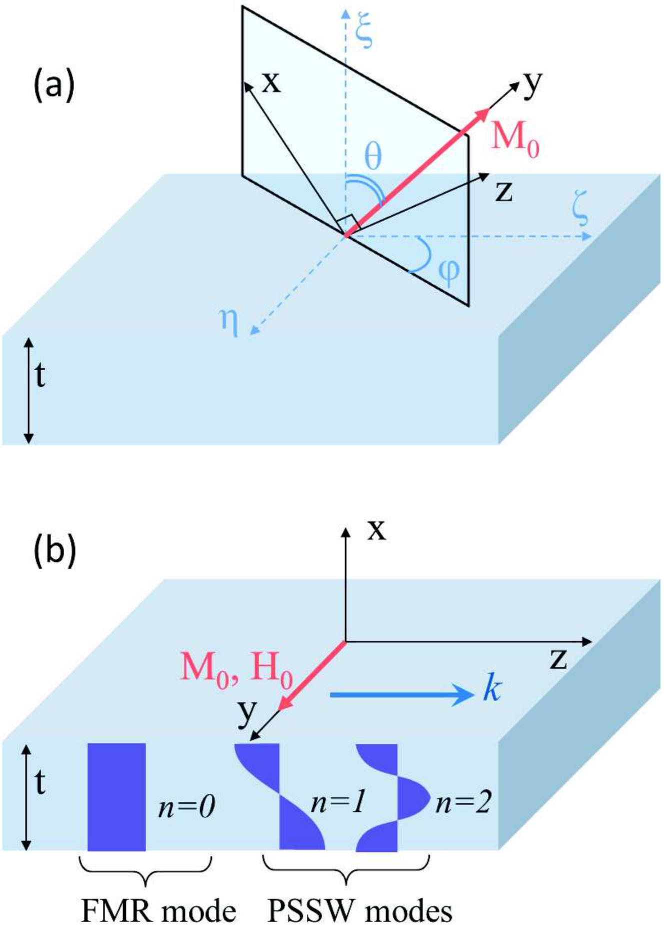

Figure 1.4: (a) Schematic illustration of the coordinate systems used to describe spin wave propagation in a film. The xyz coordinate system is attached to the direction of equilibrium magnetization and the $\xi\eta\zeta$ systems is related to the direction of spin wave propagation. (b) Geometry of the magnetization $\mathbf{M}$ and wave vector $\mathbf{k}$ in xyz coordinate system, that corresponds to MSSW configuration. The profile of the fundamental mode ($n = 0$) and perpendicular standing spin wave modes ($n = 1$ and $n = 2$) are sketched across the film thickness

Here N_{pp} ($p = x, z$) are function operators containing the exchange and dipolar contributions, and which play the role of effective demagnetizing factor

$$\begin{aligned} N_{xx} &= 1 - G_p + \Lambda^2(k^2 - \frac{\partial^2}{\partial\xi^2}) \\ N_{xz} &= -G_p + \Lambda^2(k^2 - \frac{\partial^2}{\partial\xi^2}) \\ N_{xz} &= -iG_q \\ N_{xx} &= -iG_q \end{aligned} \qquad (1.6.10)$$

To solve Eq. (1.6.8) the dynamical magnetization $\mathbf{m}(\xi)$ is expanded in series of orthogonal vector functions. For arbitrary boundary conditions (pinned or unpinned) the eigenvector $\mathbf{m}$ is given by the sum of cosine and sine functions ($\mathbf{m} \propto [\cos(k_\zeta\zeta) + d\sin(k_\zeta\zeta)]$), where d is some pinning parameter. By considering the case of totally unpinned boundary conditions ($d = 0$), the dynamic magnetization can be written as

$$\mathbf{m}_(\xi) = \mathbf{m}(\xi)_0^p + \sqrt{2}\sum_n \mathbf{m}_n^p \cos(\frac{n\pi}{t}\xi). \qquad (1.6.11)$$

Here, $\cos(\frac{n\pi}{t}\xi)$ is the nth cosine function ($n = 1, 2..$) used to represents the dipole-exchange mode profile. Note that it represents exactly the nth spin wave mode profile in the specific case of $k = 0$.

After projecting the different contributions of the effective field onto the basis functions (1.6.11) one can find the eigenfrequencies of spin wave from the condition

$$\det(\mathbf{u}_y \times \overline{C} - i\omega\overline{1}) = \det(\mathfrak{L}) = 0. \qquad (1.6.12)$$

Matrix $\mathfrak{L}$ can be represented as a sum of diagonal and non-diagonal blocks, where the diagonal blocks give the dispersion equation for the nth spin wave mode when it is assumed to be well represented by the nth basic functions, and the non-diagonal matrix makes the corrections to the dispersion relations related to the interaction between basic functions of different type ($n \neq n'$).

By solving Eq. (1.6.12) the dispersion relation for nth spin wave mode in the dipolar-exchange regime without taking into account the interaction between different modes (non-diagonal blocks are zero) is given by the expression [64]:

$$\omega_n^2 = (\omega_H + \Lambda^2\omega_M k_n^2)(\omega_H + \Lambda^2\omega_M k_n^2 + \omega_M F_{nn}) \qquad (1.6.13)$$

where $k_n^2 = k_\zeta^2 + \kappa_n^2$ with $\kappa_n = n\pi/t$ being the wave vector over film thickness, and

$$F_{nn} = P_{nn} + \sin^2\theta[1 - P_{nn}(1 + \cos^2\varphi) + \omega_M \frac{P_{nn}(1 - P_{nn})\sin^2\varphi}{\omega_H} + \Lambda^2\omega_M k_n^2], \tag{1.6.14}$$

where the matrix elements P_{nn} are obtained by a weighted average of the dipole Green's function

$$P_{nn} = \frac{1}{t}\int_0^t \int_0^t G_p(\xi, \xi^{'})\phi_n(\xi)\phi_{n'}(\xi^{'})d\xi d\xi^{'}, \tag{1.6.15}$$

where $\phi_0 = 1/\sqrt{t}$, $\phi_{n\geq 1} = \sqrt{2/t}\cos(n\pi/t)$ are the normalized basis functions. In the case of totally unpinned surface spins they take the form

$$P_{nn} = \frac{k_\zeta^2}{k_n^2}(1 - \frac{k_\zeta^2}{k_n^2}\frac{2}{1 + \delta_{0n}}\frac{1 - (-1)^n e^{-k_\zeta t}}{k_\zeta t}). \tag{1.6.16}$$

The dispersion relations of the lowest mode in the dipolar-exchange regime are plotted in Fig. (1.3) for three main spin wave configurations (MSFVW, MSBVW and MSSW). One can note, that the difference between the dispersion curves obtained in the magnetostatic and dipole-exchange regimes is negligible for a small wave vector and starts to reveal at $k > 10\mu\mathrm{m}^{-1}$.

The dispersion curves of different spin wave modes n may cross each other leading to frequency degeneracies. The degeneracies can be removed by taking into account the dipolar interaction of the different modes, i.e. by treating the non-diagonal part of matrix $\mathfrak{L}$ as a perturbation.

1.6.1 Surface spin wave in the dipolar-exchange regime

Let us now specify the aforementioned calculations for the particular case, when $\theta = \varphi = \pi/2$, that corresponds to the surface spin wave geometry, and evaluate the corresponding dispersion relation accounting for the hybridization between the first two modes. The geometry is shown in Fig. 1.4(b): x is the film normal, y is the direction of the equilibrium magnetization and z is the direction of propagation of the surface spin wave. The plane spin wave takes the form $\mathbf{m}(x) = \mathbf{m}_0(x)e^{i(\omega t - kz)}$, where only two components (m_x, m_z) do not vanish.

We expand the dynamical magnetization $\mathbf{m}(x)$ into a Fourier series keeping only terms up to first order

$$\mathbf{m} = m_x^0\mathbf{u}_x + m_z^0\mathbf{u}_z + m_x^1\sqrt{2}\cos(\frac{\pi x}{t})\mathbf{u}_x + m_z^1\sqrt{2}\cos(\frac{\pi x}{t})\mathbf{u}_z + ... \tag{1.6.17}$$

where $n = 0$ corresponds to the FMR mode with a uniform profile, and $n = 1$ is so-called first perpendicular standing spin wave mode (PSSW1), which has an antisymmetric profile across a film thickness (see Fig. 1.4(b)). The higher order PSSW modes ($n = 2$ and above) can be safely neglected because of their much higher frequency.

Substituting Eq. (1.6.17) for $\mathbf{m}(x)$ in Eq. (1.6.9) we can write a matrix eigenvalue equation $i\omega\mathbf{m} = \mathbf{u}_y \times \overline{C}\mathbf{m}$ with a new 4×4 dynamic matrix $\overline{C}$ defined as

$$\overline{C} = \begin{pmatrix} C_{00} & C_{01} \\ C_{10} & C_{11} \end{pmatrix} = \begin{pmatrix} \omega_{x0} & 0 & 0 & -i\omega_M Q \\ 0 & \omega_{z0} & -i\omega_M Q & 0 \\ 0 & i\omega_M Q & \omega_{x1} & 0 \\ i\omega_M Q & 0 & 0 & \omega_{x1} \end{pmatrix}, \tag{1.6.18}$$

where the matrix elements are given by the following expressions:

$$\begin{aligned} \omega_{x0} &= \omega_H + \omega_M(\Lambda^2 k^2 + 1 - P_{00}) \\ \omega_{z0} &= \omega_H + \omega_M(\Lambda^2 k^2 + P_{00}) \\ \omega_{x1} &= \omega_H + \omega_M(\Lambda^2 k^2 + 1 - P_{11} + \Lambda^2(\pi/t)^2) \\ \omega_{z1} &= \omega_H + \omega_M(\Lambda^2 k^2 + P_{11} + \Lambda^2(\pi/t)^2) \end{aligned} \tag{1.6.19}$$

The matrix elements P_{00}, P_{11} [obtained from (1.6.15)] and Q are given by:

$$\begin{aligned} P_{00} &= \frac{1}{t}\int_0^t\int_0^t G_p(x-x^{'})dxdx^{'} = 1 - \frac{1-e^{-|k|t}}{|k|t} \\ P_{11} &= \frac{1}{t}\int_0^t\int_0^t G_p(x-x^{'})\cos(\frac{\pi x}{t})\cos(\frac{\pi x^{'}}{t})dxdx^{'} \\ &= \frac{(kt)^2}{\pi^2+(kt)^2}(1 - \frac{2(kt)^2}{\pi^2+(kt)^2}\frac{1+e^{-|k|t}}{|k|t}) \\ Q &= \frac{\sqrt{2}}{t}\int_0^t\int_0^t G_q(x-x^{'})\cos(\frac{\pi x^{'}}{t})dxdx^{'} = \frac{\sqrt{2}kt}{\pi^2+(kt)^2}(1+e^{-|k|t}) \end{aligned} \tag{1.6.20}$$

P_{00}, P_{11} are self-demagnetizing factors describing the dipole field generated by the in-plane component of the uniform and PSSW1 modes, respectively, and Q is a mutual demagnetizing factor describing the dipolar interaction between $n = 0$ and $n = 1$ basis functions.

We find the dispersion relation of the dipole-exchange spin wave using the condition $\det(\mathbf{u}_y \times \overline{C}_k - i\omega\overline{1}) = 0$. It is easy to see, that the diagonal 2×2 blocks containing C_{00} and C_{11} give the dispersion relation for the

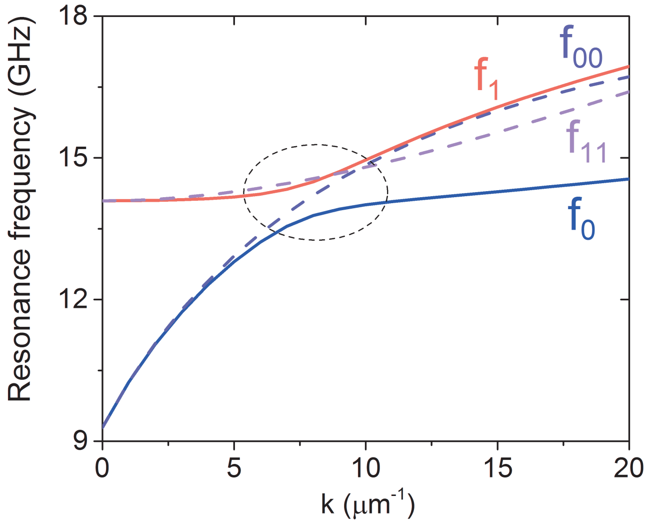

Figure 1.5: (a) Dispersion curves of unperturbed fundamental (f_{00}) and PSSW1 (f_{11}) spin wave modes are shown by dashed lines (violet and magenta respectively). Solid blue and red lines are the hybridized fundamental (f_0) and PSSW1 (f_1) spin wave modes, respectively. Dispersion relations were calculated for following parameters: film thickness $t = 50$ nm, magnetic field $\mu_0 H_0 = 100$ mT, saturation magnetization $\mu_0 M_s = 1$ T and exchange constant $A = 11$ pJ/m.

fundamental and PSSW1 modes, respectively [51]:

$$\begin{aligned}\omega_{00}^2 &= \omega_{x0}\omega_{z0} \qquad (1.6.21)\\ &= [\omega_H + \omega_M(\Lambda^2k^2 + P_{00})][\omega_H + \omega_M(1 + \Lambda^2k^2 - P_{00})]\\ \omega_{11}^2 &= \omega_{x1}\omega_{z1} \qquad (1.6.22)\\ &= [\omega_H + \omega_M(\Lambda^2k^2 + (\Lambda\pi/t)^2 + P_{11})][\omega_H + \omega_M(1 + \Lambda^2k^2 + (\Lambda\pi/t)^2 - P_{11})]\end{aligned}$$

where Λ^2k^2 and $(\Lambda\pi/t)^2$ terms are the exchange contributions to the dispersion characteristic. Since the out-of-plane exchange term varies as $1/t^2$, by increasing the film thickness the dispersion branches of the modes $n = 0$ and $n = 1$ will tend to approach closer to each other, and for some value of k may intercross.

Close to such mode intersection the dipole-dipole interaction between the modes should be taken into account. For this purpose, we solve the 4×4

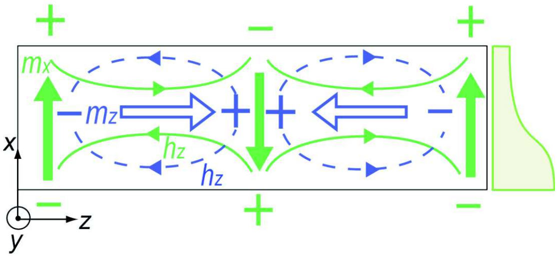

Figure 1.6: Sketch of the distribution of the dipolar field (solid and dashed lines) generated by the m_x and m_z components of the dynamic magnetization (solid and open arrow, respectively) across one wavelength for $k > 0$

determinant accounting for the off-diagonal blocks, which are responsible for the coupling between modes. As a result, one find the dispersion relation for hybridized uniform and PSSW1 modes in the following form:

$$(\omega_{00}^2 - \omega^2)(\omega_{11}^2 - \omega^2) + Q^2(Q^2 + 2\omega^2 - \omega_{z1}\omega_{x0} - \omega_{z0}\omega_{x1}) = 0, \tag{1.6.23}$$

which leads to the solutions

$$\omega_{0,1}^2 = \frac{\omega_{00}^2 + \omega_{11}^2}{2} - Q^2 \mp \\ \frac{1}{2}\sqrt{(\omega_{11}^2 - \omega_{00}^2)^2 - 4Q^2((P_{00} - P_{11})^2 + \frac{\Lambda^4\pi^4}{t^4})} \tag{1.6.24}$$

One can see, that the frequency of the hybridized fundamental and PSSW1 modes (ω_0 and ω_1 respectively) are a combination of the frequencies of the unperturbed fundamental and PSSW1 modes (ω_{00} and ω_{11} respectively), and a term describing the mode hybridization involving the quantity Q. The main consequences of the mode hybridization are that approaching to the intersection point the two branches start to repulse each other as it is shown in Fig. 1.5(a), and that the modal profile shows a certain asymmetry across the film thickness [Fig. 1.7(a)].

Let us focus on the last statement. In our description, the modal profile is a combination of an uniform function and an antisymmetric cosine function. The contribution of the latter gives rise to an asymmetric profile across the film thickness, that means that the maximum amplitude is located at one of the film surfaces depending on the sign of wave vector. A simple schematic explanation of the non-reciprocal modal profile is sketched in Fig 1.6, which shows the spatial distribution of the dynamic magnetization across a spin

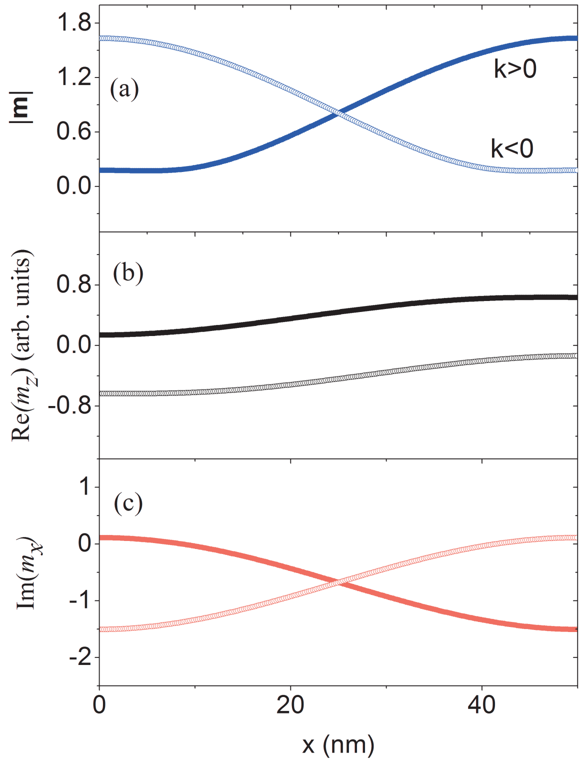

Figure 1.7: Modal profile of the dipole-exchange surface spin wave. (a) amplitude, (b) in-plane component m_z and (c) out-of-plane component m_x. The numerical calculation was done for a wave vector $k = 7.8\ \mu m^{-1}$ and $k = -7.8\ \mu m^{-1}$, film thickness $t = 50$ nm, magnetic field $\mu_0 H_0 = 100$ mT, saturation magnetization $\mu_0 M_s = 1$ T and exchange constant $A = 11$ pJ/m.

wave wavelength for the uniform mode and for a positive wave vector. As one can see, both m_x and m_z components of the dynamic magnetization (solid and open arrows, respectively) create magnetic poles, which in turn generate a dynamic dipolar field (solid and dashed lines, respectively). In the lower half of the film both components of dipolar field are parallel, whereas they are in anti-phase in the upper half. As a result, for $k > 0$, the dipolar field is larger in the lower half. The inverse situation is expected for wave moving in opposite direction ($k < 0$): as m rotates in the opposite sense in the (x, z) plane, the total dipole field is larger in the upper half of the film. This non-reciprocal asymmetry of the dynamic dipolar field is at the origin of the modal profile non-reciprocity. Indeed, the true eigenmode builds its profile to account for the dipolar field it generates.

Fig. 1.6 illustrates precisely the relation between the antisymmetric in-plane dipole field component and the uniform out-of-plane magnetization component, which can extracted from Eq. (1.6.18)

$$\begin{aligned} h_{d,z0} &= P_{00} m_{z0} - iQ m_{x1} \\ h_{d,z1} &= P_{11} m_{z1} + iQ m_{x0} \end{aligned} \tag{1.6.25}$$

Therefore, one can conclude that the surface character of the fundamental mode results from the dipolar coupling between $n = 0$ and $n = 1$ modes via the anti-diagonal component Q of the Green's function. The non-reciprocity of modal profile originates from the symmetry of Q function: since Q is odd in k, a change in the sign of k changes the sign of Q and therefore reverses the mode profile [69, 51]. This feature of the modal profile may give an important contribution to the frequency non-reciprocity of two counter-propagating surface spin waves, that will be discussed in section 4.1.

1.7 Dzyaloshinskii-Moriya interaction

In addition to the symmetric (Heisenberg) exchange interaction, which tends to align neighboring spins parallel or antiparallel, there exists an antisymmetric exchange interaction called Dzyaloshinskii-Moriya (DM) interaction, which favors a canted orientation of neighboring spins [36]. This interaction exists in materials with broken inversion symmetry, such as alloys of the B20 crystal structure (for example, $FeBO_3$ [33], MnSi [128], FeGe [141], etc.), or at the interface between a ferromagnetic and a non-magnetic material possessing a strong spin-orbit coupling. In the latter case it is called interfacial Dzyaloshinskii-Moriya (iDM) interaction [98, 91].

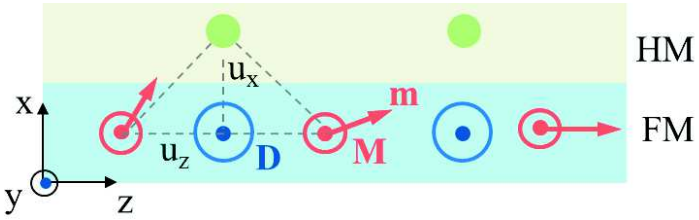

Figure 1.8: Sketch of an iDM interaction at the interface between a ferromagnetic and a heavy metal. The spin wave propagates along the z direction, the magnetization **M** is along the y direction and the broken symmetry is along the x direction. The iDM interaction between two neighboring spin moments **m** (red arrows) is considered as an indirect exchange interaction, which arises from the spin-orbit interaction with a heavy atom (green atom). The orientation of DM vector **D** is obtained from the relation $u_z \times u_x$ and it is oriented perpendicularly to the film plane.

The energy of the DM interaction between two spins $\mathbf{S}_i$ and $\mathbf{S}_j$ is given by the expression

$$E_{\mathrm{DM}} = -\mathbf{D}_{ij} \cdot (\mathbf{S}_i \times \mathbf{S}_j), \tag{1.7.1}$$

where $\mathbf{D}_{ij}$ is the Dzyaloshinskii-Moriya vector.

It has been recently shown [98, 91, 84, 125, 142], that the presence of the iDM interaction leads to a notable modification of spin wave propagation, namely a modification of the resonance frequency of the surface spin wave.

To describe the influence of the iDM interaction on MSSW, let us consider a bilayer structure (ferromagnet/heavy metal), where the x axis indicates the direction of the symmetry breaking, the y axis is parallel to the direction of magnetization, and the z axis corresponds to the spin wave propagation direction (see Fig. 1.8). In such system, two neighboring precessing spin moments are coupled by a DM vector D_{ij}, which connects two spins via the exchange mechanism that includes an atom in the adjacent nonmagnetic heavy metal layer. The vector $\mathbf{D}_{ij}$ is parallel to $u_z \times u_x$, where u_z is the vector between two neighboring spins and u_x is normal to the film plane. Switching to a micromagnetic continuous description, we can therefore write the iDM interaction energy acting on the MSSW as

$$E_{\mathrm{DM}} = -D[(\mathbf{u}_z \times \mathbf{u}_x) \cdot (\frac{\mathbf{M}}{M_s} \times \frac{\partial \mathbf{M}}{\partial z})], \tag{1.7.2}$$

where D is the average micromagnetic DM constant. Under the assumption that the DMI is a purely interfacial property, the magnitude of D should be proportional to $1/t$. According to this, we can introduce a constant D_s such that $D = D_s/t$, which is the characteristic of the FM/HM interface and is independent on the film thickness [10]. We can now calculate the dynamic field originating from the DMI as

$$\mathbf{h}_{\mathrm{DM}} = -\frac{1}{\mu_0}\frac{\delta E_{\mathrm{DM}}}{\delta \mathbf{M}} = -\frac{2D_s}{\mu_0 M_s^2 t}(\mathbf{u}_y \times \frac{\partial \mathbf{m}}{\partial z}), \tag{1.7.3}$$

which for a plane spin wave of the form $\mathbf{m}(x) = \mathbf{m}_0(x)e^{i(\omega t - kz)}$ becomes

$$\mathbf{h}_{\mathrm{DM}} = \frac{2D_s}{\mu_0 M_s^2 t}(\mathbf{u}_y \times ik\mathbf{m}). \tag{1.7.4}$$

Introducing the DM field in the LL equation (1.6.1) as a part of the dynamic effective field ($\mathbf{h} = \mathbf{h}_{\mathrm{ex}} + \mathbf{h}_{\mathrm{d}} + \mathbf{h}_{\mathrm{DM}}$), we obtain

$$\begin{aligned} i\omega\mathbf{m} &= \omega_H \mathbf{u}_y \times \mathbf{m} - \omega_M \mathbf{u}_y \times \mathbf{h}_{\mathrm{eff}} \\ &= \omega_H \mathbf{u}_y \times \mathbf{m} - \omega_M \mathbf{u}_y \times \overline{N}\mathbf{m} - \omega_M \frac{2D_s ik}{\mu_0 M_s^2 t}\mathbf{u}_y \times (\mathbf{u}_y \times \mathbf{m}) \end{aligned} \tag{1.7.5}$$

where operator $\overline{N}$ is the dipole-exchange operator defined in Eq.(1.6.4) and (1.6.7). It is easy to see, that the LL equation can be rewritten as

$$i(\omega - \frac{2\gamma D_s k}{M_s t})\mathbf{m} = \omega_H \mathbf{u}_y \times \mathbf{m} - \omega_M \frac{2D}{\mu_0 M_s^2}\mathbf{u}_y \times \overline{N}\mathbf{m}, \tag{1.7.6}$$

In the case of the uniform mode ω_{00} this yields the following dispersion relation:

$$\begin{aligned} \omega &= \omega_{00} + \omega_{\mathrm{DM}} = \\ &= [\omega_H + \omega_M(\Lambda^2 k^2 + P_{00})][\omega_H + \omega_M(1 + \Lambda^2 k^2 - P_{00})] + \frac{2\gamma D_s}{M_s t}k \end{aligned} \tag{1.7.7}$$

One can see, that the presence of the DM interaction leads to the modification of the dispersion relation of the fundamental MSSW mode by changing its eigenfrequency ω_{00} by the quantity $(2\gamma D_s k)/(M_s t)$. Depending on the sign of wave vector ($k > 0$ or $k < 0$), the resonance frequency will either increase or decrease resulting in the frequency non-reciprocity for two counter-propagating spin waves. The sign of the frequency shift also depends on the sign of iDM constant, on the direction of magnetization ($M \parallel \pm u_y$), as well as on the direction of vector u_x, which indicates at which interface (top or bottom) the symmetry is broken.

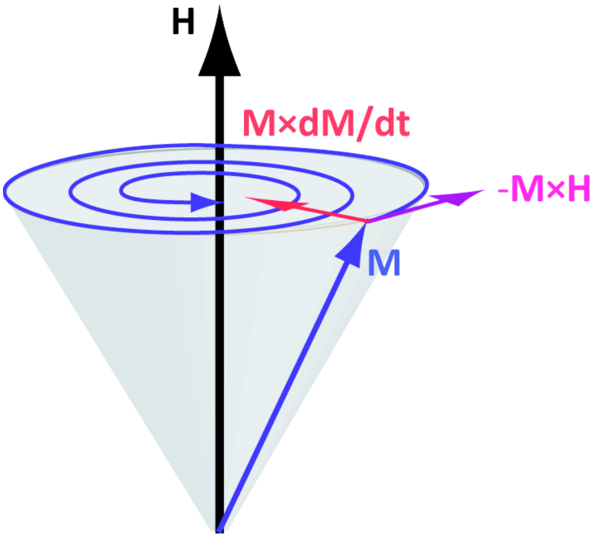

Figure 1.9: Magnetization relaxation process

1.8 Magnetization relaxation process

Up to now, we considered the magnetization precession around an applied magnetic field without dissipation. However, in a real system, there exists always a dissipation of energy from the precessing spin to other degree of freedom such as impurities, phonons or magnons, that leads to the magnetization relaxation toward an equilibrium state where $\mathbf{M} \parallel \mathbf{H}$. To account for the relaxation process, the LL equation is complemented by an additional term including a dimensionless damping parameter α:

$$\frac{\partial \mathbf{M}}{\partial t} = -\gamma\mu_0 \mathbf{M} \times \mathbf{H}_{\text{eff}} + \frac{\alpha}{M_s}(\mathbf{M} \times \frac{\partial \mathbf{M}}{\partial t}), \tag{1.8.1}$$

Performing the linearization procedure, one finds

$$i\omega\mathbf{m} = -\mathbf{z} \times [\omega_M \mathbf{h} - (\omega_H + i\alpha\omega)\mathbf{m}] \tag{1.8.2}$$

One can see that the damping parameter enters as an imaginary part to the precession frequency, and thus the loss can be introduced into the Polder tensor (1.2.9) by performing the substitution $\omega_H \rightarrow (\omega_H + i\alpha\omega)$. In the case of an isotropic infinite medium, the magnetic response to an impulse excitation field can be written as

$$\begin{aligned} m_x(t) &= \omega_M e^{-\alpha\omega_H t}\sin(\omega_H t) \\ m_y(t) &= -\omega_M e^{-\alpha\omega_H t}\cos(\omega_H t) \end{aligned} \tag{1.8.3}$$

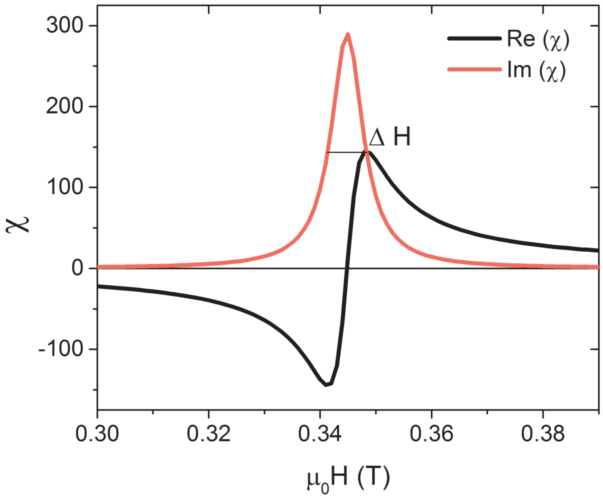

Figure 1.10: Real and imaginary parts of Polder susceptibility in presence of damping

As follows from Eq. (1.8.3), the magnetization tends to the equilibrium state describing the spiral, which decays exponentially in amplitude (Fig. 1.9).

Experimentally, the magnetic damping of the uniform precession can be determined from ferromagnetic resonance measurements. Sweeping the field, the full resonance line width at half-maximum ΔH (see Fig. 1.10) will be related to the damping parameter as:

$$\Delta H = \frac{2\alpha\omega}{\gamma\mu_0}. \tag{1.8.4}$$

However, it is worth noting, that the resonance line width may contain not only the contribution due to the damping, but other contributions related to the presence of inhomogeneities in the sample, leading to linewidth broadening.

In the case of traveling waves, it is more convenient to use the relaxation time T_2, defined as the time needed for the amplitude of the magnetization to decay by a factor $1/e$ [124]. T_2 is related to α by

$$\frac{1}{T_2} = \alpha\omega\frac{\partial\omega}{\partial\omega_H}, \tag{1.8.5}$$

For the specific case of the magnetostatic surface wave, the relaxation time is given by

$$\frac{1}{T_2} = \alpha(\omega_0 + \omega_M/2). \tag{1.8.6}$$

Chapter 2

Spin current and spin transfer torque

In this section charge and spin currents in ferromagnetic and nonmagnetic materials are described. First, we will introduce the definition of spin current (Sec. 2.1). We will show with the help of the two current model that a spin current may be generated in ferromagnetic materials as a result of spin-dependence of the electrical resistivity (Sec. 2.2.1). A spin current can be also created by the spin Hall effect, which takes place in materials with strong spin-orbit coupling and transforms a charge current into a transverse spin current (Sec. 2.2.2). In a bilayer structure the spin current can be generated by the spin-pumping process, which manifests itself as a transfer of spin angular momentum at the ferromagnetic/non-magnetic interface (Sec. 2.3.2). At the end of this chapter, the interaction between the generated spin current and the dynamical magnetization will be discussed.

2.1 Spin current

In the case of spin-up and spin-down electrons propagating in two independent channels, the spin current can be defined as:

$$j_{\mathrm{s}} = j_{\mathrm{s}}^{\uparrow} - j_{\mathrm{s}}^{\downarrow}. \tag{2.1.1}$$

In a more rigorous definition, the spin current operator is given as [5]

$$Q = \frac{1}{2}(\widehat{v}\widehat{s} + \widehat{s}\widehat{v}), \tag{2.1.2}$$

for carriers with spin momentum $\widehat{s}$ propagating with the spin velocity $\widehat{v}$.

Let us now consider the different generation mechanisms of spin current, starting with the spin dependent electrical transport in ferromagnetic metals.

2.2 Spin current generation in metal

2.2.1 Two current model

The spin dependent electrical transport in ferromagnetic transition metals can be understood from the $s-d$ electron band structure. In these materials the majority (spin-up) and minority (spin-down) $3d$ bands are exchange splitted [Fig. 2.1(a)]. This results in different spin population of $3d$ electrons at the Fermi level, which is at the origin of spin polarization of the current. Since the scattering of electrons is determined by the total DOS at the Fermi level, the s to d scattering rate will be different for ↑ and ↓ electrons. It was proposed by Mott [94] to describe the spin dependent transport in magnetic material by considering two independent conductive channels for ↑ and ↓ electrons "connected" in parallel [see schema in Fig. 2.1(b)]. The resistivity of each channel depends on the scattering events for electrons of each spin. In this so-called two current model, the total resistivity ρ is calculated as

$$\rho = \frac{\rho_\uparrow \rho_\downarrow}{\rho_\uparrow + \rho_\downarrow}, \tag{2.2.1}$$

where ρ_σ is the resistivity of channel $\sigma =\uparrow, \downarrow$. The degree of spin polarization of the electric current is defined as the difference between spin-up and spin-down resistivities normalized by the total resistivity:

$$P = \frac{J_\uparrow - J\downarrow}{J_\uparrow + J\downarrow} = \frac{\rho_\downarrow - \rho_\uparrow}{\rho_\uparrow + \rho_\downarrow} \tag{2.2.2}$$

Eq. (2.2.1) does not include the possible intermixing between the current of spin-up and spin-down electrons, which originates from the spin-flip scattering due to electron-magnon collision or spin-orbit interaction. This scattering is schematically represented in Fig. 2.1(c) by a spin mixing term $\rho_{\uparrow\downarrow}$. Accounting for this transfer of momentum between the two channels, the total resistivity is now written as

$$\rho = \frac{\rho_\uparrow \rho_\downarrow + \rho_{\uparrow\downarrow}(\rho_\uparrow + \rho_\downarrow)}{\rho_\uparrow + \rho_\downarrow + 4\rho_{\uparrow\downarrow}}, \tag{2.2.3}$$

and the degree of spin polarization of the electrical current takes the form

$$P = \frac{\rho_\uparrow - \rho_\downarrow}{\rho_\uparrow + \rho_\downarrow + 4\rho_{\uparrow\downarrow}}. \tag{2.2.4}$$

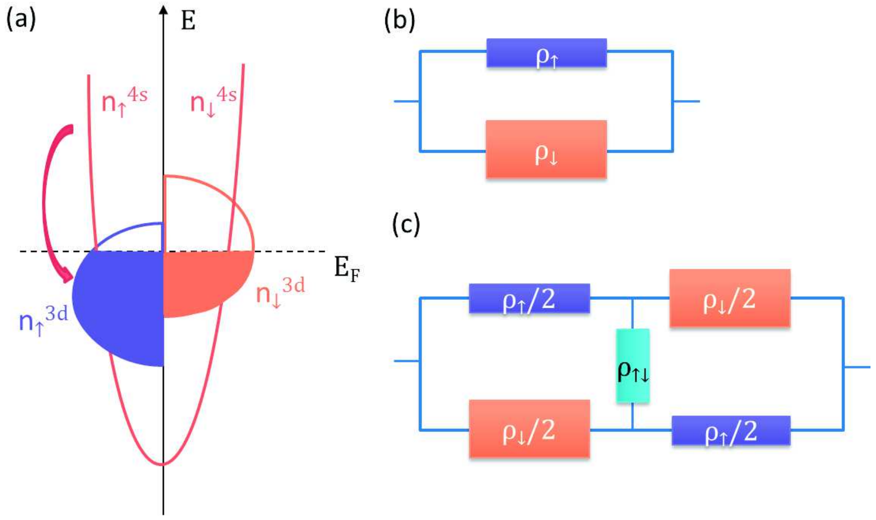

Figure 2.1: (a) The density of state of the majority and minority electrons. (b) A schema of the two current model consisting of an independent conductive channels for ↑ and ↓ electrons. (c) A schema of two current model including spin-flip scattering

Here, the Matthiessens' rule is assumed for each sub-band

$$\rho_\sigma = \sum_x \rho_\sigma^x \qquad \rho_{\uparrow\downarrow} = \sum_x \rho_{\uparrow\downarrow}^x, \tag{2.2.5}$$

where the index x corresponds to the different types of scattering centers, such as phonon, magnon or impurities.

The resistivity of each channel can be determined by measuring the deviation from Matthiessen's rule for ternary alloys at low temperature or by studying the temperature dependence of the resistivity of binary alloys. Indeed, in ferromagnetic ternary alloys with two types of impurities A and B, the total resistance ρ_{AB} differs from the sum of the resistivities $\rho_A+\rho_B$ due to the impurities A and B. This is attributed to the fact, that the Matthiessen's rule, which is satisfied for each individual channels, is not necessarily satisfied for the total resistivity. In the absence of spin-flip scattering, this deviation from Matthiessen's rule can be written as [38]

$$\Delta\rho_{AB} = \rho_{AB} - \rho_A - \rho_B = \frac{(\alpha_A - \alpha_B)^2 \rho_A \rho_B}{(1+\alpha_A)^2 \alpha_B \rho_A + (1+\alpha_B)^2 \alpha_A \rho_B}. \tag{2.2.6}$$

From this expression one can determine α_A and α_B, which are resistivity ratios $\alpha_A = \rho_{A\downarrow}/\rho_{A\uparrow}$, $\alpha_B = \rho_{B\downarrow}/\rho_{B\uparrow}$.

In the case of binary alloys the resistivity of each channel can be written as the sum of pure metal resistivities $\rho_{i\sigma}(T)$, which are temperature dependent, and impurity terms $\rho_{0\sigma}$, which are assumed to be temperature independent

$$\rho_\sigma = \rho_{0\sigma} + \rho_{i\sigma}(T). \tag{2.2.7}$$

Substituting this relation in Eq. (2.2.3), one obtains the expression for the temperature dependent resistivity of the binary alloys

$$\rho(T) = \frac{[\rho_{0\uparrow} + \rho_{i\uparrow}(T)][\rho_{0\downarrow} + \rho_{i\downarrow}(T)] + \rho_{\uparrow\downarrow}(T)[\rho_{0\uparrow} + \rho_{i\uparrow}(T) + \rho_{0\downarrow} + \rho_{i\downarrow}(T)]}{\rho_{0\uparrow} + \rho_{i\uparrow}(T) + \rho_{0\downarrow} + \rho_{i\downarrow}(T) + 4\rho_{\uparrow\downarrow}(T)} \tag{2.2.8}$$

The deviation from Matthiessen's rule is defined as [82]

$$\Delta\rho(T) = \rho(T) - \rho_0 + \rho_i(T) = [\frac{\mu - \alpha}{1 + \alpha}]^2 \frac{\rho_i(T)}{\mu + 1} + [\frac{1 - \alpha}{1 + \alpha}]^2 \rho_{\uparrow\downarrow}(T), \tag{2.2.9}$$

where

$$\rho_i(T) = \frac{\rho_{i\uparrow}\rho_{i\downarrow}}{\rho_{i\uparrow} + \rho_{i\downarrow}}, \rho_0 = \frac{\rho_{0\uparrow}\rho_{0\downarrow}}{\rho_{0\uparrow} + \rho_{0\downarrow}} \tag{2.2.10}$$

and

$$\mu = \rho_{i\downarrow}(T)/\rho_{i\uparrow}(T) \qquad \alpha = \rho_{0\downarrow}/\rho_{0\uparrow} \tag{2.2.11}$$

As follows from Eq. (2.2.9), in the alloys with $\alpha \simeq 1$, the temperature dependence of the resistivity will be dominated by the temperature dependence of the pure metal resistivity ρ_i. The main contributions to ρ_i at room temperature arises from electron-phonon and electron-magnon scattering.

For alloys with α very different from unity, the dominant contribution to the temperature dependence is proportional to the spin-mixing term $\rho_{\uparrow\downarrow}(T)$, which is associated to the electron-magnon scattering. The electron-magnon scattering vanishes at $T = 0$ K remaining the spin-orbit interaction a dominant mechanism responsible for the mixing of majority and minority spin states [9].

2.2.2 Spin Hall effect

In 1929 N.F.Mott described the elastic scattering of an electron beam on a heavy atom which, due to the spin-orbit interaction, leads to the separation of the two spin states. Based on this approach, in 1971 Dyakonov and Perel predicted theoretically the existence of the Spin Hall Effect, defined as the accumulation of oppositely polarized spins at the opposite boundaries of the sample, which leads to the creation of a spin current perpendicular to the charge current [34]. Unlike the ordinary Hall effect, where the flowing charges accumulate at the surfaces due to the action of the Lorentz force in a magnetic field, in SHE the spin accumulation originates from the spin-orbit interaction, therefore no magnetic field is needed. The inverse situation can also take place: a spin current can generate a transverse electrical current, which leads to an accumulation of electrical charges of opposite signs at the opposite lateral boundaries (Inverse Spin Hall Effect, ISHE).

In the following sections we will describe a phenomenological way to calculate the generated spin Hall current for the cases when an electric current flows in a single heavy metal. We will also discuss briefly the main mechanisms of the spin Hall effect, namely an intrinsic mechanism, which is due to the spin-dependent band structure coupling with an external electric field, and extrinsic mechanisms (skew-scattering and side-jump), which are due to the influence of spin-orbit interaction on electron scattering by impurities.

Phenomenological description of the effect

The transport of spins and charges can be described in a simple phenomenological way [34, 35]. Let q_k^c be the charge current flowing in the k direction and q_{ij}^s be the generated spin current, where the first index indicates the flow direction and the second one corresponds to the direction of spin-polarizations ($i, j, k = x, y, z$). Without spin-orbit interaction the charge current and the spin current can be written as

$$q_k^{c,0} = -\mu n E_k - D\frac{\partial n}{\partial k}, \tag{2.2.12}$$

$$q_{ij}^{s,0} = -\mu n E_i P_j - D\frac{\partial P_j}{\partial i} \tag{2.2.13}$$

where μ is the electron mobility, n is the electron concentration, D is the diffusion coefficient and $\mathbf{P}$ is the vector of spin polarization. If the spin-orbit coupling is considered, the charge current and spin current are interconnected by the following relations:

$$q_k^c = q_k^{c,0} + \theta_{SH}\varepsilon_{kij}q_{ij}^{s,0} \tag{2.2.14}$$

$$q_{ij}^s = q_{ij}^{s,0} - \theta_{SH}\varepsilon_{ijk}q_k^{c,0}, \tag{2.2.15}$$

where ε_{ijk} is the unit antisymmetric tensor and θ_{SH} is a dimensionless coupling constant called spin Hall angle, which shows the efficiency of charge-to-current conversion. The different signs in Eq. (2.2.14) and (2.2.15) originates

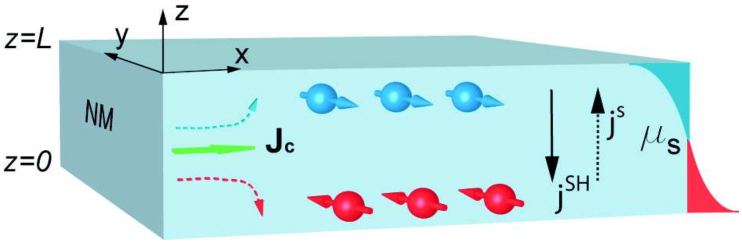

Figure 2.2: Illustration of spin Hall effect: a charge current j^c flowing in x-direction generates a transverse spin Hall current j^{SH} leading to the spin accumulation at the edges of the strip. The spin accumulation μ_s in turn generates a spin current in opposite direction j^s. The profile on the front panel shows the spin accumulation distribution over the strip width indicating the maximum of the spin accumulation at the boundary and its decay within the spin diffusion length

from the different properties of the charge and spin current with the respect to time inversion (while charge current changes sign under time inversion, the spin current does not). Let us now substitute Eq. (2.2.12) in (Eq. 2.2.14) representing the charge current in term of charge current density $\mathbf{j} = -eq$:

$$\mathbf{j}/e = \mu n\mathbf{E} + D\nabla n + \theta_{SH}\mu n\mathbf{E}\times\mathbf{P} + \theta_{SH}D\nabla\mathbf{P} \tag{2.2.16}$$

$$\mathbf{j}^s_{ij}/e = -\mu n E_i P_j - D\frac{\partial P_j}{\partial i} + \theta_{SH}\varepsilon_{ijk}(\mu n E_k + D\frac{\partial n}{\partial k}), \tag{2.2.17}$$

These simple equations show the main consequences of the charge and spin current coupling: the anomalous Hall effect, the spin Hall effect and the inverse spin Hall effect. Indeed, the third term in Eq. (2.2.16) describes the anomalous Hall effect, where the induced charge current is proportional to the magnetization produced by the spin polarization. The fourth term in Eq. (2.2.16) describes the generation of an electrical current due to the inhomogeneous spin density, known as the inverse spin Hall effect. Finally, the last term in Eq. (2.2.17) is nothing else as the spin Hall effect: the creation of a spin current induced by a charge current.

Spin Hall effect in a single heavy metal

Let us consider the case, when the charge current flows in the x direction producing a spin current flowing in the z direction being polarized in the y direction (Fig. 2.2). The generated spin Hall current $j^{\mathrm{SH}} = \theta_{SH}\sigma E_x$ produces a spin accumulation μ_s at the edge of the strip, which in turn generates a spin current in the opposite direction $j^s = \frac{\sigma}{2e}\frac{\partial\mu_s}{\partial z}$, where $\sigma = e^2ND$ is the conductivity of spin channel, N is the density of states, and D is the spin diffusion coefficient. The spin accumulation can be described by the spin-diffusion equation

$$\frac{\partial^2 \mu_s}{\partial x^2} = \frac{\mu_s}{\lambda_{\text{sd}}^2}, \tag{2.2.18}$$

where $\lambda_{\text{sd}} = \sqrt{D\tau_{\text{sf}}}$ is the spin-flip diffusion length and τ_{sf} is the spin relaxation time. The general solution of this differential equation (2.2.18) can be presented in the form:

$$\mu_{\text{s}}(x) = Ae^{-x/\lambda_{\text{sd}}} + Be^{x/\lambda_{\text{sd}}}, \tag{2.2.19}$$

where coefficients A, B are determined from the boundary conditions at the interfaces

Using Eq. (2.2.17), we define the total spin current as a sum of the spin Hall current and the diffusive current driven by spin accumulation:

$$J^s(z) = \frac{\sigma}{2e}\frac{\partial \mu_s}{\partial z} + \theta_{SH}\sigma E_x. \tag{2.2.20}$$

We can now calculate the total current J^s using the spin-diffusion equation (2.2.18) with the boundary conditions $J^s(0) = J^s(L) = 0$ (since at the edge of the strip $j^{\text{SH}} = -j^s$). The solution of spin diffusion equation (2.2.18)

$$\mu_s(z) = \frac{2e\lambda_{\text{sd}} j^{\text{SH}}}{\sigma} \frac{\sinh(L/2\lambda_{\text{sd}} - z/\lambda_{\text{sd}})}{\cosh(L/2\lambda_{\text{sd}})} \tag{2.2.21}$$

shows that the spins accumulate in thin layer near the sample boundaries and diffuse through the width of this layer over the spin diffusion length λ_{sd}. In the center of the strip ($L = L/2$) the spin accumulation is zero (see Fig. 2.2).

Intrinsic mechanism

Let us now discuss the mechanisms of the spin Hall effect, starting with the intrinsic mechanism. The intrinsic spin Hall effect arises in a perfect crystal in the presence of spin-orbit coupled band structure. The mechanism of the effect was independently elucidated by Murakami et al. [96] and Sinova et al. [119]. In the latter work, the intrinsic SHE is described for the specific case of 2D electron systems with a strong Rashba spin-orbit coupling (system with inversion symmetry breaking), where the electrons have definite momentum $p = \hbar k$ and spin polarization. Under the influence of an external electric

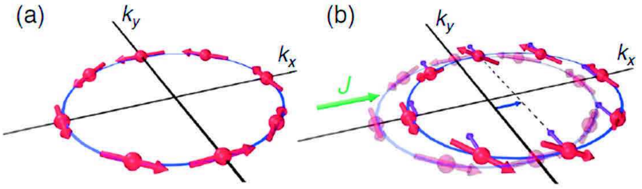

Figure 2.3: Illustration of intrinsic spin Hall effect: (a) Fermi surface of 2D Rashba spin-orbit coupled system in unperturbed regime. (b) Fermi surface displacement under the influence of an electric field. When electrons move through the momentum space they experience an additional spin-orbit field that leads to the rotation of spin down and spin up electron in opposite direction. Figure is taken from [120]

field electrons move through the momentum space experiencing an effective magnetic field, that results in the rotation of spin-up and spin-down electrons in opposite direction (Fig. 2.3).

In more general case, the intrinsic SHE can be analyzed in term of Berry phase in momentum space [96]. In this model, the momentum displacement caused by an electric field can be regarded as an adiabatically changing parameter and the Berry phase $B_{\mathrm{n}}(k)$ can be regarded as a magnetic field in **k**-space. The spin Hall conductivity is calculated from the Kubo formula as

$$\sigma_{\mathrm{xy}}^{\mathrm{sH}} = -\frac{e^2}{\hbar}\sum_n \int_{BZ} d^2k n_F(\varepsilon_n(k)) B_{nz}(k), \tag{2.2.22}$$

where $n_F(\varepsilon_n(k))$ is the Fermi distribution function for the n-th band and the integral is over the entire Brillouin zone. By introducing $B(k)$ into the Boltzmann transport equation, one obtains modified equations of motion

$$\begin{aligned} \dot{x} &= \frac{1}{\hbar}\frac{\partial \mathbf{E}_n(k)}{\partial k} + \dot{k} \times B_n(k), \\ \hbar\dot{k} &= -e[\mathbf{E} + \dot{x} \times B(x)] \end{aligned} \tag{2.2.23}$$

where the additional second term in Eq. (2.2.23) represents an anomalous electron velocity coming from the Berry phase. This result shows, that while moving in an external electric field, an electron experiences an effective magnetic field created by its own spin that gives rise to an anomalous electron velocity perpendicular to the field direction. This anomalous velocity generates the intrinsic spin Hall effect.

The effective magnetic field $B_n(k)$ and the intrinsic spin Hall conductivity can be evaluated by first principle calculations. It was first calculated for semiconductors showing that the intrinsic mechanism is dominant in p-type GaAs structures [96]. Recently, a large intrinsic SH conductivity was calculated in $4d$ and $5d$ transition metals [126], showing that the largest conductivity arises for those parts of band structure where the Fermi level is located within spin-orbit splitted branches. It was also shown that the sign of SH conductivity depends on the number of d-electrons, which was experimentally confirmed in lateral spin valve structures [92].

Extrinsic mechanisms

The extrinsic mechanisms originate from the influence of the spin-orbit interaction on electron scattering by impurities. There exists two processes through which the impurities separate different spin states: side jump and skew-scattering.

Consider first the side jump scattering [Fig 2.4(a)]. It originates from the displacement of the center of the electron wave packet. If an electron with a velocity v passes through an electric field $\mathbf{E} = -(1/e)\nabla u(\mathbf{r})$ created by the impurity potential $u(\mathbf{r})$, it experiences an effective magnetic field $\mathbf{B}_{eff}$, that leads to the spin-orbit potential [85]

$$u_{so}(r) = \mu_{\mathrm{B}}\sigma \cdot \mathbf{B_{eff}} = \eta_{\mathrm{so}}\sigma \cdot [\nabla u(\mathbf{r}) \times \nabla / i], \tag{2.2.24}$$

where σ is the Pauli spin operator and η_{so} is the spin-orbit coupling parameter. Due to the presence of such spin-orbit potential, an additional term appears in the expression of the electron velocity, which is related to the anomalous velocity of the finite wave packet. In other words, describing the electron not by an infinitely extended plane wave but by a finite wave packet, one can imagine that during the very short interval of time, in which the wave packet overlaps the impurities, the anomalous velocity caused by spin-orbit coupling will dominates leading to the small displacement of the center of the wave packet. Thus, the electron trajectory will be shifted by some distance with the respect to the electric field. Electrons with opposite spins will move in opposite directions, in turn creating the spin current. The spin Hall conductivity caused by side-jump contribution is given by [85]

$$\sigma_{\mathrm{sH}}^{\mathrm{SJ}} = \theta_{\mathrm{sH}}^{\mathrm{SJ}}\sigma_{\mathrm{N}} = e^2/\hbar\eta_{\mathrm{so}}n_e, \tag{2.2.25}$$

where σ_{N} is the electrical conductivity and n_e is the carrier density. Notably, although the effect arises from the collision of electron with impurities it does

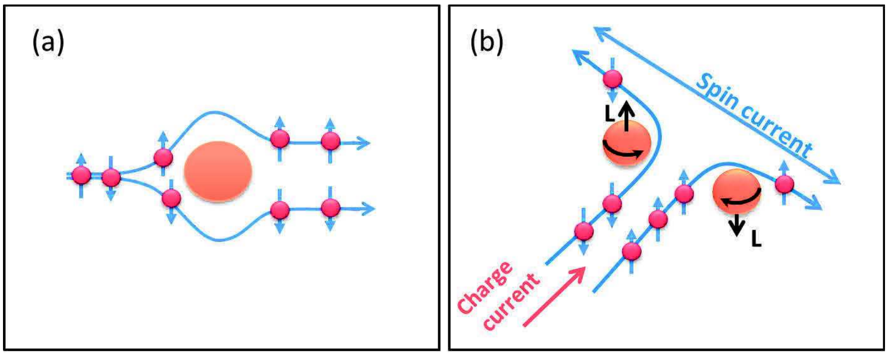

Figure 2.4: Illustration of extrinsic spin Hall effects: (a) side jump scattering; (b) skew-scattering

not depend on the impurity concentration, but only depends on the applied electric field.

Now, let us consider the skew scattering contribution to the spin Hall conductivity [Fig. 2.4(b)]. It arises from the asymmetric scattering of an electron on heavy atom impurities, which takes its origin from the Mott scattering in relativistic physics [94]. When an electric current flows in a material with strong spin-orbit coupling, the spin-up electron is strongly scattered by the down-pointing angular momentum of the heavy atom, which tents to deflect the electron motion to the right. On the contrary, the spin-down electron is affected more by the up-pointing angular momentum, which twists its direction to the left. Intuitively, this process can be understand by comparing the electron with a ball, which is deflected in one direction or the other depending on its sense of rotation.

The skew-scattering can be calculated from the asymmetric contribution of the scattering probability in the Boltzmann equation. From the calculations given in Ref. [85], one obtains the spin Hall conductivity due to the asymmetric skew-scattering:

$$\sigma_{\mathrm{sH}}^{\mathrm{SS}} = \theta_{\mathrm{sH}}^{\mathrm{SS}}\sigma_{\mathrm{N}} = -(\frac{2\pi}{3})\eta_{\mathrm{so}}[N(0)u_{\mathrm{imp}}]\sigma_{\mathrm{N}}, \tag{2.2.26}$$

where $N(0)u_{\mathrm{imp}}$ is the impurity concentration. The study of the skew-scattering using first-principle calculations was performed for different systems, where light element impurities were incorporated in heavy element hosts and vice versa [42]. It was shown, that the magnitude of spin Hall conductivity depends on the spin-orbit coupling between the impurities and the

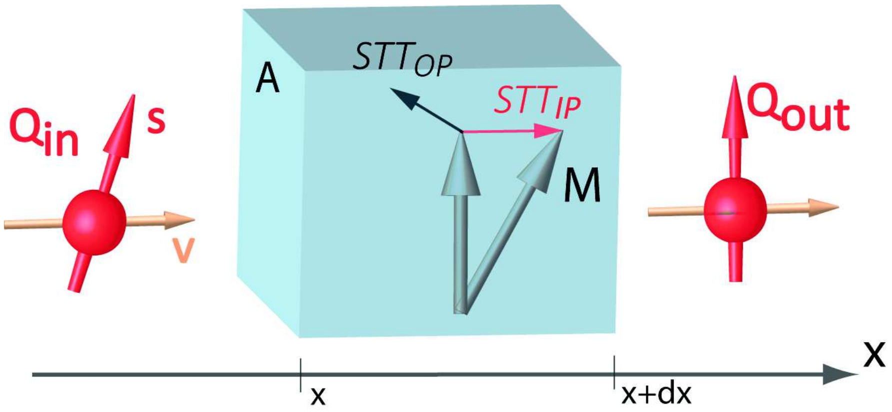

Figure 2.5: Schematic illustration of the transfer of spin momentum from incoming electrons with spin s to local magnetization $\mathbf{M}$ of a ferromagnet. The in-plane torque (IP) and the out-of-plane (OP) torque are sketched.

hosts and thus the choice of impurities and hosts may significantly influence the spin Hall conductivity.

2.3 Spin transfer torque

The first prediction of the existence of spin transfer torque has been put forward by Berger in 1980's after the experimental observation of the current induced domain wall motion in ferromagnetic material. However, at that time the effect did not attract great attention, since a huge current was required to move the domain wall in a sample of a few mm, resulting in a large heating of the sample that hindered the experimental confirmation of current driven DW. With the advance in nanofabrication process it became possible to demonstrate the effect of spin transfer torque at reasonably low current in nanoscale spin-valve structure [108, 43]. In 1996, Berger [11] and Slonczewski [121] independently showed that the current flowing perpendicularly to the film plane in a spin-valve structure (F1-N-F2) is able to reorient the magnetization of the second ferromagnet via spin transfer torque.

The physics of the spin transfer torque process is illustrated in Fig. 2.5(a). When an electron enters the ferromagnet the local magnetization $\mathbf{M}$ tends to align the spin moment $\mathbf{s}$ of the incoming electron in the direction of magnetization. As a result, an electron experiences a torque from magnetization that leads to the reorientation of the electron's spin at the exit of the ferromagnet. In turn, due to the conservation of the angular momentum, the flowing electron must exert an equal and opposite torque on the magnetization. This torque is called the spin transfer torque and is defined as

$$\mathbf{T} = \frac{P\mu_{\mathrm{B}}}{eM^2}\mathbf{M} \times (\mathbf{M} \times \mathbf{s}) \tag{2.3.1}$$

where P is the degree of the spin polarization of the electric current. This torque is called Slonczewski torque or in-plane because it lies in the plane containing $\mathbf{M}$ and $\mathbf{s}$. There exists a correction to the Slonczewski torque called out-of-plane, which is directed perpendicular to the first one. The magnitude of both torques may be more or less important depending on the material and magnetic texture.

In the following, we will consider the effect of STT on the precession magnetization for two cases: when the spin current flows through a continuously variable magnetization texture (section 2.3.1) and when it flows through the interface between a ferromagnet and a non-magnetic metal (section 2.3.1).

2.3.1 Spin transfer torque for a continuously variable magnetization texture

Consider a spin current $\mathbf{j_s}(x)$ expressed in units of μ_{B} flowing in the x direction through the volume Adx of a ferromagnet with a non-uniform magnetization $\mathbf{M}(x)$. Assuming that the dynamics of the magnetization is slow compared to the characteristic time of the electron transport, such as the decoherence time, the electron relaxation time, and the spin diffusion time. In such a case, it is reasonable to assume that the spin of the conduction electron follows the direction of the local magnetization at each point of space $\mathbf{j_s}(x) = \mathbf{M}(x)j_s/M_s$, that is known as the adiabatic hypothesis. As shown in Fig. 2.5, this alignment of the spin with the local magnetization is accompanied by a loss of magnetic momentum of the itinerant electron. Per unit volume and unit time this loss of momentum amounts to

$$\frac{\partial \mathbf{j_s}}{\partial x} = j_s \frac{\partial \mathbf{M}}{\partial x}\frac{1}{M_s}. \tag{2.3.2}$$

An equal quantity of momentum is gained by the magnetic moment in the ferromagnet due to the conservation of angular momentum:

$$\frac{\partial \mathbf{M}}{\partial t} = -\frac{\partial \mathbf{j_s}}{\partial x}. \tag{2.3.3}$$

Expressing the spin current density in terms of the charge current density $\mathbf{j}_c$ and the degree of spin polarization of the electrical current P, the adiabatic spin transfer torque can be written as

$$\frac{\partial \mathbf{M}}{\partial t} = \frac{\mu_\mathrm{B}}{eM_s} P \mathbf{j_c} \cdot \frac{\partial \mathbf{M}}{\partial x}, \tag{2.3.4}$$

where $\frac{\mu_\mathrm{B}}{eM_s} P \mathbf{j_c} = \mathbf{u}$ is the effective magnetization velocity.

A torque perpendicular to the adiabatic torque may also exist, which is called non-adiabatic spin transfer torque. It was first deduced by Zhang et Li [143] from the theoretical s-d model, where the Hamiltonian $H_\mathrm{sd} = J_\mathrm{ex}\mathbf{sM}/M_s$ relates the conduction s-electron spin with the the local magnetization $\mathbf{M}/M_s$ via the exchange coupling. The spatial and the temporal variation of the spin of the conductive electron is divided in two terms: $\langle \mathbf{s} \rangle = m(r,t) = m_0(r,t) + \delta m(r,t)$, where the first corresponds to the spin density whose direction is parallel to the magnetization and $\delta m(r,t)$ is the nonequilibrium spin density, which relaxes by spin-flip scattering. In addition to the adiabatic torque, the local magnetization also experiences a torque due to the nonequilibrium spin density $\delta m(r,t)$, which is given by the expression

$$T = \frac{\mu_\mathrm{B} P}{eM_s^2} \beta \mathbf{M} \times (j_c \cdot \nabla)\mathbf{M}, \tag{2.3.5}$$

where the parameter β characterizes the relative strength of the non-adiabatic torque with respect to adiabatic one, and is related to the spin flip scattering time τ_sf.

The dynamic magnetization affected by both adiabatic and non-adiabatic torques is described by the modified LLG equation of motion

$$\frac{d\mathbf{M}}{dt} = -\gamma \mathbf{M} \times \mathbf{H}_\mathrm{eff} + \frac{\alpha}{M_\mathrm{s}} \mathbf{M} \times \frac{d\mathbf{M}}{dt} - u\frac{d\mathbf{M}}{dx} + \beta u \frac{\mathbf{M}}{M_\mathrm{s}} \times \frac{d\mathbf{M}}{dx} \tag{2.3.6}$$

where $u = -P\mu_\mathrm{B} j/(eM_\mathrm{s})$ is the effective magnetization velocity and corresponds to the magnitude of the adiabatic STT, and β is the non-adiabatic coefficient.

Current induced domain wall motion

For a system with non-uniform magnetization, such as a domain wall (DW), the spin transfer torque leads to the displacement of the DW, that is called current induced domain wall motion (Fig. 2.6).

The DW motion is caused by both the adiabatic and the non-adiabatic torques, but depending on the magnetic material their contributions can be more or less important. For an in-plane magnetized magnetic wire (fabricated from a soft material such as permalloy), it is the non-adiabatic torque,

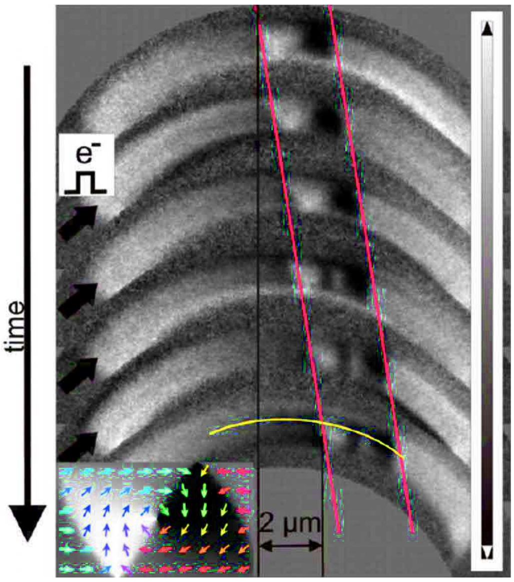

Figure 2.6: Photoemission electron microscopy image of the DW motion in a Py wire. Figure is taken from Ref [86]

which plays a dominant role in the DW displacement acting as an additional magnetic field. Indeed, in the absence of the non-adiabatic torque, the theory predicts the existence of a threshold current density, below which the DW can not move. This threshold current j_{th} is given by the DW width λ_w and the easy plane anisotropy K as [127]

$$j_{\mathrm{th}} = \frac{e\gamma\lambda_w}{P\mu_{\mathrm{B}}}K \tag{2.3.7}$$

However, the experimental results showed that DW motion is allowed below this threshold current, which is attributed to the non-adiabatic torque. In this case, the DW velocity is defined by the ratio between the non-adiabatic torque β and the Gilbert damping constant α as $v = \beta u/\alpha$.

In contrast, it was demonstrated by micromagnetic simulations [62] and confirmed experimentally [72], that the DW motion in a wire with perpendicular magnetic anisotropy is mostly governed by the adiabatic STT. It was shown, that for systems with out-of-plane magnetization, where the effective anisotropy constant K is much smaller than for the system with in-plane magnetization, the adiabatic threshold current is significantly reduced. As a result, the adiabatic torque becomes dominant compared to the non-adiabatic one.

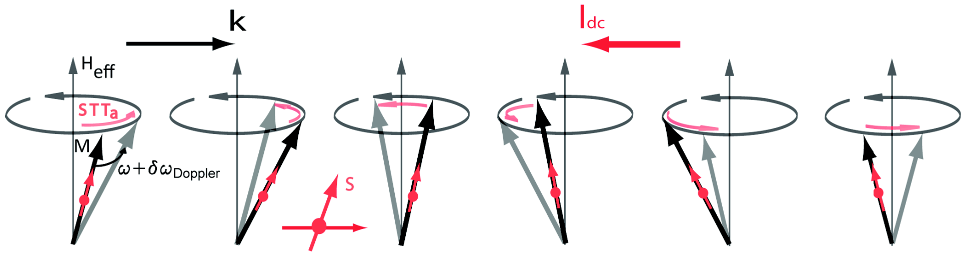

Figure 2.7: An illustration of the current-induced spin wave Doppler shift. The alignment of the spin of conduction electrons with the local magnetization **M** at each point of space leads to the adiabatic STT, which results in the change of precession frequency.

Current induced spin wave Doppler shift

Another example of non-uniform magnetization configuration is a spin wave. The effect of the spin transfer torque on a propagating spin wave, which has the form $\mathbf{m} = \mathbf{m_0}e^{i(\omega t - kx)}$ with a frequency ω and a wave vector k, can be determined from the linearized version of equation of motion (Eq. 2.3.6)

$$i\omega\mathbf{m} = -\gamma(\mathbf{m}\times\mu_0\mathbf{H_0} + \mathbf{M_0}\times\mu_0\mathbf{h}) + \frac{i\omega\alpha}{M_\mathrm{s}}\mathbf{M_0}\times\mathbf{m} + iku\mathbf{m} - ik\beta u\frac{\mathbf{M}_0}{M_\mathrm{s}}\times\mathbf{m} \tag{2.3.8}$$

From this equation one can see, that the adiabatic torque leads to a variation of the precessional frequency

$$\omega \to \omega + uk \tag{2.3.9}$$

whereas the non-adiabatic torque results in the modification of the magnetization damping

$$\alpha\omega \to \alpha\omega - \beta uk. \tag{2.3.10}$$

Note that the magnitude of the non-adiabatic torque is in general much smaller than the magnitude of the adiabatic one ($\beta < 0.1$).

The frequency shift due to the adiabatic STT is called the current induced spin wave Doppler shift (CISWDS). The phenomenon is illustrated in Fig. 2.7. In the adiabatic regime the spin of conduction electrons is aligned everywhere with the local magnetization. This alignment is accompanied by a transfer of angular momentum. The direction of this transfer is oriented along the tangent of the magnetization precession trajectory. Depending on the current direction the magnetization precession will speed up or slow down. More precisely, if the flow of magnetic moments is parallel to the direction of spin wave propagation, the spin transfer torque will increase the frequency of magnetization precession, as it is shown in Fig. 2.7. On the contrary, electrons moving in the opposite direction will exert a torque in the direction opposite to the precession, thus reducing the frequency.

The reason why this effect is called a Doppler shift can be understood by following the initial theoretical prediction by Lederer and Mills [77]. Let the spin wave propagates in a frame $\mathbf{R}'$ in the form of plane wave

$$\mathbf{m}'(x') = \mathbf{m_0} e^{i(\omega t - kx')} \tag{2.3.11}$$

When an electric current is applied to the material, the electrons start to move with some drift velocity v_d. A Galilean transformation $x = x' + v_d t$ relates the reference frame $\mathbf{R}$ linked with the material with the frame $\mathbf{R}^{'}$ linked with the electrons. As a result, the spin wave in reference $\mathbf{R}$ can be written as

$$\mathbf{m}(x) = \mathbf{m_0} e^{i(\omega t - kx + kv_d t)} = \mathbf{m_0} e^{i([\omega + kv_d]t - kx)}. \tag{2.3.12}$$

As one can see, the motion of the electrons induces a shift of the precession frequency by an amount

$$\delta\omega_{\text{Doppler}} = kv_d \tag{2.3.13}$$

Despite the spin wave Doppler shift effect was theoretically predicted half a century ago, the first experimental observation of the effect was reported in 2008 by our group in Strasbourg [135]. The experimental device is shown in Fig. 2.8(a). Two microwave antenna are used to excite and to detect the propagating spin waves with a given wave vector $\mathbf{k}$. When the dc current is applied along the ferromagnetic strip it modifies the spin wave precession frequency shifting it to the left or to the right depending on the relative orientation between the direction of the current and the spin wave wave vector, as seen in Fig. 2.8(b) and (c). Using Eq.(2.3.9), from the frequency shift on the applied current, one can extract the value of spin velocity u and therefore the degree of spin polarization P.

Spin waves can be also used to determine the non-adiabatic coefficient β. As was shown by Eq. (2.3.10), the non-adiabatic torque leads to a modification of the damping parameter of the system. Since the damping process determines the attenuation length of the spin wave and, in turn, the spin wave amplitude, the non-adiabatic torque can be experimentally estimated from the difference of amplitudes measured for two current polarities [118]

Sekiguchi et al. [117] and Chauleau et al. [18] have reported time-domain inductive and magneto-optical measurements of spin wave dynamics under

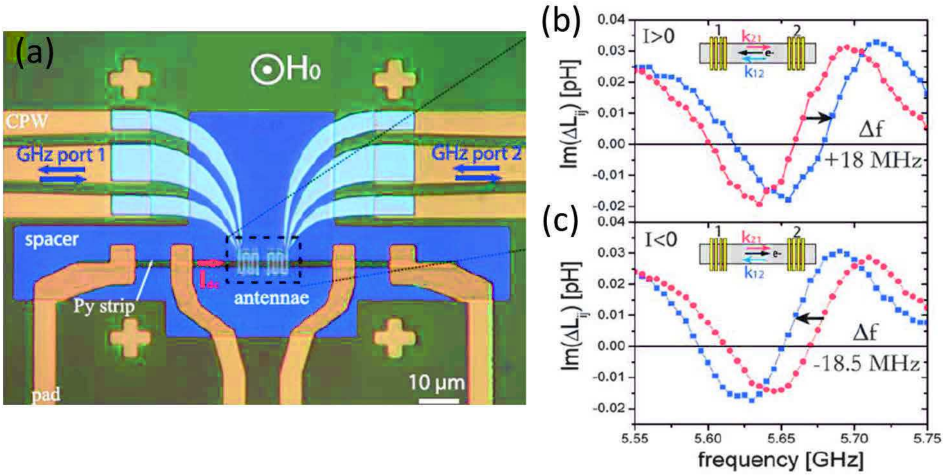

Figure 2.8: (a) Experimental device used to study spin wave Doppler shift. (b)-(c) Influence of an electric current on propagating spin wave. Mutual-inductance measured film for $k > 0$ and $k < 0$ in the presence of a ±6 mA *dc* current. Figure is taken from Ref. [135]

.

current, that allows them to estimate the magnitude of the non-adiabatic coefficient in a permalloy film, which is found to be of the order of a few damping constants, $\beta = 2\alpha$ to 3α.

2.3.2 Spin transfer torque in bilayers

Let us consider now the effects of spin transfer torque occurring at ferromagnetic/non-magnetic interfaces. In such bilayer structures, the spin current can flow perpendicularly to the film plane exerting a torque at the interface. Below we will consider two types of interfacial spin transfer torque: spin pumping and spin Hall driven spin transfer torque. In the first case, the spin current is created by the ferromagnet's magnetization precession and is injected into the normal metal exerting a torque on conduction electrons, while in the second case, the spin current generated by SHE in the normal metal is injected into the ferromagnet exerting a torque on the local magnetization. In the following sections we will describe the interplay between both these STT effects, as well as their influence on the magnetization dynamics in ferromagnetic material.

Spin pumping phenomena

The spin pumping process occurs as a result of the injection of the spin current generated by the precession of the magnetization precession of a ferromagnet into an adjacent nonmagnetic metal. This process can be considered as an adiabatic pumping. Its period is defined by the period of the magnetization precession. The theoretical description of spin pumping is based on a scattering-matrix approach, where the spin transport is described by the interface scattering parameter $A = A_r + iA_i$ [129]:

$$I_s^{\text{pump}} = \frac{\hbar}{4\pi}(A_r \mathbf{s} \times \frac{d\mathbf{s}}{dt} - A_i \frac{d\mathbf{s}}{dt}), \tag{2.3.14}$$

where

$$\begin{aligned} A_r &= \frac{1}{2}\sum[|r_{\text{mn}}^{\uparrow} - r_{\text{mn}}^{\downarrow}|^2 + |t_{\text{mn}}^{\uparrow} - t_{\text{mn}}^{\downarrow}|^2], \\ A_i &= Im \sum[r_{\text{mn}}^{\uparrow}(r_{\text{mn}}^{\downarrow})^* + t_{\text{mn}}^{\uparrow}(t_{\text{mn}}^{\downarrow})^*], \end{aligned} \tag{2.3.15}$$

are given by the reflection and transmission coefficients $r_{\text{mn}}^{\uparrow}, r_{\text{mn}}^{\downarrow}, t_{\text{mn}}^{\uparrow}, t_{\text{mn}}^{\downarrow}$ of spin-up and spin-down electrons at the interface. Here, m and n indicate the transverse modes at the Fermi energy in the normal-metal film.

Using Eq. (2.3.15), one can express the scattering parameter A as $A = g^{\uparrow\downarrow} - t^{\uparrow\downarrow}$, where $g^{\uparrow\downarrow} = g_r^{\uparrow\downarrow} + ig_i^{\uparrow\downarrow}$ is the interface spin mixing conductance and $t^{\uparrow\downarrow}$ is the transmission matrix. The physical meaning of these parameters are that the spin mixing conductance describes the longitudinal part of the spin current pumped into the normal metal, while the transmission matrix represents its transverse components. The longitudinal part of the spin current is along the steady-state magnetization direction and its propagation is defined by the spin diffusion length. The propagation of the transverse components is limited by the spin-coherence length $\lambda_c = \pi/(k_\uparrow - k_\downarrow)$, where $k_{\uparrow(\downarrow)}$ are the Fermi wave vectors. When the ferromagnetic film is thicker than λ_c (that is the case for most transition metals for which λ_c is of the order of few monolayers), the spins of electrons undergo a precession dephasing [104]. As a result, the transverse components of spins average to zero, so $t^{\uparrow\downarrow}$ vanishes, and thus the pumped spin current is only determined by the spin mixing conductance:

$$I_s^{\text{pump}} = \frac{\hbar}{4\pi} g^{\uparrow\downarrow} \mathbf{s} \times \frac{d\mathbf{s}}{dt}, \tag{2.3.16}$$

Let us consider the case, when the spin injection rate from the ferromagnet is higher than the spin diffusion rate τ_{sf}^{-1} in the normal metal. This leads

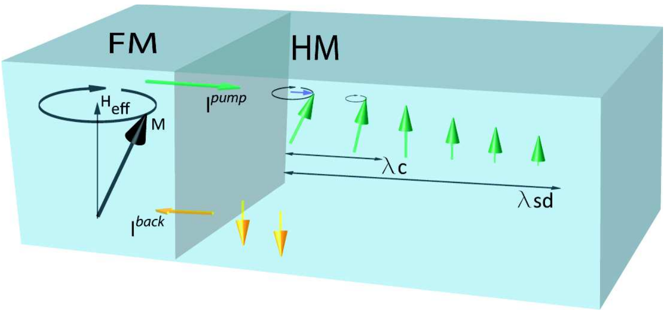

Figure 2.9: Illustration of spin pumping process in a ferromagnetic (FM)/heavy metal (HM) bilayer. The precession magnetization generates a spin current, which is injected into the heavy metal via the transfer of spin momentum to conductive electrons. The transverse part of the pumped spin current decays through the spin-coherence length λ_c and the longitudinal part decays through the spin-flip length $\lambda_{\rm sf}$.

to the spin accumulation in normal metal, which in turn yields the creation of a spin current, which will propagate in both directions, i.e. back into the ferromagnet and forth into the normal metal. Consequently, the total current at the F/N interface will be a sum of a pumped spin current and a back-flow current $I_s = I_s^{\rm pump} - I_s^{\rm back}$. It has been shown in [129], that the back-flow current $I_s^{\rm back}$ can be calculated as

$$I_s^{\rm back} = \frac{1}{2\pi} g^{\uparrow\downarrow} \mu_s. \tag{2.3.17}$$

Using the spin-diffusion equation (2.2.18) with boundary conditions $j_s(0) = j_{s0}$ and $j_s(L) = 0$, the back-flow current driven by the spin accumulation through the interface reads

$$I_s^{\rm back} = \frac{1}{2\pi} g^{\uparrow\downarrow} \frac{e\lambda_{\rm sd}}{\sigma} \frac{j_{s0}}{\tanh(L/\lambda_{\rm sd})}. \tag{2.3.18}$$

For the current density $j_{s0} = I_s/S$, where S is the area of interface, we can rewrite Eq. (2.3.18) as

$$I_s^{\rm back} = \beta G^{\uparrow\downarrow} I_s, \tag{2.3.19}$$

where $\beta = (1/2\pi)(\lambda_{\rm sd}/\sigma)$ is the back-flow factor in the limit $L \gg \lambda_{\rm sd}$ and $G^{\uparrow\downarrow} = g^{\uparrow\downarrow}/S$ in units of $[S/m^2]$. Therefore, the total current through the interface can be expressed in terms of the pumped current as

$$I_s = \frac{I_s^{\rm pump}}{1+\beta G^{\uparrow\downarrow}} = \frac{\hbar}{4\pi} \frac{G^{\uparrow\downarrow}}{1+\beta G^{\uparrow\downarrow}} (\mathbf{s} \times \frac{d\mathbf{s}}{dt}). \tag{2.3.20}$$

Let us now consider the consequence of the spin pumping on the magnetization precession in the ferromagnet. From the conservation of angular momentum, the injection of the spin current out of the ferromagnet leads to the loss of spin angular momentum $d\mathbf{s}/dt = -I_s$, where $\mathbf{s} = \mathbf{M}V/\gamma$ is the total spin in the ferromagnet. The modification of the magnetization dynamic can be thus evaluated using LLG equation by introducing an additional term, which describes the momentum loss due to the spin pumping

$$\frac{d\mathbf{M}}{dt} = -\gamma\mathbf{M} \times \mathbf{H}_{\text{eff}} + \alpha_0\mathbf{M} \times \frac{d\mathbf{M}}{dt} + \frac{\gamma}{M_sV}I_s, \tag{2.3.21}$$

where M_s is the saturation magnetization and V is the volume of the ferromagnet. Replacing the expression for I_s from Eq. (2.3.20) in the Eq. (2.3.21), one can see that the spin pumping acts as an additional damping term, enhancing the Gilbert damping α_0 by an additional term

$$\alpha^{\text{SP}} = \frac{G^{\uparrow\downarrow}}{1+\beta G^{\uparrow\downarrow}}\frac{g\mu_B}{4\pi M_s t} = G_{\text{eff}}^{\uparrow\downarrow}\frac{g\mu_B}{4\pi M_s t}, \tag{2.3.22}$$

where t is the thickness of ferromagnet. By assuming $\tau_{\text{sf}} \to 0$, i.e. treating the normal metal as a perfect spin sink, the back-flow factor β tends to 0, so the total Gilbert damping coefficient can be defined as

$$\alpha = \alpha_0 + \alpha^{\text{SP}} = \alpha_0 + \frac{g\mu_B G^{\uparrow\downarrow}}{4\pi M_s t}. \tag{2.3.23}$$

The damping factor of the magnetic films with and without the nonmagnetic spin sink layer can be extracted from the line width of the FMR spectra. The enhancement of the damping can be used to extract the spin mixing conductance of the F/N interface by analyzing the modification of the damping factor as a function of t [89].

Spin Hall effect in bilayer structure

By applying an electrical current in a heavy metal, one generates a transverse spin current. The total spin current is the sum of the spin current induced by the SHE and the spin current driven by the gradient of spin accumulation (see Sec. 2.2.2): For the charge current applied in the x direction, the generated spin current in the z direction is written as

$$J^s(z) = \frac{\sigma}{2e}\frac{\partial \mu_s}{\partial z} + j^{\text{SH}}. \tag{2.3.24}$$

In the presence of an adjacent ferromagnetic layer at the bottom side of HM (at $z = 0$), the induced spin current will penetrate through the NM/FM interface with an efficiency governed by the effective interfacial spin mixing conductance $G^{\uparrow\downarrow}$

$$J^s(z=0) = j_{s0} = \frac{1}{2\pi} G^{\uparrow\downarrow} \mu_s. \tag{2.3.25}$$

The spin accumulation in the normal metal is calculated using the drift-diffusion equation (2.2.18) with two boundary conditions: Eq. (2.3.25) at the NM/FM interface ($z = 0$) and $J^s = 0$ at the vacuum/NM interface ($z = L$). For the given boundary conditions the expression for spin accumulation takes the form

$$\mu_s(z) = -\frac{2e\lambda_{\mathrm{sd}}}{\sigma} j^{\mathrm{SH}} \frac{\sinh[(2z-L)/2\lambda_{\mathrm{sd}}]}{\cosh(L/2\lambda_{\mathrm{sd}})} + \frac{2e\lambda_{\mathrm{sd}}}{\sigma} j^{s0} \frac{\cosh((z-L)/\lambda_{\mathrm{sd}})}{\sinh(L/\lambda_{\mathrm{sd}})}. \tag{2.3.26}$$

If there is no spin transfer at the interface, i.e. the spin-mixing conductance is zero, the second term in Eq.(2.3.26) becomes zero and the spin accumulation at the interface is the same as was calculated for a single heavy metal layer (Eq. 2.2.21). In the case when $G^{\uparrow\downarrow} \neq 0$, the spin accumulation at the magnetic interface is determined as

$$\mu_{s0} = \frac{2e\lambda_{\mathrm{sd}} j_{\mathrm{SH}} \tanh(L/2\lambda_{\mathrm{sd}})}{\sigma + (2e\lambda_{\mathrm{sd}})/(2\pi) G^{\uparrow\downarrow} \coth(L/\lambda_{\mathrm{sd}})}. \tag{2.3.27}$$

The spin current traversing the interface can be thus expressed as

$$j_{s0} = \frac{1}{2\pi} G^{\uparrow\downarrow} \mu_{s0} = j^{\mathrm{SH}} \cdot T, \tag{2.3.28}$$

where T is the so-called spin interfacial transparency defined as

$$T = \frac{G^{\uparrow\downarrow} \tanh(L/2\lambda_{\mathrm{sd}})}{G_{\mathrm{NM}}/2 + G^{\uparrow\downarrow} \coth(L/\lambda_{\mathrm{sd}})}, \tag{2.3.29}$$

with $G_{\mathrm{NM}} = \sigma/\lambda_{\mathrm{sd}}$ being the spin conductance of the nonmagnetic material. As one can see from Eq. (2.3.28), the spin interfacial transparency is the ratio between the spin current diffusing into the ferromagnet to the spin current generated in the nonmagnetic material, thus showing the ability of the spin current to penetrate trough the NM/FM interface.

The spin-mixing conductance can be deduced from [144, 101]

$$G^{\uparrow\downarrow} = \frac{G^{\uparrow\downarrow}_{\mathrm{eff}}}{1 - 2G^{\uparrow\downarrow}_{\mathrm{eff}}/G_{\mathrm{NM}}}, \tag{2.3.30}$$

where the effective spin-mixing conductance $G^{\uparrow\downarrow}_{\text{eff}}$ is derived from the the damping increase when the nonmagnetic layer is adjacent (Eq. 2.3.22). For the thickness of a nonmagnetic metal larger than the spin-diffusion length, the interfacial transparency can be simply expressed as

$$T = 2G^{\uparrow\downarrow}_{\text{eff}}/G_{\text{NM}}. \tag{2.3.31}$$

To calculate the effect of the spin Hall induced spin transfer torque on the dynamical magnetization, we use the LLG equation by introducing the Slonczewski STT term (2.3.1)

$$\frac{d\mathbf{M}}{dt} = -\gamma\mathbf{M}\times\mathbf{H}_{\text{eff}} + \alpha_0\mathbf{M}\times\frac{d\mathbf{M}}{dt} + \frac{\gamma}{tM_s^2}[\mathbf{M}\times(\mathbf{j}_{s0}\times\mathbf{M})]. \tag{2.3.32}$$

For a geometry in which the spin polarized current is collinear with the static component of magnetization, the Slonczewski spin transfer torque acts as a damping-like torque, which modifies the intrinsic damping by the term α^{SHE} [79] (see subsection 5.3.3 for a derivation of this result)

$$\alpha = \alpha_0 + \alpha^{\text{SHE}} = \alpha_0 + \frac{\gamma}{tM_s^2}\frac{TJ^{SH}}{2\omega_0+\omega_M}, \tag{2.3.33}$$

where $(2\omega_0+\omega_M)$ is proportional to the relaxation rate of the uniform precession mode [see Eq. (1.8.6)]. Depending on the orientation of the injected spin (up or down) with the respect to the local magnetization, the spin transfer torque will either increase or decrease the magnetic damping. Writing the spin current in term of the charge current $J^{SH} = \theta_{\text{SH}}J^c$, one can see that the spin relaxation process can be controlled by simply tuning the direction of the electric current with an efficiency given by spin Hall angle θ_{SH}.

In conclusion, a heavy metal layer adjacent to the ferromagnet leads to spin-orbit related phenomena such as spin transfer torque induced by spin Hall induced spin transfer torque and spin pumping. In both cases, the effect of this spin transfer torque is to modify the magnetic damping. In case of spin pumping, the STT always leads to the increase of damping. In case of STT-SHE, the damping can be either reduced or enhanced depending on the current polarity.

Chapter 3

Experimental setup

In this section the experimental method used to measure the magnetization dynamics will be described. First, the operational principle of propagating spin wave spectroscopy will be presented. Afterwards, the fabrication process of the devices needed for this technique will be discussed. Finally, the complete set-up including the electromagnet and the vector network analyzer (VNA) will be presented.

3.1 Propagating spin wave spectroscopy

Propagating spin wave spectroscopy (PSWS) is a technique, which is based on the inductive coupling between a conducting antenna and a ferromagnetic film. Its operational principle is schematically represented in Fig. 3.1. The device consists of a pair of meander-shape metallic lines (the spin-wave antennas) placed on the ferromagnetic strip. By injecting a microwave current $I(\omega)$ into the antenna one generates an oscillating magnetic field $h(\omega)$ around each metallic line. This oscillating field couples with the magnetization inducing a non-uniform precessional motion, i.e. generating a spin wave. The excited spin wave can propagate in both positive and negative directions with a wave length defined by the spatial periodicity of the antenna. The spin wave induces a variation of magnetic flux, which in turn generates an oscillating voltage $V(w)$, which can be measured by the antenna. An important feature of such devices is that each antenna can be used as emitter and receiver, i.e. the spin wave can be excited and detected by the same antenna, or can be excited by the one antenna and detected by another one. By measuring the voltage V_i and current I_i, where $i = 1, 2$ are the antenna number, one can determine the inductance matrix ΔL_{ij} (see sec. 3.3.1). From the

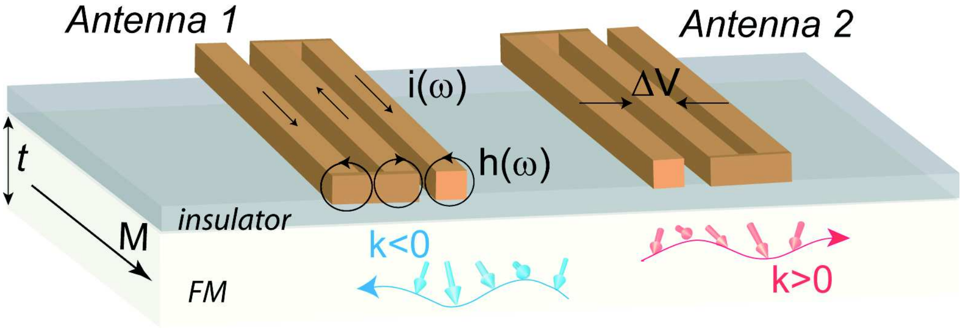

Figure 3.1: Sketch of the operating principle of propagating spin wave spectroscopy: a microwave current $I(\omega)$ is injected into the first antenna generating an oscillating magnetic field $h(\omega)$. This field excites a spin wave, which can be detected, in particular, by the second antenna.

self-inductances ΔL_{11} and ΔL_{22} one can evaluate the efficiency of spin wave excitation, and from the mutual-inductances ΔL_{12} and ΔL_{21} one can extract the propagation characteristic of the spin wave. A more detailed description of the spin wave devices is given in Refs. [134, 136].

3.2 Spin wave device fabrication

We will now describe the fabrication process of the spin wave devices. We used standard lithography processes, which contain both optical and electron-beam lithography parts. A device consists of a ferromagnetic strip, a pair of SW antennas connected to coplanar wave guides and patterned on top of a magnetic stripe, four DC pads and an insulator (Fig. 3.2). As a magnetic material we used both the nickel-iron alloy $Ni_{80}Fe_{20}$ (permalloy, Py) and pure Fe. Because different film deposition techniques and different substrates were used in the two cases, we will first describe in details the fabrication process on Py films, and then explain the specificities of the fabrication process on Fe films. We will also discuss the possible obstacles which may occur during each fabrication process.

All fabrication work has been done in the nanofabrication platform STnano in Strasbourg.

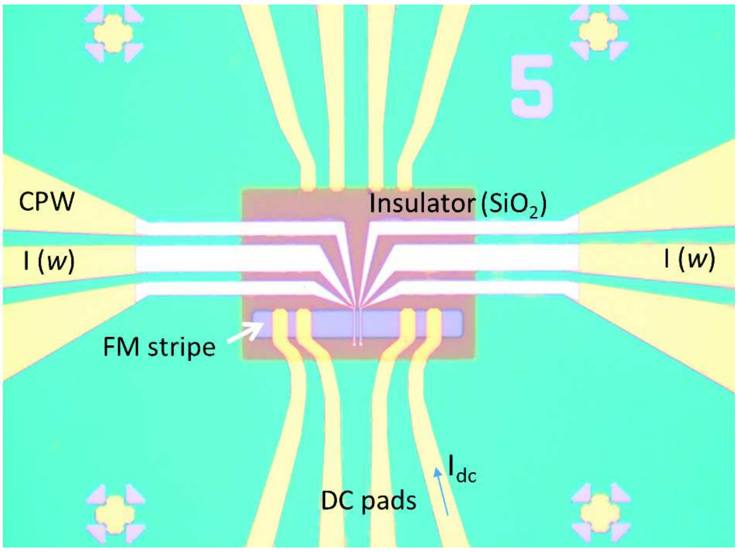

Figure 3.2: Optical microscopy image of a Py/Pt device consisting of a Py stripe, the coplanar waveguides connected to a pair of microwave antenna and four DC pads.

3.2.1 Sample fabrication on Py films

The spin wave devices were fabricated from a set of Ti(5)/Py(t)/Pt(5) trilayers with varying Py film thickness $t = 4, 7, 20$ nm, together with Ti(5)/Py(10)/Pt(10) and Ti(5)/Py(4)/Ti(5) trilayers. All films have been deposited by magnetron sputtering on intrinsic silicon substrates with a thermal oxide layer of about 100 nm. For each Py thickness several devices with different magnetic strip widths and different distances between antennas were realized. The following description of the sample fabrication on Py films will be done using as example the Ti(5)/Py(t)/Pt(5) multilayers (the procedure for the other two trilayers is identical).

Strip

The first step is the patterning of the magnetic strip from the extended film. The strips of a length of 80 μm long and a width of $w = 5, 10, 20$ μm were patterned from the films by using a positive photolithography process, which is shown in Fig. 3.3. The sample was covered with 0.5 μm of photoresist S1805 and then baked at 115° on a hotplate for 2 minutes. Then it was placed against a chromium mask, on which we designed 9 blocks each

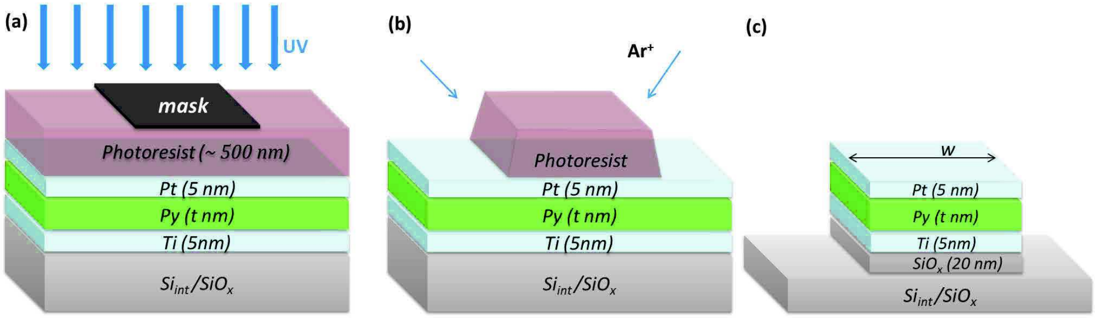

Figure 3.3: Fabrication process of the strip: (a) Positive photolithography process: resist exposure by UV light. (b) Ar^+ ion etching. (c) The strip after the removal of photoresist.

containing 6 strips and alignment crosses (different blocks correspond to different strip widths). Using a MJB4 mask aligner, the sample was exposed by ultraviolet light during 3 sec [Fig. 3.3(a)], after which it was immersed in a bath of developer MF319 for 30 sec. As a result, the resist exposed by UV light was completely dissolved, thus leaving only the part protected by the photomask and creating a resist profile with the typical sidewall slope shown in Fig. 3.3(b). To obtain the required resist profile, a low exposure dose is needed. In this case, the resist is subjected to more intensive irradiation near the mask region, whereas the resist near the substrate is less irradiated. Too high exposure dose leads to homogenous resist irradiation resulting in rectangular resist profile (perpendicular sidewall).

After photolithography, the sample was etched using the Ar^+ ion gun available in the loadlock of our Plassys 550 evaporator. The etching is performed at an incidence of 45° and with a continuous rotation of the sample to minimize the atom re-deposition. The etching time was adjusted to etch the whole metal trilayer [Ti(5 nm)/Py(t)/Pt(5 nm)] and 20 nm of SiO_x. The etching rate, which have been determined for each material, is given in Table 3.1. As a final step, the sample was immersed in acetone (lift-off process) for a few minutes ($\sim$ 30 min) to dissolve the remaining resist as shown in Fig. 3.3(c). A successful lift-off process requires a stooped resist sidewall to minimize the re-deposition of the etched material. If the latter happens, it is recommended to use a remover solution or oxygen plasma cleaning in order to facilitate the lift-off.

Coplanar waveguides and DC pads

Metal	Rate (nm/min)	Deposition technique
Py	12	sputtering
Ti	4	sputtering
Pt	16	sputtering
SiO_x	16	rf sputtering
Fe	9.5	MBE
MgO	9.4	MBE
Ti	1.5	MBE

Table 3.1: The etching rate of the different materials grown by different deposition technique

A pair of coplanar waveguides (CPW) together with four DC pads were patterned by a negative photolithography process, as shown in Fig. 3.4. The sample was coated with image reversal resist AZ 5214, with a thickness of 1.4 μm suitable for lift-off process, and baked on a hotplate at 105° for 1 min 40 sec (the resist thickness should be at least tree times higher than the thickness of deposited material). We used a second photomask, on which we designed the CPW, DC pads, and alignment marks. This pattern was aligned on the strips and alignment crosses already fabricated on the sample. The sample was exposed by UV light during 2.8 sec followed by a post exposure bake (PEB) at 120° for 1 min. Then the sample was irradiated again by UV light for 30 sec without any mask (flood exposure). Since PEB makes the exposed resist insoluble in the developer, areas initially protected by the mask become soluble. So, after developing the sample in AZ-726MIF developer for 25 sec, we got the structure shown in Fig. 3.4(a). Such undercut resist profile is obtained by using a low exposure dose (for the same reason as explained for positive tone lithography). After developing and a few seconds of Ar^+ etching to get a good electrical contact between the DC pads and the Py strip, the sample was covered by Ti(10 nm)/Au(60 nm) in our Plassys 550 evaporator. Then the resist was dissolved in acetone (lift-off precess), resulting in the structure shown in Fig. 3.4(b). The undercut resist profile is essential for a successful lift-off process since the deposited film covers discontinuously the pattern and thus the metal deposited on the resist can be easily removed.

Insulator

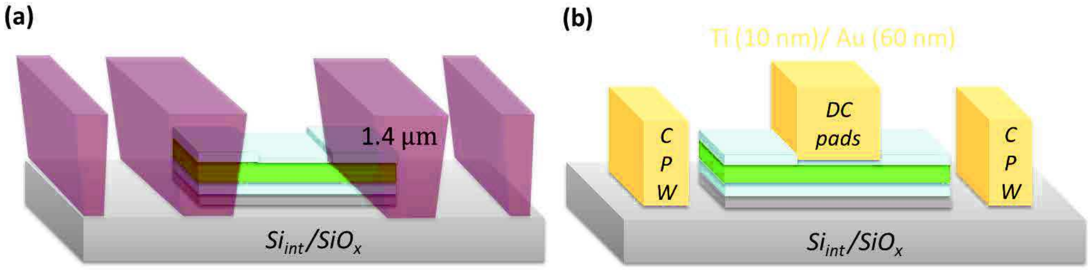

Figure 3.4: Fabrication process of the CPW and DC pads: (a)Negative photolithography process. (b) CPW and DC pads formed after metal deposition and lift-off process

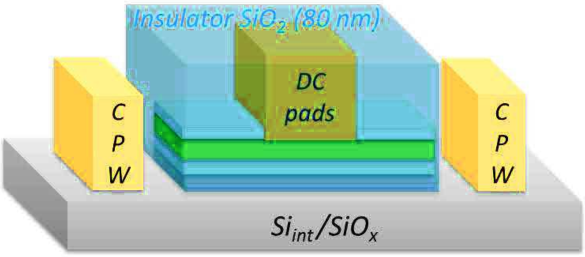

Figure 3.5: Insulator patterned on top of FM stripe

An insulator was patterned on top of the FM strip to avoid any electrical contact between the strip and the microwave antenna, as shown in Fig. 3.5. The same negative photolithography recipe as above was used. After the photolithography, 80 nm layer of SiO_2 was deposited by RF sputtering using our Alliance Concept EVA300+ machine. This is followed by a lift-off in acetone of a few minutes. Using the RF sputtering one may expect the formation of lateral walls (co-called "collars") due to a lack of directionality of sputtered atoms (Fig. 3.6). To avoid the "collar" formation the sputtering should be performed without wafer rotation, which results in a more directional material deposition. Also, one can reduce the resist thickness to reduce the height of the material deposited on the resist sidewall.

Spin wave antenna

As a final step we patterned the spin wave antennas on top of the FM strip using electron beam lithography. The sample was covered with a positive tone electron resist bilayer PMMA 600K/PMMA 950K (AR-P 669.04/AR-P

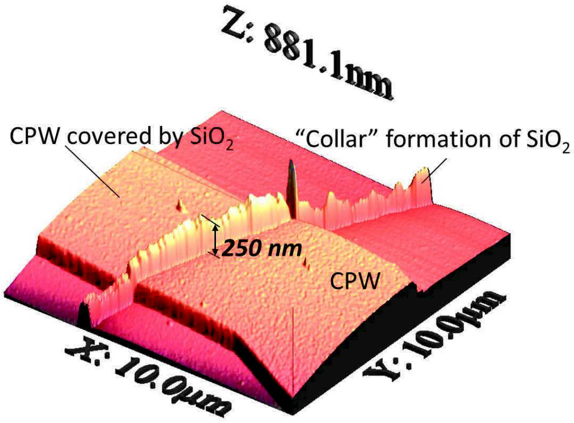

Figure 3.6: AFM image of a CPW pad partially covered by an insulator. A "collar" formation of 250 nm at the edge of insulator, which results in circuit interruption when a metal track is deposited on top.

679.02). The two resist layers are used to increase the resist thickness and to facilitate the lift-off. The sample was baked at 180° for 1 min 30 sec. The exposure was performed at an acceleration voltage of 20 kV in our Zeiss Supra 40 Scanning Electron Microscope equipped with a Raith Elphy Plus pattern generator. Preliminary tests allowed us to determine the nominal exposure dose of the resist, which is of 200 $\mu C/cm^2$. The latter is an important parameter: since the width of the wires and their spacing are of the order of hundred nanometers, overexposure may lead to the lines merging, while underexposure may cause a hard lift-off process. After the resist exposure the sample was developed in AR 600.56 developer for 30 sec and rinsed in AR 600.60 for 30 sec. Then the sample was cleaned by an oxygen plasma for a few seconds in order to remove any organic contamination. At last, a deposition of 10 nm of Ti and 120 nm of Al was carried out in the e-beam evaporator followed by a lift-off of a few minutes.

Fig. 3.7(a) shows a SEM image of antennas fabricated on top of a 10 μm wide stripe with an edge-to-edge distance $D = 2$ μm. The antenna is composed of a central conductor and two narrow ground lines adapted to the configuration of a coplanar waveguide. By calculating the Fourier transform of the current distribution normalized by the current injected one obtains the distribution of the wave vector of the spin wave generated. For the given antenna geometry, the calculated Fourier transform shows one broad peak centered at 7 μm^{-1}.

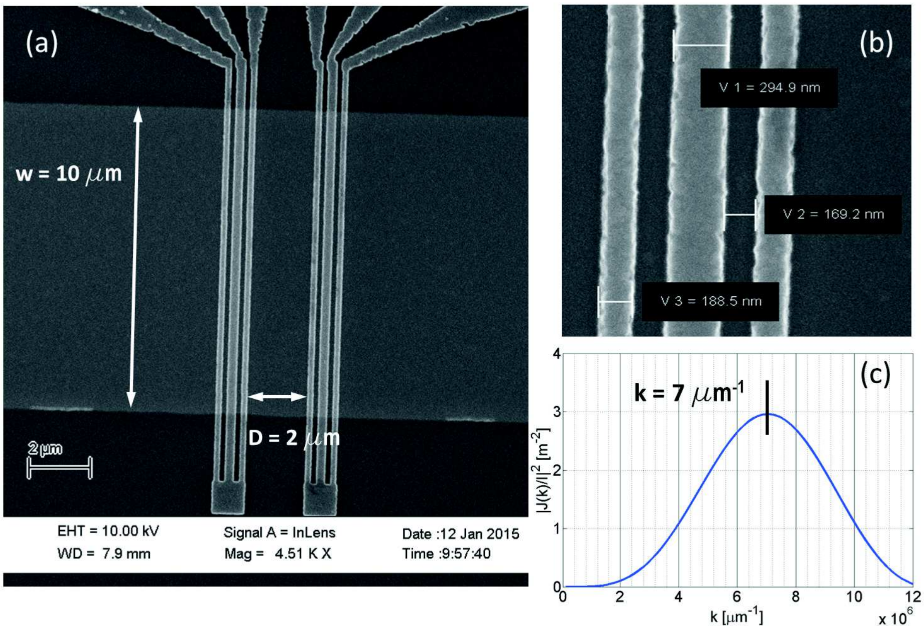

Figure 3.7: (a) A spin wave antennas patterned on a 10 μm wide Py strip. (b) A zoomed view of the conductors lines of one antenna. (c) Corresponding Fourier transform, which shows one broad peak at 7 μm^{-1}.

The final devices

The optical microscope image of a final device is shown in Fig. 3.2. As was mentioned at the beginning, for each Py thickness we fabricated several devices with different strip width w and different distances between the antennas D. For the thickest films the separation between antennas is chosen to be $D = 1, 3, 5$ μm, while for the thinnest films it scales down to $D = 0.5, 0.8, 1.1$ μm in order to detect an intense enough signal. The total amount of fabricated devices is around 40.

3.2.2 Sample fabrication on Fe films

Thin Fe (001) films of a thickness of 10-20 nm were grown by molecular beam epitaxy (MBE) on MgO(001) substrate by David Halley. A buffer MgO layer (20 nm) was first grown on top of the MgO substrate at 550°C, then the Fe film was grown at 100°C. Both films were annealed at 480°C before to be capped with a MgO (8 nm) layer. Most of the films were covered by a 4.5 nm Ti layer to protect the MgO surface from degradation. Due to the lattice mismatch between Fe and MgO ($a_{Fe} = 2.86$, $a_{MgO} = 4.21$), the Fe film grows such that the Fe[100] easy axis is rotated by 45° with the respect to the MgO[100] axis, as shown in Fig. 3.8. For most devices, we have chosen to orient the strip along the Fe[100] axis. For this purpose the strips were patterned at 45° with respect to the [100] edges of the MgO substrates.

As one can see from this microscopic image, the main components and the general view of the devices are almost the same as for the Py-based devices (except a stripe orientation). However, there exists few significant differences in the fabrication, which will be emphasized below.

Using the same photomask as above, we pattern 5 or 10 μm wide Fe stripes. Using an Ar^+ ion gun, we etched MgO(10)/Fe(t)/MgO(8)/Ti(4.5) (the etching rates is given in Table 3.1). After being etched, the samples were immersed in acetone for a few minutes.

Then, we deposited an insulator layer of SiO_2 of 70 nm on the whole sample surface to improve adhesion on the MgO. Thereafter, the CPW and DC pads were patterned using a negative photolithography process with an exposure time of 2.4 sec. Then, the samples were etched to remove the SiO_2 layer with a following etching of Ti, MgO and 2-3 nm of Fe layers to get an electrical contact with the Fe stripe. Then, 10 nm of Ti and 70 nm of Au were deposited and the lift-off process was carried out.

As the final step, the spin wave antennas were fabricated using e-beam lithography. The main difficulty arising during this process is that the in-

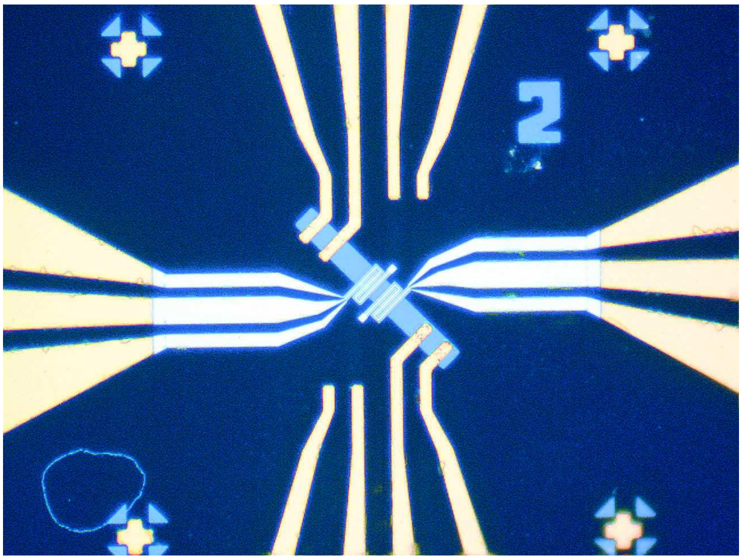

Figure 3.8: (a)A schematic illustration of the device designed on the Fe film with the strip patterned along a Fe[100] axis.

sulating MgO substrates accumulates the charges, which causes a deflection of electron beam and a distortion of the pattern. To avoid this problem, we used a conductive resist, which was directly deposited on top of PMMA resists and removed in DI water for 2 min after exposure. After cleaning the samples in plasma oxygen, 10 nm of Ti and 120 nm of Al was deposited by e-beam evaporator.

This time, a meander shape antenna with three meanders was patterned, where the central and the lateral conductor lines are two times larger than the central and the lateral lines in the simple antenna patterned on Py stripe, respectively (Fig. 3.9). The Fourier transform of the current distribution flowing in the antenna shows a main peak situated at 3.9 μm^{-1}, a much less intense secondary peak at 1.55 μm^{-1}, and an even less intense peak in between the main and the secondary peaks at 2.6 μm^{-1}.

As in the case of Py-based devices, for each Fe film thickness and strip width we fabricated three devices with difference distances between antenna, namely $D = 2, 3, 4$ μm. Three series of devices with different geometries and compositions (with or without Ti capping layer) were fabricated:

1. DH190: MgO(20)/Fe(20)/MgO(8), $w = 10$ μm, $D = 2, 3, 4$ μm
2. DH228: MgO(20)/Fe(10)/MgO(8)/Ti(4.5), $w = 5$ μm, $D = 2, 3, 4$ μm

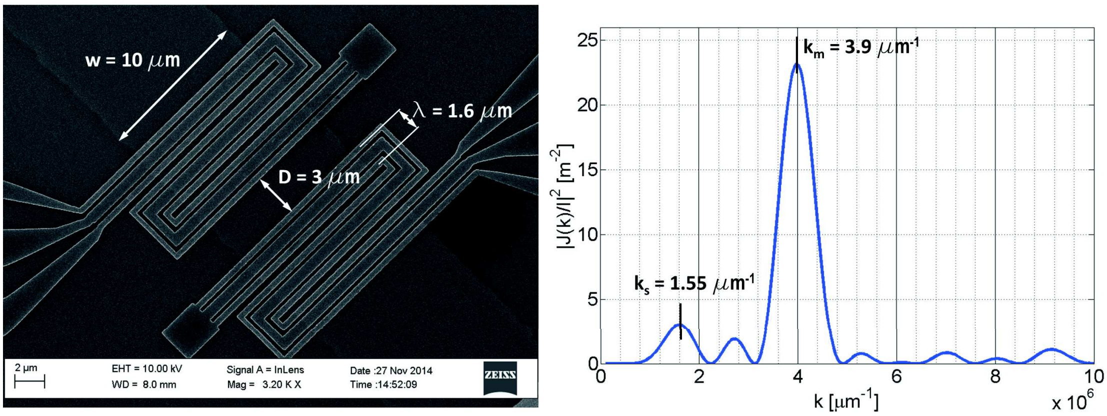

Figure 3.9: (left) SEM image of the microwave antennas patterned on top of MgO stripe of 10 μm wide with a separation distance of 3 μm.(right) The corresponding Fourier transform, which shows the main peak at 3.9 μm^{-1} and the secondary peak at 1.55 μm^{-1}.

3. DH232: MgO(20)/Fe(20)/MgO(8)/Ti(4.5), $w = 10\ \mu$m, $D = 2, 3, 4\ \mu$m

All the devices have the same antenna design thus producing the same wave vectors of $k_m = 3.8\ \mu\text{m}^{-1}$ and $k_s = 1.5\ \mu\text{m}^{-1}$.

3.3 Experimental procedure

The experimental setup used is shown in Fig. 3.10(a). The sample is placed at the center of an electromagnet and the microwave probes (picoprobes) are connected to the coplanar wave guides on the sample [Fig. 3.10(c)]. In turn, the probes are connected to a vector network analyzer (VNA) (Agilent PNA E8364B) using phase-stable coaxial cables [Fig. 3.10(b)]. These cables provide an excellent phase-stability against temperature changes in a large frequency range between 10 MHz and 50 GHz. To inject DC electrical current we use four DC tips connected to a Keithley 2600 source-meter.

3.3.1 Device characterization using vector network analyzer

A device characterization by means of a VNA is based on the measurement of the $S-$parameters, which are extracted from the magnitude and phase of the signals reflected and transmitted at the two ports. Fig. 3.11 illustrates a S-parameters measurement. By injecting a signal in port 1 with a voltage

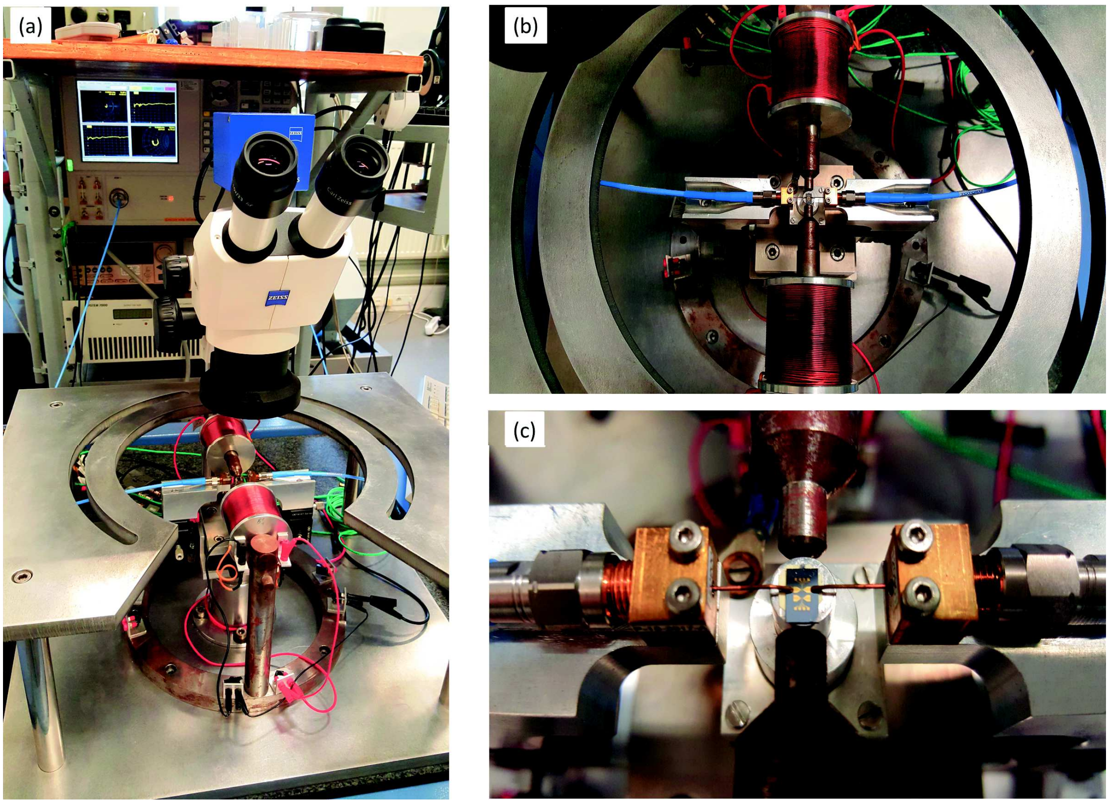

Figure 3.10: (a)Picture of the experimental setup containing an electromagnet, a vector network analyzer and a microscope. (b) A zoomed view showing a coils and pole pieces of the electromagnet. (c) Zoomed view showing the end of the coaxial cables and the picoprobes connected to the coplanar waveguides.

V_1^+, a part of the signal is reflected at the same port with the amplitude V_1^-, whereas another part is transmitted with the amplitude V_2^- detectable at port 2. By placing the source at port 2 with a voltage V_2^+ one can measure the reflected signal V_2^- at port 2 and the transmitted one V_1^- at port 1. We can build the S-matrix, which relates the incident waves V_1^+, V_2^+ and the transmitted ones V_1^-, V_2^- as

$$\begin{pmatrix} V_1^- \\ V_2^- \end{pmatrix} = \begin{pmatrix} S_{11} & S_{12} \\ S_{21} & S_{22} \end{pmatrix} \cdot \begin{pmatrix} V_1^+ \\ V_2^+ \end{pmatrix}. \tag{3.3.1}$$

In other words, the parameters $S_{ii} = V_i^-/V_i^+$ define the ratio between the magnitude of reflected and incident voltage signal on the same port i and the parameters $S_{ij} = V_i^-/V_j^+$ correspond to the ratio between the transmitted signal at port j to the incident signal at port i.

From the S-parameters measured by the network analyzer we can extract the impedance matrix Z_{ij} as

$$V_i = \sum_j Z_{ij}(\omega) I_j(\omega), \tag{3.3.2}$$

where $V_i = V_i^+ + V_i^-$ and $I_j = I_j^+ + I_j^-$ are the voltage and the current at the ports $(i, j) = (1, 2)$, and [134]

$$\begin{aligned} Z_{ii} &= Z_c \frac{(1 + S_{ii})(1 - S_{jj}) + S_{ij} S_{ji}}{(1 - S_{ii})(1 - S_{jj}) - S_{ij} S_{ji}} \\ Z_{ij} &= Z_c \frac{2 S_{ij}}{(1 - S_{ii})(1 - S_{jj}) - S_{ij} S_{ji}} \end{aligned} \tag{3.3.3}$$

During our PSWS measurements, the impedance matrix is always measured at two different magnetic fields: the first one $Z_{ij}(\omega, H_{\text{res}})$ at the resonance field H_{res} and the second one $Z_{ij}(\omega, H_{\text{ref}})$ at a reference field H_{ref} chosen such that no resonance occurs within the given frequency range. The difference between these two matrixes thus gives a signal only attributed to the spin waves and eliminates the field-independent electromagnetic peaks. Since the impedance variation induced by the spin wave originates from the inductive coupling between the strip and the antenna, we can transform the impedance matrix into the inductance matrix $\Delta L_{ij}(\omega)$:

$$\Delta L_{ij}(\omega) = \frac{1}{i\omega} [Z_{ij}(\omega, H_{\text{res}}) - Z_{ij}(\omega, H_{\text{ref}})]. \tag{3.3.4}$$

The self-inductance (ΔL_{11} and ΔL_{22}) and the mutual-inductance (ΔL_{12} and ΔL_{21}) are the signal of interest of propagating spin wave spectroscopy (see section).

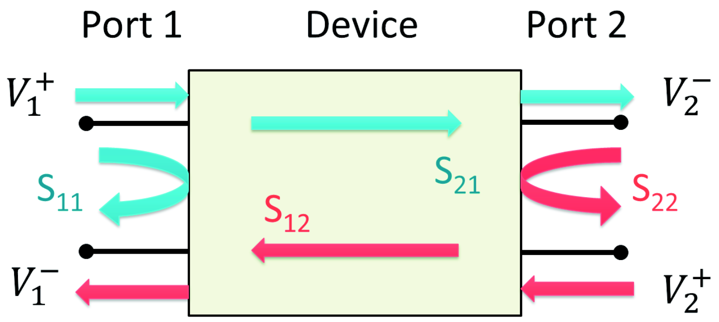

Figure 3.11: Schematic illustration of the S-parameters definition for a 2-port measurements

Before starting the measurements we perform a calibration of the microwave circuit and of the magnetic field as explained below.

3.3.2 The microwave circuit calibration

An important factor for microwave measurements is the good impedance adaptation of all elements (the VNA, the coaxial cables, the coplanar waveguides) in order to minimize the signal loss due to reflections at the connection of different elements. The coplanar waveguide is designed to have a characteristic impedance of 50 Ω, which is determined by the relative permittivity of the substrate (SiO_2 or MgO in our case) and the ratio between the central conductor width and its spacing with the ground line. To eliminate systematic errors arising from residual reflections, we use a calibration substrate, which contains a short (0Ω), an open (∞ Ω), a load (50 Ω), and a through microwave line. The calibration is performed over the whole frequency range of the VNA (from 10 MHz to 50 GHz) at conditions similar to that used during the measurements on real devices (power, bandwidth, number of points). After the calibration, we define an additional electrical delay corresponding to the propagation along the coplanar waveguide before reaching the antenna. We estimate an electrical delay of about 12 ± 2 ps.

3.3.3 The magnetic field calibration

We use a home made electromagnet consisting of two iron-core coils. The electromagnet is calibrated with the help of a Hall probe placed in its center. The center of the gap is determined by searching the maximum field measured for a small current value. Then the magnetic field is measured

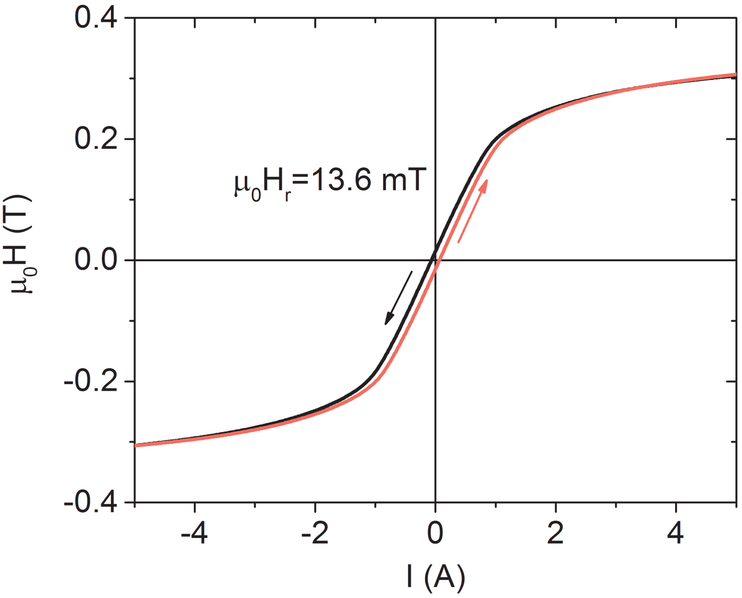

Figure 3.12: The calibration of magnetic field in a range between +5 A and -5 A

as a function of the DC current between +5 A and -5 A with a step of 2 mA. We obtain an hysteresis loop, which is almost saturated at $\pm 5A$ (which corresponds to a field of 0.306 T), and shows a remanent field of 13.6 mT (Fig. 3.12). Therefore, to follow the same magnetic history during the measurements, we first apply a high DC current and then decrease it down to the desired value.

Chapter 4

Frequency non-reciprocity of surface spin waves

In this chapter we will start with the qualitative and quantitative explanation of the frequency non-reciprocity observed experimentally in the thin Al_2O_3/Py/Al_2O_3 films. These measurements are interpreted with the help of the dipole-exchange theory accounting for different surface anisotropies at the top and bottom film surfaces. The effect of the iDM interaction on the spin wave spectrum will be then investigated in Py/Pt films and discussed in sec. 4.2.

Most of the measurements reported for Py/Al_2O_3 films have been performed by M. Haidar during his PhD thesis [49, 50, 51]. I build upon this previous work by measuring a few extra Py/Al_2O_3 devices and completed the data analysis, which have been published in Ref. [40].

4.1 Frequency non-reciprocity induced by the magnetic asymmetry of the film

4.1.1 Experimental observation of the frequency non-reciprocity in Al_2O_3/Py/Al_2O_3 trilayers

In this investigation Al_2O_3(21 nm)/Py(t)/Al_2O_3(5 nm) trilayers have been used with a thickness of magnetic material of $t = 6 - 40$ nm. We used propagating spin wave spectroscopy devices consisting of a ferromagnetic stripe with a width of $w = 2 - 8$ μm and a pair of microwave antenna patterned atop. We also used two different antenna geometries with different values of antenna pitch (Fig. 4.1). The Fourier transform of the current

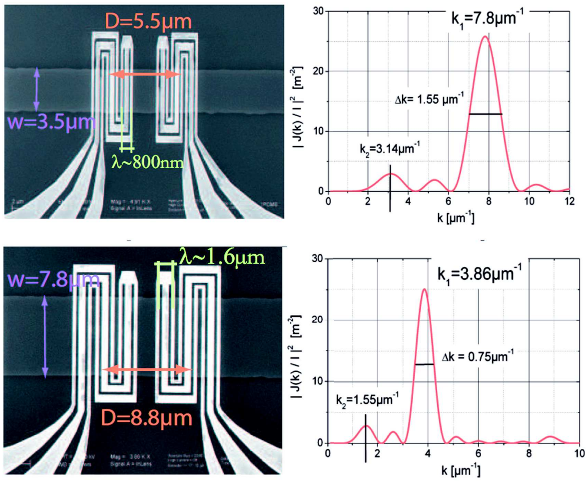

Figure 4.1: SEM images of the microwave antennas and corresponding Fourier transform. The image is taken from Ref. [134]

density flowing in antenna shows two distinct peaks for each device, where the main (more intense) peak corresponds to a wave vector k_M and the secondary (less intense) peak corresponds to a wave vector k_s. Therefore, using two different antenna pitches we are able to excite the spin waves with four values of k: $1.5, 3.1, 3.9, 7.8$ $\mu\mathrm{m}^{-1}$.

Before starting the analysis of the non-reciprocal spin wave propagation, we first performed reflection measurements in order to extract the efficiency of spin wave excitation and to characterize the magnetic properties of the film. An example of self-inductance spectrum measured at an applied field of 37 mT for device with 40 nm is shown in Fig. 4.2, where both real and imaginary parts are plotted in units of picohenry (pH). The latter shows two absorption peaks of a Lorentzian form, which correspond to the resonance peaks of spin waves with wave vector $k_M = 3.9$ $\mu\mathrm{m}^{-1}$ (peak at higher frequency) and $k_s = 1.5$ $\mu\mathrm{m}^{-1}$ (peak at lower frequency). We measured the dependence of these resonance frequencies f_{res} on the applied field for 12 devices with varying film thickness t and wave vector k. For all devices, a monotonic increase of the resonance frequency as a function of the field was observed. We analyze these dependencies by following the procedure described in Appendix A. From this analysis we extract the value of the gyromagnetic ratio $\gamma/2\pi = 30 \pm 1$ GHz/T, the saturation magnetization M_s, which decreases from 1.02 T to 0.92 T with varying the film thickness from 40 nm to 6 nm, and the effective magnetization $\mu_0 M_{\mathrm{eff}} = 0.99 - 0.83$ T

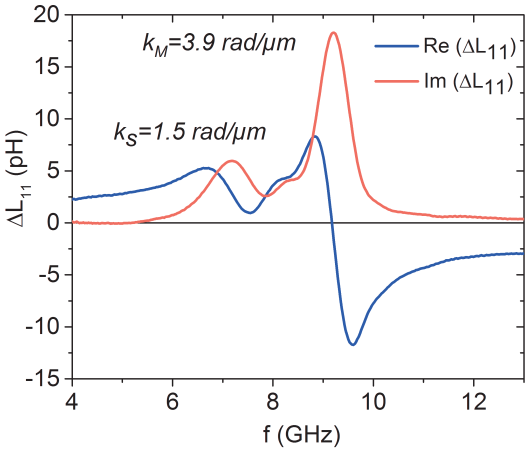

Figure 4.2: The self-inductance spectrum measured at an applied field of 37 mT for the device of the 40 nm film with a width of 7 μm. The two absorption peaks, seen on Im(ΔL_{11}) (red line), lie at $f_M = 9.2$ GHz (corresponding to a spin wave with $k_M = 3.9\ \mu\mathrm{m}^{-1}$) and at $f_s = 7.15$ GHz (corresponding to $k_s = 1.5\ \mu\mathrm{m}^{-1}$).

for $t = 40 - 6$ nm. The total surface anisotropy is estimated from the difference between the saturation magnetization and effective magnetization $[2\sum K_s = (\mu_0 M_s t)(M_s - M_{\mathrm{eff}})]$ [see Eq. (1.3.12)], which yields a value of $\sum K_s = 0.1 \pm 0.1\ \mathrm{mJ/m}^2$.

Next, we performed the transmission measurements, which actually carry the information about the propagation of the spin wave in the magnetic material. Since each microwave antenna can be used as emitter or receiver, we measure two mutual inductance signal ΔL_{ij}. The wave excited on the first antenna and detected on the second one ($k > 0$) is associated to the mutual-inductance ΔL_{21}, while the wave generated on the second antenna and detected on the first one ($k < 0$) is associated to the mutual-inductance ΔL_{12}. Fig. 4.3(a) shows a typical mutual-inductance spectrum measured at $\mu_0 H = 37$ mT in a 40 nm Py film (the mutual-inductance spectrum presented here and the self-inductance spectrum shown in Fig. 4.2 were measured in the same device). As one can see, the real and imaginary parts of both ΔL_{12} and ΔL_{21} signals exhibit well pronounced oscillations, which are due to the phase delay acquired during the wave propagation between two antennas. One can also note, that the amplitudes of the oscillations [black lines in Fig. 4.3(a)] show two well-defined peaks, which are located at the same frequencies as the two absorption peaks of the self-inductance spectra in Fig. 4.2. This means that the oscillations under the first envelope peak ($f = 6.4 - 7.7$ GHz) correspond to the wave propagating with $k_s = 1.5\ \mu\mathrm{m}^{-1}$ and the oscillations under the second envelope peak ($f = 8.7 - 9.7$ GHz) correspond to the wave propagating with $k_M = 3.9\ \mu\mathrm{m}^{-1}$.

From Fig. 4.3(a) one can clearly see that the waves propagating in positive and negative directions differ in their amplitude and in their frequency showing thus a non-reciprocal behavior. We notice that the wave propagating in the positive direction ΔL_{21} has a smaller amplitude than the wave propagating in the opposite direction (ΔL_{12}). The origin of the observed amplitude non-reciprocity is well-known and is attributed to the coupling between the field excited by the antenna and the dynamical magnetization [49]: for $k < 0$ the direction of the out-of-plane component of the magnetization is in phase with that of the excitation field, whereas for $k > 0$ they are in anti-phase. Therefore, the wave with $k < 0$ will propagate with higher amplitude than the wave with $k > 0$. When the magnetic field is applied in the opposite direction the reverse situation is observed: the wave with $k < 0$ will possess smaller amplitude than that with $k > 0$.

Let us focus now on the frequency non-reciprocity. In Fig. 4.3(b),(c) we zoom the oscillations under the two peaks to show the frequency shift between the imaginary parts of the inductance signals ΔL_{12} and ΔL_{21} for $k_s = 1.5\ \mu\mathrm{m}^{-1}$ [panel (b)] and $k_M = 3.9\ \mu\mathrm{m}^{-1}$ [panel (c)]. The frequency non-reciprocity $f_{NR} = f_{12} - f_{21}$ is measured to be 15 MHz for k_s and 34 MHz for k_M. We then performed the same measurements for different values of the applied field and observe a slight decay of the frequency non-reciprocity as a function of the magnetic field (Fig. 4.4). By switching the direction of the magnetic field the frequency non-reciprocity changes sign, i.e. the frequency of the positive SW wave vector (ΔL_{21}) becomes higher than that of the negative SW wave vector ($f_{NR} = f_{12} - f_{21} < 0$).

In Fig. 4.5 and 4.6 we collected the data from all devices and plotted the dependence of the frequency non-reciprocity as a function of the film thickness and the wave vector, respectively. In Fig. 4.5 the frequency non-reciprocity for different wave vectors is plotted as a function of t on a semilogarithmic scale. One observes a bell shape dependence of f_{NR} on t, whose amplitude increases with k. From Fig. 4.6, one can see that the frequency non-reciprocity increases linearly with k is a linear function for $t \leq 20$ nm, whereas for $t = 40$ nm, it first increases and then seems to saturate between $3.9\ \mu\mathrm{m}^{-1}$ and $7\ \mu\mathrm{m}^{-1}$.

To interpret these data we use the theory of dipole-exchange spin wave [64]

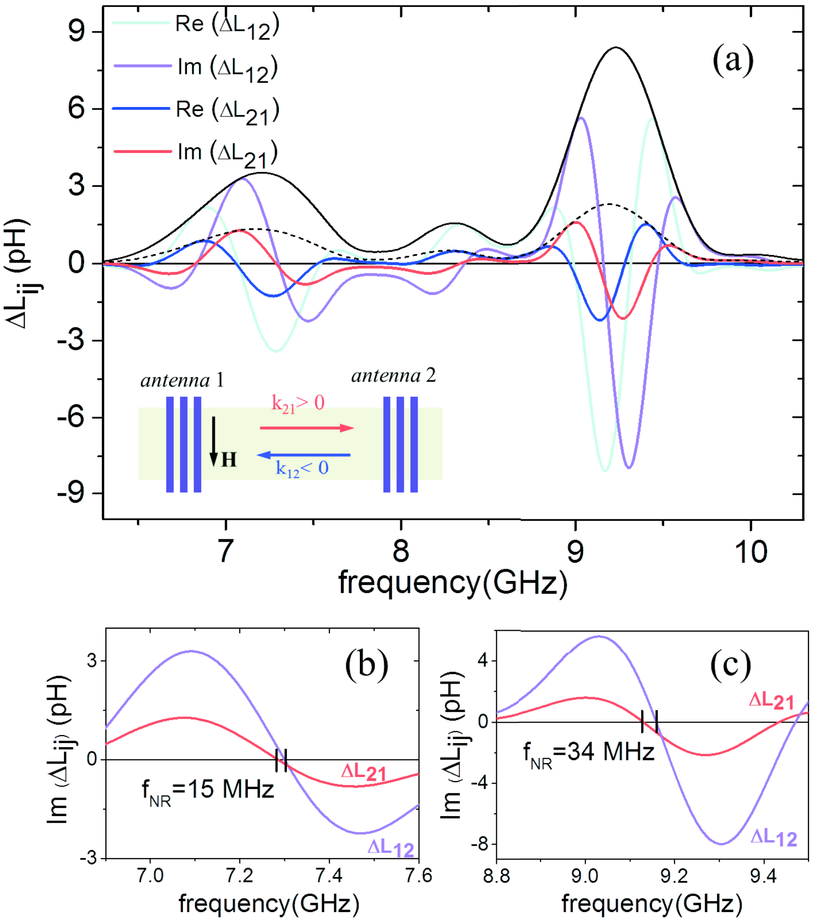

Figure 4.3: (a) The mutual-inductance spectrum measured at an applied field of 37 mT for the device of the 40 nm film with a width of 7 μm. The inductance ΔL_{12} and ΔL_{21} correspond to the signals measured for $k < 0$ and $k > 0$, respectively. The black solid and dashed lines are the amplitudes for $k < 0$ and $k > 0$, respectively. The frequency shift between the imaginary parts of the inductance signals ΔL_{12} and ΔL_{21} for $k_s = 1.5\ \mu\mathrm{m}^{-1}$ and $k_M = 3.9\ \mu\mathrm{m}^{-1}$ is shown in panel (b) and (c), respectively.

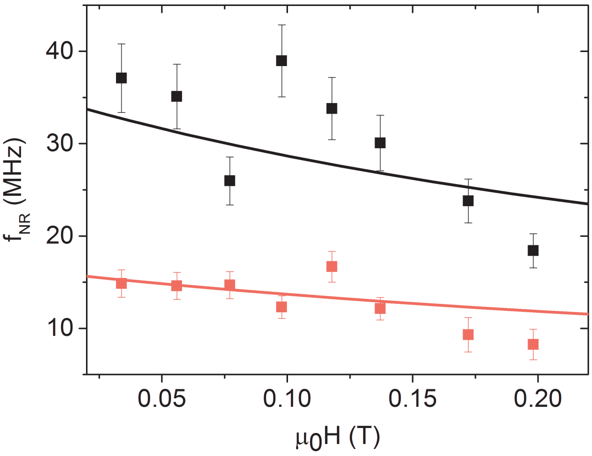

Figure 4.4: Frequency non-reciprocity versus applied magnetic field. Black and red symbols show the measured frequency non-reciprocity for $k_M = 3.9\ \mu\mathrm{m}^{-1}$ and $k_s = 1.5\ \mu\mathrm{m}^{-1}$, respectively. Solid lines are the theoretical fit obtained for $K_\mathrm{s}^\mathrm{bot} = 0.15\ \mathrm{mJ/m^2}$, $K_\mathrm{s}^\mathrm{top} = -0.05\ \mathrm{mJ/m^2}$, $A = 11.5\ \mathrm{pJ/m}$, $\mu_0 M_\mathrm{s} = 1\ \mathrm{T}$, $\mu_0 H_0 = 37\ \mathrm{mT}$, $\gamma/2\pi = 29.02\ \mathrm{GHz/T}$.

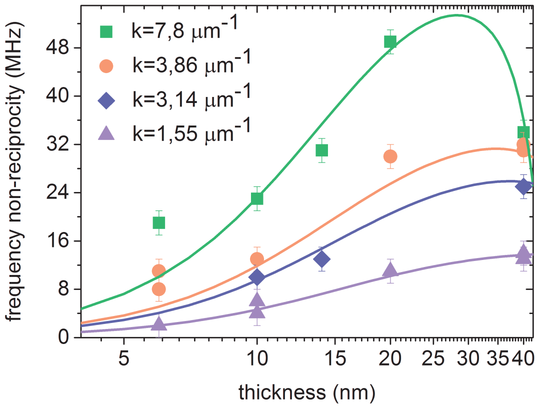

Figure 4.5: Measured frequency non-reciprocity as a function of film thickness for $k = 7.8\ \mu\text{m}^{-1}$ (squares), $k = 3.86\ \mu\text{m}^{-1}$ (circles), $k = 3.14\ \mu\text{m}^{-1}$ (diamonds), $k = 1.55\ \mu\text{m}^{-1}$ (triangles up). Solid lines are the theoretical results (Eq. 4.1.6) obtained for the set of parameters indicated in the caption of Fig. 4.4.

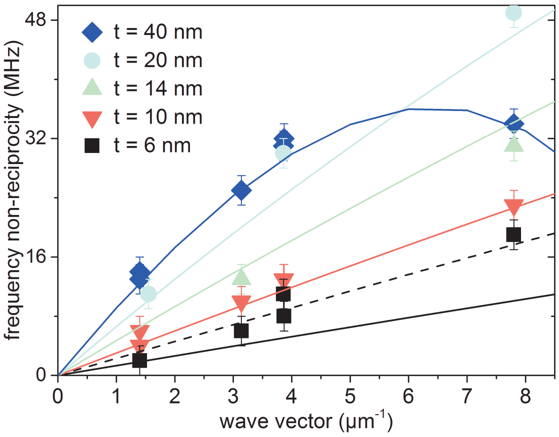

Figure 4.6: Same data as in Fig. 4.5 plotted as a function of wave vector for $t = 6$ nm (squares), $t = 10$ nm (triangles down), $t = 14$ nm (triangles up), $t = 20$ nm (circles), $t = 40$ nm (diamonds). The dashed lines are obtained when including iDMI ($D_{\mathrm{s}} = -0.04$ mJ/m^2, see text for details) only for $t = 6$ nm.

and extend it for the case when the surface anisotropy is present and makes a non negligible contribution to the spin wave frequency.

4.1.2 Theoretical explanation

Let us first explain qualitatively how the frequency non-reciprocity may arise due to the presence of the surface anisotropy. As was shown in section 1.6.1, one of the specific features of the surface spin waves is their non-reciprocal modal profile. The result of such modal profile non-reciprocity is the spin wave localization at the different surfaces while propagating in the opposite directions, as it is shown in Fig. 4.7.

Let us assume now that the magnetic properties are also asymmetric across the thickness of the film, i.e. the dynamic and/or static effective fields are different in the top and bottom halves of the film. This can happens, for example, if a homogeneous ferromagnetic film has out-of-plane uniaxial surface anisotropies of different magnitudes on both sides ($K_\mathrm{s}^\mathrm{top}$ and $K_\mathrm{s}^\mathrm{bot}$), as illustrated in Fig. 4.7. One can see that the wave propagating in the positive direction and having larger amplitude in the lower half will be more sensitive to the anisotropy at the bottom surface, while the wave propagating in the opposite direction and having larger amplitude in the upper half will be more affected by the surface anisotropy at the top. If the magnitude of these surface anisotropies are different (and consequently the effective fields), the wave having larger amplitude in the half with higher effective field will oscillate at higher frequency than the wave having larger amplitude in the half with lower effective field, thus leading to the frequency non-reciprocity. We thus conclude, that a frequency non-reciprocity (f_NR) can result from the mutual influence of two factors: an intrinsic non-reciprocity of the modal profile and an asymmetry of the magnetic film properties [40].

To estimate quantitatively the effect of the surface anisotropies on the spin wave spectrum we use the theory of hybridized dipole-exchange spin wave [see subsection (1.6.1)], extending it by introducing the surface magnetic anisotropy term in the effective field. For this purpose, the dynamic effective field is written as

$$\mathbf{h} = \mathbf{h}_\mathrm{ex} + \mathbf{h}_\mathrm{d} + \mathbf{h}_\mathrm{s} \tag{4.1.1}$$

where the exchange field $\mathbf{h}_\mathrm{ex}$ and dipolar field $\mathbf{h}_\mathrm{d}$ are given by Eqs.[(1.6.6),(1.6.3)], and the out-of-plane magnetic anisotropy field $\mathbf{h}_\mathrm{s}$ is given by

$$\mathbf{h}_\mathrm{s} = \frac{2}{\mu_0 M_\mathrm{s}^2}\mathbf{u}_x(K_\mathrm{s}^\mathrm{bot}\delta(x)m_x(0) + K_\mathrm{s}^\mathrm{top}\delta(x-t)m_x(t)). \tag{4.1.2}$$

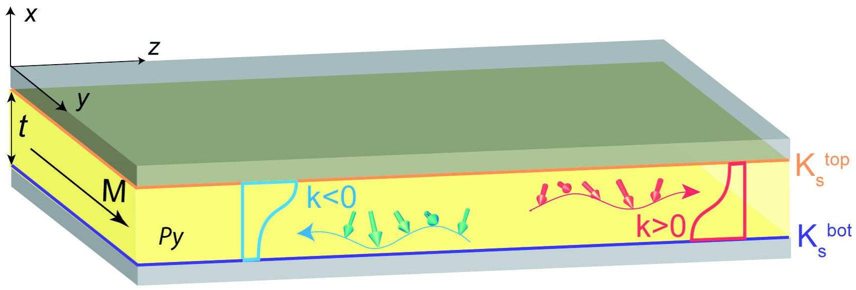

Figure 4.7: Schematic representation of the MSSWs possessing an asymmetric modal profile across the film thickness t for $k < 0$ and $k > 0$, which propagate in thin magnetic film with different surface anisotropy at top and bottom sides ($K_{\mathrm{s}}^{\mathrm{top}}$ and $K_{\mathrm{s}}^{\mathrm{bot}}$) with $\mathbf{M} \parallel +y$.

We use the basis of the ortho-normal functions containing the fundamental FMR mode with a uniform profile ($n = 0$) and the first perpendicular standing spin wave mode ($n =$ 1,PSSW1) with an antisymmetric profile across a film thickness [$\cos(\pi x/t)$] [see Eq.(1.6.17)]. Using the formalism of the dynamic effective tensor ($\mathbf{h} = -\overline{N}\mathbf{m}$), we define the components of the tensor $\overline{N}_s$ associated to the uniaxial out-of-plane surface anisotropies as

$$\begin{aligned}
N_{s,00} &= \frac{1}{t\mu_0 M_{\mathrm{s}}^2}\int_0^t\int_0^t [-K_{\mathrm{s}}^{\mathrm{bot}}\delta(x)\delta(x^{'}) - K_{\mathrm{s}}^{\mathrm{top}}\delta(x-t)\delta(x^{'}-t)]dxdx^{'} \\
&= -\frac{2}{t\mu_0 M_{\mathrm{s}}^2}(K_{\mathrm{s}}^{\mathrm{bot}} + K_{\mathrm{s}}^{\mathrm{top}}) = -\varepsilon \\
N_{s,11} &= \frac{2}{t\mu_0 M_{\mathrm{s}}^2}\int_0^t\int_0^t [-K_{\mathrm{s}}^{\mathrm{bot}}\delta(x)\delta(x^{'}) - K_{\mathrm{s}}^{\mathrm{top}}\delta(x-t)\delta(x^{'}-t)] \\
\cos & \ (\frac{\pi x}{t})\cos(\frac{\pi x^{'}}{t})dxdx^{'} = -\frac{4}{t\mu_0 M_{\mathrm{s}}^2}(K_{\mathrm{s}}^{\mathrm{bot}} + K_{\mathrm{s}}^{\mathrm{top}}) = -2\varepsilon \qquad (4.1.3) \\
N_{s,01} &= \frac{\sqrt{2}}{t\mu_0 M_{\mathrm{s}}^2}\int_0^t\int_0^t [-K_{\mathrm{s}}^{\mathrm{bot}}\delta(x)\delta(x^{'}) - K_{\mathrm{s}}^{\mathrm{top}}\delta(x-t)\delta(x^{'}-t)] \\
\cos & \ (\frac{\pi x^{'}}{t})dxdx^{'} = -\frac{2\sqrt{2}}{t\mu_0 M_{\mathrm{s}}^2}(K_{\mathrm{s}}^{\mathrm{bot}} - K_{\mathrm{s}}^{\mathrm{top}}) = \delta
\end{aligned}$$

One can see, that the projection of the surface anisotropy field on the basis of the functions $n = 0, 1$ produces two terms related to the sum of the two surface anisotropies ε and a term related to their difference δ. This yields the modification of the dynamical operator $\overline{C}$ of Eq. 1.6.18, which now takes the following form

$$\overline{C} = \begin{pmatrix} C_{00} & C_{01} \\ C_{10} & C_{11} \end{pmatrix} = \begin{pmatrix} \omega_{x0} - \varepsilon & 0 & \delta & -i\omega_M Q \\ 0 & \omega_{z0} & -i\omega_M Q & 0 \\ \delta & i\omega_M Q & \omega_{x1} - 2\varepsilon & 0 \\ i\omega_M Q & 0 & 0 & \omega_{x1} \end{pmatrix} \tag{4.1.4}$$

In other words, the addition of the surface anisotropies in the matrix equation leads to a modification of the ω_x terms in the expression of fundamental and PSSW1 mode frequencies by a term ε and 2ε, respectively, as well as a modification of the off-diagonal blocks responsible for the coupling between two modes by a terms δ related to the difference in the surface anisotropies. The solution of the eigenvalue equation $\det(\mathbf{u}_y \times \overline{C}_k - i\omega\overline{1}) = 0$ takes the form

$$(\omega_0^2 - \omega^2)(\omega_1^2 - \omega^2) - 2\delta Q\omega(\omega_{z1}^2 - \omega_{z0}^2) = 0, \tag{4.1.5}$$

where ω_0, ω_1 are the spin wave eigenfrequency obtained for $\delta = 0$ [see Eq. (1.6.24)].

To demonstrate the effect of the surface anisotropy on the dispersion characteristic we calculate the frequency of positive and negative wave vectors for some typical values of the surface anisotropy. Fig. 4.8 shows that for the same magnitude of magnetic anisotropy at top and bottom surfaces ($K_\mathrm{s}^\mathrm{bot} = K_\mathrm{s}^\mathrm{top} = 1$ mJ/m^2) no divergence between $k > 0$ and $k < 0$ is observed (solid green line). However, this relatively high value of total surface anisotropy ($\Sigma K_\mathrm{s} = 2$ mJ/^{2}) leads to significant decrease of the effective magnetization and, as a result, to a significant decrease of the resonance frequency at zero k comparing with the zero anisotropy case (magenta line). If we now consider the presence of the surface anisotropy only at the one side, for example $K_\mathrm{s}^\mathrm{top} = 1$ mJ/m^2 and $K_\mathrm{s}^\mathrm{bot} = 0$, one observe not only the decay of the resonance frequency at zero k caused by the total anisotropy of $\Sigma K_\mathrm{s} = 1$ mJ/^{2}, but also a divergence between the positive and negative waves caused by the difference in the surface anisotropies at the top and bottom sides $\Delta K_\mathrm{s} = 1$ mJ/^{2} (red dashed lines). This difference in the dispersion characteristic of the oppositely propagating waves yields a substantial frequency non-reciprocity, which can be calculated treating the surface anisotropy in Eq. (4.1.5) as a perturbation (δQ is assumed to be a small parameter). Note, that the same effect was calculated by Hillebrand et al. [56] using a different approach.

As a result, the frequency shift induced by the magnetic asymmetry is given by the expression:

$$\Delta\omega_0 = \delta Q \frac{\omega_{z1} - \omega_{z0}}{\omega_1^2 - \omega_0^2}. \tag{4.1.6}$$

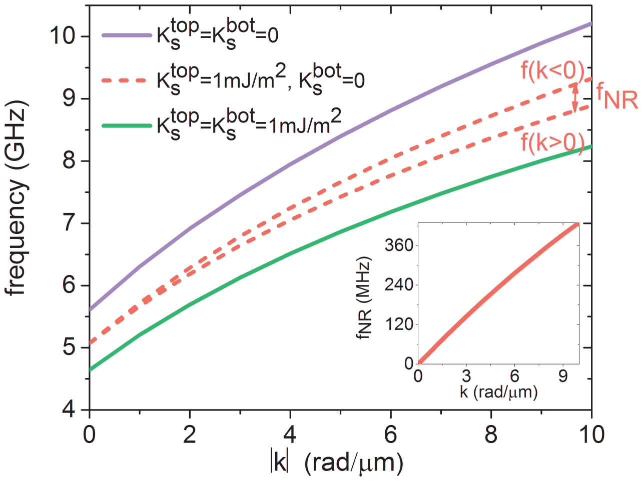

Figure 4.8: Dispersion curves calculated for the case when the surface anisotropy is absent (magenta solid line), when the surface anisotropy is present having the same magnitude at top and bottom sides (green solid line), and when the surface anisotropy differs at opposite sides (red dashed lines). The difference in surface anisotropies leads to the frequency non-reciprocity linear in k (inset).

Q being odd in k, this frequency shift changes sign when k is reversed so that it corresponds to a frequency non-reciprocity $\omega_{\mathrm{NR}} = \omega_0(k < 0) - \omega_0(k > 0) = -2\Delta\omega_0(|k|)$. As follows from Eq. (4.1.6), the frequency non-reciprocity scales linearly with the difference in surface anisotropy and is inversely proportional to the difference between the two unperturbed spin wave frequencies ω_0 and ω_1. In most cases, this difference $(\omega_1^2 - \omega_0^2)$ is positive. However, close to the avoided crossing point in the dispersion relation $(\omega_0 = \omega_1)$ it changes sign and becomes responsible for the saturation observed for the 40 nm film at k between 4 and 8 $\mu\mathrm{m}^{-1}$ (see Fig. 4.6).

In the small thickness limit ($kt \ll 1$ and $\frac{\Lambda^2\pi^2}{t^2} \gg P_{00}, P_{11}, h, \varepsilon, \Lambda^2k^2$), Eq. (4.1.6) can be rewritten in a more simple form

$$f_{\mathrm{NR}} \simeq \frac{8\gamma}{\pi^3}\frac{K_{\mathrm{s}}^{\mathrm{bot}} - K_{\mathrm{s}}^{\mathrm{top}}}{M_{\mathrm{s}}}\frac{k}{1 + \frac{\Lambda^2\pi^2}{t^2}}, \tag{4.1.7}$$

which indicates a linear dependence of f_{NR} on the wave vector and a nearly quadratic dependence on the film thickness and explains quantitatively the frequency non-reciprocity we measured in thin films (up to 20 nm)(Fig. 4.6).

Let us now discuss the quantitative comparison with the experimental results. As shown in Fig. 4.6, the model (solid lines) reproduces quite well the experimental data using a single value of the difference in surface anisotropies: $K_{\mathrm{s}}^{\mathrm{bot}} - K_{\mathrm{s}}^{\mathrm{top}} = 0.20 \pm 0.01$ mJ/m^2. The order of magnitude of this difference is consistent with typical values reported for surface anisotropies in permalloy films, which are in the range of $0 - 0.5$ mJ/m^2 (Refs. [105, 58, 57]). At first sight, the large difference may appear surprising for two nominally identical interfaces (Py/Al_2O_3 and Al_2O_3/Py). However, surface anisotropies are known to depend quite strongly on the details of the interface structure, which in turn can dependent on the material deposition sequence. More specifically, we suspect a partial surface oxidation to play a role in our case [50]. Indeed, using X-ray photoelectron spectroscopy and polarized neutron reflectivity, we have detected a non-magnetic nanometer-thick iron oxide forming mostly at the top surface, probably during the Al_2O_3 sputter deposition. In this picture, one expects a quite pronounced easy-axis surface anisotropy for the bottom Al_2O_3/Py interface (as observed in most ferromagnet/non-magnetic oxide interfaces) and a reduced value for the top Py/Al_2O_3 interface. The sign of the observed frequency non-reciprocity is consistent with this expectation (i.e. $K_{\mathrm{s}}^{\mathrm{bot}} > K_{\mathrm{s}}^{\mathrm{top}}$). It is worth noting that to determine the strength of two individual surface anisotropies one requires to estimate their sum, in addition to their difference. Referring to the reflection measurements, where the sum of surface anisotropy was extracted by measuring the effective magnetization of the films, we found the magnitude of the surface anisotropy at top and bottom surfaces to be $K_{\mathrm{s}}^{\mathrm{top}} = -0.05$ mJ/m^2 and $K_{\mathrm{s}}^{\mathrm{bot}} = 0.15$ mJ/m^2.

One can note however the deviation between theory and experiment observed for thinnest film of $t = 6$ nm. This deviation is due to the additional contribution to the frequency shift, which arises from the Dzyaloshinkii-Moria interaction (DMI) [91, 125, 31, 70]. Indeed a value as small as $D_{\mathrm{s}} = 0.04$ pJ/m at one of the film interfaces generates an additional contribution of the form given in Eq. (4.2.1) that explains the values measured experimentally (dotted lines in Fig. 4.6). Because it scales as the inverse of the film thickness, this contribution becomes significant only for the thinnest film investigated. Such a small value of D_{s}, about fourty times smaller than the value observed in $Pt/Co/AlOx$ ultrathin films [10], seems plausible in a system which does not contain any heavy metal with strong spin-orbit interaction.

In conclusion, we have shown that for the magnetostatic surface spin waves, which possess an antisymmetric modal profile across the film thickness, an asymmetry of the magnetic properties through the film thickness leads to a difference of the frequencies of counter-propagating spin waves. We have measured this frequency non-reciprocity as a function of film thickness and wave vector. Using a theory of dipole-exchange spin waves, in which asymmetric surface anisotropies are included as a perturbation, we have deduced a simple analytical formula allowing predict the magnitude of f_{NR} as a function of difference in surface anisotropies at top and bottom sides. We have shown that in the limit of small t, the frequency non-reciprocity has a linear dependence on k and a quasi-quadratic dependence on t.

4.2 Frequency non-reciprocity induced by the Dzyaloshinskii-Moriya interaction

4.2.1 Experimental observation of the frequency non-reciprocity induced in Ti/Py/Pt trilayers

To study the effect of the Dzyaloshinskii-Moriya interaction on the surface spin waves we use the set of Si$_{int}$/SiO$_2$/Ti(5 nm)Py(t)/Pt(5 nm) films $t = 4, 7, 20$ nm and Si$_{int}$/SiO$_2$/Ti(5 nm)Py(10 nm)/Pt(10 nm) films described in chapter 3. Remind that the strips have the width of $w = 5 - 20$ μm and the microwave antennas contain only one meander (Fig. 3.7), contrary to the case of Py/Al$_2$O$_3$ films, where three or five meanders were used. The pitch of the antenna (that defines the spin wave wavelength) is about 900 nm and the corresponding Fourier transform shows one broad peak at $k = 7\ \mu\text{m}^{-1}$. We also use a reference sample consisting of a 4 nm Py layer sandwiched between two 5 nm Ti layers, where the iDM interaction is not expected to be present.

As before, we first perform the reflection measurements, i.e. we measure the resonance frequency dependence on the magnetic field. The obtained curves for all devices are shown in Fig. 6.15 in Appendix A. The magnetic parameters extracted from these curves are approximately the same as those obtained for Py/Al$_2$O$_3$ films ($\gamma/(2\pi) = 30 \pm 1$ GHz/T, $\mu_0 M_s = 1 - 0.92$ T and $\mu_0 M_{\text{eff}} = 0.99 - 0.83$ T for $t = 20 - 4$ nm, respectively, which yields $K_s \simeq 0.1$ mJ/m^2).

In the next step, we perform the transmission measurements with varying Py film thickness. Fig. 4.9 shows the mutual-inductance spectra measured at $\mu_0 H = 37$ mT in Py(4)/Ti, Py(4)/Pt and Py(20)/Pt strips with a width of 20μm. The maximum of amplitude is located at $f = 5.5$ GHz for $t = 4$ nm and at $f = 8$ GHz for $t = 20$ nm. In the right side of Fig. 4.9 we plot the imaginary part of the inductance signals ΔL_{12} and ΔL_{21}, that correspond to the wave with $k < 0$ and $k > 0$, respectively. In the case of the Py(4)/Ti(5) stack, no significant difference between the ΔL_{12} and ΔL_{21} signals is observed (the frequency non-reciprocity is as small as 0.8 MHz). On the contrary, the presence of the Pt layer on top of the Py layer leads to a substantial frequency shift of the counter-propagating spin waves. We measure a frequency non-reciprocity $f_{NR} = f_{12} - f_{21} = 65$ MHz for $t = 4$ nm and -15 MHz for $t = 20$ nm. The positive frequency non-reciprocity indicates a higher frequency for the wave traveling in negative direction, whereas the negative sign indicates a higher frequency for the wave moving in positive direction.

By increasing the Py film thickness we observe a decrease of the frequency non-reciprocity, which for $t = 7$ nm reaches a value of 32 MHz and for $t = 10$ nm a value of 20 MHz (squares in Fig. 4.10).

4.2.2 Discussion

Referring to Eq. (1.7.7), the frequency shift between oppositely propagating waves induced by the DMI can be calculated as

$$f_{NR} = [\omega(-k) - \omega(+k)]/(2\pi) = \frac{2\gamma D_s}{\pi M_s t} k. \tag{4.2.1}$$

The DMI-induced frequency shift is linear and odd in k and inversely proportional to the film thickness. Therefore, using the dependence of the

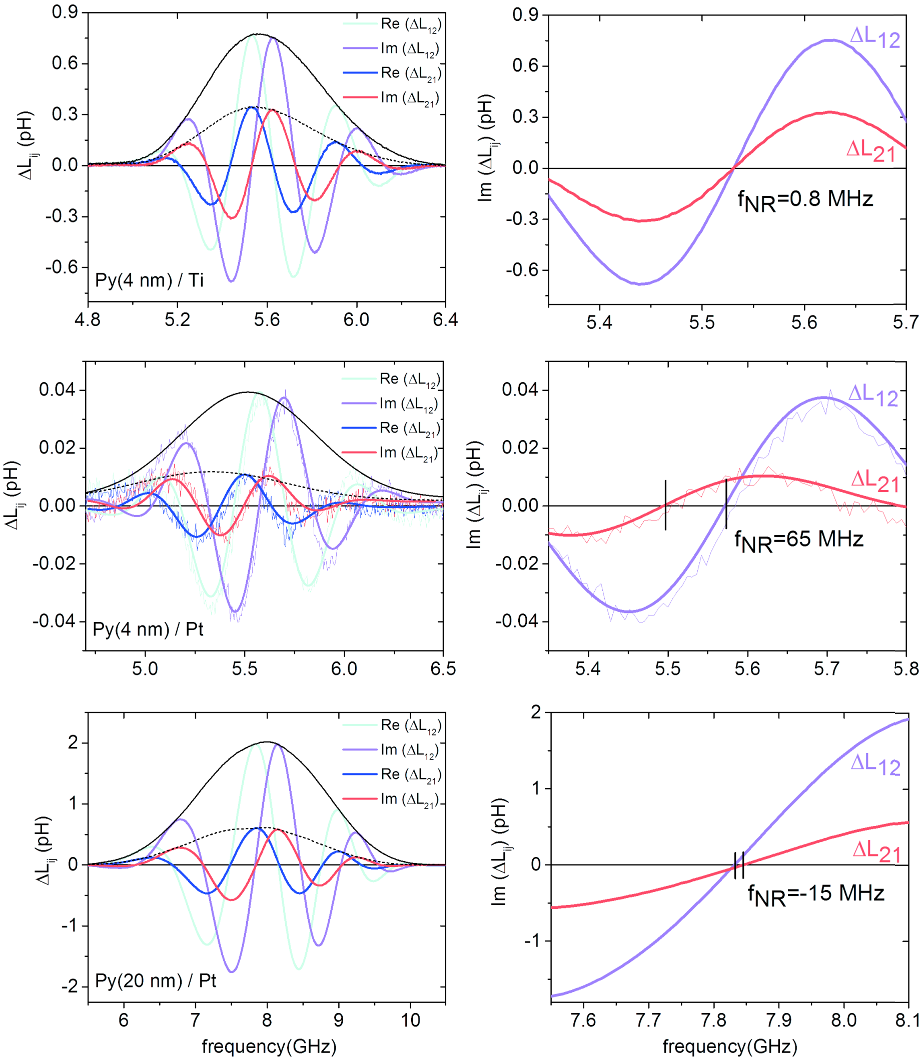

Figure 4.9: (left panels) Mutual-inductance spectrum measured at $\mu_0 H =$ 37 mT in Py(4)/Ti, Py(4)/Pt and Py(20)/Pt films. (right panels) A zoom of difference between inductance signals ΔL_{12} and ΔL_{21} showing a minor frequency non-reciprocity in Py(4)/Ti film, a large f_{NR} of +65 MHz in Py(4)/Pt film, and a negative f_{NR} of -15 MHz in Py(20)/Pt film. In middle panels the noise in raw signal is due to the small Py film thickness.

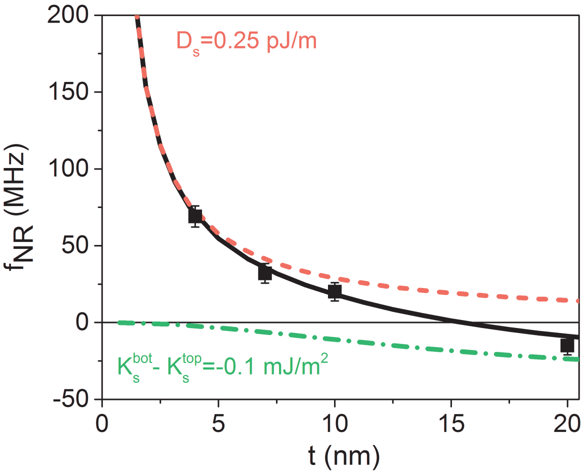

Figure 4.10: Magnetic asymmetry and iDMI contributions to the frequency non-reciprocity for a ferromagnet/heavy metal bilayer with $A = 11.5$ pJ/m, $\mu_0 M_\mathrm{s} = 1$ T, $k = 7.8\ \mu\mathrm{m}^{-1}$ and $\mu_0 H_0 = 37$ mT. The magnetic asymmetry contribution (green dash-dotted line) is calculated for $K_\mathrm{s}^\mathrm{bot} = -0.1\ \mathrm{mJ/m}^2$, the iDMI contribution (red dashed line) is calculated for $D_\mathrm{s} = 0.3$ pJ/m and the combined contribution from both effects is shown by solid black line. This reproduces well the measured frequency non-reciprocity (black squares).

frequency non-reciprocity as a function of $1/t$, the value of the iDM constant can be easily extracted.

In Fig. 4.10 we show the dependence of the measured frequency non-reciprocity as a function of the Py thickness (symbols). One observes a drastic decrease of the frequency shift with increasing the film thickness. For thicker films the frequency non-reciprocity starts deviating from a $1/t$ law and changes a sign for $t = 20$ nm. Such behavior is attributed to the influence of an asymmetry between the surface pinning at the top and bottom surfaces of the Py film, which leads to an additional frequency non-reciprocity opposite to that induced by the iDMI. To calculate the frequency non-reciprocity induced by the magnetic asymmetry between the top and bottom surfaces we use our analytical formula [Eq. (4.1.7)], which predicts a nearly quadratic dependence of f_{FN} on the film thickness. This distinct thickness dependence is actually the main criterium to separate the contributions of both effects on the frequency shift. The iDMI induces a shift proportional to $1/t$, which is the standard scaling for a purely interfacial effect. The difference of surface anisotropy generates a shift varying as t^2, which is attributed to the influence of exchange interaction which limits the inhomogeneity of the mode across the film. The best fit was obtained for an iDM constant of $D_s = 0.25$ pJ/m and a difference of surface anisotropy of $\Delta K = -0.1$ mJ/m^2 [solid line in Fig. 4.10]. To confirm these analytical findings, we also performed a rigorous numerical calculation [55], where the film was subdivided into a set of single elements N of thickness $a = 0.125$ nm with the total thickness defined as $N \cdot a$ resulting in a DM constant $D = 2.4$ mJ/m^2. The simulated frequency non-reciprocity is exactly the same as the one derived from an analytical formula. In Fig. 4.10 the individual contribution of the DMI and surface anisotropy is plotted by the red dashed line and green dot-dashed line, respectively. One sees, that in very thin films the dominant contribution is due to the DMI, which clearly demonstrates its interfacial nature, while the contribution of the difference in surface anisotropies is negligible. On the contrary, in moderately thin film the influence of the magnetic asymmetry becomes more important: it fully compensates the DMI-induced frequency shift at t=15 nm and becomes dominant in thicker films.

A similar value of the iDM constant for Py/Pt interface was reported by Stashkevich et al. [125]. In their work, the frequency non-reciprocity was studied in 4-10 nm Py film using Brillouin light scattering (BLS). In a 4 nm film, they observe a frequency non-reciprocity of 100 MHz for $k = 8$ μm^{-1} and about 300 MHz for $k = 20.5$ μm^{-1}, which corresponds to an iDM interaction with $D = 1.2$ mJ/m^2 ($D_s = 0.3$ pJ/m). However, for a film of thickness of 10 nm, the BLS measurements show a zero frequency non-reciprocity at $k = 20.5$ μm^{-1}, which is not expected if only the DM interaction is considered. The authors attribute this to the effect of a perpendicular uniaxial anisotropy at one of the film surfaces, which for this thickness has almost equal contribution to f_{FN} as the DMI, but with opposite sign. Their numerical calculations show that accounting for a surface anisotropy the total frequency non-reciprocity should be -36 MHz which, due to the limited resolution of BLS technique (±75 MHz), can not be measured. On the contrary, by using PSWS with a resolution of a few MHz, we can precisely determine the contribution of surface anisotropy from both interfaces and estimate the frequency non-reciprocity induced by their difference, as well as the frequency shift induced by iDM interaction.

It was also shown by Nembach et al. [98] and Belmeguenai et al. [10], that the sign of D_s may vary depending at which interface an adjacent heavy metal is placed. By using BLS, they found a negative value of $D_s =$

-0.3 pJ/m for the interface Pt/Py [98] and -1.7 pJ/m for Pt/Co [10].

4.3 Conclusion

The frequency non-reciprocity of MSSWs can arise in magnetic films as soon as the top/ bottom symmetry is broken and/or as a result of the iDM interaction, which becomes important in FM/HM bilayers. In order to identify the contribution of both effects, the spin wave propagation have been studied in both Py/Al_2O_3 and Py/Pt systems. In Py/Al_2O_3 films we observed a frequency non-reciprocity, which increases linearly with wave vector and nearly quadratically with the permalloy thickness. Using a theoretical model of dipole-exchange spin waves we could account for the measured frequency non-reciprocity by introducing asymmetric surface anisotropies. We deduced a simple analytical formula allowing to predict the magnitude of f_{NR} as a function of the difference in surface anisotropies at the top and bottom sides. In Ti/Py/Pt films, the measured frequency non-reciprocity was attributed to the combined effect of iDMI and a difference in surface anisotropies. We could extract the magnitude of both effects and demonstrate that in ultrathin films the frequency non-reciprocity is mostly induced by iDMI, while, by increasing the film thickness, the contribution from magnetic asymmetry becomes more important.

Chapter 5

Spin wave propagation and its modification by an electrical current in permalloy/Pt bilayers

In this chapter, by studying the spin wave propagation in a Py film with an adjacent heavy metal layer and its modification by an electrical current, we show that the spin-orbit spin transfer torque arising at the interface can significantly modify the propagating characteristics of a spin wave. In this study we focus mainly on two spin-orbit related phenomena, namely spin pumping (sec 5.2) and spin transfer torque induced by spin Hall effect (sec. 5.3.3). We also briefly consider the effect of adiabatic spin transfer torque arising while electrical current flows trough the spin wave (current-induced spin wave Doppler shift, sec. 5.3.5).

5.1 Experimental devices

The experimental study was performed by using the Ti/Py/Pt devices described in chapter 3 and already used for frequency non-reciprocity measurements. Ti/Py/Ti devices were used as reference devices, for which no spin no spin Hall induced spin transfer torque is expected due to the weak spin-orbit coupling in Ti. Another set of samples have been fabricated by our collaborators from UMPhy CNRS Thales (M. Collet, C. Cheng, K. Garcia-Hernandez, A. Anane). The film is a SiO_x/Py(15)/Pt(10) trilayer without Ti

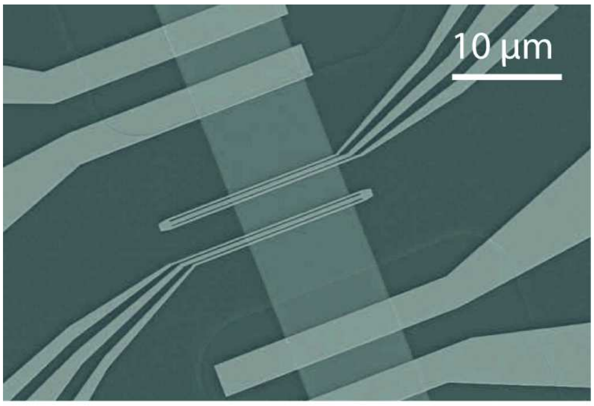

Figure 5.1: Scanning electron microscopy image of the Thales device with $w = 10$ μm and $D = 3$ μm.

underlayer. The sample design and the nanofabrication process are slightly different (Fig. 5.1): a Py/Pt strip of width $w = 5-50\mu$m is covered by a 330 nm thick insulating SiO_2 layer to avoid the electrical contact with antenna. The wave vector of the excited spin wave is $k = 7.1\mu\text{m}^{-1}$. As before, different devices with different edge-to-edge distances between antenna were used ($D = 1, 3, 5\mu$m). The spin wave propagation characterization and SHE-STT measurements on these devices have been published in [39].

The geometrical parameters of all fabricated devices are collected in Table 5.1, where the successfully measured samples (over 20) are marked by the check marks.

5.2 Spin wave propagation at zero current

Before analyzing the effect of spin current on the spin wave, we start characterizing the propagation of spin wave at zero current. Fig. 5.2(a) shows typical mutual-inductance spectra ΔL_{12} and ΔL_{21} measured at $\mu_0 H = 37$ mT for $w = 10$ μm and $D = 1$ μm device of the Thales series. Note that the detailed discussion below will be shown for this series and then summarized for all devices. The mutual-inductance consist of a real and an imaginary part, which oscillate with a 90° phase lag between each other. These oscillations are attributed to the phase delay $\phi = -kD$ accumulated by the spin wave during the propagation. The relatively broad envelop of

Device	Py(15)/Pt(10) (Thales)			PF8: Py(10)/Pt(10)			PF6: Py(20)/Pt(5)		
D w	1	3	5	1	1.5	2	1	2	3
5	✓	✓	x						
10	✓	✓	✓	✓	✓	x			
20	x	✓	✓	✓	✓	✓	✓	x	✓
50	x	✓	✓						

Device	PF4: Py(7)/Pt(5)			PF2: Py(4)/Pt(5)			PF9: Py(4)/Ti(5)		
D w	0.5	1	1.5	0.5	0.8	1	0.5	0.8	1
20	✓	✓	✓	✓	✓	✓	✓	✓	✓

Table 5.1: List of Py/Pt devices. Samples that could be measured are indicated by the check marks.

the waveform [black line in Fig. 5.2(a)] is associated to the finite width δk of peak of the Fourier transform of the antenna (see Fig. 3.7). For a change δk the phase accumulation changes by $\delta\phi = -\delta k D$. On the other hand, the frequency change $\delta\omega$ corresponding to this wave vector change is given by the spin wave group velocity v_g as $\delta\omega = v_g \delta k$. For a full period of oscillation $\delta\phi = 2\pi$. Therefore, $\delta k = 2\pi/D = 2\pi f_p/v_g$, so the group velocity is determined as $v_g = D f_p$, where f_p is the period of the oscillation.

Another important characteristic of the transmitted signal is its amplitude. The propagation of the spin wave in the dissipative medium is limited by the damping factor, which is related to the attenuation length of spin wave L_{att} (the length over which the amplitude of the magnetization precession decay by a factor e). Experimentally, we extract the attenuation length from the amplitude of the normalized transmitted signal A using the relation $A = exp(-D/L_{\mathrm{att}})$.

An important point of this kind of measurements is a realistic determination of the effective propagation distance D_{eff}. We define D as the edge-to-edge distance between two antenna. However, the waves also propagate under the emitting and receiving antenna, giving rise to an additional phase accumulation. A correction term D_0 accounting for the finite width of the antenna should be included, such that $D_{\mathrm{eff}} = D + D_0$. For a relatively large antenna it is not obvious to define at which point of space the dominating signal is generated (for example, at the central conductor or at the

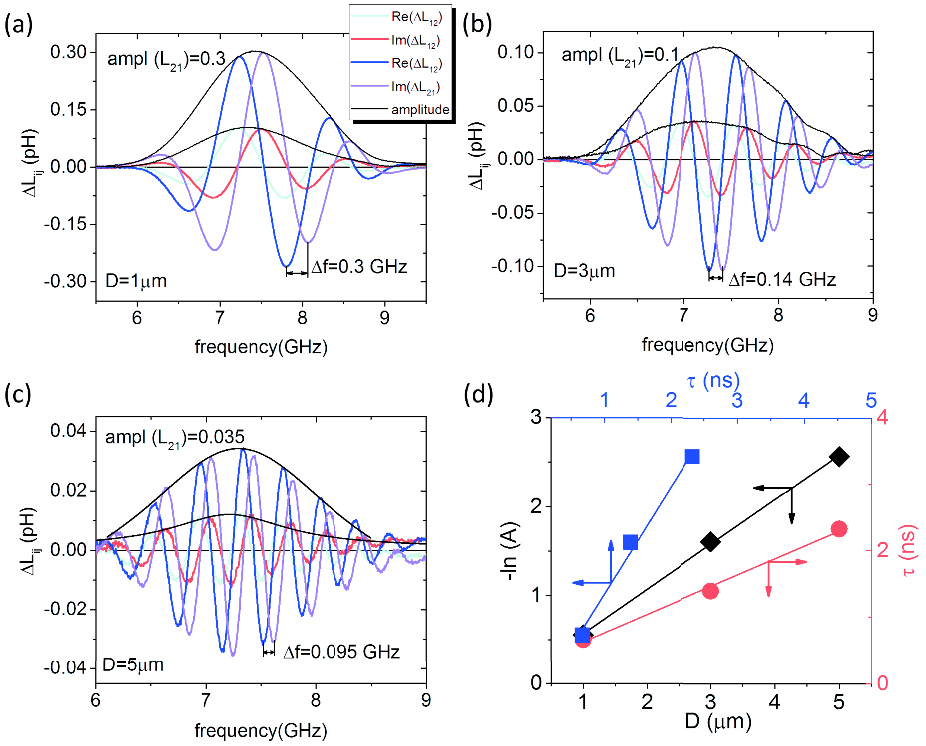

Figure 5.2: (a-c) Mutual-inductance spectrum measured in the Py(15)/Pt(10) film with $w = 10\ \mu$m and $D = 1, 3, 5\ \mu$m at $\mu_0 H = 36$ mT. Black solid lines are the amplitude of ΔL_{12} and ΔL_{21}, and Δf is a quarter of the signal period. (d) Dependence of the logarithm of the maximum SW signal amplitude -ln(A) on the distance D (diamonds), of the propagation time τ on D (circles), and of -ln(A) on τ (squares). Solid lines are linear fits.

edge of antenna). To clarify this point, we used devices with three different distances between antenna. Comparing the corresponding periods and amplitudes of the signals we can deduce both the group velocity and the attenuation length, as well as evaluate the real propagation distance traveled by the wave.

Group velocity

Fig. 5.2(b),(c) show the mutual-inductance spectra measured at $\mu_0 H =$ 36 mT for the 10μm width devices with edge-to-edge distance $D = 3\mu$m and $D = 5\mu$m, respectively. We measure the period of the oscillation as $f_p = 4\Delta f$, where Δf is the frequency difference between adjacent maxima of the real and imaginary parts. One sees that the period of the signal notably decreases with increasing the distance between antenna. We can express the period of the oscillation in the term of a propagation time $\tau = 1/f_p$ and plot the dependence of the propagation time as a function of distance D [red circles in Fig. 5.2(d)]. Using the relation $\tau = (D + D_0)/v_g$ we determine the group velocity from the slope of the linear fit and the distance D_0 traveled by the wave under the antenna from the fit intercept. For the given frequency, we found a group velocity of 2.2 km/s. The offset distance is found to be $D_0 = 900$ nm, which corresponds to the full width of one antenna. We can therefore assume that the total traveling distance is the distance between the central conductors of the antennas, that agrees well with the modeling performed in Ref. [17].

We then performed the same measurements for different values of magnetic field. For each value of field, the propagation time was plotted as a function of the distance and the group velocity was extracted. The dependence of the group velocity on the magnetic field is shown in Fig. 5.3 for all studied Py thicknesses (symbols). A clear decay of v_g with H is observed. One can also note a clear dependence of the group velocity on the thickness, which reaches 2.9 km/s for the 20 nm films and goes down to 0.9 km/s for the 4 nm films at $\mu_0 H = 14$ mT.

To compare these values with the theoretical ones, we use the expression of the group velocity deduced from the dispersion relation [Eq. (1.5.7)]:

$$v_g = \frac{\partial \omega}{\partial k} = \frac{\omega_M \omega_{\text{eff}} t}{4\omega} e^{-2kt}, \tag{5.2.1}$$

where ω_M and ω_{eff} are the saturation and effective magnetization, respectively, converted in angular frequencies. We calculated the group velocity for different thickness by accounting for a decrease of the saturation magnetization from 1 T for the thickest film down to 0.92 T for thinnest film

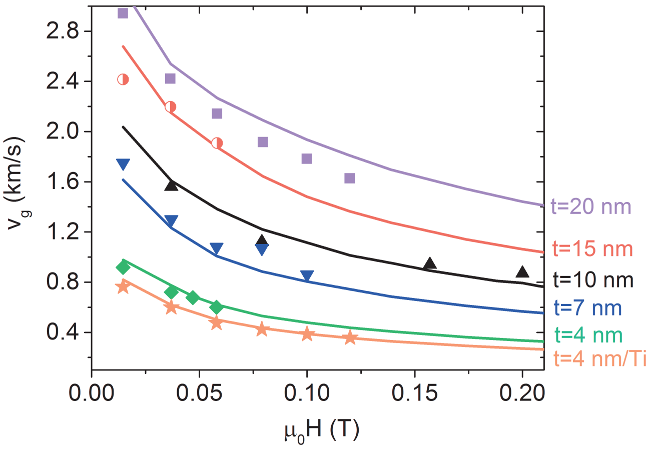

Figure 5.3: Magnetic field dependence of the group velocity measured for $t = 20$ nm (squares), $t = 15$ nm (circles), $t = 10$ nm (triangles up), $t = 7$ nm (triangles down) and $t = 4$ nm (diamonds and stars for Py/Pt and Py/Ti films, respectively). The solid lines are the theoretical values of v_g calculated with $\mu_0 M_s = 1 - 0.92$ T and $\mu_0 M_{\text{eff}} = 0.98 - 0.85$ T for $t = 20 - 4$ nm.

and by accounting for an additional decrease of the effective magnetization with decreasing thickness due to the surface anisotropy. From Eq. (1.3.12) and for a total surface anisotropy $\Sigma K_s = 0.1\text{mJ/m}^2$, we estimate the effective magnetization $\mu_0 M_{\text{eff}} = 0.98 - 0.85$ T for $t = 20 - 4$nm, respectively. The values calculated in this way are shown as solid lines in Fig. 5.3. We note that these values fit well with those extracted experimentally for all film thicknesses. A slight difference between the group velocity measured for Py(4)/Pt and Py(4)/Ti films was observed, which might be due to slightly different values of saturation and effective magnetization for the two films.

Attenuation length

To extract the attenuation length of the propagating spin waves, we monitor the dependence of the amplitude of the transmission signal as a function of the propagation distance. In Fig. 5.2(a-c) the amplitudes of the mutual-inductance signals $\sqrt{(Re(L_{ij}))^2 + (Im(L_{ij}))^2}$ are plotted for positive and negative wave vectors. As one sees, by increasing the distance between antenna, the amplitude of the signal significantly decreases with the same ratio for both $k > 0$ and $k < 0$. Accounting for the finite width of the antenna we write the amplitude decay with the distance as

$$A = A_0 e^{-[D+D_0]/L_{\rm att}}, \tag{5.2.2}$$

where $A = \Delta L_{ij}/\sqrt{L_{ii}L_{jj}}$ is the maximum amplitude of the mutual-inductance normalized to the maximum amplitudes of both self-inductance spectra, and A_0 is a prefactor related to the amplitude non-reciprocity of the counter-propagating spin waves.

In Fig. 5.2(d) we plot the logarithm of the normalized amplitude [-ln(A)] as a function of D (diamonds). A nice linear dependence is observed, where the slope of the linear fit gives a value $1/L_{\rm att}$. For this value of the magnetic field we found an attenuation length of 2 μm.

As for the case of group velocity, we then analyze the variation of the attenuation length as a function of the magnetic field. The results are plotted in Fig. 5.4. For all film thicknesses a notable decay of $L_{\rm att}$ with H is observed. At zero field extrapolation, one also notes a monotonous decrease of the attenuation length with reducing film thickness. Strongly different values of attenuation length were measured for 4 nm Py films in a contact with Pt or Ti overlayer, that indicates the different damping factor α in these systems. Indeed, from the definition of the attenuation length

$$L_{\rm att} = v_g T_2 = \frac{\omega_M \omega_{\rm eff} t}{4\omega} e^{-2kt} \frac{1}{\alpha(\omega_0 + \omega_M/2)}, \tag{5.2.3}$$

we find that an agreement between the theoretical and experimental values of $L_{\rm att}$ may be observed if α is assumed to be thickness and interface dependent. To verify this point and to determine the damping coefficient of Py(t)/Pt and Py/Ti films, we now analyze directly the spin wave relaxation rate.

Relaxation rate

As shown in Eq. (5.2.3), the group velocity and the attenuation length are related by the spin relaxation time T_2, which is inversely proportional to the damping factor. Since $L_{\rm att}$ and v_g are related to the amplitude and the period of the oscillating signal, we can determine the relaxation rate $\Gamma = 1/T_2$ directly from the amplitude decay as a function of the propagation time τ as

$$A = A_0 exp(-\Gamma\tau). \tag{5.2.4}$$

Therefore, by plotting -ln(A) as a function of τ [squares in Fig. 5.2(d)] we can directly extract the value of Γ from the slope of the corresponding linear fit. The obtained values are plotted in Fig. 5.5, where the corresponding values of damping factor are shown in the right y-axis. To account for the thickness

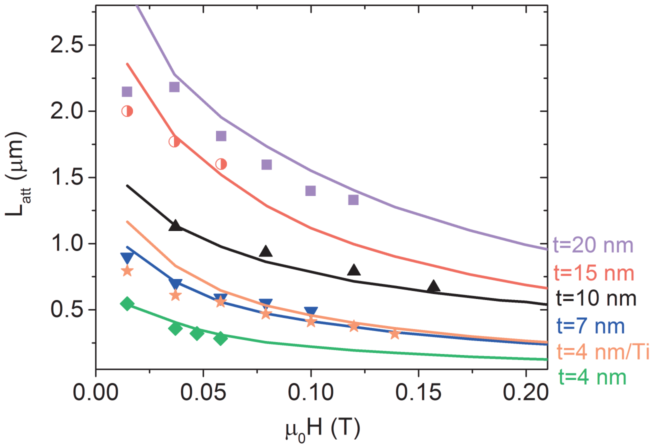

Figure 5.4: Attenuation length dependence on the magnetic field for the same film thicknesses as in Fig. 5.3. The theoretical values (solid lines) are calculated with the parameters used for v_g analysis and accounting for a thickness dependent damping factor.

dependence of the saturation magnetization, Γ is plotted as a function of $1/\mu_0 M_s t$. One can see, that (i) Γ exhibits a linear dependence on the inverse of the ferromagnetic film thickness and does not depend on the thickness of nonmagnetic layer [since no obvious deviation between bilayers with 10 nm of Pt ($t_{\mathrm{Py}} = 10, 15$ nm) and these with 5 nm of Pt ($t_{\mathrm{Py}} = 4, 7, 20$ nm)]; (ii) Γ significantly differs between 4 nm Py films capped with a Pt or a Ti layer. These two facts are consistent with the spin pumping process, which takes place when a nonmagnetic metal with a strong SOC is adjacent to a ferromagnetic film.

Spin pumping

In the spin pumping theory (see section 2.3.2) the increase of the dynamic magnetic loss is proportional to the spin pumping efficiency. Our spin wave measurements can be therefore used to quantify the spin mixing conductance $G_{\mathrm{eff}}^{\uparrow\downarrow}$, which is a characteristics of the NM/FM interface governed by the spin pumping process. For this purpose, we use:

$$\alpha = \alpha_0 + \alpha^{\mathrm{SP}} = \alpha_0 + \frac{g\mu_B G_{\mathrm{eff}}^{\uparrow\downarrow}}{4\pi M_s t}. \tag{5.2.5}$$

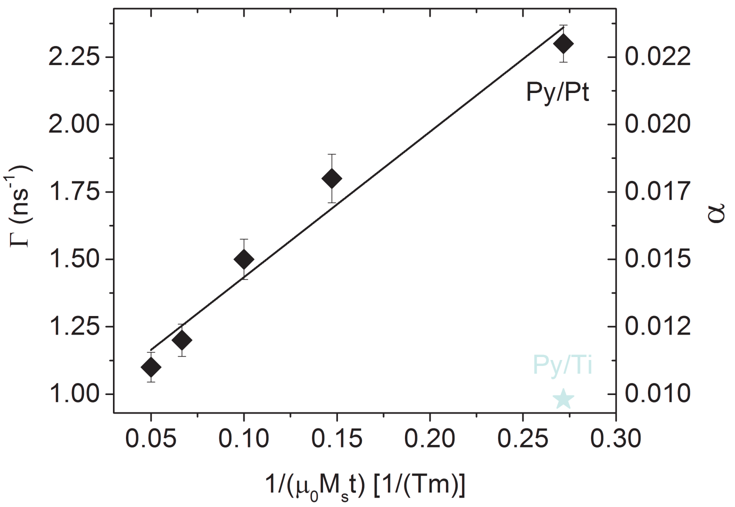

Figure 5.5: Relaxation rate/damping factor versus $1/\mu_0 M_s t$ (symbols). Solid line is a corresponding linear fit.

Using the measured dependence of $\alpha = \Gamma/(\omega_0 + \omega_M/2)$ on $1/\mu_0 M_s t$, one can determine the spin-mixing conductance from the slope of the corresponding linear fit, which gives us $G_{\text{eff}}^{\uparrow\downarrow} = 3.2 \cdot 10^{19}\ \text{m}^{-2}$. The fit intercept corresponds to $\alpha_0 = 0.008$, which is the typical value of damping factor for Py films [49]. This value is also close to the value $\alpha = 0.009$ measured for the Ti/Py(4)/Ti reference film, for which the spin pumping is expected to be very small.

In Table 5.2 we collected some of the values of $G_{\text{eff}}^{\uparrow\downarrow}$ for the Py/Pt interface reported in literature deduced from the ST-FMR or ISHE techniques. In the former case the spin-mixing conductance is extracted from the enlargement of the FMR line width due to the enhancement of Gilbert damping in Py, while in the latter case it is measured from the dc voltage generated in Pt by means of the inverse spin Hall effect. We first note that the value we measured at $k = 7\ \mu\text{m}^{-1}$ is the same order of magnitude than the one measured with other techniques for which a $k = 0$ FMR mode is used. This is in agreement with the theoretical expectation, since the effect is not expected to be k dependent. However, in principle, the efficiency of spin current generation by the spin waves can be improved by enhancing the coupling of the conduction electrons with the dynamic magnetization [110, 74, 95]. The latter can be achieved by using surface spin wave with a pronounced mode

Reference	Method	$G_{\text{eff}}^{\uparrow\downarrow}$, 10^{19} m^{-2}	$G_{\text{eff}}^{\uparrow\downarrow}$, 10^{15} Ω^{-1}m^{-2}
Our	PSWS	3.2	1.2
[144]	ST-FMR	3.96	1.5
[7]	ISHE	2.4	0.91
[93]	ST-FMR	2.1	0.8
[97]	ST-FMR	3	1.1
	dc-tuned ST-FMR	2.1	0.8
[81]	ab-initio calculation	2.5	0.95

Table 5.2: Comparison of the values of spin-mixing conductance of Py/Pt films extracted by different techniques.

localization at the surface that can be possible by increasing the thickness of magnetic film. The difference between our result and the reported ones may be due to the different experimental techniques used, which are more or less sensitive to additional interfacial scattering process or interfacial spin-orbit effects, which give rise to an enhancement of the damping. As shown in [97], the spin-mixing conductance conventionally extracted from the difference between damping factor with and without adjacent heavy metal is greater ($G_{\text{eff}}^{\uparrow\downarrow} = 3 \cdot 10^{19}$ m^{-2}) than that determined from dc-tuned ST-FMR (ST-FMR combined with a dc bias current) ($G_{\text{eff}}^{\uparrow\downarrow} = 2.1 \cdot 10^{19}$ m^{-2}), for which these additional interfacial effects are assumed not to contribute.

Note that applications usually require one to minimize the magnetization losses while maximizing the spin current transmission across the FM/NM. A way to fulfill this condition is to add a nonmagnetic material, which doesn't exhibit strong SOT, as an interlayer between the FM and HM layers [97, 109, 107]. It was shown [109], that the Cr and Al metals with a large spin-diffusion length used as a spacers between Pt and Py layers limit the enhancement of damping, but at the same time do not prevent the spin pumping process.

5.3 Spin wave propagation at non-zero current

Let us now analyze the propagating characteristics of spin wave under the effect of an external electric field. In Fig. 5.6 the inductive signals measured in the 15/10 nm Py/Pt bilayer with $w = 10$ μm and $D = 1$ μm at $\mu_0 H = 36$ mT are plotted for different values of dc current (to simplify the graph only the imaginary part of ΔL_{21} is shown). The presence of dc current leads to several modifications of mutual inductance spectrum. First, we observe an enhancement or a reduction of the signal amplitude depending on the current direction. The difference in amplitude ΔA between the signals measured at $-I_{\mathrm{dc}}$ and $+I_{\mathrm{dc}}$ increases with increasing magnitude of dc current. Second, we note a slight decrease of the signal period f_{per} with increasing I_{dc} (not really visible from this graph), which is independent on the current direction $[f_{\mathrm{per}}(-I_{\mathrm{dc}}) = f_{\mathrm{per}}(+I_{\mathrm{dc}})]$. Third, we observe a frequency shift Δf between the signals measured at positive and negative current, which increases monotonously with the I_{dc}. And finally, for large values of electric current, a significant decrease of the resonance frequencies for the two current polarities is observed. Each of these modifications is the result of different current induced effects, namely SHE-STT, Joule heating, Oersted field, and current induced Doppler shift, which simultaneously affect the propagating spin wave. The effect of SHE-STT is to modify the amplitude of the signal, the effect of Joule heating and Oersted field is to change the resonance frequency and the period of the signal, and the spin wave Doppler shift reveals as a small non-reciprocal current-induced frequency shift.

5.3.1 Detailed analysis for Py(15)/Pt(10) devices

Consider first the effect of SHE-STT on spin wave parameters Γ, v_g, and L_{att}. For this, we perform the same procedure as described in section 5.2, i.e., we look at the variation of the amplitude and period of the transmitted signal as a function of D for different values of I_{dc} (from -50 mA to +50 mA). For each value of I_{dc}, we extract the group velocity from the dependence of the period on D, the attenuation length from the dependence of the amplitude on D, and the spin relaxation rate from the dependence of the amplitude on the period. The results are shown in Fig. 5.7. We observe a linear variation of Γ as a function of current [Fig. 5.7(a)], that is a clear evidence of the SHE-induced spin transfer torque effect. Indeed, when an electric current is applied into the Pt layer it generates a transverse spin current by the SHE, which is injected into the Py layer and modifies its magnetization precession via the spin transfer torque. Since for the surface spin wave configuration the spin transfer torque is collinear with the damping torque it leads to an enhancement or reduction of the spin relaxation rate depending on the current polarity. As one can see from the graph, by applying $I_{\mathrm{dc}} = \pm 50$ mA the relaxation rate (and the damping) changes by up to 14%. This is the main result of this chapter, which will be analyzed later.

Before that, let us now look at the current-dependence of v_g and L_{att}. As shown in Fig. 5.7(b), no significant changes of group velocity is observed for a current less than ±20 mA. With further increasing the magnitude of

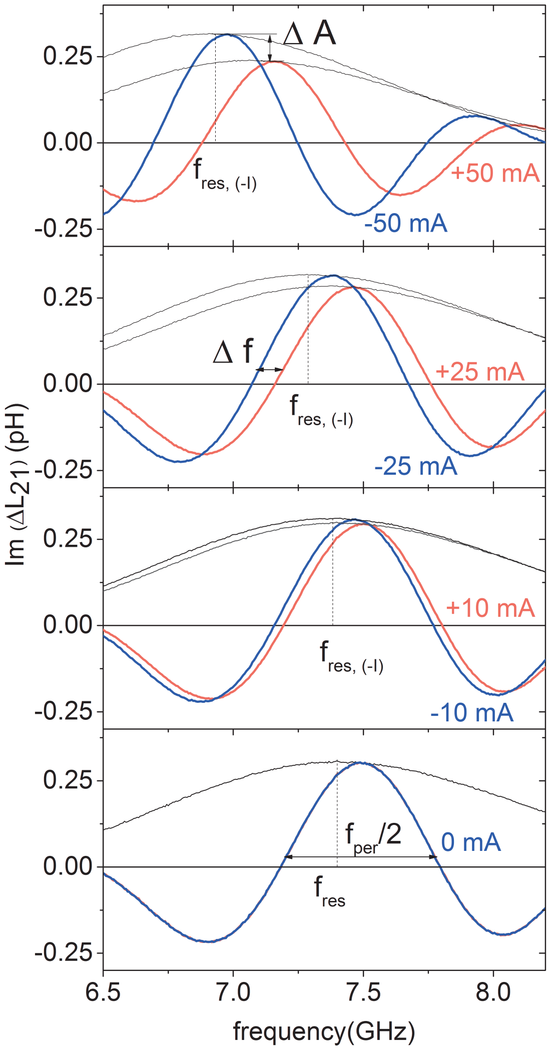

Figure 5.6: Current induced modification of the transmitted signal measured in a 15/10 nm Py/Pt strip with $w = 10$ μm and $D = 1$ μm at $\mu_0 H = 36$ mT. The change of amplitude ΔA, period f_{per}, resonance frequency shift f_{res}, and the frequency shift Δf between the signals measured at $I > 0$ and $I < 0$ are defined on the graphs.

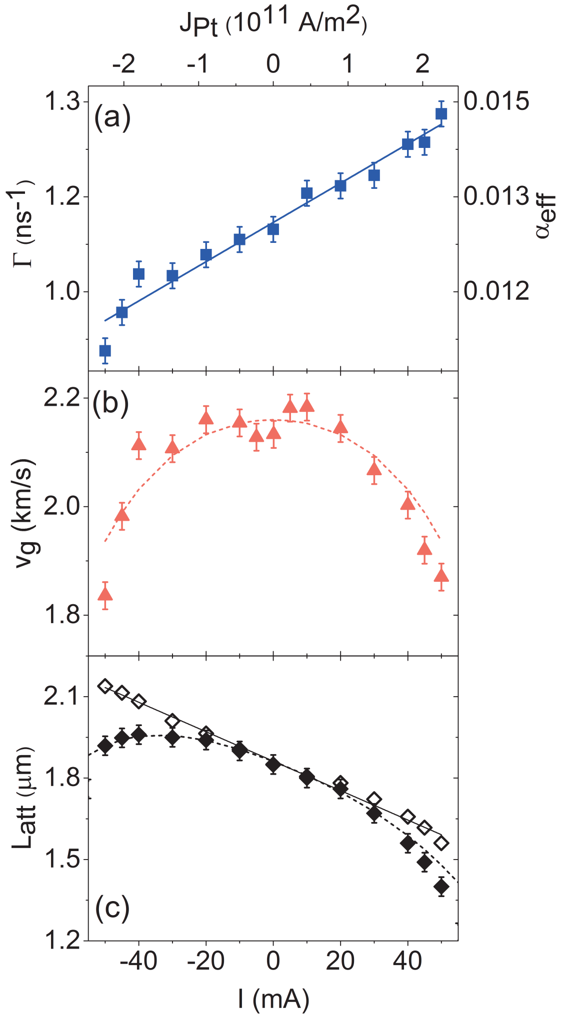

Figure 5.7: Influence of the electrical current on the spin-wave relaxation rate Γ (a), the group velocity v_{g} (b), and the attenuation length L_{att} (c). The right-scale in panel (a) gives the conversion of Γ in effective Gilbert damping parameter α_{eff}. The solid line in (a) is a linear fit. The dashed line in (b) shows the values of v_{g} calculated accounting for Joule heating (see text). Solid diamonds in (c) are the raw L_{att} data. Open diamonds are obtained after subtraction of the Joule contribution and the solid line is a linear fit of these corrected data. The dashed line is obtained by combining the v_{g} affected by Joule heating with the Γ affected by STT.

electric current the group velocity drastically decreases and at maximum applied current of ±50 mA falls down to 1.87 km/s that corresponds to a change of 14% with respect to zero current. As for attenuation length [filled symbols in Fig. 5.7(c)], we also observe the decrease of L_{att} at high current values, but contrary to group velocity, which symmetrically decays at $-I_{\mathrm{dc}}$ and $+I_{\mathrm{dc}}$, the attenuation length shows an asymmetric dependence on I_{dc}.

Such current-dependence of v_g and L_{att} is associated with the effect of Joule heating and Oersted field, which become important at high current. To analyze these effects, we rely on the variation of the spin-wave resonance frequency f_{res} with current. As was shown in Fig. 5.6 the resonance frequency decreases for both current polarities with respect to the zero current reference waveform, with a significantly larger decrease for a negative current than for a positive one. The overall variation of f_{res} is best seen by plotting the frequency of the maximum of $|\Delta L_{21}|$ as a function of I [squares in Fig. 5.8]. This variation may be decomposed into odd and even contributions, $f_{\mathrm{res}}^{\mathrm{even/odd}}(I) = f_{\mathrm{res}}(0) + (f_{\mathrm{res}}(I) \pm f_{\mathrm{res}}(-I))/2$, where the odd contribution [circles in Fig. 5.8] is attributed to the Oersted field and the even contribution [triangles in Fig. 5.8] is attributed to the Joule heating.

By applying an electric current into the Py/Pt film the current will partially flow in Py and Pt layers creating an Oersted field around each layer. The Oersted field induced frequency shift can be estimated by differentiating the Damon-Eshbach dispersion relation with respect to the field

$$f_{\mathrm{res}}^{\mathrm{odd}} = \frac{\partial f_{\mathrm{res}}}{\partial H} H_{\mathrm{Oe}}, \tag{5.3.1}$$

where $H_{\mathrm{Oe}} = I_{\mathrm{Pt}}/(2w)$ is the Oersted field generated by the fraction of the current I_{Pt} that flows in the Pt layer. Therefore, using this relation and the linear dependence of $f_{\mathrm{res}}^{\mathrm{odd}}$ on I_{dc} with a slope of 1.5×10^{-3} GHz/mA, we estimate the fraction of the current I_{Pt} to be 45% of the total current. This value is consistent with that extracted from resistivities of individual Pt and Py films by means of four probe measurements (see section 5.3.3).

Let us now analyze the contribution of Joule heating to the resonance frequency shift. The current induced Joule heating yields a decrease of the saturation magnetization $M_{\mathrm{s}}(I)$, which can be calculated by differentiating the Damon-Eshbach dispersion relation with respect to M_{s}

$$f_{\mathrm{res}}^{\mathrm{even}} = \frac{\partial f_{\mathrm{res}}}{\partial M_{\mathrm{s}}} M_{\mathrm{s}}(I). \tag{5.3.2}$$

$f_{\mathrm{res}}^{\mathrm{even}}(I)$ may be fitted to a polynomial law $f_{\mathrm{res}}(0) - aI^2 - bI^4$, where $a = 1.18 \times 10^{-4}$ GHz.mA^{-2} and $b = 1.9 \times 10^{-8}$ GHz.mA^{-4}. From the frequency

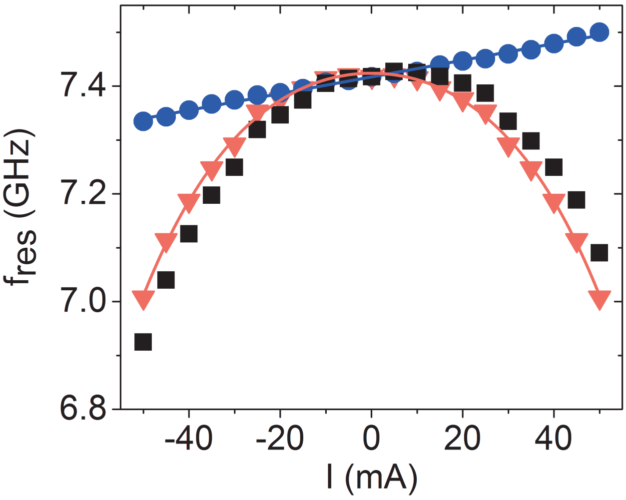

Figure 5.8: Variation of the SW resonance frequency $f_{\rm res}$ with the *dc* current. The squares are the experimentally measured data, whereas the circles and the triangles represent, respectively, the odd and even parts of $f_{\rm res}(I)$.

decrease of 5% observed for $|I| = 50$ mA, we can therefore estimate a saturation magnetization decrease of 7%, and the corresponding temperature increase, which is about 150 K. A very similar temperature increase is estimated by monitoring the resistance of the strip, which varies from 31.4 Ω at small current to 39.5 Ω at ±50 mA, and by using an average temperature coefficient of $0.2\%/K$ for the bilayer resistance.

The consequence of the Joule heating and Oersted field induced variation of the resonance frequency is the variation of group velocity $v_g = \partial\omega/\partial k$ and as a result the variation of the attenuation length. Thus, using the Damon-Eshbach expressions of $v_{\rm g}$ [Eq. 5.2.1] and evaluated $f_{\rm res}(I)$ and $M_s(I)$ dependencies we calculate the change in group velocity expected from Joule heating and Oersted field [dashed line in Fig. 5.7(b)], which accounts quantitatively for the measured variation. We can note, that the group velocity decay at high current values is mostly caused by Joule heating, whereas the contribution from Oersted field is very small. If we now combine the change in group velocity induced by Joule heating with the change in relaxation rate induced by the SHE-STT, we can account for the measured variation of $L_{\rm att}$ [dashed line in Fig. 5.7(c)]. After subtracting out the effect of Joule heat-

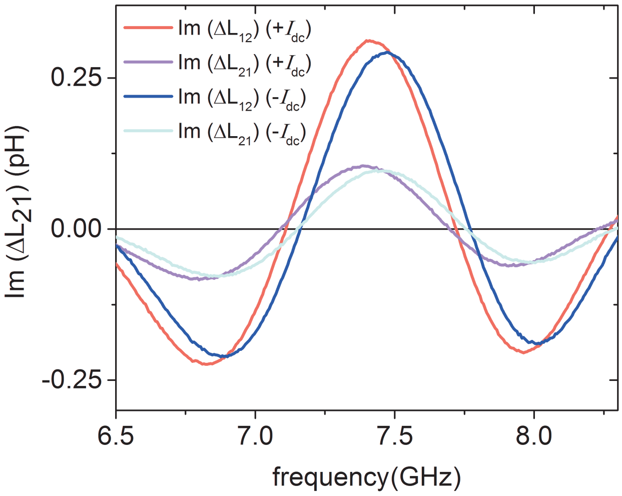

Figure 5.9: Mutual-inductance spectrum measured in a Py(15)/Pt(10) strip with $w = 10$ μm and $D = 1$ μm at $\mu_0 H = -36$ mT and at $I_{\mathrm{dc}} = \pm 15$ mA for both positive and negative wave vectors.

ing, the remaining variation of L_{att} is found to be linear (open diamonds), as expected for a purely SHE-STT-induced effect. This confirms that our analysis is self-consistent.

As expected for SHE-STT, the effect is reversed when the magnetic field is reversed. For a negative applied field an enhancement of the signal amplitude is observed at a positive current, while a negative current leads to a reduction of amplitude (Fig. 5.9). We also observed, that SHE-STT works in the same manner for positive and negative wave vector, i.e. it either amplifies or damps the spin wave depending on the current polarity but independently the spin wave propagation direction. Indeed, we extracted similar values of $\Gamma(I)$ from the ΔL_{12} and from the ΔL_{21} mutual inductance spectra.

5.3.2 Analysis for the Ti/Py(t)/Pt series

In a next step, we carried out a similar analysis for Ti/Py/Pt samples. Fig. 5.10 shows typical mutual-inductance spectra measured under current for the thinnest (4 nm) and the thickest (20 nm) film of the series. For the same value of the current, one observe a pronounced change of the amplitude signal for 4 nm film, while for 20 nm the effect of *dc* current is less visible. To quantify the SHE-STT for this films, we used a simplified method of analysis. Instead of following systematically the mutual-inductance as a function of the distance (which was not always possible due the lack of working samples), we concentrate on the quantity, which gives the more direct access to the SHE-STT, namely the current induced change of Γ. For this purpose, we write the mutual-inductance as $|\Delta L_{21}|^{max} = \Delta L_0 \exp(-\Gamma\tau)$. Comparing the measurements taken at positive and negative currents, and assuming the current dependence to be dominated by that of Γ one obtains:

$$\frac{|\Delta L_{21}^{+}|^{max}}{|\Delta L_{21}^{-}|^{max}} = \exp^{-\Delta\Gamma\tau} \tag{5.3.3}$$

and

$$\Delta\Gamma = \Gamma^{+} - \Gamma^{-} = -\frac{1}{\tau}\ln(\frac{|\Delta L_{21}^{+}|^{max}}{|\Delta L_{21}^{-}|^{max}}), \tag{5.3.4}$$

where $|\Delta L_{21}^{+}|^{max}$ and $|\Delta L_{21}^{-}|^{max}$ are the maximum amplitude measured at positive and negative current, respectively, and τ is deduced from the period of the oscillations. The advantage of this expression is that it provides the current-induced change of relaxation rate from a pair of measurements ($+I$ and $-I$) on a single device. To compare the effect obtained on the same films, but for different values of I, w or D, we calculate a normalized value of current-induced change of relaxation rate $\Delta\Gamma/E$. Here $E = V/L$ is the electric field and V is the voltage measured at the inner pads separated by the distance L. As expected, we obtain similar values for this quantity when comparing different measurements and devices for the same film. In Fig. 5.11 the change of the relaxation rate $\Delta\Gamma/E$ as a function of Py thickness is shown, where $\Delta\Gamma$ shows a rapid increase by decreasing Py film thickness.

5.3.3 Spin transfer torque induced by spin Hall effect

Let us now analyze quantitatively the observed SHE-STT effect, for which the relevant quantity is the spin-wave relaxation rate Γ. To do this we use the Landau-Lifshitz equation of motion with the additional term corresponding to spin transfer torque

$$\frac{d\mathbf{M}}{dt} = -\gamma\mathbf{M}\times\mathbf{H}_{\text{eff}} + \frac{\alpha\mathbf{M}}{M_s}\frac{d\mathbf{M}}{dt} + \frac{J_s}{M_s t}(\mathbf{M}\times\sigma\times\mathbf{M}), \tag{5.3.5}$$

After performing the linearization procedure ($\mathbf{M} = \mathbf{M}_{\text{eq}} + \mathbf{m}$) we can write the LLG equation for the surface spin wave configuration in as

$$\frac{d\mathbf{m}}{dt} = -i\omega_0\mathbf{m} - \Gamma_0\mathbf{m} + \frac{J_s}{M_s t}\mathbf{m}, \tag{5.3.6}$$

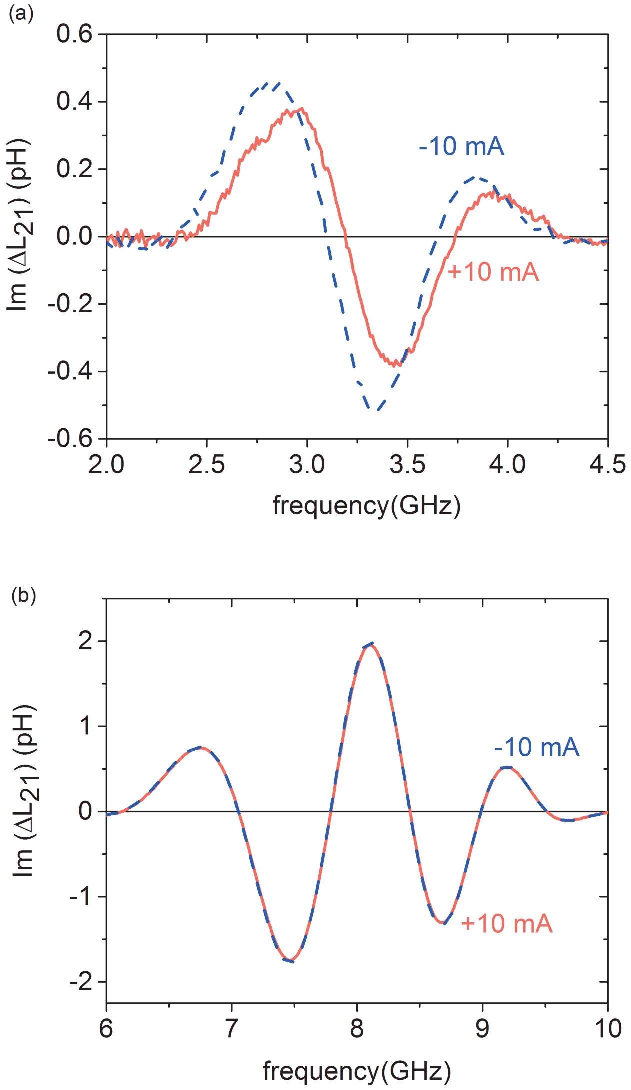

Figure 5.10: Mutual-inductance spectrum measured at $I_{\mathrm{dc}} = \pm 10$ mA (a) in Py(4)/Pt(5) film with $w = 20$ μm and $D = 0.5$ μm at $\mu_0 H = -5$ mT and (b) in Py(20)/Pt(5) film with $w = 20$ μm and $D = 1$ μm at $\mu_0 H = 36$ mT.

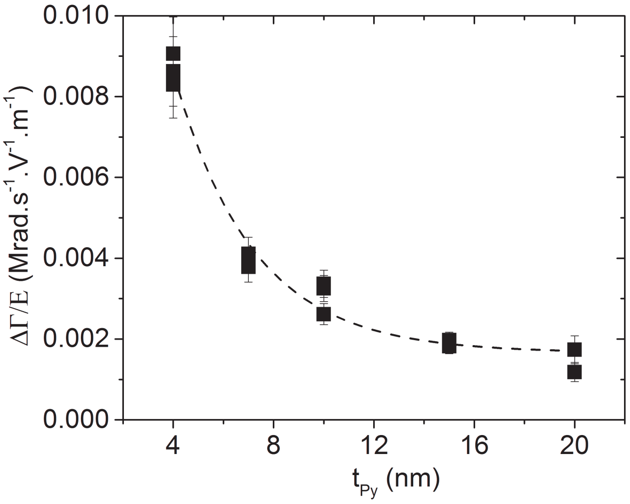

Figure 5.11: Measured change of relaxation rate $\Delta\Gamma$ induced by STT-SHE per unit of electric field versus Py thickness (symbols). The line is a guide for the eyes.

where ω_0 is the SW oscillation frequency determined in the absence of damping and STT. The solution of this equation can be simply expressed as $\omega = \omega_0 - i\Gamma$, where the imaginary part of the oscillation frequency is given by the relaxation rate $\Gamma = \Gamma_0 - \xi I_{dc}$. Here, Γ_0 is the natural relaxation rate governed by the Gilbert damping. Therefore, the SHE-STT translates directly into a current-induced change of the spin wave relaxation rate

$$\Delta\Gamma_{\mathrm{STT}} = \theta_{\mathrm{SH}}^{\mathrm{STT}} \frac{\mu_B}{e M_s t_{\mathrm{Py}}} J_{\mathrm{Pt}}, \tag{5.3.7}$$

where $\theta_{\mathrm{SH}}^{\mathrm{STT}}$ is the effective spin Hall angle (SHA) of the Pt film including possible losses of angular momentum in the interface region, μ_B is the Bohr magneton, e is the electron charge and J_{Pt} is the current density in the Pt layer.

To calculate the ratio of the currents flowing in the two films of our Py/Pt bilayers, we use the 4 wires electrical resistance measurements of our strips. From the resistance R measured with a voltage probe we extract the sheet conductance $G_s = (1/R)(L/w)$, where L is the spacing between the probes. In Fig. 5.12 the dependence of the sheet conductance G_s on t_{Py} is plotted. For a given Pt thickness G_s is expected to scale linearly with t_{Py}, where the intercept corresponds to the sheet conductivity of the Pt layer and the slope corresponds to the "bulk" conductivity of Py. For the set of Py(t)/Pt(5) films we found $G_{s,Pt5} = 0.025$ S ($\sigma_{\mathrm{Pt5}} = 4 \cdot 10^6$ S/m) and $\sigma_{\mathrm{Py}} = 2.5 \cdot 10^6$ S/m. Assuming the same Py conductivity for our Py(10)/Pt(10) film and for the Py(15)/Pt(10) films provided by the Thales group, the conductivity of the 10 nm Pt film grown at IPCMS is found to be higher ($G_{s,Pt10} = 0.065$ S, $\sigma_{\mathrm{Pt10}} = 6 \cdot 10^6$ S/m) than that of the 10 Pt film grown at Thales ($G_{s,Pt10} = 0.045$ S, $\sigma_{\mathrm{Pt10}} = 4 \cdot 10^6$ S/m). From the ratio of the conductances of the individual layers we calculate the ratio between the currents flowing in the Py and Pt layers. The result is shown in Fig. 5.13 as diamonds. We observe a gradual decrease of $I_{\mathrm{Pt}}/I_{\mathrm{dc}}$ from 0.85 for the 4 nm films down to 0.3 for the 20 nm one.

Now, using the value I_{Pt}/I_{dc} we calculate J_{Pt} and using the measured current-induced changes of the relaxation rate we deduce from Eq. (6.4.7) the effective spin Hall angle. We found a value $\theta_{\mathrm{SH}}^{\mathrm{STT}} = 0.10 \pm 0.02$, which does not dependent significantly on the magnetic film thickness (see Fig. 5.14), as it is expected from the spin transfer torque induced by spin Hall effect. The oscillation around the value 0.1 can be associated with the estimation of the fraction of current flowing in Pt layer, which is not very accurate (see the dispersion of the data points in Fig. 5.13).

To avoid the problem with the estimation of the value I_{Pt}/I_{dc}, the SHE-STT can be quantify by means of spin Hall conductivity σ_{SH}, which is defined as $\sigma_{\mathrm{SH}} = J_{\mathrm{s}}/E$. In this case, the current-induced changes of the relaxation rate can be written as

$$\Delta\Gamma_{\mathrm{STT}} = \sigma_{\mathrm{SH}}^{\mathrm{STT}} \frac{\mu_B}{e M_s t_{\mathrm{Py}}} E. \tag{5.3.8}$$

Using this relation we extract the spin Hall conductivity, which is found to be $\sim 4 \cdot 10^5$ S/m. In Fig. 5.14 we plot the spin Hall conductivity as a function of Py thickness. As in the case of spin Hall angle, the spin Hall conductivity remains almost constant within the studied thickness range.

5.3.4 Discussion

Let us now comment the obtained values of the effective spin Hall angle and spin Hall conductivity. To account for the spin backflow effect (chapter 2) the effective spin Hall angle can be written as $\theta_{\mathrm{SH}}^{\mathrm{STT}} = T\theta_{\mathrm{SH}}$, where θ_{SH} is the intrinsic SHA and T is the interfacial transparency, which is the ratio of the spin current density is transmitted into the Py film to the spin current density generated on the Pt side [144, 101]. For a film much thicker than the

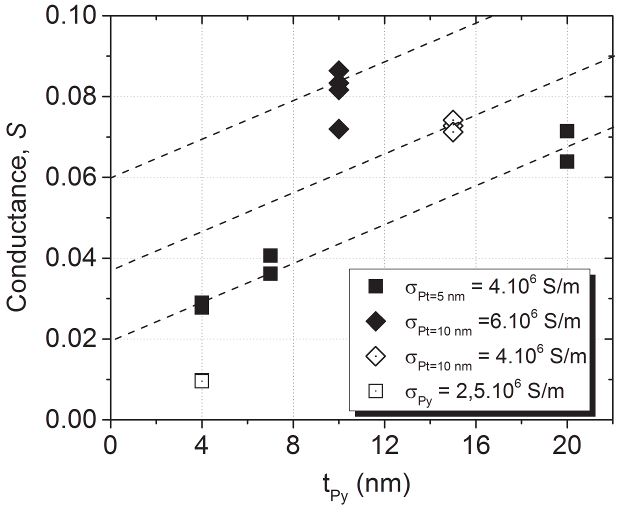

Figure 5.12: Dependence of the electrical conductance on Py thickness for 5 and 10 nm Pt film

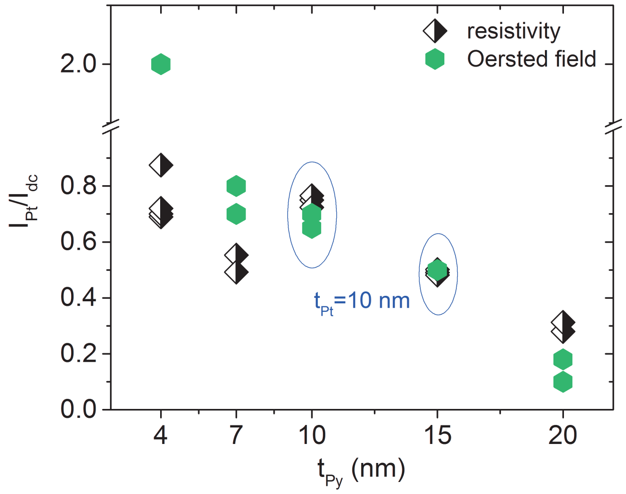

Figure 5.13: The fraction of current flowing in Pt layer extracted from the Oersted field measurements (hexagons) and from the four points probe measurements (diamonds) as a function of Py thickness.

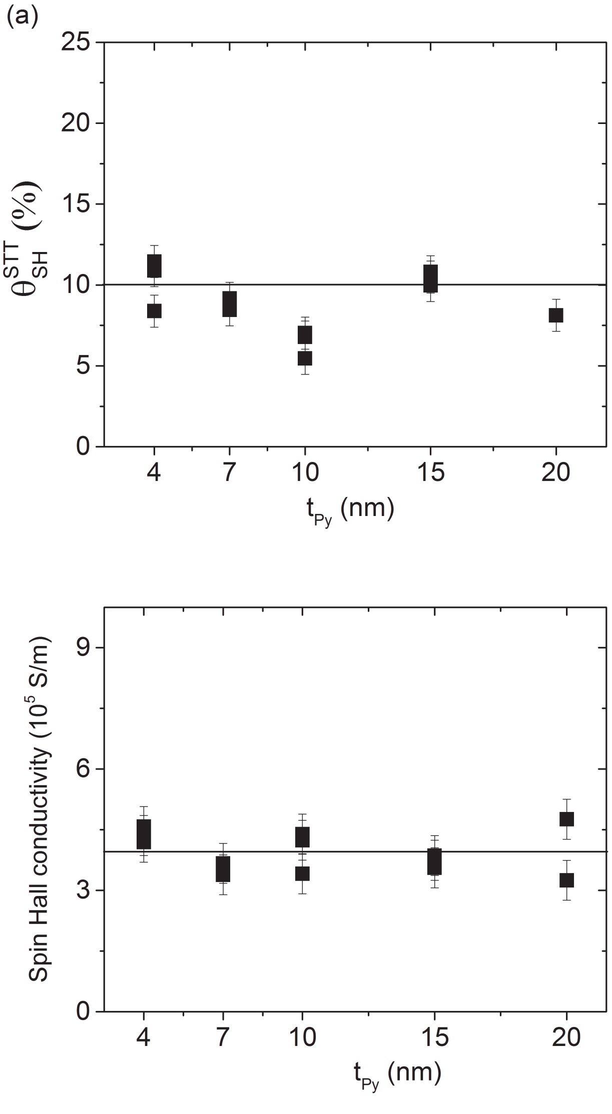

Figure 5.14: Dependence of the effective spin Hall angle (a) and corresponding spin Hall conductivity (b) versus Py film thickness.

spin diffusion length (which is our case, as $t_{\mathrm{Pt}} = 4 - 20\mathrm{nm} > \lambda_{\mathrm{sd}} = 1.4$ nm), the interfacial transparency can be calculated as a ratio between the effective spin mixing conductance $G_{\mathrm{eff}}^{\uparrow\downarrow}$ extracted from the damping enhancement and the spin conductivity of the Pt layer $G_{\mathrm{Pt}} = \sigma_{\mathrm{Pt}}/\lambda_{\mathrm{sd}}$, $T = 2G_{\mathrm{eff}}^{\uparrow\downarrow}/G_{\mathrm{Pt}}$. Using $\lambda_{\mathrm{sd}} = 1.4$ nm [101, 99], the value of $G_{\mathrm{eff}}^{\uparrow\downarrow}$ found in section 5.2, and the values of conductivity for different Pt thicknesses given in Fig. 5.13, we obtain an interfacial transparency in the range $0.55 \leq T \leq 0.9$, which translates into an intrinsic spin Hall angle $0.11 \leq \theta_{\mathrm{SH}} \leq 0.2$.

Referring to the literature, one finds a very large range for the reported values of the spin Hall angle $0.0037 \leq \theta_{\mathrm{SH}} \leq 0.20$ [120, 144, 78], which takes its origin from both the theoretical analysis and the experimental method used (mainly ISHE and ST-FMR).

The iSHE technique is based on the detection of the charge current in NM generated by the spin current pumped from FM by means of the inverse spin Hall effect. From the measured potential difference at the sides of NM, one estimates the efficiency of spin-to-charge current conversion governed by the spin Hall angle, as

$$\frac{J_c}{J_s} = \frac{2e}{h}\theta_{\mathrm{SH}}^{\mathrm{ISHE}}\frac{\lambda_{\mathrm{sd}}}{t_{\mathrm{NM}}}\tanh(\frac{t_{\mathrm{NM}}}{2\lambda_{\mathrm{sd}}}). \tag{5.3.9}$$

As one can note, depending on the value of λ_{sd} for a given material, the value of $\theta_{\mathrm{SH}}^{\mathrm{ISHE}}$ extracted from the measured charge current will vary. As was emphasized in [107], since the values of spin-diffusion length used in literature differ by one order of magnitude, naturally the values of spin Hall angle is also scattered within a large range. As was also pointed out in the aforementioned paper, the spin current absorption at the interface is usually neglected, that may also give rise to an incorrect estimation of the spin Hall angle.

In the ST-FMR technique one deals with voltage measurements arising from the anisotropic magnetoresistance (AMR): an oscillating spin current injected from a heavy metal into a ferromagnet exerts a spin torque inducing the magnetization precession, that in turn induces an oscillation of the resistance due to the anisotropic magnetoresistance. In this geometry, the external magnetic field is applied at an oblique angle from the strip axis.

In our opinion, the propagating spin wave spectroscopy enables measuring quite directly the spin transfer torque induced by the direct spin Hall effect and extracting the spin Hall angle by accurately measuring the variation of the spin relaxation rate as a function of the *dc* current. We avoid most of the complication appearing in ISHE and ST-FMR measurements: difficulty to determine the microwave current (both techniques), uncertainty on λ_{sd} (on which the ISHE depends strongly), and complex oblique measurement geometry (ST-FMR). From that perspective, the most relevant points of comparison are measurements of SHE-STT induced changes of damping in Py/Pt by cavity-FMR [6] and micro-BLS [27], which are performed in the same geometry as our PSWS experiments but at $k = 0$. By analyzing these data using Eq. (6.4.7), we obtain effective spin Hall angles of 0.05-0.09. Our value for $k = 7\ \mu\mathrm{m}^{-1}$ is comparable to, and even larger than these estimates. In the linear regime of excitation investigated here, i.e., far below the self-oscillation threshold, the only effect of the SHE-STT is to change the magnetization relaxation rate and, as expected from the form of the STT term [Eq. (6.4.7)], we find that the process is as efficient for a propagating spin-wave with finite k as for the FMR mode or for the thermally excited spin-wave manifold [28].

Let us now discuss the value of the spin Hall conductivity (SHC). The interest to identify this quantity is that it can be compared with the values obtained from ab-initio calculations. Until recently, only the intrinsic spin Hall conductivity related to the electronic band structure could be calculated from first principle [45, 44]. Recently, the calculation was extended to account for the extrinsic contribution to spin Hall conductivity [42, 83]. The value of intrinsic SHC calculated for Pt was found to be about 4×10^5 S/m [44, 83], which is very close to that obtained from our experimental measurement. Moreover, in Ref. [83], the presence of impurity electron scattering was found to reduce slightly the total spin Hall conductivity. Therefore, based on these numerical calculations, we can assume that the dominant mechanism of the SHE in our Pt film is the intrinsic one.

5.3.5 Current induced frequency shift

The additional torques which can appear when the *dc* current is injected into the Py/Pt film are the torques induced by the Oersted field and the Doppler effect. The fraction of the current flowing in Py film exerts an in-plane torque on the magnetization, which in the adiabatic limit leads to a modification of the precession frequency. This effect is known as a current induced spin wave Doppler shift (CISWDS). Additionally, the charge current flowing across the strip generates an Oersted field, which also leads to a frequency shift. Contrary to CISWDS, the Oersted field does not depend on the sign of the wave vector. Therefore, the contribution of each effect to the frequency shift can be distinguished by following the corresponding symmetry in k.

In Fig. 5.15(b) the current induced frequency shift measured for $I_{dc} =$

±15 mA in the Py(15)/Pt(10) bilayer is shown for $k > 0$ and $k < 0$. As one can see from the graph, a positive/negative current decreases/increases the frequencies of both $k > 0$ and $k < 0$ signals, with a slightly higher frequency shift $\delta f_{ij} = f_{ij}(+I) - f_{ij}(-I)$ for ΔL_{21} than for ΔL_{12}. As follows from the symmetry of each contribution to the frequency shift, the Oersted field induced shift can be calculated as $\delta f_{Oe} = (\delta f_{12} + \delta f_{21})/4$ and the Doppler shift can be calculated as $\delta f_{dop} = (\delta f_{12} - \delta f_{21})/4$. The simplest way to determine δf_{ij} is to measure the difference between the curves at $+I$ and $-I$ at the intercept with the horizontal axis, as shown in Fig. 5.15(b). A more accurate way to measure small current induced frequency shifts is based on the extraction of the phase change from differential mutual inductance signals [49].

Fig. 5.16 shows the values of δf_{Oe} and δf_{dop} extracted for different values of electrical current. One observes a linear dependence of both δf_{Oe} and δf_{dop} for $I \leq 30$ mA. For data extracted using the phase shift method, one observes a deviation from linearity for higher current values (filled symbols). This is explained by the fact that this method becomes unapplicable for frequency shifts much larger than the period of the signal, which occurs for large enough current (see Fig. 5.6). By evaluating the frequency shift directly from the curves at $+I$ and $-I$ one observes a linear scaling of δf_{Oe} with *dc* current (open symbols) within all measured range, as expected for an Oersted induced frequency shift. Due to the fact, that the magnitude of Doppler induced frequency shift is much smaller than that induced by the Oersted field ($\delta f_{\mathrm{dop}} = 9$ MHz and $\delta f_{\mathrm{Oe}} = 100$ MHz at $I_{dc} = 50$ mA), the "manual" extraction of δf_{dop} is not very accurate and the corresponding data is not shown. The smallness of the Doppler induced frequency shift justifies the fact that CISWDS was not accounted in the analysis of the resonance frequency shift given in section 5.3.1. Indeed, the f_{res} dependence on $+I$ and $-I$, was decomposed into odd and even functions, where the odd function was attributed to the effect of Oersted field. Strictly speaking, the odd part of the frequency shift also contains a contribution from the current-induced spin-wave Doppler shift. But as we demonstrate here, due to its relatively small magnitude, this contribution could be neglected.

From similar measurements carried out in Ti/Py(t)/Pt films we extract the dependence of δf_{dop} and δf_{Oe} on I_{dc} for each film thickness (Fig. 5.17). As discussed in section 2.3.1, the current induced Doppler shift can be used to determine the degree of spin polarization. Using Eq. (6.3.3) and following the variation of δf_{dop} as a function of the current flowing in Py layer, we deduce values of spin polarization in the range 0.4-0.75. The values are quite similar to the ones found for Py/Al_2O_3 films [50]. This indicates that the electrical

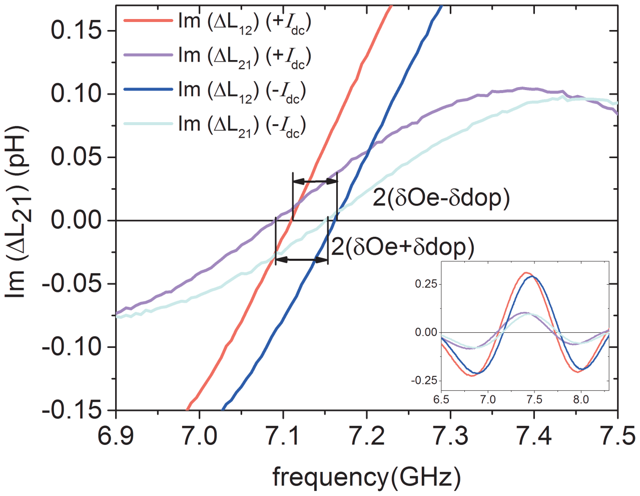

Figure 5.15: Mutual-inductance spectrum measured for Py(15)/Pt(10) film at $\mu_0 H = -36$ mT, $I_{\rm dc} = \pm 15$ mA for both positive and negative wave vectors. The inset shows the whole spectrum and the main panel panel shows its zoomed part, where the frequency shift δf_{ij} induced by the Oersted field and Doppler effect is shown for $k > 0$ and $k < 0$.

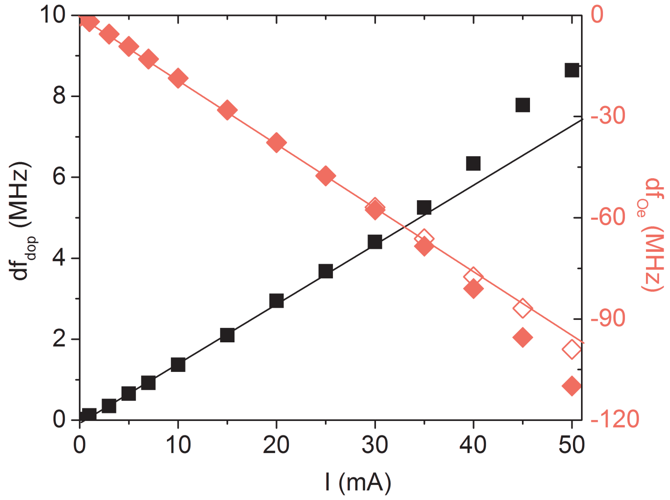

Figure 5.16: Doppler induced- and Oersted field induced frequency shift dependence on the current (squares and diamonds, respectively) measured at $\mu_0 H = -36$ in Py(15)/Pt(10) film. Filled symbols correspond to the values extracted from the phase change using the method described in Appendix A, and open symbols correspond to the values extracted directly from the curves intercept with horizontal axis.

current remains highly spin polarized despite the spin-flip scattering induced by the Pt layer. However, we did not observe any obvious dependence of the spin polarization on the Py thickness. We also extracted a small degree of spin polarization in the Py(4)/Ti film ($P = 0.3$), which may be caused by the important interface effects leading to the depolarization of current at such small thickness.

From the dependence of δf_{Oe} on I_{dc} (Fig. 5.17), we estimate the fraction of current flowing in Py and Pt layers. We calculate the theoretical values of frequency shift by differentiating the Damon-Eshbach dispersion relation with respect to the field [Eq. (5.3.1)] and adjust the coefficient I_{Pt}/I_{dc} to put the theoretical values in agreement with the experimental ones. The dependence of the ratio I_{Pt}/I_{dc} on t_{Py} is plotted in Fig. 5.13 by full-filled symbols. We found the same trend as was deduced from the conductivity measurements, i.e. a gradual decrease of I_{Pt}/I_{dc} by increasing the Py film thickness (half-filled symbols in Fig. 5.13). The larg difference is observed for the 20 nm Py film, where the I_{Pt}/I_{dc} extracted from Oersted field calculations is 2 times smaller than that extracted from conductivity measurement. This divergence may originate from a non-trivial current distribution inside the Py film making more complicated the Oersted field calculation. For the thinnest 4 nm film the Oersted field is even found to be higher than the one expected assuming that all current flows in Pt. Such high value of apparent Oersted field can be explained by an additional source of field-like torque such an out-of-plane STT-induced by SHE. Nevertheless, the Oersted field calculations confirm the value of the fraction of current flowing in both materials deduced from conductance measurements at intermediate film thickness (7-15 nm).

5.4 Conclusion

In conclusion, we have demonstrated that the presence of a heavy metal adjucent to a ferromagnet can induce several spin-orbit phenomena resulting in a significant modification of the propagation of spin waves. On one hand, we have shown that, due to the spin pumping process, the spin wave relaxation rate notably increases. By analyzing the thickness dependence of Γ we have deduced the value of the spin-mixing conductance, which is a characteristic of the FM/NM interface. On the other hand, we have demonstrated that by applying a *dc* current the spin wave relaxation rate can be enhanced if the perpendicularly injected spin current, generated via SHE, possesses a polarization opposite to the local magnetization. By estimating the corre-

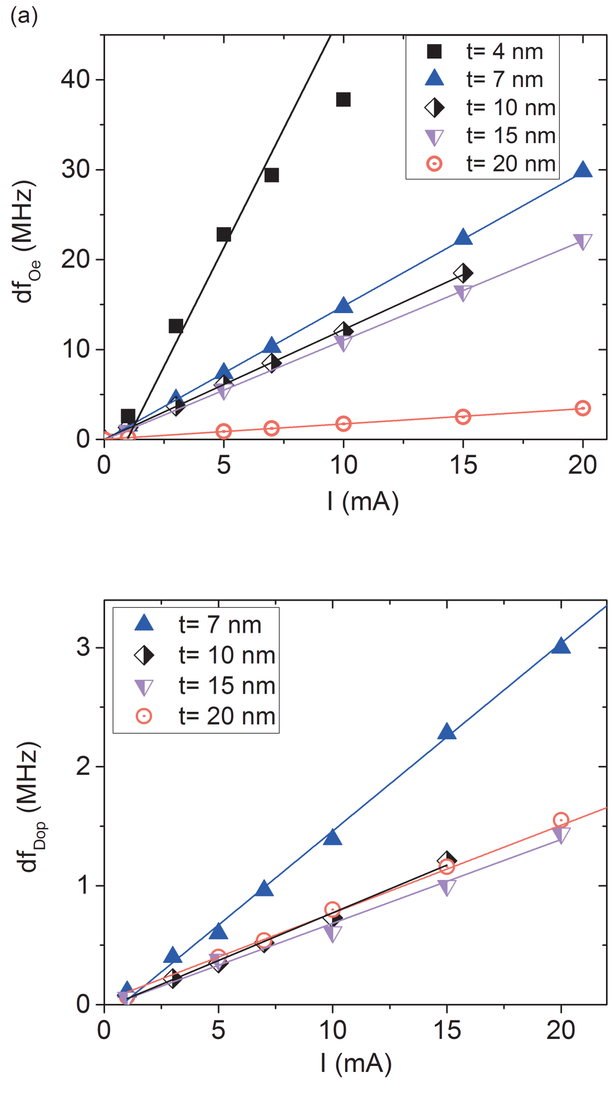

Figure 5.17: (a)Oersted field- and (b) Doppler-induced frequency shift as a function of current. The measurements are carried out in Py(t)/Pt(d) films of the width $w = 20\ \mu\text{m}$ at $\mu_0 H = 36$ mT.

sponding torque and spin Hall angle, we have shown that the spin transfer torque induced by the spin Hall effect modifies the relaxation rate of a finite k spin wave as efficiently as it does in the case of an uniform precession mode. From a more general point of view, we proposed a new technique, which can be used to study the direct spin Hall effect.

Chapter 6

Spin wave propagation and its modification by an electrical current in Fe/MgO films

In this section, we study the spin wave propagation in pure crystalline iron films. As a preliminary, we perform reflection measurements to characterize the magnetic film (sec. 6.1). Based on transmission measurements, we first analyze the frequency non-reciprocity and then extract the propagation parameters of the spin wave, namely attenuation length, group velocity and relaxation rate (sec. 6.2). Finally, by applying a *dc* current along the direction of propagation of spin wave, we perform current-induced Doppler shift measurements in order to extract the degree of spin polarization of the electrical current (sec. 6.3).

6.1 Reflection measurements

The spin waves are studied in 10 and 20 nm thick Fe(001)/MgO films, where the Fe[100] easy axes are rotated by 45° with respect to the MgO[100] axes (Fig. 6.1). Three sets of samples are investigated: Fe(10)/MgO/Ti, Fe(20)/MgO/Ti and Fe(20)/MgO film without Ti capping layer (see stack composition and growth conditions in chapter 3). The measurements are performed for the magnetostatic surface spin wave configuration, i.e. with a magnetic field $\mathbf{H}$ applied in the film perpendicularly to the wave vector k. In order to examine the efficiency of spin wave excitation and to determine the magnetic properties of the Fe films reflection measurements have been performed first. They was carried out for two geometries: when the spin

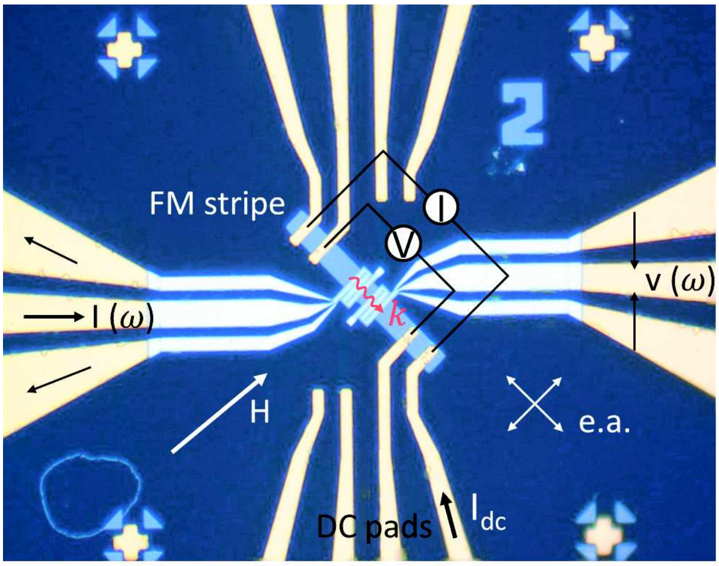

Figure 6.1: Design of the PSWS devices used for investigating spin wave propagation in Fe. The Fe[100] easy axis is rotated by 45° with the respect to MgO[100] axis and the magnetic field is applied along Fe[010] easy axis.

wave propagates along the easy axis [100] (as shown in Fig. 6.1) and along the hard axis [110]. In the latter case, other devices are used, where the Fe stripe is patterned along the Fe[110] axis and the field is still applied in the MSSW configuration ($\mathbf{H} \parallel [1-10]$).

Fig. 6.2(a) and (b) show the imaginary parts of the self-inductance measured at $\mu_0 H = 13.6$ mT ($\mathbf{H} \parallel [010]$) for the 10 nm and 20 nm Fe/MgO/Ti films, respectively. For both thicknesses, one observes two peaks in the frequency range 10-20 GHz, which, according to Fourier transform (see Fig. 3.9), correspond to the MSSW mode with wave vectors of 3.9 μm^{-1} and 1.5 μm^{-1}. We note that the intensity of the main peak k_{M} scales with the film thickness and reaches 30 pH for the 20 nm film. This amplitude is about two times larger than that measured in Py films of the same thickness for the same frequency range. (Note, that at $\mu_0 H = 13.6$ mT, the resonance frequency measured in 20 nm Fe and Py films are 17.5 GHz and 7.8 GHz, respectively, so a field of about 200 mT is needed to obtain a resonance frequency of 15-20 GHz in Py). In the 20 nm Fe film we also observe a low intensity peak at higher frequency, which corresponds to the first perpendicular standing spin wave (PSSW1) mode with an in-plane wave vector of

3.9 μm^{-1} [Fig. 6.2(b)]. This mode has an antisymmetric profile across the film thickness. The peak intensity is 270 times smaller than the intensity of the main peak, which we attribute to the very small overlap between the microwave field (mostly uniform across the film thickness) and PSSW1 mode (mostly antisymmetric across the film thickness). Because of such tiny intensity the PSSW1 mode with lower wave vector k_s was not observed. Since the position of this peak is primarily governed by the exchange energy, which is in the limit of small k scales as $1/t^2$, the PSSW1 mode in the 10 nm Fe film can not be observed due to the limited frequency range of our experimental set-up.

Fig. 6.2(c,d) show the field dependence of the frequencies for the 10 nm and 20 nm film, respectively. The open squares correspond to the MSSW peak with $k_s = 1.5$ μm^{-1} and the filled squares to the MSSW peak with $k_{\mathrm{M}} =$ 3.9 μm^{-1}. Panel (c) and (d) show the measurements carried out in 10 and 20 nm film, respectively. The dependence of the PSSW1 peak frequency on **H** is plotted as diamonds in Fig. 6.2(d). In all cases a monotonous increase of f_{res} with **H** is observed. We fit the MSSW peak frequency using the dispersion relation for the magnetostatic regime [Eq. 1.5.7], where the effective field $H_{\mathrm{eff}} = H - H_d + H_K$ includes both the demagnetizing field H_d associated to the finite width of the strip and the magnetocrystalline cubic anisotropy field H_K [solid lines in Fig. 6.2(c,d)]. From the fitting parameters we extract the magnetic parameters of films, namely $\gamma/(2\pi) = 29$ GHz/T, $\mu_0 M_s = 2.15$ T, and $\mu_0 H_K = 58$ mT, corresponding to $K_c = 5\cdot 10^4$ J/m^3, which are the same for the 10 and 20 nm thick films. The effective magnetization $\mu_0 M_{eff}$ slightly differs for different film thickness and equals 1.9 T and 2.08 T for the 10 and 20 nm films, respectively. From the difference between the saturation and the effective magnetization, we deduce an out-of-plane uniaxial anisotropy, which is attributed to the surface anisotropy. For the 10 nm and 20 nm film we obtain $\sum K_s = 2$ mJ/m^2 and $\sum K_s = 1.2$ mJ/m^2, respectively.

Contrary to MSSW, the PSSW1 is strongly influenced by the exchange interaction. With that respect, the high frequency dispersion branch is fitted using the dipole-exchange dispersion relation for PSSW1 (Eq.[1.6.22]), where the exchange term $\Lambda^2 k^2$ can be neglected due to its smallness (of the order of 10^{-12}), and only the out-of-plane quantization exchange term $(\Lambda\pi/t)^2$ is kept:

$$\begin{aligned} f_1^2 = (\gamma\mu_0)^2[H_{\mathrm{eff}}^2 &+ H_{\mathrm{eff}} M_{\mathrm{eff}}(2(\Lambda\pi/t)^2 + 1) \\ &+ M_s M_{\mathrm{eff}}(P_{11} - P_{11}^2 + (\Lambda\pi/t)^2 + ((\Lambda\pi/t)^2)^2)] \end{aligned} \tag{6.1.1}$$

Using the values of magnetic parameters defined above we obtain a value of exchange length $\Lambda = 3.1$ nm that corresponds to an exchange constant $A = 19.1$ pJ/m^2. Note that the result of this analytical formula in excellent agreement with result from numerical calculations [55].

To illustrate directly the influence of the cubic anisotropy, we performed the same measurements for devices containing a strip aligned along a Fe[110] in-plane hard axis with the magnetic field applied along the other in-plane hard axis Fe[1-10] [see sketch in the inset of Fig.6.2(c)]. The field dependence of the peak frequencies measured for both k_s and k_M in 10 and 20 nm films are shown in Fig. 6.2(c) and (d) by open and filled hexagons, respectively. In this case, when increasing the field, the resonance frequency starts to decrease up to a field of about 58 mT with a subsequent increase for higher field. The observed decrease of f_{res} is associated with the rotation of the magnetization vector $\mathbf{M}$ to the field direction, where the minimum of the spectrum indicates the value of the field needed to align $\mathbf{M}$ along $\mathbf{H}$, which is the value of the cubic anisotropy field H_{K}. Numerical calculations of the MSSW frequency performed for this hard axis geometry with the magnetic parameters indicated above are in excellent agreement with the measured data [solid lines in Fig. 6.2(c,d)]. This confirms our determination of the cubic magnetic anisotropy. Note that all the magnetic parameters determined for our Fe thin films are almost the same as those reported for the bulk material [59, 20].

6.2 Transmission measurements

In the next step, we perform transmission measurements in order to analyze the propagating properties of the spin waves. The measurements were carried out for the devices in which the strip is along an easy axis. In Fig. 6.3(a) the mutual-inductance spectra measured at $\mu_0 H = 58$ mT in a Fe(20)/MgO/Ti device is shown. From the envelop of the signal one distinguishes two main peaks. The high and low frequency packets of oscillation correspond to the main and secondary spin-wave wave vector, respectively. The high amplitude signal ΔL_{21} depicts the wave moving in one direction ($k > 0$) and the low amplitude signal ΔL_{12} corresponds to the opposite wave ($k < 0$). A first important observation which can be done from these spectra, is the remarkable frequency non-reciprocity.

6.2.1 Frequency non-reciprocity

In Fig. 6.3(b) and (c) the frequency shifts between the imaginary parts of the inductance signals ΔL_{12} and ΔL_{21} are shown for $k_M = 3.9$ μm^{-1} and

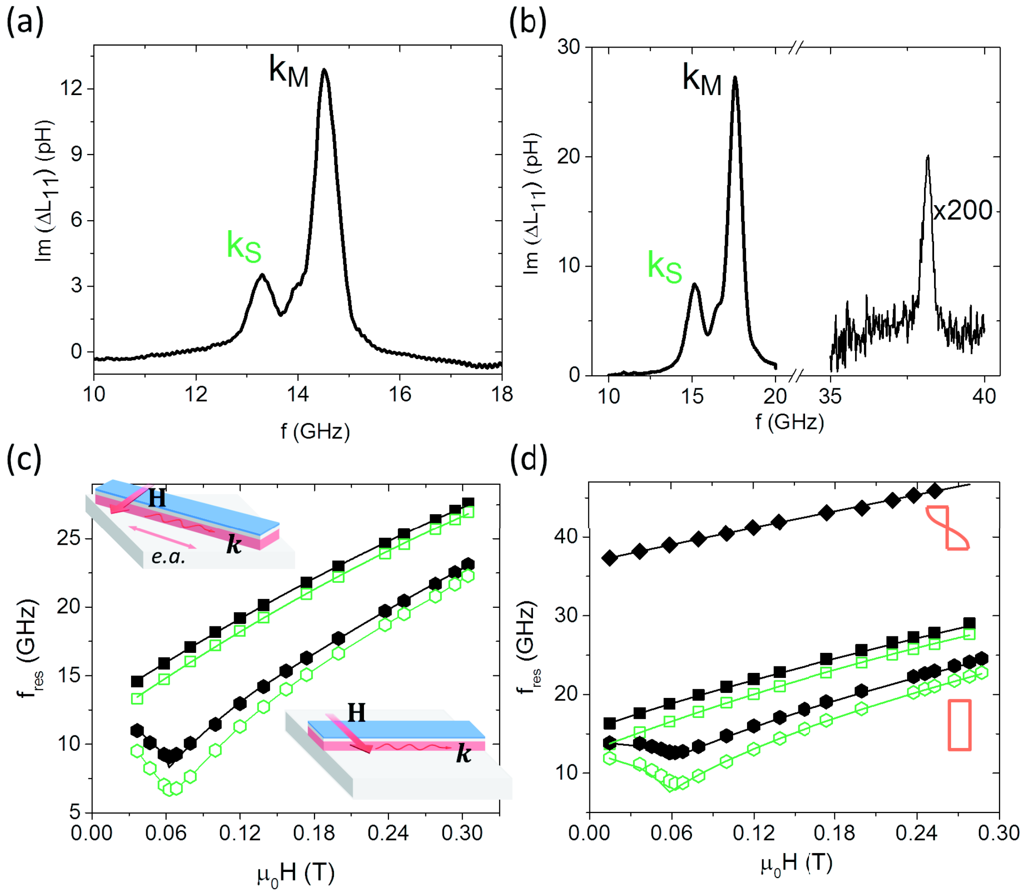

Figure 6.2: Imaginary part of the self-inductance signal measured at $\mu_0 H =$ 36 mT with $\mathbf{H} \parallel [010]$ for 10 nm (a) and 20 nm (b) Fe stips with $w = 10$ μm. The two peaks at low frequency correspond to MSSW mode k_s and k_M and the peak at high frequency in panel (b) corresponds to the PSSW1 mode. (c)-(d) Resonance frequency as a function of H for the 10 and 20 nm film, respectively. Full and open symbols correspond to the main and secondary MSSW peak, respectively. Diamonds are for the PSSW1 mode. Peak frequencies marked by squares and hexagons represent the measurements carried out for different devices with ($k \parallel [100]$, $\mathbf{H} \parallel [010]$) and ($k \parallel [110]$, $\mathbf{H} \parallel [1-10]$, respectively [see sketches in panel (c)].

$k_s = 1.5\ \mu\text{m}^{-1}$, respectively. We measure a frequency shift $f_{\text{NR}} = f_{21} - f_{12} =$ 84 MHz for k_M and 35 MHz for k_s. We note that the observed frequency shift is much larger than that measured in Py films for the same thickness and wave vectors. By following the frequency non-reciprocity as a function of magnetic field, we observe a slight decrease of f_{NR} with increasing H for both wave vectors [symbols in Fig. 6.4(a)]. The same measurements performed in the 10 nm Fe film show that the values of the frequency non-reciprocity for k_M and k_s are almost two times smaller than the respective values obtained in the 20 nm film [Fig. 6.4(b)]. At 10 nm no clear field dependence is observed.

In Fig. 6.5 the frequency non-reciprocity is plotted as a function of the wave vector k for the 10 and 20 nm Fe films capped by Ti (filled circles and diamonds, respectively). As was discussed in chapter 4, in a magnetic film sandwiched between two oxide layers a frequency non-reciprocity can occur as a result of different surface anisotropy at the top and bottom surfaces. We thus account for the observed values of f_{NR} by means of the dipole-exchange theory, in which asymmetric surface anisotropies are included as a perturbation (see section4.1.2). Using formula (4.1.7), we deduce a difference in surface anisotropy $\Delta K_s = 0.7\ \text{mJ/m}^2$ and $1\ \text{mJ/m}^2$ for the 10 and 20 nm films, respectively. Numerical calculations confirm these values of ΔK_s. Moreover, the numerical simulations [solid lines in Fig. 6.4] are in good agreement with the H-dependent behavior obtained experimentally: a pronounced decrease with increasing magnetic field for the 20 nm film (with a more rapid decrease for k_M than for k_s), and a weak dependence on magnetic field for the 10 nm. From the estimation of the difference and the sum of the top and bottom surface anisotropies, we can determine the uniaxial anisotropy of individual interfaces, which is found to be high for the bottom surface ($K_s^{\text{bot}} = 0.9 - 1.4\ \text{mJ/m}^2$) and small for the top surface ($K_s^{\text{top}} = -0.1 - 0.7\ \text{mJ/m}^2$).

Interestingly, the frequency non-reciprocity measured in the 20 nm Fe film covered by a single MgO layer without Ti capping layer was found to be significantly larger than that observed in Fe(20)/MgO/Ti films (open diamonds in Fig. 6.5). For a wave vector of $3.8\ \mu\text{m}^{-1}$ the frequency shift between two counter-propagating spin waves reaches 120 MHz and for $k_s =$ $1.55\ \mu\text{m}^{-1}$ is 40 MHz. The difference of the f_{NR} measured in films of the same thickness is attributed to the different state of the top interface, which induce different surface anisotropy. The observed f_{NR} corresponds to $\Delta K_s =$ $1.4\ \text{mJ/m}^2$.

The different surface anisotropy for the two nominally identical interfaces in MgO/Fe/MgO is attributed to the partial oxidation of interfacial Fe

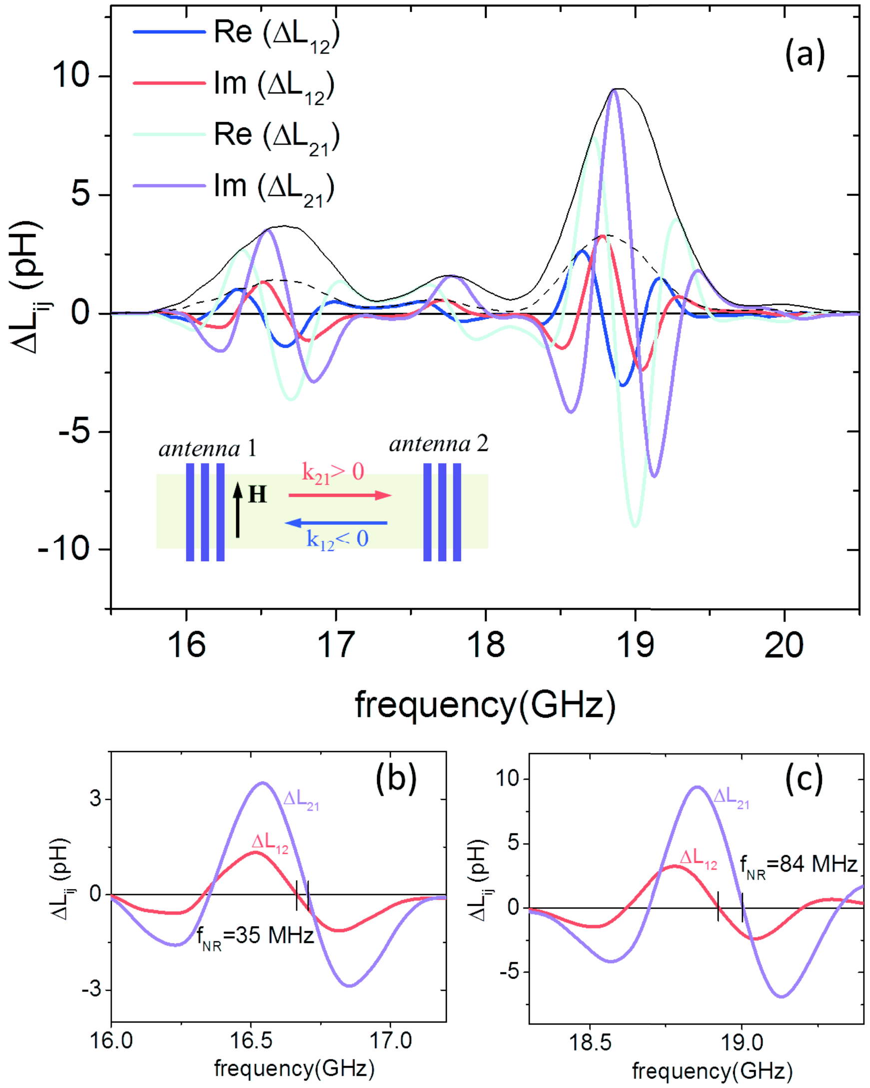

Figure 6.3: (a) Mutual-inductance spectrum measured at $\mu_0 H = 58$ mT in the Fe(20)/MgO/Ti strip with $w = 10$ μm and $D = 4$ μm. (b) and (c) show the frequency shifts between the imaginary parts of the inductance signals ΔL_{12} and ΔL_{21} for $k_M = 3.9$ μm^{-1} and $k_s = 1.5$ μm^{-1}, respectively.

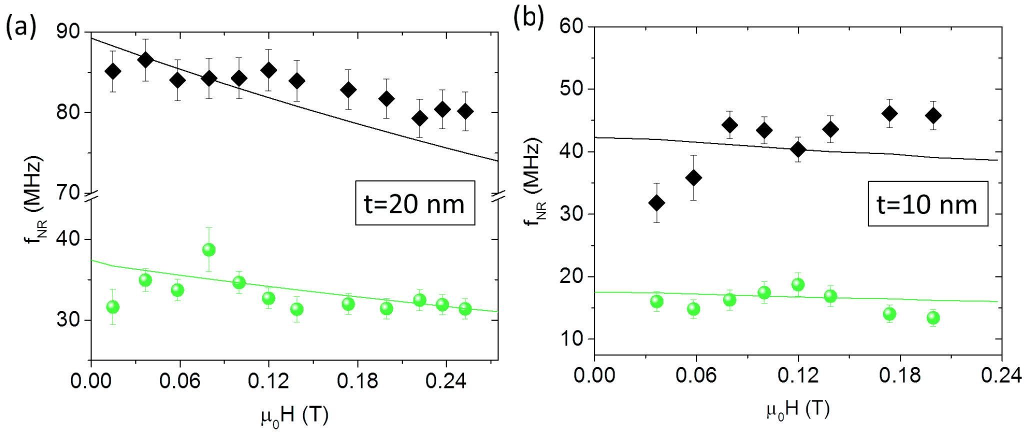

Figure 6.4: Frequency non-reciprocity as a function of magnetic field measured in 20 nm (a) and 10 nm (b) thick films for a wave vector of 3.8 μm^{-1} (diamonds) and 1.55 μm^{-1} (circles). Solid lines are the numerical calculation done for the following parameters: $\gamma/(2\pi) = 29$ GHz/T, $\mu M_s = 2.15$ T, $A = 19.1$ pJ/m^2, $K_c = 5 \cdot 10^4$ J/m^3. In (a) $\Delta K_s = 1$ mJ/m^2 and $\sum K_s = 0.8$ mJ/m^2. In (b) $\Delta K_s = 0.7$ mJ/m^2 and $\sum K_s = 2.1$ mJ/m^2.

atoms, which is not the same for Fe/MgO and MgO/Fe interfaces. Indeed, an experimental study by Mossbauer spectroscopy [90] showed, that the two interfaces are not equivalent. In particular, at the MgO/Fe interface (Fe is deposited on MgO) a larger amount of interfacial Fe atoms is oxidized (86%) than at the Fe/MgO interface (63%). The ab-initio calculations reported in [52] showed an influence of the surface oxidation on the perpendicular magnetic anisotropy. The oxidation process is known to depend on the growing conditions, such as for example annealing temperature [139, 100]. Since MgO is quite sensitive to environmental and thermal degradation, in the samples without protective Ti layer one may expect a hydroxydation of the top MgO layer, that can also cause a chemical or structural change at the top Fe/MgO interfaces.

These structural and chemical effects might therefore explain the results we obtain by probing the magnetic asymmetries with the help of propagating spin waves.

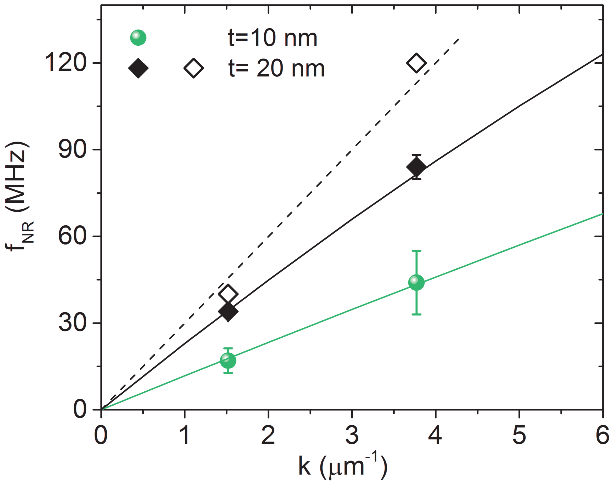

Figure 6.5: Frequency non-reciprocity as a function of wave vector. The circles are the values measured in the Fe(10)/MgO/Ti film, the full and open diamonds are for the Fe(20)/MgO/Ti and Fe(20)/MgO films, respectively. The solid lines are the values simulated with the parameters given in the caption of Fig. 6.4 for Fe(t)/MgO/Ti films. For Fe(20)/MgO, $\Delta K_s = 1.4$ mJ/m^2 is used.

6.2.2 Propagating characteristics of spin waves in a Fe film

Let us now determine the spin wave propagation parameters in the Fe(20)/MgO/Ti film. As in the study of Py/Pt films, the propagation was analyzed by using devices with different distances D between antennas and by comparing the transmitted signal. In Fig. 6.6(a-c) we plot the imaginary part of the mutual-inductance signal corresponding to a wave vector of 3.8 μm^{-1} for the devices with $D = 2, 3, 4$ μm, respectively. The measured waveform is characterized by two parameters: the period of the oscillation [the half of which is marked by a solid arrow in Fig. 6.6(a-c)] and the maximum amplitude $|L_{21}|^{\text{max}}$. By increasing the distance D one observes a decrease of both signal period and maximum amplitude. As was discussed in section 5.2, the period of the signal can be identified to the inverse of the group delay time $\tau = (D + D_0)/v_g$, where D_0 is an offset accounting for the finite width of the antenna. By plotting the dependence of the propagation time τ as a function of D we extract the value of the group velocity v_g [circles in Fig. 6.6(d)]. The amplitude of the signal is related to the spin wave attenuation length L_{att} as $A = A_0 exp(-(D + D_0)/L_{\text{att}})$, where A is the maximum amplitude of the transmitted signal normalized by the amplitude of the reflected ones. To evaluate the attenuation length we thus plot $-ln(A)$ as a function of D. The slope of the linear fit corresponds to $1/L_{\text{att}}$ [squares in Fig. 6.6(d)]. We can also evaluate the spin wave relaxation rate Γ from the dependence of $-ln(A)$ on τ [diamonds in Fig. 6.6(d)]. Therefore, based on mutual-inductance signals obtained for devices with different D, we directly determine the values of L_{att}, v_g and Γ for a given magnetic field.

Repeating the same measurements for different values of external magnetic field we analyze the H-dependence of the main spin wave propagation characteristics. Let us first comment on the group velocity, which is plotted in Fig. 6.7 for $k_M = 3.8$ μm^{-1} (top panel) and $k_s = 1.5$ μm^{-1} (bottom panel) for both propagation directions ($k > 0$ and $k < 0$). One observes a monotonous decrease of v_g with increasing H, which reproduce well the behavior expected from theory (solid lines). However, the calculated v_g for both k_M and k_s are about 15% larger than the measured ones and we do not have any explanation for this behaviour at the moment. As one can see from both measured and calculated values, the group velocity is larger for the small wave vector ($v_g = 7.5$ km/s at $\mu_0 H = 14$ mT) than for the high one ($v_g = 5$ km/s). Due to the large frequency nonreciprocity measured in this samples, the group velocities of the counter-propagating spin waves are expected to be slightly different, but because of the smallness in the difference between $v_g(k > 0)$ and $v_g(k > 0)$, it is rather difficult to identify it

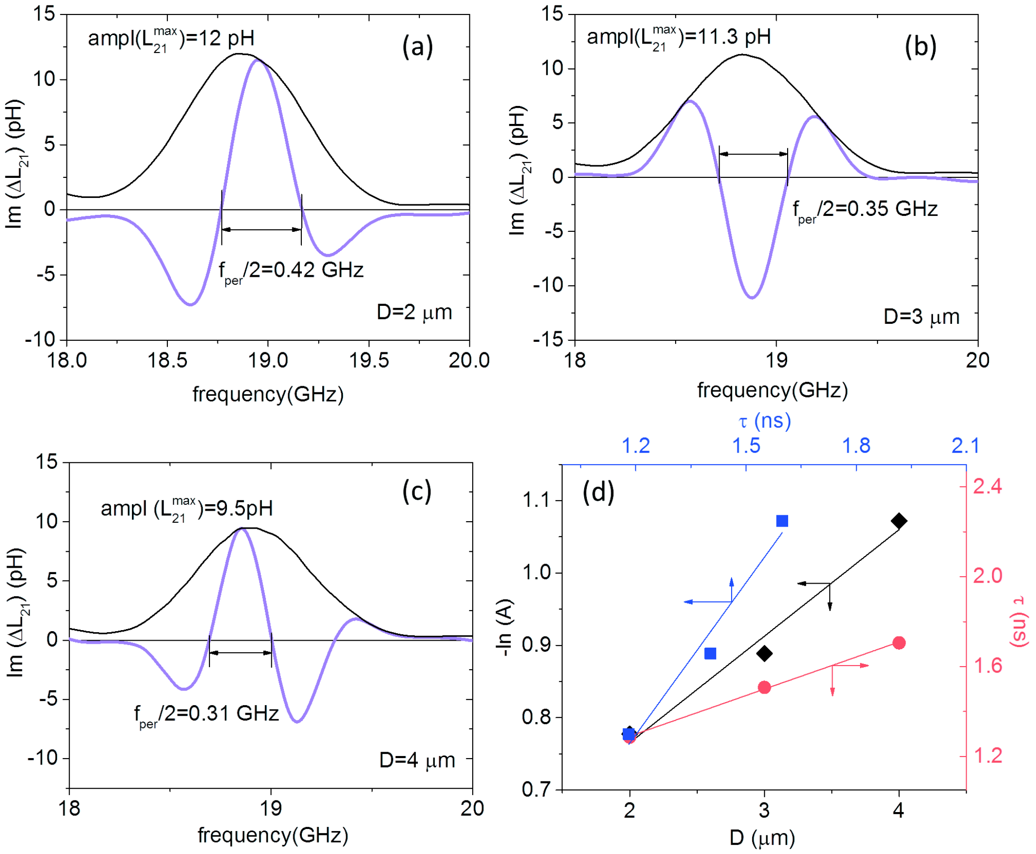

Figure 6.6: Imaginary part of the mutual-inductance spectra measured in the Fe(20)/MgO/Ti strip with $w = 10\ \mu$m in devices with an edge-to-edge distance $D = 2\mu$m (a), $D = 3\ \mu$m (b), $D = 4\mu$m (c) at a field $\mu_0 H =$ 58 mT. (d) Dependence of the logarithm of the normalized amplitude A (black diamonds) and of the propagation time τ (red circles) on the distance; dependence of $-ln(A)$ on τ (blue squares)

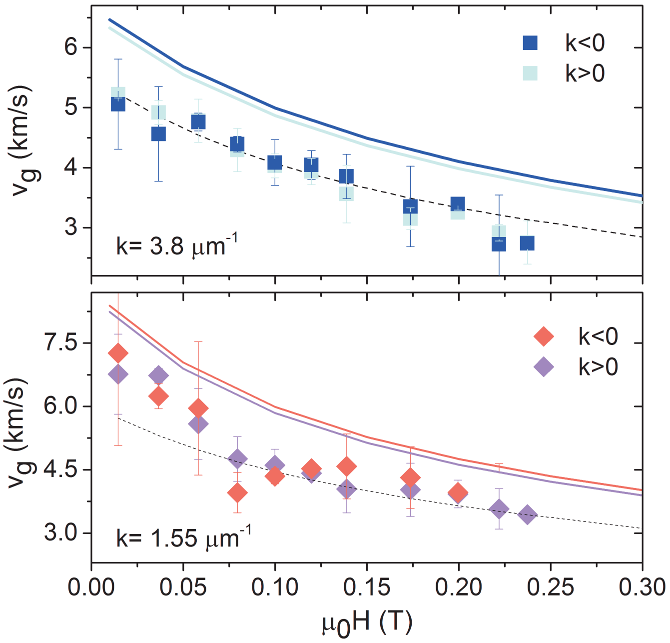

Figure 6.7: Dependence of the group velocity on the magnetic field for the main (top panel) and secondary (bottom panel) SW wave vectors measured for Fe(20)/MgO/Ti film. Symbols are the experimental values extracted for both propagation directions $k > 0$ and $k < 0$ and the dashed lines are polynomial fit guided for the eyes. Solid lines are the theoretical values calculated for $k > 0$ and $k < 0$ with the parameters given in the caption of Fig. 6.4

experimentally.

In Fig. 6.8(a) the effective damping parameter is plotted as a function of magnetic field for both wave vectors. The values of damping factor were extracted from the measured Γ by using the relation appropriate for the surface spin wave geometry, namely $\Gamma = \alpha_{\text{eff}}(\omega_0 + \omega_M/2)$. One can see, that α_{eff} decreases with increasing H and reaches an asymptotic value of 0.0025 at high field. Because the intrinsic Gilbert damping of metals which arises mainly due to the interaction of spin waves with conduction electrons [114, 37], is frequency independent, the observed dependence of α_{eff} on H is attributed to the presence of extrinsic damping due to sample defects. This is supported by the broadband ferromagnetic resonance measurements performed on a plain film of the same composition [1]. In Fig. 6.8(b) the FMR linewidth $\mu_0 \Delta H$ is plotted as a function of resonance frequency. By fitting this data using the expression $\mu_0 \Delta H = \mu_0 \Delta H_0 + \alpha \frac{2\pi f}{\gamma}$, we find an intrinsic damping constant $\alpha = 0.0025$ and an inhomogeneous broadening $\mu_0 \Delta H_0 = 0.9$ mT. The high field extrapolate of the SW effective damping is therefore in good agreement with the damping evaluated by FMR, which is also in line with the values measured in bulk Fe [12, 132] and in good quality epitaxial films [112, 131]. The increase of effective damping observed at low field could have the same origin as the observed inhomogeneous broadening extracted from FMR, which can be attributed the influence of the lattice defects such as atomic network dislocations [112, 138]. In this in-plane configuration, such defects are likely to give rise to two magnon scattering [138, 73]. According to the theory of this process [102, 16, 73], a spin wave mode can scatter off the lattice defects into degenerate spin wave mode with higher wave vector leading to an additional relaxation process, which enhances the measured relaxation rate/linewidth.

In metallic film, eddy current can also contribute to an increase of damping, which scales quadratically with the film thickness as [112]

$$G_{\text{eddy}} = \frac{\sigma}{12}(4\pi M_s \gamma)^2 (\frac{t}{c})^2. \tag{6.2.1}$$

Here, G_{eddy} is relaxation rate in cgs units (Hz), $\sigma = 9.11 \cdot 10^{16}$ Hz is the conductivity and c is the speed of light in vacuum. For the 20 nm film the magnitude of the eddy current relaxation rate is about 5 MHz, which is much smaller than the effective relaxation rate of 80 MHz converted from α_{eff} measurements as $G_{\text{eff}} = \alpha_{\text{eff}} \gamma M_s$. The influence of eddy current can be therefore neglected in our case.

Finally, in Fig. 6.9 we plot the dependence of the attenuation length (symbols) on magnetic field. The data show a nearly constant values of L_{att} of about 6 μm and 9 μm for $k_M = 3.8$ μm^{-1} and $k_s = 1.55$ μm^{-1}, respectively. These results differ from the theoretical values (dashed lines) calculated using the expression $L_{\text{att}} = v_g T_2$ with a constant value of damping of 0.0025. The observed dependence of L_{att} on H can be understood by taking into account a decrease of v_g and a field dependence of α_{eff} (dashed lines in Fig. 6.7 and Fig. 6.8, respectively). A similar situation was observed in the 10 nm Fe films, where the attenuation length keeps almost constant at low field with the values of about 3 μm and 5 μm for $k_M = 3.8$ μm^{-1} and $k_s = 1.55$ μm^{-1}, respectively. As in the case of the 20 nm film, these values are almost two times smaller than the theoretically expected ones.

Despite this deviation, the attenuation are quite high compared to other

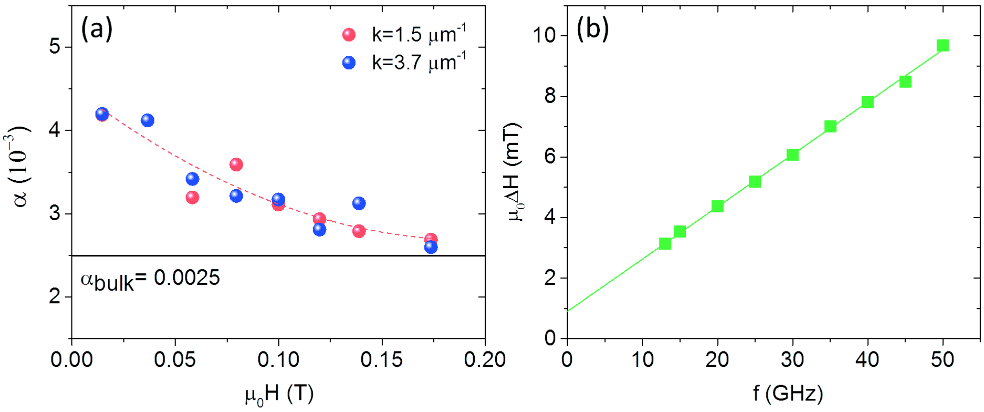

Figure 6.8: (a) Dependence of the effective damping on the magnetic field for the same 20 nm film. Dashed line is a polynomial fit showing the decrease of α_{eff} with H approaching to the bulk value of 0.0025. (b) Dependence of FMR linewidth (full width with at half maximum) on the frequency measured on a similar film by broadband ferromagnetic resonance.

materials. For example, for a wave vector of 3.8 μm^{-1} and a film thickness of 20 nm, the attenuation length found to be of the order of 1 μm in both Py ($\alpha = 0,008$) and YIG ($\alpha = 0,0004$) for a frequency of 18 GHz. Note, to reach such a frequency, the external field should be increased to 0.3 and 0.6 T, respectively.

To summarize, spin waves propagating in a single crystal iron film induces inductive signals with stronger amplitude and much higher frequency as compared to Permalloy films for the same conditions. The damping factor measured in our thin films is close to the value measured in bulk Fe at high frequency and increases by about 35% at low frequency. This value of damping is of the same order than the one measured in Co-based Heusler alloys [115] and almost 3 times smaller than that of Py films. Moreover, due to the high saturation magnetization of Fe, the spin wave group velocity in this material is found to be much higher comparing to other material. Due to this low damping and high group velocity, spin waves can propagate in Fe films over long distances (ten micrometers).

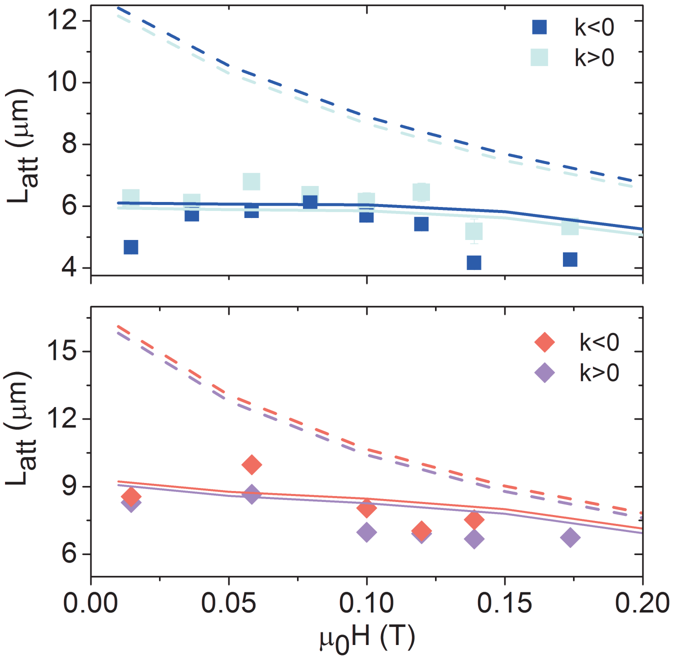

Figure 6.9: Dependence of the attenuation length on the magnetic field for main (top panel) and secondary (bottom panel) SW wave vectors for the same 20 nm Fe film. Symbols are the experimental values for $k > 0$ and $k < 0$. Dashed lines are the theoretical values calculated using the expression $L_{\rm att} = v_g T_2$ with a constant value of damping of 0.0025. Solid lines are the values calculated using the same expression but accounting a field dependent increase of $\alpha_{\rm eff}$ and v_g. Calculations were done for the parameters noted in caption of Fig. 6.4

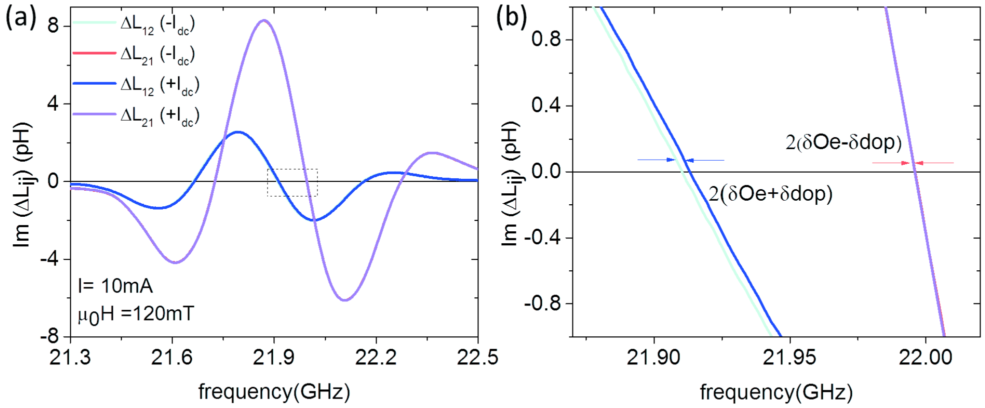

Figure 6.10: (a) Mutual-inductance spectra measured on the 20 nm film with $D = 4\ \mu$m and $k_M = 3.8\ \mu\text{m}^{-1}$ under an applied field $\mu_0 H = 120$ mT and a DC electrical current $I_{\text{dc}} = \pm 10$ mA. Blue and cyan lines are the signals measured at $+I_{\text{dc}}$ and $-I_{\text{dc}}$ for $k < 0$, respectively, and the magenta and red lines represent respectively the signal at $+I_{\text{dc}}$ and $-I_{\text{dc}}$ for $k > 0$. (b) A zoom of waveforms allowing to visualize the current-induced frequency shifts.

6.3 Spin polarized electrical transport

6.3.1 Current induced spin wave Doppler shift measurements

In order to investigate the spin polarized electrical transport in our Fe films, we perform current induced Doppler shift measurements. In the configuration sketched in Fig. 6.1, the DC current flows along Fe[100] axis and the magnetic field is along the Fe[010] axis. As was already mentioned in section 2.3.1, flowing through the continuously variable magnetization distribution of the spin wave, the conduction electrons interact adiabatically with the local magnetization via spin transfer torque. The result of this interaction is a spin wave frequency shift $\delta\omega = uk$, where $u = P\mu_{\text{B}}J/(eM_s)$ is related to the degree of spin polarization of the electrical current $P = (J_\uparrow - J_\downarrow)/(J_\uparrow + J_\downarrow)$.

Fig. 6.10(a) shows the imaginary part of the mutual-inductance measured for the main MSSW peak for $k > 0$ (ΔL_{21}) and $k < 0$ (ΔL_{12}) under a *dc* current of ±10 mA in the Fe(20)/MgO/Ti film. We measure the frequency shift by comparing the frequency for positive and negative current at the curve intersection with the x-axis. As one can see from Fig. 6.10(b), where a zoomed part of the graph (a) is plotted, the frequency shift between the $\Delta L_{12}(+I_{\rm dc})$ (blue line) and $\Delta L_{12}(-I_{\rm dc})$ (cyan line) differs from the frequency shift between $\Delta L_{21}(+I_{\rm dc})$ (magenta line) and $\Delta L_{21}(-I_{\rm dc})$ (red line) (for the latter case the frequency shift is too small to be visible on this scale). As already explained in section 5.3.5, this difference is due to the combination of the Doppler shift with an additional contribution due to the Oersted field, which has a distinct symmetry in k. Indeed, the Doppler effect leads to a frequency shift $+\delta f_{\rm dop}$ for the current moving in the direction opposite to the spin wave propagation direction and to a frequency shift $-\delta f_{\rm dop}$ for the inverse situation. On the contrary, the Oersted field, which does not average strictly to zero due to some asymmetries across a film thicknesses (e.g. different probabilities of diffuse electron scattering on the two film surfaces) results in the same current-induced frequency shift for both spin wave propagation directions. Therefore, the frequency shift for $k > 0$ is $\delta f_{21} = 2(\delta f_{\rm Oe} - \delta f_{\rm dop})$, while the frequency shift for $k < 0$ is $\delta f_{12} = 2(\delta f_{\rm Oe} + \delta f_{\rm dop})$. The Doppler shift and Oersted field contributions can be therefore calculated as

$$\delta f_{\rm dop} = (\delta f_{21} - \delta f_{12})/4 \tag{6.3.1}$$

$$\delta f_{\rm Oe} = (\delta f_{21} + \delta f_{12})/4 \tag{6.3.2}$$

In Fig. 6.11(a),(b) the Oersted field- and Doppler induced frequency shifts are plotted for the 10 and 20 nm films. Both contributions are found to be of the order of few MHz. Following the variation of $\delta f_{dop}/k$ as a function of applied *dc* current [Fig. 6.11(b)], we can estimate the degree of spin polarization using the relation

$$\delta f_{dop} = \frac{\mu_0 \mu_{\rm B}}{2\pi e \mu_0 M_s} \frac{I}{wt} kP, \tag{6.3.3}$$

where $\mu_0\mu_{\rm B}/(\pi e) = 23 \cdot 10^{-12}$ m^3.T.A^{-1}.s^{-1}, and w and t are the width and the thickness of the ferromagnetic stripe. From the slope of the fit and by using the geometric and magnetic parameters of the strip we can deduce the degree of spin polarization. For both film thicknesses and for wave vectors k_M and k_s we obtain a value of $P = 0.83 \pm 0.05$. Note that a very similar value was also deduced from the current-induced shift for an external field of different magnitude and sign, which is an indication that artifacts have been correctly accounted for by our extraction procedure. The nonreciprocal Oersted field induced frequency shift, which arises due to the asymmetric spin-wave modal profile [51], and which about one order of magnitude smaller that the reciprocal Oersted field, was also taken into account.

The value P = 0.83 we measure on our Fe film at room temperature (RT) can be compared to values determined using the same technique on different materials. The spin polarization measured in Py are P=0.5-0.7 [135, 50, 117] and P=0.85-0.95 for the Heusler alloy $\mathrm{CoFe}_{1-x}\mathrm{Ge}_x$ [145]. In these two examples the large spin-polarizations are attributed to a strong spin-asymmetry of the electron scattering induced by the random alloy disorder [88, 9]. However, in a pure metal such alloy disorder scattering is absent. With this respect, the high value of spin polarization has to be related to a more intrinsic source of electron scattering. Before analyzing its origin, we will first review the values of spin polarization measured for Fe using other techniques, insisting on the definition of spin polarization relevant in each case.

6.3.2 Degree of spin polarization of the electrical current in Fe

In spin polarized photoemission experiments, the quantity of emitted electrons depends primarily on the density of state [61]. The spin-polarization measured is therefore that of the electron density

$$P_N = \frac{N_\uparrow(E_F) - N_\downarrow(E_F)}{N_\uparrow(E_F) + N_\downarrow(E_F)}. \tag{6.3.4}$$

The reported values for Fe spread in a range between −0.8 and −0.2 showing the domination of minority electrons at the Fermi energy [25, 26, 75]. P_N can be calculated numerically using ab-initio methods, which yield the values of about 0.4-0.5 [130, 146].

Another experimental method to probe the degree of spin polarization is to use Andreev reflection measurements [24, 123]. In such experiments the current flowing through the interface between a ferromagnet (FM) and a superconductor (S) is measured: when an electron reflects from the FM/S interface as a hole it creates a Cooper pair flowing into the superconductor. For interface S/normal metal [where $N_\uparrow(E_F) = N_\downarrow(E_F)$], each up electron will combines with one down electron increasing the conductance by a fraction of two. Since in a ferromagnet the number of spin-up and spin-down electrons is not the same, the electrons incoming into the superconductor will not necessarily find a partner to form the pair with, thus reducing or enhancing the conductance depending on the ratio $N_\downarrow(E_F)/N_\uparrow(E_F)$. Depending on the size of the point contact two transport regimes are distinguished. If the size of the point is smaller that the electron mean free path, the electron flows ballistically through the contact. In such a case, the conductivity for each channel depends on the average of the product of DOS and Fermi

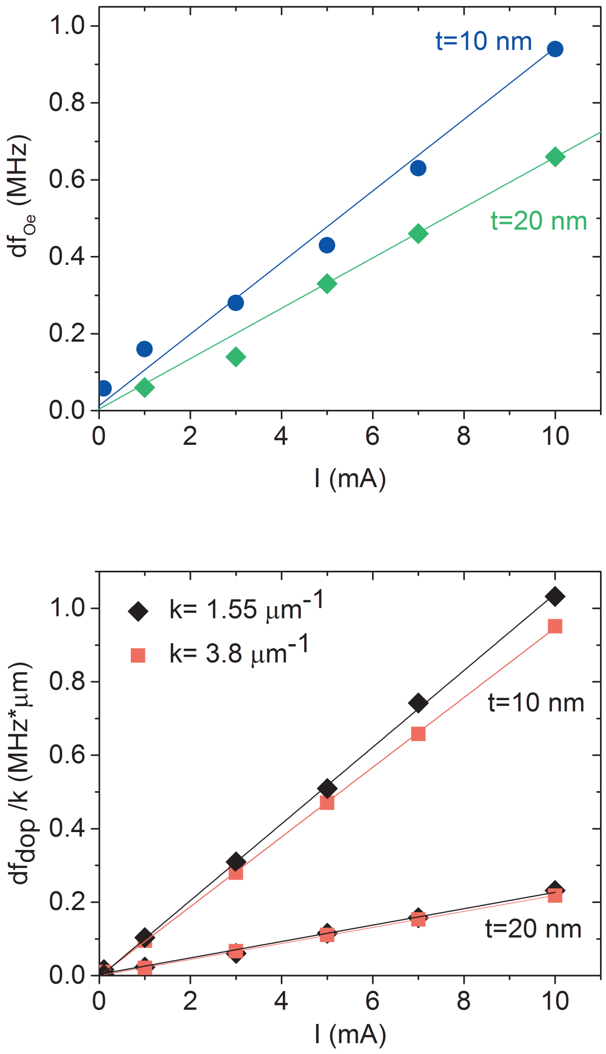

Figure 6.11: Oersted field (a) and Doppler (b) induced frequency shift as a function of DC current measured in Fe(10)/MgO/Ti and Fe(20)/MgO/Ti films with $w = 10$ μm at $\mu_0 H = 36$ mT and $\mu_0 H = 120$ mT, respectively. In (b) the red squares corresponds to the main peak and the black diamonds are for the secondary peak. The measured frequency are normalized to the wave vector.

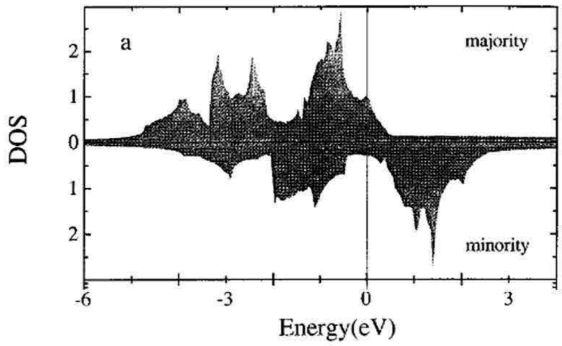

Figure 6.12: Electronic density of state of bcc iron. Figure from Ref. [130]

velocity [87], and the spin-polarization is then written as:

$$P_{Nv} = \frac{\langle N(E_F)v\rangle_\uparrow - \langle N(E_F)v\rangle_\downarrow}{\langle N(E_F)v\rangle_\uparrow + \langle N(E_F)v\rangle_\downarrow}. \tag{6.3.5}$$

In the case when the size of the point contact is bigger that the electron mean free path, the electron travels diffusively through the contact. For this regime the conductance is proportional to the square of the Fermi velocity. Assuming a spin-independent electron relaxation time, the spin-polarization is written as

$$P_{Nv^2} = \frac{\langle N(E_F)v^2\rangle_\uparrow - \langle N(E_F)v^2\rangle_\downarrow}{\langle N(E_F)v^2\rangle_\uparrow + \langle N(E_F)v^2\rangle_\downarrow}. \tag{6.3.6}$$

The degree of spin polarization deduced from Andreev reflection measurements in ballistic regime is $P = 0.45$ [122, 123]. It is clear that for materials with different Fermi velocity for up and down electrons the polarization P_N, P_{Nv} and P_{Nv^2} will differ. The difference in velocity can be related with the band character near the Fermi energy, because *s*-electrons have much higher velocity than *d* ones [146].

6.3.3 Spin dependent diffusive electrical transport in Fe

In propagating spin wave spectroscopy, the relevant degree of spin polarization that of the electrical current is the diffusive regime, as described in section 2.2.1. Using the expression of conductivity derived from the classical Boltzmann transport theory one gets [3]:

$$P = \frac{\langle N(E_F)v^2\rangle_\uparrow\tau_\uparrow - \langle N(E_F)v^2\rangle_\downarrow\tau_\downarrow}{\langle N(E_F)v^2\rangle_\uparrow\tau_\uparrow + \langle N(E_F)v^2\rangle_\downarrow\tau_\downarrow}, \tag{6.3.7}$$

where $\tau_{\uparrow(\downarrow)}$ is the relaxation time for spin up (down), and $\langle N(E_F)v^2\rangle_\sigma$ is defined as [87]

$$\langle N(E_F)v^2\rangle_\sigma = \frac{1}{(2\pi)^3}\sum_\alpha \int v_{k\alpha\sigma} dS_{\mathrm{F}}. \tag{6.3.8}$$

Here, $v_{k\alpha\sigma}$ is the velocity of an electron in the band α with the wave vector k, and dS_{F} is the area of the Fermi surface. Therefore, in addition to band structure $[N(E_F)v^2]$, we recognize a direct influence of the electron scattering process trough $\tau_{\uparrow(\downarrow)}$. Among the different spin-dependent scattering processes listed in Ref. [50], we can consider only the contribution of the thermal disorder, namely that of the phonons (thermal disorder of the lattice) and the magnons (thermal disorder of the local magnetization), as well as the contribution from the surface scattering. Indeed, both random alloy disorder and grain boundary scattering can be neglected because we use a single-crystal pure material.

Consider first the electron scattering by the film surface. From magnetotransport measurements of spin-valve structures (F-N-F), it was shown that the change in the magnetoresistance is related to the different mean-free paths of majority and minority electrons [32, 47]. It was found that in Fe the mean-free paths of majority and minority electrons are of the order of 1-2 nm [47], which is much smaller our film thickness. Therefore, the contribution of the surface scattering to resistivity can be neglected.

In Ref. [106], the electron-magnon scattering was studied by performing high field (up to 40 T) magnetoresistance measurements in large temperature lange (4 to 500 K). A high magnetic field leads to an upward energy shift of spin waves and thus reduces the electron-magnon collision. In Fig. 6.13 the magnon resistivity dependence on the magnetic field for different temperature is shown. One can note that this resistivity reduces when the magnetic field increases and when the temperature decreases. From these measurements, authors estimated the contribution of spin-flip scattering via magnon to be 2 $\mu\Omega cm$, which is about 15% of the total resistivity.

We are left with the contribution of electron-phonon scattering, which seems to be dominant at room temperature. To calculate the spin-dependent electron-phonon interaction a theoretical approach based on the transport spectral function $\alpha^2_{\mathrm{tr}}F(w)$ is used. It was fist proposed by Allen in the superconductivity theory [4] and then implemented in ab-initio calculations by Savrasov et al. [111]. The function $\alpha^2_{\mathrm{tr}}F(w)$ is the phonon density of states weighted by the scattering matrix, which describes the scattering of an electron from k to k' state on a phonon with frequency ω [2]. It is directly

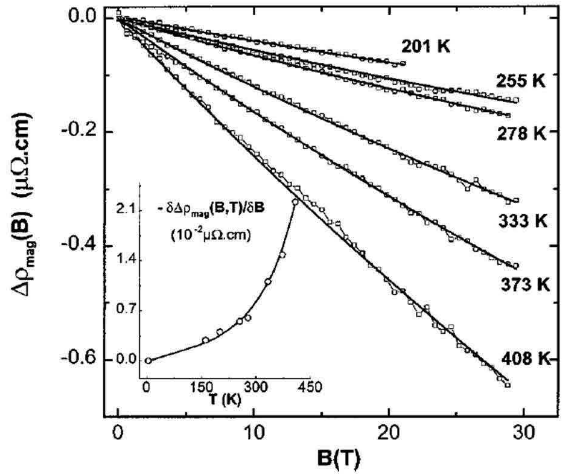

Figure 6.13: Magnon resistivity dependence on the applied pulsed magnetic filed measured at different temperature for Fe(80 nm)/MgO films. Figure from Ref. [106]

related to the resistivity as a function of temperature:

$$\rho(T) = \frac{\pi \Omega k_{\mathrm{B}} T}{N(E_{\mathrm{F}})\langle v_x^2 \rangle} \int_0^{\infty} \frac{d\omega}{\omega} \frac{x^2}{\sinh^2 x} \alpha_{\mathrm{tr}}^2 F(w) \tag{6.3.9}$$

where $x = \omega/(2k_{\mathrm{B}}T)$, $\langle v_x^2 \rangle$ is the average square of the x component of the Fermi velocity. The integral over the transport spectral function defines the transport electron-phonon coupling constant λ_{tr}. For a high enough temperature, Eq. (6.3.9) can be rewritten as

$$\rho(T) = \frac{\pi \Omega k_{\mathrm{B}} T}{N(E_{\mathrm{F}})\langle v_x^2 \rangle} \lambda_{\mathrm{tr}}, \tag{6.3.10}$$

where λ_{tr} is the transport electron-phonon coupling constant, obtained by integrating the transport spectral function. The spin-dependent electron-phonon coupling constants for ferromagnetic Fe were calculated in Ref. [133], as $\lambda_{\mathrm{tr}\uparrow} = 0.102$ and $\lambda_{\mathrm{tr}\downarrow} = 0.199$. The difference between the two electron-phonon coupling can be explained by the electronic state at the Fermi energy: since the majority electrons lie in the end of the d band, the electron-phonon coupling is weaker comparing with that of minority electrons located in the middle of the d band. Form the Eq. (6.3.10), one can extract the spin polarization as

$$P = \frac{\langle N(E_F)v^2\rangle_\uparrow/\lambda_{\mathrm{tr},\uparrow} - \langle N(E_F)v^2\rangle_\downarrow/\lambda_{\mathrm{tr},\downarrow}}{\langle N(E_F)v^2\rangle_\uparrow/\lambda_{\mathrm{tr},\uparrow} + \langle N(E_F)v^2\rangle_\downarrow/\lambda_{\mathrm{tr},\downarrow}}. \tag{6.3.11}$$

Combining the ratios $\lambda_{\mathrm{tr},\uparrow}/\lambda_{\mathrm{tr},\downarrow}$ and $\langle N(E_F)v^2\rangle_\uparrow/\langle N(E_F)v^2\rangle_\downarrow$ [146], we find a spin polarization of the current of the order of 0.6, which is quite close to the value we measure.

We can thus conclude, that in Fe at room temperature, the phonon contribution to the electron resistivity is quite strongly spin-polarized, while the magnon contribution remains moderate.

6.4 Conclusion

We have shown that a single-crystal iron film is a suitable medium for the propagation of spin waves. Thank to the large saturation magnetization and small damping factor, the spin waves propagate in Fe with a large attenuation length and a relatively high velocity. These results qualify Fe as a very promising candidate for future magnon devices operating at high frequency, since the propagation distance is a crucial factor in information transport and signal processing. We have also shown that diffusive electron transport in iron at room temperature is strongly spin-polarized, which is attributed to a significant spin-asymmetry of the electron-phonon coupling. This indicates that, despite the absence of spin-polarized impurity or surface scattering, a pure material such as iron can be efficient for the generation of spin currents.

General conclusion

In this thesis, the spin dynamics and its modification by a spin current has been studied in different magnetic systems, namely Py/Al_2O_3, Py/Pt and Fe/MgO films, using propagating spin wave spectroscopy. The aim of this study was to find the optimal conditions and/or materials for efficient spin wave propagation and spin current generation.

By analyzing the spin wave propagation in both Py-based and Fe-based devices, we have observed a much more efficient spin wave generation and propagation in crystalline iron film than in Py. The reason is the small Gilbert damping of Fe, which enables to propagate the spin wave over long distances, and its high saturation magnetization, which translates into a high group velocity. Moreover, the high degree of spin polarization of the electrical current measured in Fe indicates its good ability to generate a spin-polarized current. However, the origin of such high spin polarization remains unclear and requires additional studies.

The measurements of spin dynamics in Py/Pt devices enables us to study different spin-orbit related phenomena, such as interfacial Dzyaloshinskii-Moria interaction, spin pumping and spin transfer torque driven by spin Hall effect. In chapter 4, the strength of iDMI interaction was studied by measuring the frequency non-reciprocity of counter-propagating spin waves. However, we have shown, that in moderately thin magnetic films the frequency non-reciprocity is actually due to the combined influence of iDMI and magnetic asymmetry across a film thickness. Using a theoretical model developed in sec. 4.1, we could quantify the magnitude of both effects.

We have also shown that the spin wave can be efficiently used to probe different types of spin transfer torque arising when an electrical current is injected into a FM/HM bilayer. We distinguish two types of STT: (i) the interfacial STT, which arises at the FM/HM interface due to the transfer of spin momentum from the conduction electron to local magnetization (SHE-STT) and the volume STT (current-induced spin wave Doppler shift). We have demonstrated, that the effect of interfacial STT is to modify the spin wave relaxation rate, while the effect of adiabatic volume STT is to modify the resonance frequency. From the current-induced change of the relaxation rate we could extract the spin Hall angle, which is the quantity governed by the efficiency of the spin transfer torque induced by the spin Hall effect. Our study shows that the SHE-STT is as efficient for a non-uniform excitation as for an uniform one, and can thus be used to control electrically the spin wave propagation. From another point of view, our studies on Py/Pt bilayers shows that the spin wave can be used as a very accurate probe to study different spin-orbit related phenomena.

Perspectives

Electrical control of damping in Py/Pt devices

From the practical point of view, the electrical control of spin wave damping in FM/HM films by using spin Hall induced spin transfer torque remains a challenging goal. The main problem arising for such systems is the damping enhancement due to spin pumping. Indeed, before reducing the natural Gilbert damping of the FM by SHE-STT, one should compensate the increase of α due to spin pumping. Recently, a full compensation of damping was reported for YIG/Pt films, enabling one to reach auto-oscillation regime [53, 22]. For Py/Pt films the threshold current is quite high and could be reached only in strongly confined geometries [30] (the limitation of the current density which can be injected in Py/Pt, is due to the strong heating of the samples). Therefore, one could try to engineer the interface using suitable metal interlayer in order to limit the magnetization losses but maintain an efficient SHE-STT at a reasonable current density [97].

Spin polarization of electrical current in Fe/MgO films

Performing current-induced Doppler shift measurements in Fe/MgO films we found an unexpectedly high degree of spin-polarization of the electrical current of 0.83 at room temperature. This high value of P is attributed to a strong spin-dependence of electrons scattering on phonons. As was discussed in sec. 2.2.1, the scattering mechanism in the metal can be analyzed by following the resistivity change of a binary alloy with temperature, where the total resistivity is a combination of the resistivity of the pure metal (which is assumed to be temperature dependent) and the resistivity due to the impurities (which is temperature independent). In the same spirit we propose to perform temperature dependent Doppler shift measurements in $\mathrm{Fe}_{1-x}\mathrm{V}_x$/MgO films. Measuring the deviation from Matthiessen's rule within each channel we should be able to quantify the contribution of both electron-phonon and electron-magnon scattering. Preliminary results indicate a room temperature degree of spin polarization of 0.55 and 0.4 for $x = 2$ and 8%, respectively. These measurements should be extended to low temperature to proceed further with the analysis of the electron scattering mechanisms

Appendix A

In Fig. 6.14 and 6.15 the dependencies of the frequency on the magnetic field are plotted for Py(40)/Al_2O_3 and for Py(t)/Pt(d) films, where $t = 4-20$ nm and $d = 5, 10$ nm, respectively. In the magnetostatic regime, this dependency is given by the following expression:

$$f^2 = (\gamma\mu_0)^2[(H_{\text{eff}}^2 + H_{\text{eff}}M_{\text{eff}} + \frac{M_s M_{\text{eff}}}{4}(1 - e^{-2kt})]. \tag{6.4.1}$$

The field $H_{\text{eff}} = H - H_d$ is the effective field accountin for the in-plane demagnetizing field $H_d = \frac{2t}{\pi w}M_s$, $M_{\text{eff}} = M_s - H_K$ is the effective magnetization, which accounts for an uniaxial surface anisotropy $H_K = 2\sum K_s/(\mu_0 M_s t)$, and M_s is the saturation magnetization.

We fit the dependence of the frequency on the field by using a second order polynomial fit:

$$f^2 = A(\mu_0 H_{\text{eff}})^2 + B(\mu_0 H\text{eff}) + C. \tag{6.4.2}$$

From the fitting parameters A, B and C we extract the magnetic parameters of the film:

- the gyromagnetic ration $\gamma/(2\pi)$ is given by the square root of A,
- the effective magnetization is defined as $\mu_0 M_{\text{eff}} = B/A$,
- the saturation magnetization is deduced from the relation $\mu_0 M_s \mu_0 M_{\text{eff}}(1 - e^{-2kt}) = 4C/A$.

For Py(t)/Al_2O_3 and Py(t)/Pt(d) films we found the similar parameters: $\gamma/(2\pi) = 30 \pm 1$ GHz/T, $\mu_0 M_s = 1.02 - 0.92$, $\mu_0 M_{\text{eff}} = 0.99 - 0.83$ T for $t = 40 - 6$ nm, and $\sum K_s = 0.1 \pm 0.1$ mJ/m^2.

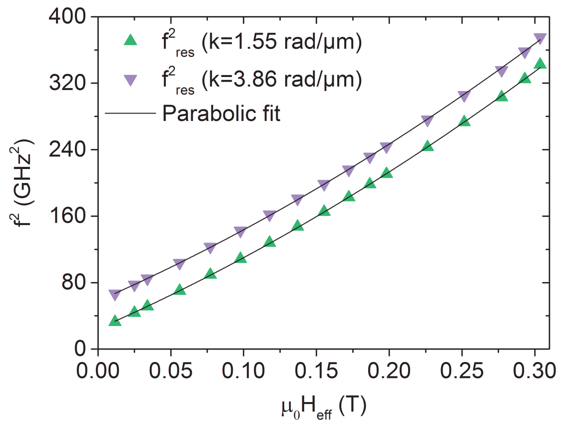

Figure 6.14: The dependence of the spin wave frequency on the magnetic field for $k_1 = 3.86\ \mu\mathrm{m}^{-1}$ (triangles down) and $k_2 = 1.55\ \mu\mathrm{m}^{-1}$ (triangles up) for Py(40)/Al_2O_3. The lines are second order polynomial fits.

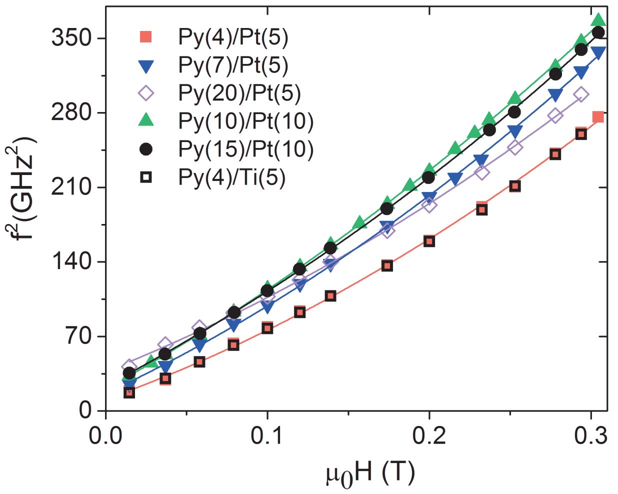

Figure 6.15: Dependence of the frequency on the magnetic field measured in Py(t)/Pt film with t=4-20 nm and in Py(4)/Ti films for $k = 7\ \mu\mathrm{m}^{-1}$

Appendix B

Par analogie avec l'électronique traditionnelle, où la charge de l'électron est utilisée pour transférer et stocker information, l'électronique de spin cherche à utiliser le moment cinétique de l'électron, appelé spin, comme un degré de liberté supplémentaire pour réaliser des dispositifs de mémoire et de logique. Deux possibilités pour coder et transporter l'information sont d'utiliser les ondes de spin et le courant polarisé en spin. La propagation des ondes de spin dans un matériau ferromagnétique (FM) est caractérisée par la vitesse de propagation et la distance sur laquelle elles peuvent se propager, cette distance étant limitée par leur facteur d'amortissement. La recherche de matériaux avec un faible coefficient d'amortissement et une vitesse de propagation élevée est donc d'un intérêt particulier. Les paramètres caractéristiques des ondes propagatives dépendent fortement du matériau utilisé et de nombreux facteurs externes, tels que la direction et la valeur du champ magnétique appliqué ou un éventuel courant électrique continu. En particulier, pour la configuration d'ondes de spin de surface, où l'aimantation est dans le plan et perpendiculaire au vecteur d'onde, un comportement non-réciproque est observé (l'amplitude et la fréquence ne sont pas les mêmes pour les ondes de spin qui se propagent dans les sens inverse). En injectant un courant électrique dans un matériau magnétique un autre décalage de la fréquence de l'onde de spin dépendant de la direction du courant se présente. Ce décalage est dû au transfert de spin entre les électrons de conduction et l'aimantation dynamique, et il permet de mesurer la polarisation en spin du courant (effet Doppler d'onde de spin [136]).

Par ailleurs, les ondes de spin peuvent être considérablement influencées par d'autre effets liés au couplage spin-orbite, tels que l'interaction Dzyaloshinskii-Moriya (DMI) et le transfert de spin induit par l'effet Hall de spin (SHE-STT, pour Spin Hall induced spin transfer torque), lesquels apparaissent quand le couche ferromagnétique est en contact direct avec le métal lourd (ML). Dans tels système FM/ML le DMI provoque un décalage en fréquence entre les ondes propageant dans les sens inverses [10] et le SHE-STT cause une modification du taux de relaxation des ondes de spin propagatives [29]. Dans le cadre de ma thèse, j'étudie l'influence de ces différents effets sur la propagation des ondes de spin, en utilisant différent systèmes magnétiques tels que les bicouches permalloy (Py=$Ni_{80}Fe_{20}$)/Al_2O_3, Py/Pt et Fe/MgO, où les système Py/Al_2O_3 et Py/Pt sont utilisés pour étudier les effets lié au couplage spin-orbite, et le système Fe/MgO est utilisé pour sonder la capacité de ce matériau de propager les ondes de spin et le courant polarisé en spin. Pour réaliser ces études, une technique expérimentale appelée spectroscopie d'ondes de spin propagatives (PSWS pour Propagating Spin Wave Spectroscopy) a été utilisée [136]. Dans cette technique, les ondes de spin sont excitées et détectées par couplage inductif à des antennes fabriquées sur le ruban ferromagnétique (Fig. 6.16). Nous mesurons ainsi deux types de signal: un signal réfléchis généré par une variation d'inductance sur l'antenne émettrice (auto-inductance) et un signal transmis généré par une variation d'inductance sur l'antenne réceptrice (inductance mutuelle). Le signal réfléchi porte une information sur l'efficacité de l'excitation des ondes de spin, tandis que le signal transmis donne une information sur l'efficacité de la propagation des ondes de spin.

Propagation non-réciproque d'ondes de spin

Nous avons d'abord étudié la propagation non-réciproque d'onde de spin. C'est une particularité des ondes de spin de surface qui se manifeste par différentes amplitudes et fréquences quand deux ondes de spin se propagent en sens inverse. Tandis que la non-réciprocité en amplitude, qui est liée au couplage entre le champ d'excitation et l'aimantation dynamique, est bien connue, l'origine de la non-réciprocité en fréquence était mal comprise. Pour étudier l'origine de la non-réciprocité en fréquence nous avons effectué une série de mesures dans des couches Al_2O_3(21 nm)/Py(t)/Al_2O_3(5 nm) pour différentes épaisseurs de couche de Py ($t = 6 - 40$ nm) et pour différentes valeurs de vecteur d'onde de l'onde de spin k.

Les résultats expérimentaux ont montré la forte dépendance de la non-réciprocité en fréquence en fonction de vecteur d'onde et de l'épaisseur [voir la Fig. 6.17(a)] [40]. Les différences de fréquence mesurées ont pu être attribuées à la combinaison de deux facteurs : une non-réciprocité intrinsèque du profil du mode et une asymétrie des propriétés du matériau ferromagnétique, en l'occurrence une différence d'anisotropie magnétique de surface entre la face supérieure et la face inférieure du film. La non-réciprocité du profil du mode est due à l'asymétrie du champ dipolaire généré par l'aimantation dynamique, qui se traduit par une localisation du mode près de différentes

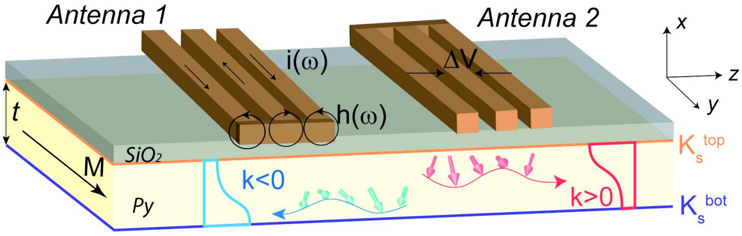

Figure 6.16: Une représentation schématique de dispositif de spectroscopie d'onde de spin. Des profils de mode d'ondes de spin asymmetriques à travers l'epaisseur du film sont montré pour $k > 0$ et $k < 0$.

surfaces pour des ondes se propageant dans des sens opposés (Fig. 6.16). Par conséquence, l'onde ayant une amplitude plus grande près de la face supérieure est plus sensible à l'anisotropie de surface de la face supérieure, tandis que l'onde localisée près de la face inférieure est influencée davantage par l'anisotropie de surface de la face inférieure, ce qui amène à une différence de fréquence pour des ondes se propageant en sens inverse. En utilisant la théorie des ondes de spin dans le régime dipôle-échange et en introduisant l'anisotropie de surface comme une perturbation, nous avons développé un modèle permettant de prédire la valeur de la différence de fréquence f_{NR} en fonction des constantes d'anisotropie de surfac K_s^{bot} et K_s^{top}:

$$f_{\mathrm{NR}} \simeq \frac{8\gamma}{\pi^3} \frac{K_{\mathrm{s}}^{\mathrm{bot}} - K_{\mathrm{s}}^{\mathrm{top}}}{M_{\mathrm{s}}} \frac{k}{1 + \frac{\Lambda^2 \pi^2}{t^2}}, \tag{6.4.3}$$

où γ est le rapport gyromagnétique, M_s est l'aimantation à saturation et Λ est la longueur d'échange. Cette formule asymptotique indique une dépendance linéaire de la non-réciprocité en fréquence en fonction du vecteur d'onde et une dépendance presque quadratique en fonction de l'épaisseur du film. Ce modèle théorique décrit bien les résultats expérimentaux obtenus pour différentes épaisseurs du film et différents vecteurs d'onde [lignes continues sur la Fig. 6.17(a)].

Dans un deuxième temps, pour étudier l'effet de DMI sur le spectre d'onde de spin, nous avons analysé la propagation des onde de spin dans les bicouches Py(t)/Pt, avec $t = 4 - 20$ nm, où la présence d'un métal lourd avec un fort couplage spin-orbite induit une forte interaction d'échange antisymétrique appelée interaction Dzyaloshinskii-Moriya interfaciale (iDMI). La présence de iDMI amène un décalage de fréquence entre les ondes de spin qui se propagent dans les sens inverses qui peut être calculé comme

$$f_{NR} = [\omega(-k) - \omega(+k)]/(2\pi) = \frac{2\gamma D_s}{\pi M_s t} k. \tag{6.4.4}$$

où D_s est la constante iDMI.

Nous avons mesuré une forte non-réciprocité en fréquence induite par iDMI dans les couches ultra-mince qui se réduit considérablement en augmentant l'épaisseur du film et change même de signe pour le film le plus épais [symboles sur la Fig. 6.17(b)]. Cette dépendance observée dévie du modèle théorique de iDMI qui prédit une décroissance de la non-réciprocité en fréquence en 1/t [courbe rouge pointillée sur la Fig. 6.17(b)] [10]. Cette déviation est liée à la présence de l'asymétrie magnétique à travers l'épaisseur du film qui induit la non-réciprocité additionnelle. En utilisant Py/Al_2O_3 comme un système de référence et en utilisant le modèle théorique développé, nous avons extrait l'amplitude des deux effets (la différence d'anisotropie de surface $\Delta K_s = K_s^{bot} - K_s^{top} = -0.1$ mJ/m^2 et une constante iDMI $D_s = 0.3$ pJ/m qui est une caractéristique de l'interface FM/ML) et donc évalué la contribution de ces deux effets dans la non-réciprocité en fréquence. Nous avons montré que dans les couches très minces la contribution dominante est due à iDMI, tandis qu'en augmentant l'épaisseur du film l'anisotropie de surface entre en jeu [courbe vert sur la Fig. 6.17(b)]: elle compense totalement la non-réciprocité en fréquence induit par la DMI pour $t = 15$ nm (courbe noire) et induit un changement du signe de la non-réciprocité pour $t = 20$ nm.

Ainsi, notre étude sur la propagation des ondes de spin dans les matériaux Py/Al_2O_3 et Py/Pt permet de comprendre comment la non-réciprocité en fréquence est influencée par les différents effets surfaciques pouvant coexister sur une même interface et d'évaluer l'amplitude de ces effets.

Amplification des ondes de spin

La propagation des ondes de spin dans un métal ferromagnétique est limitée par le facteur d'amortissement qui, si il est trop élevé, se traduit par une courte distance de propagation. Un moyen pour diminuer le facteur d'amortissement (et par conséquence augmenter la distance de la propagation) est le modifier par le transfert de spin induit par l'effet Hall de spin. Cet effet se présente dans une bicouche FM/ML pendant qu'un courant électrique est appliqué: en circulant dans un métal lourd avec un fort couplage spin-orbite un courant longitudinal de charges se transforme en un courant transverse de spin (effet Hall de spin) [34]. Une fois transféré dans une couche ferromagnétique adjacente, ce courant de spin interagit avec l'aimantation

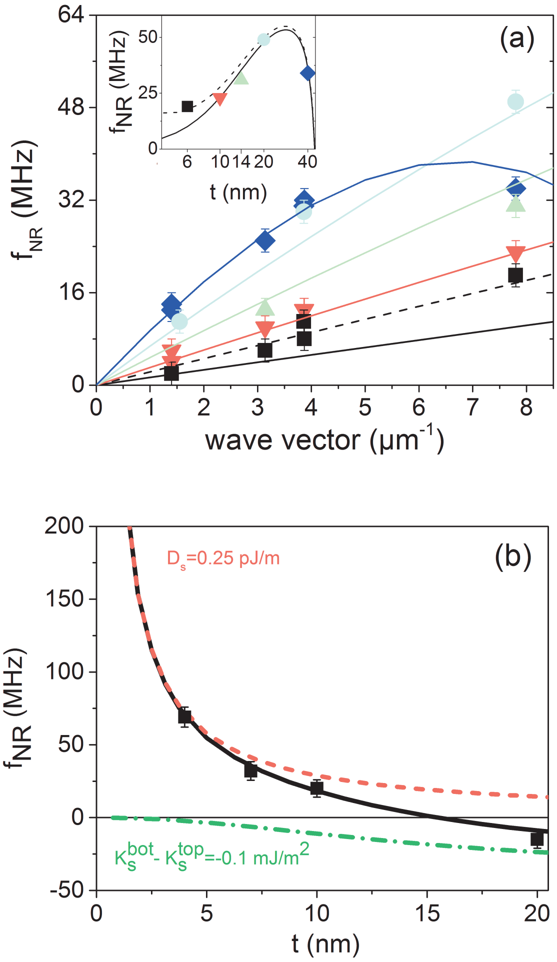

Figure 6.17: (a) Non-réciprocité en fréquence mesurée dans des films Al_2O_3/Py(t)/Al_2O_3 en fonction du vecteur d'onde pour t = 6 nm (carrés), t = 10 nm (triangles vers le bas), t = 14 nm (triangles vers le haut), t = 20 nm (cercles) et t = 40 nm (diamants). Les lignes continues montrent les résultats théoriques. La ligne pointillé est obtenue en prenant en compte iDMI. (b) Les points noirs montrent la non-réciprocité en fréquence mesurée en fonction de l'épaisseur de Py dans des bicouches Py(t)/Pt. Courbes rouge et verte montrent la non-réciprocité en fréquence induite par iDMI et par la différence d'anisotropie de surface, respectivement. La courbe noire est obtenue en additionnant les contributions des deux effets.

dynamique en modifiant le temps de relaxation de la précession [79]. Nous avons étudié l'influence d'un tel courant de spin sur la propagation des ondes de spin dans des couches de Py(t)/Pt, avec $t = 4 - 20$ nm, à l'aide de la technique PSWS.

Tout d'abord, le taux de relaxation Γ ainsi que la vitesse de groupe v_g et la longueur d'atténuation L_{att} ont été analysés sans application de courant DC et en utilisant des dispositifs avec different distances entre antennes. La figure 6.18(a) montre une spectre d'inductance mutuelle mesuré dans Py(15)/Pt(10) avec une largeur de ruban $w = 10$ μm et des distances entre antennes $D = 1, 3, 5$ μm. Comme on peut le voir, l'amplitude et la période du signal transmis décroissent rapidement lorsque la distance entre antennes augmente. Ces deux quantités sont reliées aux paramètres essentiels de propagation L_{att}, v_g et Γ par les relations

$$\begin{aligned} A &= exp(-D_{\mathrm{eff}}/L_{\mathrm{att}}) \\ A &= exp(-\Gamma\tau) \\ \tau &= D_{\mathrm{eff}}/v_g \end{aligned} \tag{6.4.5}$$

où $D_{\mathrm{eff}} = D_0 + D$, D_0 étant la largeur effective de l'antenne, τ est le temps de propagation de l'onde de spin et $A = \Delta L_{21}/(\Delta L_{11}\Delta L_{22})$ est l'amplitude maximale de l'inductance mutuelle normalisée à celle de l'auto-inductance. Ainsi, à courant nul nous extrayons la valeur de L_{att} en traçant -ln(A) en fonction de D, la valeur du v_g en traçant τ en fonction de D, et la valeur du Γ en traçant -ln(A) en fonction de τ [39]. Nous avons trouvé une diminution de L_{att} et v_g avec la diminution de l'épaisseur du film magnétique, comme est prévu de la relation de dispersion. Nous avons également observé une augmentation de Γ en $1/t$ qui est due au pompage de spin. Le pompage de spin apparait à l'interface FM/ML. Il est induit par la précession d'aimantation dans le métal ferromagnétique et se manifeste par un transfert de spin de l'aimantation locale aux électrons de conduction dans le métal lourd. Ce transfert de spin est accompagné par une perte de moment angulaire et donc par l'augmentation du taux de relaxation. En analysant la dépendance de Γ en fonction du l'epaisseur du couche magnétique t, nous avons extrait l'efficacité du pompage de spin définie par la conductance avec mélange de spin $G_{\mathrm{eff}}^{\uparrow\downarrow} = 3 \cdot 10^{19}$ m^{-2}. Cette valeur est comparable avec les valeurs déduites par autre techniques expérimentales [144, 97, 7] et par les calculs numériques [81].

En appliquant le courant DC nous avons observé une augmentation ou une diminution de l'amplitude et de la période du signal de propagation d'onde de spin selon la direction du courant (un exemple d'un spectre d'inductance mutuelle modifié par le courant dc dans Py(15)/Pt(10) est montré dans l'insert de la Fig. 6.18). En réalisant la même analyse qu'à courant nul, nous extrayons la variation du temps de relaxation, de la vitesse de groupe et de la longueur d'atténuation. En soustrayant l'effet Joule qui amène à une variation additionnelle de L_{att} et v_g, nous observons une dépendance linéaire du taux de relaxation en fonction de courant [Fig. 6.18(b)]. C'est une manifestation claire du transfert de spin induit par l'effet Hall de spin: le courant de spin généré par SHE dans le Pt est injecté dans le Py et modifie la précession de l'aimantation via le transfert de spin, ce qui se traduit par une augmentation ou une diminution du taux de relaxation selon la direction du courant.

L'efficacité du transfert de spin induit par l'effet Hall de spin peut être quantifié à l'aide de l'équation de Landau et Lifshitz en introduisant le terme qui correspond au transfert de spin:

$$\frac{d\mathbf{M}}{dt} = -\gamma \mathbf{M} \times \mathbf{H}_{\text{eff}} + \frac{\alpha \mathbf{M}}{M_s}\frac{d\mathbf{M}}{dt} + \frac{J_s}{M_s t}(\mathbf{M} \times \sigma \times \mathbf{M}), \tag{6.4.6}$$

où J_s est la courant de spin et σ est la direction du moment magnétique des électrons injectés.

Pour les ondes de spin de surface, où la composante statique de l'aimantation est colinéaire avec le courant de spin injecté, le transfert de spin agit directement sur le taux de relaxation comme

$$\Delta\Gamma_{\text{STT}} = \theta_{\text{SH}}^{\text{STT}} \frac{\mu_B}{e M_s t_{\text{Py}}} J_{\text{Pt}} = \sigma_{\text{SH}}^{\text{STT}} \frac{\mu_B}{e M_s t_{\text{Py}}} E, \tag{6.4.7}$$

où $\theta_{\text{SH}}^{\text{STT}}$ est l'angle de Hall effectif, J_{Pt} est la fraction de courant qui circule dans le Pt et $\sigma_{\text{SH}}^{\text{STT}}$ est la conductance de Hall. Pour évaluer la valeur de l'angle de Hall effectif, nous avons d'abord estimé la fraction de courant qui circule dans le Pt. Pour cela nous avons utilisé des mesures 4 points de la résistance des bicouches de Py/Pt. Nous avons ensuite estimé les conductivités des couches individuelles et les fractions de courant qui circulent dans le Py et Pt. En se basant sur la dépendance de $\Delta\Gamma_{\text{STT}}$ en fonction de J_{Pt} mesurée expérimentalement, nous avons déduit un angle de Hall effectif de 0.1, qui ne dépend pas significativement de l'épaisseur du Py. Pour éviter le problème lié à l'estimation de la fraction de courant qui circule dans le Pt, l'effet Hall de spin peut être quantifié à l'aide de la conductance de Hall $\sigma_{\text{SH}}^{\text{STT}}$, laquelle est définie comme $\sigma_{\text{SH}}^{\text{STT}} = J_s/E$, où $E = V/L$ est le champ électrique et V est la tension mesurée sur les contacts intérieurs séparés par la distance L. Comme dans le cas de l'angle de Hall, nous avons trouvé que la conductivité de Hall reste pratiquement constante dans la gamme

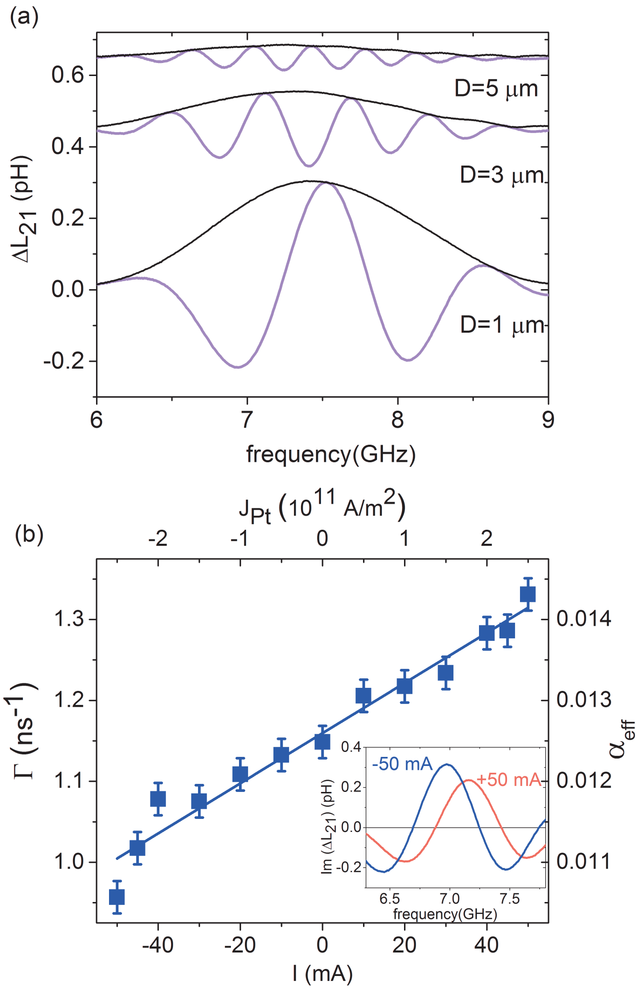

Figure 6.18: (a) Spectres d'inductance mutuelle mesurés à $\mu_0 H = 37$ mT dans une bicouche Py(15 nm)/Pt(10 nm) avec $w = 10$ μm, $D = 1, 3, 5$ μm. (b) Taux de relaxation de l'onde de spin en fonction du courant appliqué. (insert en bas) Signal mesuré à $I = \pm 50$ mA.

d'épaisseur étudiée et vaut environ $4 \cdot 10^5$ S/m. Cette valeur est comparable à la valeur de la conductance de Hall intrinsèque calculée pour le platine par méthode ab-initio [44, 83], ce qui nous permet de supposer que le mécanisme dominant est le SHE intrinsèque.

En conclusion, nous avons pu montrer qu'une onde de spin propagative peur être considérablement amplifiée par le transfert de spin induit par effet Hall de spin. Nous avons quantifié l'efficacité de SHE-STT en montrant que SHE-STT modifie le taux de relaxation d'une onde de spin avec un vecteur d'onde k fini aussi efficacement qu'un mode uniforme avec $k = 0$ [6]. Une amplification encore plus significative demanderait une optimisation de la multicouche utilisée.

Propagation des ondes de spin dans des couches minces epitaxiées de Fe

Une autre façon d'obtenir une propagation d'onde de spin sur une longue distance est d'utiliser un matériau possédant un facteur d'amortissement intrinsèque faible, comme le fer. Malgré les propriétés particulièrement prometteuses de Fe, telles qu'une aimantation à saturation élevée et un faible coefficient d'amortissement de la précession, la propagation des ondes de spin dans le fer pur n'avait jamais été étudiée. Nous avons étudié les couches minces de Fe(001) de 10-20 nm qui ont été déposées sur des substrats de MgO par épitaxie à jet moléculaire.

Dans un premier temps, nous avons effectué des mesures en réflexion pour sonder les propriétés magnétique du matériau. Pour cela, nous avons mesuré la variation de la fréquence de résonance des ondes de spin (Fig. 6.19). Deux valeurs de vecteur d'onde ($k_{\mathrm{M}} = 3.9\ \mu\mathrm{m}^{-1}$ et $k_{\mathrm{s}} = 1.5\ \mu\mathrm{m}^{-1}$) et deux géométries ($k \parallel [100], \mathbf{H} \parallel [010]$ et $k \parallel [110], \mathbf{H} \parallel [1-10]$) ont été utilisées. D'après les courbes obtenues, nous avons pu extraire une aimantation effective $\mu_0 M_{\mathrm{eff}} = 2.08$ T, ainsi qu'un champ d'anisotropie cubique $H_K = (2K_1)/(\mu_0 M_s) = 58$ mT où $K_1 = 5 \cdot 10^4$ J/m^3 est la constante d'anisotropie cubique. D'après la fréquence mesurée pour le mode PSSW1 (first perpendicular standing spin wave, diamants sur la Fig 6.19), qui possède un profil antisymetrique à travers l'epaisseur du film, nous avons déterminé une constante d'échange $A = 19$ pJ/m. Tous les paramètres magnétiques déterminés dans notre film sont en excellent accord avec ceux rapportés pour le fer massif [20, 59].

Dans un deuxième temps, nous avons effectué des mesures en transmission pour étudier la propagation des ondes de spin en analysant les paramètres principaux de la propagation tels que la vitesse de propagation, la

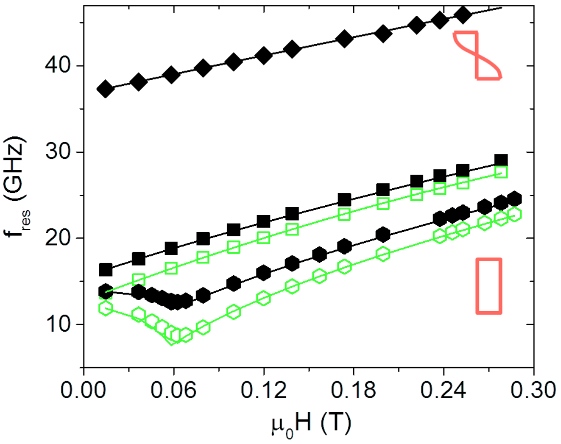

Figure 6.19: Dépendance en champ magnétique de la fréquence mésuré dans une couche de Fe de 20 nm. Les symboles pleins et ouverts correspondent respectivement au pic principal ($k_{\mathrm{M}} = 3.9\ \mu\mathrm{m}^{-1}$) et au pic secondaire ($k_{\mathrm{M}} = 1.5\ \mu\mathrm{m}^{-1}$). Les carrés et hexagones montrent la fréquence du mode MSSW dans deux configurations: ($k \parallel [100], \mathbf{H} \parallel [010]$) et ($k \parallel [110], \mathbf{H} \parallel [1-10]$), respectivement; les diamants montrent la fréquence du mode PSSW1 dans la première géométrie.

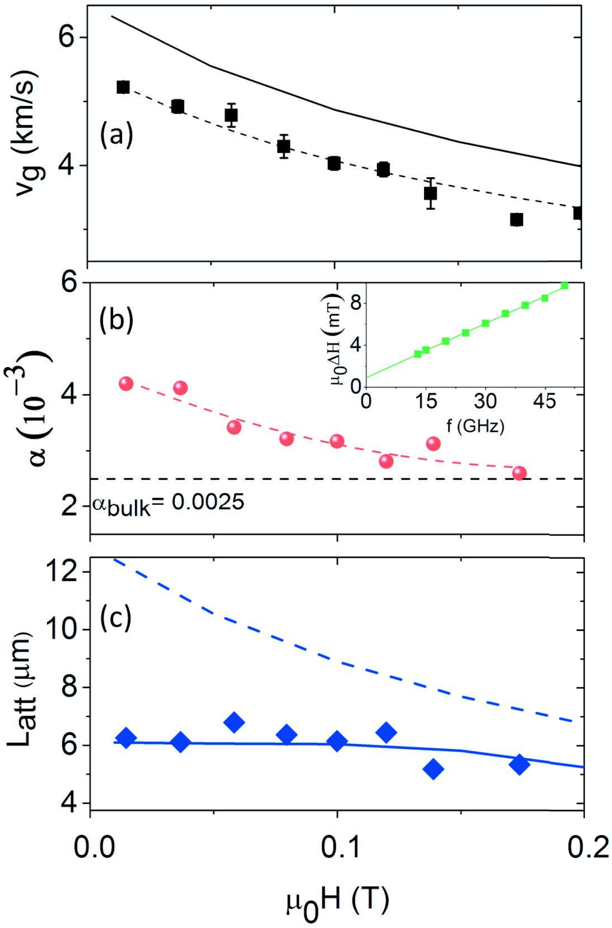

Figure 6.20: Propagation des ondes de spin dans un film MgO/Fe(20nm)/MgO. Dépendance de la vitesse de groupe (a), de l'amortissement (b) et de la longueur d'atténuation (c) en fonction du champ magnétique. Les points correspondent aux données expérimentales; les lignes continues représentent le modèle théorique; les lignes pointillés sur (a) et (b) sont des fits polynomiaux, la ligne pointillée sur (c) est déduite en utilisant ces fits selon la relation $L_{\text{att}} = v_g/\Gamma$.

longeure d'attenuation et le facteur d'amortissement. Pour ce faire, la méthode d'analyse décrite dans le cas de Py/Pt a été utilisé, i.e. nous avons comparé les spectres d'inductance mutuelle mesurés pour différentes distances de propagation et nous avons analysé la dépendance en distance de l'amplitude et de la période des signaux de propagation. Les résultats sont montrés sur la figure 6.20. Nous avons mesuré une vitesse de groupe de 5 km/s à $\mu_0 H = 36$ mT qui décroît avec le champ magnétique [Fig. 6.20(a)], ce qui est en relativement bon accord avec la dépendance théorique calculée en utilisant les paramètres magnétiques cités plus haut. L'amortissement de l'onde de spin α_{eff} a été estimée à partir de la mesure du taux de relaxation, en utilisant la relation $\Gamma = \alpha_{\mathrm{eff}}(\omega_0 + \omega_M/2)$ avec $\omega_0 = \gamma\mu_0(H + H_K)$ et $\omega_M = \gamma\mu_0 M_s$. Nous avons observé que α_{eff} décroît significativement en fonction de H et atteint une valeur asymptotique de 0.0025 à champ élevé [Fig. 6.20(b)]. Cette valeur est une valeur typique pour le Fe massif [12, 132] et pour des couches minces épitaxiales de bonne qualité [112, 131]. L'augmentation de l'amortissement à champ faible est attribuée à d'autres sources de relaxation des ondes de spin s'ajoutant à l'amortissement de Gilbert conventionnel [138]. Finalement, nous avons analysé la variation de la longueur d'atténuation en fonction du champ [Fig. 6.20(c)]. Les mesures montrent que L_{att} a une valeur presque constante de 6 μm. Cette valeur est significativement plus petite que celle calculée théoriquement en prenant compte le facteur d'amortissement constant de 0.0025. Néanmoins, la longueur d'atténuation mesurée dans la couche mince de Fe reste assez élevée en comparaison avec les valeurs mesurées dans d'autres matériaux.

Dans un troisième temps, nous avons analysé la capacité de ce matériau à conduire un courant polarisé en spin. Pour cela, nous avons effectué des mesures d'effet Doppler d'onde de spin induit par un courant électrique [136]. L'effet se manifeste par un décalage de la fréquence de l'onde de spin dû à l'interaction entre les électrons de conduction et l'aimantation dynamique via le transfert de spin adiabatique. Ce décalage en fréquence est proportionnel au produit du vecteur d'onde $\mathbf{k}$ et de la vitesse effective des électrons $\mathbf{u}$, $\delta f_{\mathrm{dop}} = \mathbf{k} \cdot \mathbf{u}$, où $\mathbf{u} = \mu_B/(eM_s)P\mathbf{J}$, P étant le degré de polarisation en spin du courant. La figure 6.21 montre le décalage en fréquence mesuré en inversant le sens du courant ($I = \pm 10$ mA). Ce décalage a été mesuré pour les deux sens de propagation (δ_{12} correspond à $k < 0$ et δ_{21} correspond à $k > 0$). La différence entre ces deux décalages en fréquence ($|\delta_{12}| < |\delta_{21}|$) est due au fait que les quantités δ_{12} et δ_{21} contiennent le décalage en fréquence induit par l'effet Doppler (impair en k), mais aussi le décalage en fréquence induit par le champ d'Oersted (pair en k) [50]. Le décalage Doppler peut être donc déterminé comme $\delta f_{\mathrm{dop}} = (\delta_{21} - \delta_{12})/4$. En mesurant le décalage

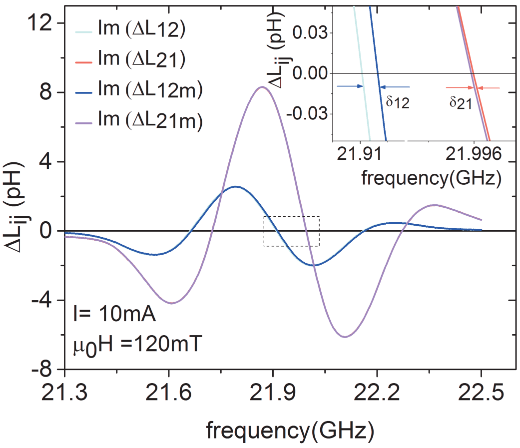

Figure 6.21: Spectres d'inductance mutuelle mesurés sur un film MgO/Fe(20 nm)/MgO à $\mu_0 H = 120$ mT et à courant électrique $I = \pm 10$ mA. Les décalages en fréquence sont montré pour un vecteur d'onde positif (k_{21}) et pour un courant $I > 0$ (courbe rose) et $I < 0$ (courbe rouge), ainsi que pour un vecteur d'onde négatif (k_{12})et pour un courant $I > 0$ (courbe cyan) et $I < 0$ (courbe bleue).

Doppler en fonction du courant nous avons pu extraire le degré de polarisation en spin du courant P qui atteint une valeur de 83% à température ambiante. Cette valeur est nettement plus élevée que les valeurs mesurées dans le permalloy [50] et également plus élevé que d'autres valeurs de polarisation prédites théoriquement ou mesurées par d'autres techniques dans le fer [146, 123]. Cette valeur élevée du degré de polarisation peut être attribuée à une forte asymétrie en spin de la diffusion des électrons par les phonons [133].

Ainsi, nous avons montré qu'une couche mince epitaxiée de fer est un milieu approprié pour la propagation des onde de spin grâce à son faible amortissement et à sa forte aimantation à saturation. De plus, nous avons montré que le transport électrique dans le fer à température ambiante est fortement polarisé en spin, ce qui est attribué à une significative asymétrie en spin du couplage électron-phonon.

Conclusion

Les systèmes magnétiques Py/Al_2O_3, Py/Pt et Fe/MgO ont été étudiés par spectroscopie d'ondes de spin. En analysant la propagation des ondes de surface dans les couches Py/Al_2O_3 et Py/Pt, nous avons montré que la non-réciprocité en fréquence, qui est généralement présente pour ce mode d'onde de spin, est induite par deux sources, l'interaction Dzyaloshinskii-Moriya interfaciale et l'asymétrie des anisotropies magnétiques de surface. La première domine dans les couches ultra-minces et la deuxième domine dans les couches épaisses. En injectant un courant électrique dans les couches Py/Pt nous avons observé une modification du taux de relaxation des ondes de spin due au transfert de spin induit par effet Hall de spin. Nous avons montré que cet effet est aussi efficace pour une excitation non-uniforme que pour un mode uniforme, et donc qu'il peut être utilisé pour controler électriquement la propagation des ondes de spin.

D'autre part, nous avons montré que dans une couche épitaxiée de fer les ondes de spin peuvent se propager sur des distances beaucoup plus longues que dans Py (dizaines de μm) principalement grâce au faible coefficient d'amortissement mesuré dans ce matériau. Nous avons aussi trouvé une valeur élevée du degré de polarisation en spin de courant qui atteint 83% à température ambiante. Ces propriétés font du fer un candidat très prometteur pour des développements futurs de dispositifs magnoniques.

Bibliography

[1] F. Abiza. Résonance ferromagnétique large-bande dans un film de fer monocristallin. Master's thesis, Université de Strasbourg, 2015.

[2] P. B. Allen. Electron-phonon effects in the infrared properties of metals. *Physical Review B*, 3(2):305–320, Jan 1971.

[3] P. B. Allen. New method for solving boltzmann equation for electrons in metals. *Physical Review B*, 17(10):3725–3734, May 1978.

[4] P. B. Allen. Empirical electron-phonon Î» values from resistivity of cubic metallic elements. *Physical Review B*, 36(5):2920–2923, Aug 1987.

[5] Z. An, F. Q. Liu, Y. Lin, and C. Liu. The universal definition of spin current. *Scientific Reports*, 2, May 2012.

[6] K. Ando, S. Takahashi, K. Harii, K. Sasage, J. Ieda, S. Maekawa, and E. Saitoh. Electric manipulation of spin relaxation using the spin hall effect. *Physical Review Letters*, 101(3):036601, Jul 2008.

[7] A. Azevedo, L. H. Vilela-Leão, R. L. Rodríguez-Suárez, A. F. Lacerda Santos, and S. M. Rezende. Spin pumping and anisotropic magnetoresistance voltages in magnetic bilayers: Theory and experiment. *Physical Review B*, 83:144402, Apr 2011.

[8] G. C. Bailey and C. Vittoria. Presence of magnetic surface anisotropy in permalloy films. *Physical Review B*, 8(7):3247–3251, Oct 1973.

[9] J. Banhart, H. Ebert, and A. Vernes. Applicability of the two-current model for systems with strongly spin-dependent disorder. *Physical Review B*, 56(16):10165–10171, Oct 1997.

[10] M. Belmeguenai, J.-P. Adam, Y. Roussigné, S. Eimer, T. Devolder, J.-V. Kim, S. M. Cherif, A. Stashkevich, and A. Thiaville. Interfacial Dzyaloshinskii-Moriya interaction in perpendicularly magnetized

Pt/Co/AlO$_x$ ultrathin films measured by Brillouin light spectroscopy. *Physical Review B*, 91:180405, May 2015.

[11] L. Berger. Emission of spin waves by a magnetic multilayer traversed by a current. *Physical Review B*, 54(13):9353–9358, Oct 1996.

[12] S. M. Bhagat and P. Lubitz. Temperature variation of ferromagnetic relaxation in the 3 d transition metals. *Physical Review B*, 10(1):179–185, Jul 1974.

[13] F. Bloch. Zur theorie des ferromagnetismus. *Zeitschrift für Physik*, 61(3-4):206–219, Mar 1930.

[14] T. Bŕacher, F. Heussner, P. Pirro, T. Fischer, M. Geilen, B. Heinz, B. Ĺagel, A. A. Serga, and B. Hillebrands. Time- and power-dependent operation of a parametric spin-wave amplifier. *Applied Physics Letters*, 105(23):232409, Dec 2014.

[15] P. Bruno and J. P. Renard. Magnetic surface anisotropy of transition metal ultrathin films. *Applied Physics A Solids and Surfaces*, 49(5):499–506, Nov 1989.

[16] A. C. Bland and B. Heinrich, editors. *Ultrathin Magnetic Structures III*. Springer Berlin Heidelberg, 2004.

[17] C. S. Chang, M. Kostylev, E. Ivanov, J. Ding, and A. O. Adeyeye. The phase accumulation and antenna near field of microscopic propagating spin wave devices. *Applied Physics Letters*, 104(3):032408, Jan 2014.

[18] J.-Y. Chauleau, R. Weil, A. Thiaville, and J. Miltat. Magnetic domain walls displacement: Automotion versus spin-transfer torque. *Physical Review B*, 82(21):214414, Dec 2010.

[19] S. Cherepov, P. Khalili Amiri, J. G. Alzate, K. Wong, M. Lewis, P. Upadhyaya, J. Nath, M. Bao, A. Bur, T. Wu, and et al. Electric-field-induced spin wave generation using multiferroic magnetoelectric cells. *Applied Physics Letters*, 104(8):082403, Feb 2014.

[20] S. Chikazumi. *Physics of Ferromagnetisme*. Oxford University Press, 1997.

[21] A. V. Chumak, V. Vasyuchka, A. Serga, and B. Hillebrands. Magnon spintronics. *Nature Physics*, 11(6):453–461, Jun 2015.

[22] M. Collet, X. de Milly, O. d'Allivy Kelly, V. V. Naletov, R. Bernard, P. Bortolotti, J. Ben Youssef, V. E. Demidov, S. O. Demokritov, J. L. Prieto, and et al. Generation of coherent spin-wave modes in yttrium iron garnet microdiscs by spin-orbit torque. *Nat Comms*, 7:10377, Jan 2016.

[23] R. Damon and J. Eshbach. Magnetostatic modes of a ferromagnet slab. *Journal of Physics and Chemistry of Solids*, 19(3-4):308–320, May 1961.

[24] M. J. M. de Jong and C. W. J. Beenakker. Andreev reflection in ferromagnet-superconductor junctions. *Physical Review Letters*, 74(9):1657–1660, Feb 1995.

[25] Y. Dedkov, M. Fonin, U. Rüdiger, and G. Güntherodt. Spin-resolved photoelectron spectroscopy of the mgo/fe(110) system. *Applied Physics A*, 82(3):489–493, Nov 2005.

[26] Y. S. Dedkov, M. Fonin, U. Rüdiger, and G. Güntherodt. Growth and spin-resolved photoemission spectroscopy of the epitaxial α-al$_2$o$_3$/fe(110) system. *Applied Physics Letters*, 81(14):2584, 2002.

[27] V. E. Demidov, S. Urazhdin, E. R. J. Edwards, and S. O. Demokritov. Wide-range control of ferromagnetic resonance by spin hall effect. *Applied Physics Letters*, 99(17):172501, 2011.

[28] V. E. Demidov, S. Urazhdin, E. R. J. Edwards, M. D. Stiles, R. D. McMichael, and S. O. Demokritov. Control of magnetic fluctuations by spin current. *Physical Review Letters*, 107(10):107204, Sep 2011.

[29] V. E. Demidov, S. Urazhdin, A. B. Rinkevich, G. Reiss, and S. O. Demokritov. Spin hall controlled magnonic microwaveguides. *Applied Physics Letters*, 104(15):152402, Apr 2014.

[30] V. E. Demidov, S. Urazhdin, H. Ulrichs, V. Tiberkevich, A. Slavin, D. Baither, G. Schmitz, and S. O. Demokritov. Magnetic nano-oscillator driven by pure spin-current. *Nat Mater*, 11:1028–1031, Oct 2012.

[31] K. Di, V. L. Zhang, H. S. Lim, S. C. Ng, M. H. Kuok, J. Yu, J. Yoon, X. Qiu, and H. Yang. Direct observation of the Dzyaloshinskii-Moriya interaction in a Pt/Co/Ni film. *Physical Review Letters*, 114:047201, Jan 2015.

[32] B. Dieny. Quantitative interpretation of giant magnetoresistance properties of permalloy-based spin-valve structures. *EPL (Europhysics Letters)*, 17(3):261, Dec 1992.

[33] V. E. Dmitrienko, E. N. Ovchinnikova, S. P. Collins, G. Nisbet, G. Beutier, Y. O. Kvashnin, V. V. Mazurenko, A. I. Lichtenstein, and M. I. Katsnelson. Measuring the dzyaloshinskiiâ-moriya interaction in a weak ferromagnet. *Nature Physics*, 10(3):202–206, Feb 2014.

[34] M. Dyakonov and V. Perel. Current-induced spin orientation of electrons in semiconductors. *Physics Letters A*, 35(6):459–460, Jul 1971.

[35] M. I. Dyakonov. Magnetoresistance due to edge spin accumulation. *Physical Review Letters*, 99(12):126601, Sep 2007.

[36] I. E. Dzialoshinskii. Thermodynamic theory of "weak" ferromagnetism in antiferromagnetic substances. *Soviet Physics JETP*, 5(6):1259, 1957.

[37] H. Ebert, S. Mankovsky, D. Ḱodderitzsch, and P. J. Kelly. AbÂ initio calculation of the gilbert damping parameter via the linear response formalism. *Physical Review Letters*, 107(6):066603, Aug 2011.

[38] A. Fert and I. A. Campbell. Electrical resistivity of ferromagnetic nickel and iron based alloys. *Journal of Physics F: Metal Physics*, 6(5):849–871, May 1976.

[39] O. Gladii, M. Collet, K. Garcia-Hernandez, C. Cheng, S. Xavier, P. Bortolotti, V. Cros, Y. Henry, J.-V. Kim, A. Anane, and et al. Spin wave amplification using the spin hall effect in permalloy/platinum bilayers. *Applied Physics Letters*, 108(20):202407, May 2016.

[40] O. Gladii, M. Haidar, Y. Henry, M. Kostylev, and M. Bailleul. Frequency nonreciprocity of surface spin wave in permalloy thin films. *Physical Review B*, 93(5):054430, Feb 2016.

[41] Y. I. Gorobets and S. A. Reshetnyak. Reflection and refraction of spin waves in uniaxial magnets in the geometrical-optics approximation. *Technical Physics*, 43(2):188–191, Feb 1998.

[42] M. Gradhand, D. V. Fedorov, P. Zahn, and I. Mertig. Extrinsic spin hall effect from first principles. *Physical Review Letters*, 104:186403, May 2010.

[43] J. Grollier, P. Boulenc, V. Cros, A. Hamzić, A. Vaures, A. Fert, and G. Faini. Switching a spin valve back and forth by current-induced domain wall motion. *Applied Physics Letters*, 83(3):509, 2003.

[44] G. Y. Guo, S. Murakami, T.-W. Chen, and N. Nagaosa. Intrinsic spin hall effect in platinum: First-principles calculations. *Physical Review Letters*, 100(9):096401, Mar 2008.

[45] G. Y. Guo, Y. Yao, and Q. Niu. AbÂ initio calculation of the intrinsic spin hall effect in semiconductors. *Physical Review Letters*, 94(22):226601, Jun 2005.

[46] A. G. Gurevich and G. Melkov. *Magnetization oscillations and waves*. CRC Press, Boca Raton, 1996.

[47] B. A. Gurney, V. S. Speriosu, J.-P. Nozieres, H. Lefakis, D. R. Wilhoit, and O. U. Need. Direct measurement of spin-dependent conduction-electron mean free paths in ferromagnetic metals. *Physical Review Letters*, 71(24):4023–4026, Dec 1993.

[48] K. Y. Guslienko and A. N. Slavin. Magnetostatic green's functions for the description of spin waves in finite rectangular magnetic dots and stripes. *Journal of Magnetism and Magnetic Materials*, 323(18-19):2418–2424, Oct 2011.

[49] M. Haidar. *Role of surfaces in magnetization dy dynamics and spin polarized transport: a spin wave study*. PhD thesis, Université de Strasbourg, 2012.

[50] M. Haidar and M. Bailleul. Thickness dependence of degree of spin polarization of electrical current in permalloy thin films. *Physical Review B*, 88(5):054417, Aug 2013.

[51] M. Haidar, M. Bailleul, M. P. Kostylev, and Y. Lao. Nonreciprocal Oersted field contribution to the current-induced frequency shift of magnetostatic surface waves. *Physical Review B*, 89:094426, Mar 2014.

[52] A. Hallal, H. X. Yang, B. Dieny, and M. Chshiev. Anatomy of perpendicular magnetic anisotropy in fe/mgo magnetic tunnel junctions: First-principles insight. *Physical Review B*, 88(18):184423, Nov 2013.

[53] A. Hamadeh, O. d'Allivy Kelly, C. Hahn, H. Meley, R. Bernard, A. H. Molpeceres, V. V. Naletov, M. Viret, A. Anane, V. Cros, and et al.

Full control of the spin-wave damping in a magnetic insulator using spin-orbit torque. *Physical Review Letters*, 113(19):197203, Nov 2014.

[54] P. M. Haney, H.-W. Lee, K.-J. Lee, A. Manchon, and M. D. Stiles. Current induced torques and interfacial spin-orbit coupling: Semiclassical modeling. *Physical Review B*, 87(17), May 2013.

[55] Y. Henry, O. Gladii, and M. Bailleul. Propagating spin-wave normal modes: A dynamic matrix approach using plane-wave demagnetizating tensors. *arXiv:1611.06153*, 2016.

[56] B. Hillebrands. Spin-wave calculations for multilayered structures. *Physical Review B*, 41(1):530–540, Jan 1990.

[57] H. Hurdequint, N. Bouterfas, and A. Vaurés. Ferromagnetic resonance studies of Py bilayers for the system (Permalloy/Al_2O_3). *Journal of Applied Physics*, 75(10):6476, 1994.

[58] S. Ingvarsson, G. Xiao, S. Parkin, and W. Gallagher. Thickness-dependent magnetic properties of $Ni_{81}Fe_{19}$, $Co_{90}Fe_{10}$ and $Ni_{65}Fe_{15}Co_{20}$ thin films. *Journal of Magnetism and Magnetic Materials*, 251(2):202–206, Oct 2002.

[59] H. Jaffres, L. Ressier, K. Postava, A. Schuhl, F. Nguyen Van Dau, M. Goiran, J. Redouĺas, J. Peyrade, and A. Fert. Uniaxial magnetic anisotropy of thin epitaxial fe films nanostructured by the atomic saw method. *Journal of Magnetism and Magnetic Materials*, 184(1):19–27, Apr 1998.

[60] M. Jamali, J. H. Kwon, S.-M. Seo, K.-J. Lee, and H. Yang. Spin wave nonreciprocity for logic device applications. *Scientific Reports*, 3(3160):1, Nov 2013.

[61] P. D. Johnson. Spin-polarized photoemission. *Reports on Progress in Physics*, 60(11):1217, 1997.

[62] S.-W. Jung, W. Kim, T.-D. Lee, K.-J. Lee, and H.-W. Lee. Current-induced domain wall motion in a nanowire with perpendicular magnetic anisotropy. *Applied Physics Letters*, 92(20):202508, 2008.

[63] B. A. Kalinikos, N. G. Kovshikov, M. P. Kostylev, and H. Benner. Parametric amplification of propagating spin waves in ferrite films. *Le Journal de Physique IV*, 07(C1):455–456, Mar 1997.

[64] B. A. Kalinikos and S. A. N. Theory of dipole-exchange spin wave spectrum for ferromagnetic films with mixed exchange boundary conditions. *Journal of Physics C: Solid State Physics*, 19(35):7013, 1986.

[65] P. Khalili Amiri, B. Rejaei, M. Vroubel, and Y. Zhuang. Nonreciprocal spin wave spectroscopy of thin Ni-Fe stripes. *Applied Physics Letters*, 91(6):062502, 2007.

[66] A. Khitun, D. E. Nikonov, and K. L. Wang. Magnetoelectric spin wave amplifier for spin wave logic circuits. *Journal of Applied Physics*, 106(12):123909, 2009.

[67] C. Kittel. On the theory of ferromagnetic resonance absorption. *Physical Review*, 73(2):155–161, Jan 1948.

[68] S. Klingler, P. Pirro, T. Brächer, B. Leven, B. Hillebrands, and A. V. Chumak. Design of a spin-wave majority gate employing mode selection. *Applied Physics Letters*, 105(15):152410, Oct 2014.

[69] M. Kostylev. Non-reciprocity of dipole-exchange spin waves in thin ferromagnetic films. *Journal of Applied Physics*, 113(5):053907, 2013.

[70] M. Kostylev. Interface boundary conditions for dynamic magnetization and spin wave dynamics in a ferromagnetic layer with the interface dzyaloshinskii-moriya interaction. *Journal of Applied Physics*, 115(23):233902, Jun 2014.

[71] M. Kostylev, A. A. Stashkevich, A. O. Adeyeye, C. Shakespeare, N. Kostylev, N. Ross, K. Kennewell, R. Magaraggia, Y. Roussigné, and R. L. Stamps. Magnetization pinning in conducting films demonstrated using broadband ferromagnetic resonance. *Journal of Applied Physics*, 108(10):103914, 2010.

[72] T. Koyama, D. Chiba, K. Ueda, K. Kondou, H. Tanigawa, S. Fukami, T. Suzuki, N. Ohshima, N. Ishiwata, Y. Nakatani, and et al. Observation of the intrinsic pinning of a magnetic domain wall in a ferromagnetic nanowire. *Nat Mater*, 10(3):194–197, Feb 2011.

[73] B. K. Kuanr. Relaxation in epitaxial fe films measured by ferromagnetic resonance. *Journal of Applied Physics*, 95(11):6610, 2004.

[74] H. Kurebayashi, O. Dzyapko, V. E. Demidov, D. Fang, A. J. Ferguson, and S. O. Demokritov. Spin pumping by parametrically excited short-wavelength spin waves. *Applied Physics Letters*, 99(16):162502, 2011.

[75] R. Kurzawa, K.-P. Kämper, W. Schmitt, and G. Güntherodt. Spin-resolved photoemission study of in situ grown epitaxial fe layers on w(110). *Solid State Communications*, 60(10):777–780, 1986.

[76] L. D. Landau and E. M. Lifshitz. On the theory of the dispersion of magnetic permeability in ferromagnetic bodies. *Phys. Z. Sowjetunion*, 8(153):101–114, 1935. Collected papers of L.D. Landau,.

[77] P. Lederer and D. L. Mills. Possible experimental test of the band theory of magnetism. *Physical Review*, 148(2):542–547, Aug 1966.

[78] L. Liu, R. A. Buhrman, and D. C. Ralph. Review and analysis of measurements of the spin hall effect in platinum. *arXiv:1111.3702*, pages 1–32, 2012.

[79] L. Liu, T. Moriyama, D. C. Ralph, and R. A. Buhrman. Spin-torque ferromagnetic resonance induced by the spin hall effect. *Physical Review Letters*, 106(3):036601, Jan 2011.

[80] T. Liu, H. Chang, V. Vlaminck, Y. Sun, M. Kabatek, A. Hoffmann, L. Deng, and M. Wu. Ferromagnetic resonance of sputtered yttrium iron garnet nanometer films. *Journal of Applied Physics*, 115(17):17A501, May 2014.

[81] Y. Liu, Z. Yuan, R. J. H. Wesselink, A. A. Starikov, and P. J. Kelly. Interface enhancement of gilbert damping from first principles. *Physical Review Letters*, 113(20):207202, Nov 2014.

[82] B. Loegel and F. Gautier. Origine de la resistivite dans le cobalt et ses alliages dilues. *Journal of Physics and Chemistry of Solids*, 32(12):2723–2735, Jan 1971.

[83] S. Lowitzer, M. Gradhand, D. Ködderitzsch, D. V. Fedorov, I. Mertig, and H. Ebert. Extrinsic and intrinsic contributions to the spin hall effect of alloys. *Physical Review Letters*, 106(5):056601, Feb 2011.

[84] F. Ma and Y. Zhou. Interfacial Dzialoshinskii-Moriya interaction induced nonreciprocity of spin waves in magnonic waveguides. *RSC Adv.*, 4(87):46454–46459, 2014.

[85] S. S. Maekawa, S. O. Valenzuela, E. Saitoh, and T. Kimura. *Spin current*. Oxford University Press, 2012.

[86] G. Malinowski, O. Boulle, and M. Klöui. Current-induced domain wall motion in nanoscale ferromagnetic elements. *J. Phys. D: Appl. Phys.*, 44(38):384005, Sep 2011.

[87] I. I. Mazin. How to define and calculate the degree of spin polarization in ferromagnets. *Physical Review Letters*, 83(7):1427–1430, Aug 1999.

[88] I. Mertig, R. Zeller, and P. H. Dederichs. Ab initio calculations of residual resistivities for dilute ni alloys. *Physical Review B*, 47(24):16178–16185, Jun 1993.

[89] S. Mizukami, Y. Ando, and T. Miyazaki. Ferromagnetic resonance linewidth for nm/80Nife/nm films (nm=cu, ta, pd and pt). *Journal of Magnetism and Magnetic Materials*, 226-230:1640–1642, May 2001.

[90] E. Młyńczak, K. Freindl, N. Spiridis, and J. Korecki. Epitaxial mgo/fe(001) and fe/mgo(001): Structures of the interfaces. *Journal of Applied Physics*, 113(2):024320, 2013.

[91] J.-H. Moon, S.-M. Seo, K.-J. Lee, K.-W. Kim, J. Ryu, H.-W. Lee, R. D. McMichael, and M. D. Stiles. Spin-wave propagation in the presence of interfacial Dzyaloshinskii-Moriya interaction. *Physical Review B*, 88:184404, Nov 2013.

[92] M. Morota, Y. Niimi, K. Ohnishi, D. H. Wei, T. Tanaka, H. Kontani, T. Kimura, and Y. Otani. Indication of intrinsic spin hall effect in 4 d and 5 d transition metals. *Physical Review B*, 83(17):174405, May 2011.

[93] O. Mosendz, V. Vlaminck, J. E. Pearson, F. Y. Fradin, G. E. W. Bauer, S. D. Bader, and A. Hoffmann. Detection and quantification of inverse spin hall effect from spin pumping in permalloy/normal metal bilayers. *Physical Review B*, 82:214403, Dec 2010.

[94] N. Mott. Electrons in transition metals. *Advances in Physics*, 13(51):325–422, Jul 1964.

[95] S. S. Mukherjee, P. Deorani, J. H. Kwon, and H. Yang. Attenuation characteristics of spin-pumping signal due to traveling spin waves. *Physical Review B*, 85(9):094416, Mar 2012.

[96] S. Murakami. Intrinsic spin hall effect. *Advances in Solid State Physics*, 45:197–209, 2005.

[97] T. Nan, S. Emori, C. T. Boone, X. Wang, T. M. Oxholm, J. G. Jones, B. M. Howe, G. J. Brown, and N. X. Sun. Comparison of spin-orbit torques and spin pumping across nife/pt and nife/cu/pt interfaces. *Physical Review B*, 91(21):214416, Jun 2015.

[98] H. T. Nembach, J. M. Shaw, M. Weiler, E. Jué, and T. J. Silva. Linear relation between Heisenberg exchange and interfacial Dzyaloshinskii-Moriya interaction in metal films. *Nature Physics*, 11(10):825–829, Aug 2015.

[99] M. Obstbaum, M. Hartinger, H. G. Bauer, T. Meier, F. Swientek, C. H. Back, and G. Woltersdorf. Inverse spin hall effect in $\mathrm{ni}_{81}\mathrm{fe}_{19}$ /normal-metal bilayers. *Physical Review B*, 89(6):060407, Feb 2014.

[100] J. Okabayashi, J. W. Koo, H. Sukegawa, S. Mitani, Y. Takagi, and T. Yokoyama. Perpendicular magnetic anisotropy at the interface between ultrathin fe film and mgo studied by angular-dependent x-ray magnetic circular dichroism. *Applied Physics Letters*, 105(12):122408, Sep 2014.

[101] C.-F. Pai, Y. Ou, L. H. Vilela-LeÃ£o, D. C. Ralph, and R. A. Buhrman. Dependence of the efficiency of spin hall torque on the transparency of pt/ferromagnetic layer interfaces. *Physical Review B*, 92(6):064426, Aug 2015.

[102] C. E. Patton. Relaxation processes for ferromagnetic resonance in thin films. *Journal of Applied Physics*, 38(3):1358, 1967.

[103] K. Perzlmaier, G. Woltersdorf, and C. H. Back. Observation of the propagation and interference of spin waves in ferromagnetic thin films. *Physical Review B*, 77(5), Feb 2008.

[104] D. Ralph and M. Stiles. Spin transfer torques. *Journal of Magnetism and Magnetic Materials*, 320(7):1190–1216, Apr 2008.

[105] J. O. Rantschler, P. J. Chen, A. S. Arrott, R. D. McMichael, W. F. Egelhoff, and B. B. Maranville. Surface anisotropy of permalloy in NM/NiFe/NM multilayers. *Journal of Applied Physics*, 97(10):10J113, 2005.

[106] B. Raquet, M. Viret, E. Sondergard, O. Cespedes, and R. Mamy. Electron-magnon scattering and magnetic resistivity in 3 d ferromagnets. *Physical Review B*, 66(2):024433, Jul 2002.

[107] J.-C. Rojas-Sánchez, N. Reyren, P. Laczkowski, W. Savero, J.-P. Attané, C. Deranlot, M. Jamet, J.-M. George, L. Vila, and H. Jaffrès. Spin pumping and inverse spin hall effect in platinum: The essential role of spin-memory loss at metallic interfaces. *Physical Review Letters*, 112(10):106602, Mar 2014.

[108] U. Roy, H. Seinige, F. Ferdousi, J. Mantey, M. Tsoi, and S. K. Banerjee. Spin-transfer-torque switching in spin valve structures with perpendicular, canted, and in-plane magnetic anisotropies. *Journal of Applied Physics*, 111(7):07C913, 2012.

[109] A. Ruiz-Calaforra, T. Bracher, V. Lauer, P. Pirro, B. Heinz, M. Geilen, A. V. Chumak, A. Conca, B. Leven, and B. Hillebrands. The role of the non-magnetic material in spin pumping and magnetization dynamics in nife and cofeb multilayer systems. *Journal of Applied Physics*, 117(16):163901, Apr 2015.

[110] C. W. Sandweg, Y. Kajiwara, K. Ando, E. Saitoh, and B. Hillebrands. Enhancement of the spin pumping efficiency by spin wave mode selection. *Applied Physics Letters*, 97(25):252504, 2010.

[111] S. Y. Savrasov and D. Y. Savrasov. Electron-phonon interactions and related physical properties of metals from linear-response theory. *Physical Review B*, 54(23):16487–16501, Dec 1996.

[112] C. Scheck, L. Cheng, and W. E. Bailey. Low damping in epitaxial sputtered iron films. *Applied Physics Letters*, 88(25):252510, 2006.

[113] T. Schneider, A. A. Serga, T. Neumann, B. Hillebrands, and M. P. Kostylev. Phase reciprocity of spin-wave excitation by a microstrip antenna. *Physical Review B*, 77:214411, Jun 2008.

[114] M. A. W. Schoen, D. Thonig, M. L. Schneider, T. J. Silva, H. T. Nembach, O. Eriksson, O. Karis, and J. M. Shaw. Ultra-low magnetic damping of a metallicÂ ferromagnet. *Nature Physics*, 12(9):839–842, May 2016.

[115] T. Sebastian, Y. Ohdaira, T. Kubota, P. Pirro, T. Brächer, K. Vogt, A. A. Serga, H. Naganuma, M. Oogane, Y. Ando, and et al. Low-damping spin-wave propagation in a micro-structured co2mn0.6Fe0.4Si heusler waveguide. *Applied Physics Letters*, 100(11):112402, 2012.

[116] K. Sekiguchi, K. Yamada, S. M. Seo, K. J. Lee, D. Chiba, K. Kobayashi, and T. Ono. Nonreciprocal emission of spin-wave packet in FeNi film. *Applied Physics Letters*, 97(2):022508, 2010.

[117] K. Sekiguchi, K. Yamada, S.-M. Seo, K.-J. Lee, D. Chiba, K. Kobayashi, and T. Ono. Time-domain measurement of current-induced spin wave dynamics. *Physical Review Letters*, 108(1):017203, Jan 2012.

[118] S.-M. Seo, K.-J. Lee, H. Yang, and T. Ono. Current-induced control of spin-wave attenuation. *Physical Review Letters*, 102(14):147202, Apr 2009.

[119] J. Sinova, D. Culcer, Q. Niu, N. A. Sinitsyn, T. Jungwirth, and A. H. MacDonald. Universal intrinsic spin hall effect. *Physical Review Letters*, 92(12):126603, Mar 2004.

[120] J. Sinova, S. O. Valenzuela, J. Wunderlich, C. H. Back, and T. Jungwirth. Spin hall effects. *Rev. Mod. Phys.*, 87(4):1213–1260, Oct 2015.

[121] J. Slonczewski. Current-driven excitation of magnetic multilayers. *Journal of Magnetism and Magnetic Materials*, 159(1-2):L1–L7, Jun 1996.

[122] R. J. Soulen, M. S. Osofsky, B. Nadgorny, T. Ambrose, P. Broussard, S. F. Cheng, J. Byers, C. T. Tanaka, J. Nowack, J. S. Moodera, and et al. Andreev reflection: A new means to determine the spin polarization of ferromagnetic materials. *Journal of Applied Physics*, 85(8):4589, 1999.

[123] R. J. Soulen Jr. Measuring the spin polarization of a metal with a superconducting point contact. *Science*, 282(5386):85–88, Oct 1998.

[124] D. D. Stancil and A. Prabhakar. *Spin Waves. Theory and applications.* Springer US, 1 edition, 2009.

[125] A. A. Stashkevich, M. Belmeguenai, Y. Roussigné, S. M. Cherif, M. Kostylev, M. Gabor, D. Lacour, C. Tiusan, and M. Hehn. Experimental study of spin-wave dispersion in Py/Pt film structures in the presence of an interface Dzyaloshinskii-Moriya interaction. *Physical Review B*, 91:214409, Jun 2015.

[126] T. Tanaka, H. Kontani, M. Naito, T. Naito, D. S. Hirashima, K. Yamada, and J. Inoue. Intrinsic spin hall effect and orbital hall effect in 4 d and 5 d transition metals. *Physical Review B*, 77(16):165117, Apr 2008.

[127] G. Tatara and H. Kohno. Theory of current-driven domain wall motion: Spin transfer versus momentum transfer. *Physical Review Letters*, 92(8):086601, Feb 2004.

[128] A. Tonomura, X. Yu, K. Yanagisawa, T. Matsuda, Y. Onose, N. Kanazawa, H. S. Park, and Y. Tokura. Real-space observation of skyrmion lattice in helimagnet mnsi thin samples. *Nano Lett.*, 12(3):1673–1677, Mar 2012.

[129] Y. Tserkovnyak, A. Brataas, and G. E. W. Bauer. Spin pumping and magnetization dynamics in metallic multilayers. *Physical Review B*, 66(22):224403, Dec 2002.

[130] E. Y. Tsymbal and D. G. Pettifor. Effects of band structure and spin-independent disorder on conductivity and giant magnetoresistance in co/cu and fe/cr multilayers. *Physical Review B*, 54(21):15314–15329, Dec 1996.

[131] R. Urban, G. Woltersdorf, and B. Heinrich. Gilbert damping in single and multilayer ultrathin films: Role of interfaces in nonlocal spin dynamics. *Physical Review Letters*, 87(21):217204, Nov 2001.

[132] L. van Bockstal and F. Herlach. Ferromagnetic relaxation in 3d metals at far infrared frequencies in high magnetic fields. *Journal of Physics: Condensed Matter*, 2(34):7187, 1990.

[133] M. J. Verstraete. Ab initio calculation of spin-dependent electron-phonon coupling in iron and cobalt. *J. Phys.: Condens. Matter*, 25(13):136001, Mar 2013.

[134] V. Vlamicnk. *Décalage Doppler d'onde de spin induit par un courant electrique*. PhD thesis, Institut de Physique et chimie des matériaux de Strasbourg, 2008.

[135] V. Vlaminck and M. Bailleul. Current-induced spin-wave doppler shift. *Science*, 322(5900):410–413, Oct 2008.

[136] V. Vlaminck and M. Bailleul. Spin-wave transduction at the submicrometer scale: Experiment and modeling. *Physical Review B*, 81:014425, 2010.

[137] L. R. Walker. Magnetostatic modes in ferromagnetic resonance. *Physical Review*, 105(2):390–399, Jan 1957.

[138] G. Woltersdorf and B. Heinrich. Two-magnon scattering in a self-assembled nanoscale network of misfit dislocations. *Physical Review B*, 69(18):184417, May 2004.

[139] T. K. Yamada, Y. Sakaguchi, L. Gerhard, and W. Wulfhekel. Temperature control of the growth of iron oxide nanoislands on fe(001). *Japanese Journal of Applied Physics*, 55(8S1):08NB14, Jul 2016.

[140] H. Yu, O. d. Kelly, V. Cros, R. Bernard, P. Bortolotti, A. Anane, F. Brandl, R. Huber, I. Stasinopoulos, and D. Grundler. Magnetic thin-film insulator with ultra-low spin wave damping for coherent nanomagnonics. *Scientific Reports*, 4:6848, Oct 2014.

[141] X. Z. Yu, N. Kanazawa, Y. Onose, K. Kimoto, W. Z. Zhang, S. Ishiwata, Y. Matsui, and Y. Tokura. Near room-temperature formation of a skyrmion crystal in thin-films of the helimagnet fege. *Nat Mater*, 10(2):106–109, Dec 2010.

[142] K. Zakeri, Y. Zhang, J. Prokop, T.-H. Chuang, N. Sakr, W. X. Tang, and J. Kirschner. Asymmetric spin-wave dispersion on fe(110): Direct evidence of the dzyaloshinskii-moriya interaction. *Physical Review Letters*, 104(13):137203, Mar 2010.

[143] S. Zhang and Z. Li. Roles of nonequilibrium conduction electrons on the magnetization dynamics of ferromagnets. *Physical Review Letters*, 93(12):127204, Sep 2004.

[144] W. Zhang, W. Han, X. Jiang, S.-H. Yang, and S. S. P. Parkin. Role of transparency of platinum/ferromagnet interfaces in determining the intrinsic magnitude of the spin hall effect. *Nature Physics*, 11(6):496–502, Apr 2015.

[145] M. Zhu, B. D. Soe, R. D. McMichael, M. J. Carey, S. Maat, and J. R. Childress. Enhanced magnetization drift velocity and current polarization in $(\mathrm{cofe})_{1-x}\mathrm{ge}_x$ alloys. *Applied Physics Letters*, 98(7):072510, 2011.

[146] Z. Y. Zhu, H. W. Zhang, S. F. Xu, J. L. Chen, G. H. Wu, B. Zhang, and X. X. Zhang. Intrinsic anisotropy of degree of transport spin polarization in typical ferromagnets. *J. Phys.: Condens. Matter*, 20(27):275245, Jun 2008.

UNIVERSITÉ DE STRASBOURG

Olga GLADII

Spin wave propagation and its modification by an electrical current in Py/Al_2O_3, Py/Pt and Fe/MgO films

ECOLE DOCTORALE pcp

Résumé

Des mesures d'ondes de spin propagatives ont été réalisées pour caractériser deux effets de l'interaction spin-orbite ainsi que le transport électrique dépendant du spin. Les effets du couplage spin-orbite ont été étudiés dans des bicouches nickel-fer/platine. Dans ces films, les fréquences de deux ondes de spin contre-propageantes ne sont pas les mêmes, ce qui est attribué à l'effet combiné d'une interaction magnétique chirale appelée interaction Dzyaloshinskii-Moriya et d'une asymétrie dans l'épaisseur du film magnétique. En appliquant le courant électrique dans ce système nous avons observé une modification du taux de relaxation de l'onde de spin qui est attribuée au transfert de spin induit par effet Hall de spin. D'autre part, les études de propagation d'ondes de spin dans une couche mince de fer épitaxié à température ambiante ont montré une polarisation en spin du courant électrique de 83%, ce qui est attribué à une forte asymétrie du couplage électron-phonon.

Mots-clés: interaction Dzyaloshinskii-Moriya, transfert de spin induit par effet Hall de spin, transport polarisé en spin, onde de spin

Résumé en anglais

Propagating spin wave measurements were realised to characterize two spin-orbit related phenomena, as well as spin dependent electrical transport. The effects of spin-orbit coupling have been studied in nickel-iron/platinum bilayers. It has been shown that in these films the frequencies of two counter-propagating spin waves are not the same, which is attributed to the combined effects of a chiral magnetic interaction named Dzyaloshinskii-Moriya interaction and an asymmetry of the magnetic properties across the film thickness. By applying an electrical current in such system we have observed a modification of the spin wave relaxation rate due to the spin transfer torque induced by spin Hall effect. On the other hand, from the study of spin wave propagation in thin epitaxial iron films at room temperature, a degree of spin polarization of the electrical current of 83% was extracted, which is attributed to a significant spin-asymmetry of the electron-phonon coupling.

Keywords: Dzyaloshinskii-Moriya interaction, spin Hall induced spin transfer torque, spin-polarized transport, spin wave